Scramjet Combustion Modeling Using Eddy Dissipation Model

Jimmy-John O.E. Hoste

Department of Mechanical and Aerospace Engineering
University of Strathclyde

This dissertation is submitted for the degree of
Doctor of Philosophy

August 2018

I would like to dedicate this thesis to my loving grandfather that left us before I could
finalize this work. I know you would be proud of me.

Declaration

This thesis is the result of the author's original research. It has been composed by the author and has not been previously submitted for examination which has led to the award of a degree.

Jimmy-John O.E. Hoste
August 2018

Abstract

In order to aid in the design of scramjet propulsion systems at high Mach number operation, this works considers the Eddy Dissipation Model (EDM) to describe the combustion process inside an open-access Computational Fluid Dynamics (CFD) solver. Typical CFD modeling approaches for turbulent supersonic reacting flows are associated with a high computational cost. This in turn inhibits the use of CFD in scramjet combustor design or in higher level preliminary designs such as the trajectory optimization process of a scramjet powered vehicle. Instead, low-fidelity models are preferred to charaterize the propulsion system in the latter type of application. The EDM relies on simplified assumptions regarding the combustion process whose validity is thought to be prevalent at high Mach number scramjet operation. It is therefore a suitable candidate model in order to introduce more routinely CFD in scramjet preliminary design phases. As part of the present work, first steps include the selection of an open-source CFD solver followed by several validation studies. After its implementation, a critical numerical analysis of the EDM is performed by considering three hydrogen-fueled experimental scramjet configurations with different fuel injection approaches. Its application is further investigated with a mainly kinetically controlled scramjet design where the underlying assumptions of the EDM are not valid anymore. Finally, the EDM is applied to a combustor design problem demonstrating the metrics of interest that can be relied on for this task.

Acknowledgements

I would like to start by thanking Richard Brown for giving me the opportunity to come to Glasgow and start a new chapter of my life. I'm also very grateful to my supervisors Ian Taylor and Marco Fossati for guiding me during my PhD adventure as it has been a very challenging period. Thank you Edmondo Minisci, Christie Maddock and Tom Scanlon for always being available at and outside the office. David Garcia Cava for the many discussions over coffee.

Thanks to the many friends at FASTT whom became my family during those years: Robert Garner, Federico Toso, Viola Renato, Alessandro "Master" Mogavero, Javier Herrera Montojo, Daniel Espinoza, Martin Kubícek and Romain Wuilbercq. It was my pleasure to be amongst you. Especially my partner in crime Rob in those last stressful Glaswegian months. Merci Vincent Casseau d'avoir été un très bon ami, j'ai vraiment bien apprecié notre collaboration et j'espère que l'on pourra continuer dans le futur. Thank you Áine for making my last months in Glasgow so cheerful. I wish you good luck with your coming PhD years. Special thanks to Nicolas Thiry for the great moments in my early time in Glasgow as well as Ciara McGrath. Thank you my Napolitan friends Giuseppe Daniele Di Martino, Daniela Puorto and Giulia Esposito for the fun times during your stay in Glasgow: "Op a bakkes". Thank you for introducing me to the wings Wednesday events Chimney Bryan and Thomas Lilley. Thank you Mateusz Polnik for your expertise and participation in my coffee addiction. Gaetano Pascarella for the last culinary months in Glasgow: stay sweet.

Special thanks to the many friends whom came to visit me in Glasgow: Glenn, Bjorn, Amelie, Dieter, Julie, Nymfa, Quentin, Paulien, Ruben, Daan, Annemie, Sam, Tanguy, Alexandre, Robin, Aline, Vincent, Eleonora, Sholto, Máté and others I might have omitted.

Thank you Tamás Józsa for being a brother in arms since our time in Cranfield. It's always a pleasure to catch up with you in Glasgow or Edinburgh and I'm sure this is going to be like that in the future too wherever we end up.

To my brothers of the almighty Boves Luci.

This PhD would have never been a reality without the help from many people at

the University of Queensland. First of all thank you Michael Smart for initiating the opportunity for a research visit to the Center for Hypersonics (CfH). The visit has been made possible through the Mac Robertson and JM Lessells scholarships. Thank you Rowan Gollan for your warm welcome in Brisbane and the indispensable guidance you provided to me during and after my stay. Thanks Peter Jacobs for the many advices over coffee and shared anecdotes. A special thanks to Juanra Llobett whom has been like a brother to me in Australia. You introduced me to everyone and I never really felt alone. Thank you all at the CfH for sharing great moments and exchanging knowledge on scramjets and hypersonics in general: Will, Nick, Eric, Kyle, Sholto, Sam, Wilson, Tamara, Augusto, Jens, Zach, Pierpaolo, Tristan, Kevin, Andreas and Alex. Thank you to my co-visting researchers Cor and Luuk with whom we had so much fun at level 3. Thank you Bart and Glenn for joining me in the ozzy roadtrip.

Finally I wish to thank my family for the continuing support in this seemingly never ending path. To my amazing mother, father, brother, sister and grandma.

List of Publications

Conference proceedings and unpublished conference papers

JJOE Hoste, V Casseau, M Fossati, IJ Taylor, and RJ Gollan. Numerical modeling and simulation of supersonic flows in propulsion systems by open-source solvers. In 21st AIAA International Space Planes and Hypersonics Technologies Conference, Xiamen, China, page 2411, 2017.

JJOE Hoste, M Fossati, IJ Taylor, and RJ Gollan. Modeling scramjet supersonic combustion via eddy dissipation model. In 68th International Astronautical Congress (IAC), Adelaide, 2017.

JJOE Hoste, M Fossati, IJ Taylor, and RJ Gollan. Turbulence chemistry interaction via eddy dissipation model for scramjet analysis and design. In 7th European Conference on Computational Fluid Dynamics (ECFD 7), Glasgow, 2018.

Submitted for publication

JJOE Hoste, M Fossati, IJ Taylor, and RJ Gollan. Characterization of the Eddy Dissipation Model for the Design of Hydrogen-fueled Scramjets. Currently under review by The Aeronautical Journal.

Table of contents

List of figures

List of tables

Nomenclature

Roman Symbols

A	Arrhenius pre-exponential constant
A	area, m^2
a	local speed of sound, $m\ s^{-1}$
$\bar{a}$	$= a + a^{'}$, Reynolds average of variable a
$\mathrm{A_{edm}}$	constant of the EDM
$a^{'}, a^{''}$	fluctuating part in decomposition of a
$\tilde{a}$	$= a + a^{''}$, Favre average of variable a
$\mathrm{B_{edm}}$	constant of the EDM
C_{lim}	turbulence model constant
C_{μ}	turbulence model constant
d	distance to closest wall
D_s	mean species molecular diffusion coefficient, $m^2\ s^{-1}$
D_t	area-equivalent total jet diameter
E	mixture total internal energy per unit mass, $J\ kg^{-1}$
e	specific internal energy, $J\ kg^{-1}$
$\vec{F}_{inv}$	inviscid flux vector
$\vec{F}_{vis}$	viscous flux vector

$\mathscr{H}$	Heavyside function
H	mixture total enthalpy per unit mass, $J\ kg^{-1}$
h	specific enthalpy, $J\ kg^{-1}$
J	jet to cross-flow momentum ratio
J_{s_j}	diffusion flux components of species s, $kg\ m^{-2}\ s^{-1}$
k_f	forward reaction rate constant
k_r	reverse reaction rate constant
l_0	characteristic length of largest eddies, m
Le_s	Lewis number of species s
L	integral length scale, m
l	characteristic length of an eddy, m
M_c	convective Mach number
$\dot{m}$	mass flow rate, $kg\ s^{-1}$
M or Ma	Mach number
M_t	turbulent Mach number
M_{t_0}	constant of compressibility correction
$\vec{n}$	normal vector
p	static pressure, Pa
p_{pitot}	Pitot pressure, Pa
Pr	Prandtl number
Pr_t	turbulent Prandtl number
Q	array of source terms
q_i	heat flux components, $W\ m^{-2}$
Re	Reynolds number

R	specific gas constant, $m^2\ s^{-2}\ K^{-1}$
R_u	universal gas constant = 8.314 $J\ mol^{-1}\ K^{-1}$
Sc_s	Schmidt number of species s
Sc_t	turbulent Schmidt number
S_{ij}	strain-rate tensor components, s^{-1}
s	mass stochiometric coefficient
t	time, s
T_A	Arrhenius activation temperature, K
k	turbulent kinetic energy, $m^2\ s^{-2}$ or $J\ kg^{-1}$
T	static temperature, K
u_0	characteristic velocity of largest eddies, $m\ s^{-1}$
U_c	convective velocity, $m\ s^{-1}$
u_i	velocity components, $m\ s^{-1}$
u(l)	characteristic velocity of an eddy, $m\ s^{-1}$
U	integral velocity, $m\ s^{-1}$ or array of conserved variables
V	cell volume, m^3
V_{s_j}	diffusion velocity components of species s, $m\ s^{-1}$
W_s	molar mass of species s, $kg\ mol^{-1}$
X_s	molar fraction of species s
$[X_s]$	molar concentration of species s, $mol\ m^{-3}$
Y_s	mass fraction of species s

Greek Symbols

α	turbulence model constant
β	turbulence model constant

β^*	turbulence model constant
δ_{ij}	kronecker delta: 0 $(i \neq j)$, 1 $(i = j)$
ε	dissipation of turbulent kinetic energy, $m^2\ s^{-3}$
ε_d	dilatation dissipation, $m^2\ s^{-3}$
η_c	combustion efficiency, %
γ	ratio of specific heat capacities
γ_{sj}	third body efficiency of species s in reaction j
κ	wavenumber, m^{-1} or thermal conductivity, $kg\ m\ s^{-3}\ K$
λ	secondary viscosity coefficient, $Pa\ s$
μ	molecular viscosity, $Pa\ s$
μ_t	turbulent or eddy viscosity, $Pa\ s$
ν	kinematic viscosity, $m^2\ s^{-1}$
$\nu_{sj}^{'}$	forward molar stochiometric coefficient of species s in reaction j
$\nu_{sj}^{''}$	reverse molar stochiometric coefficient of species s in reaction j
ω	dissipation rate of turbulent kinetic energy, s^{-1}
ω_s	reaction rate of species s, $kg\ m^{-3}\ s^{-1}$
ϕ	equivalence ratio
ρ	mixture density, $kg\ m^{-3}$
ρ_s	partial density of species s, $kg\ m^{-3}$
$\bar{\rho}\widetilde{u_i^{''}u_j^{''}}$	Reynolds stress tensor components, $kg\ m^{-1}\ s^{-2}$
σ_d	turbulence model constant
σ_k	turbulence model constant
σ^*	turbulence model constant
τ	characteristic time scale, s^{-1}

τ_{ij}	molecular stress tensor components, $kg\ m^{-1}\ s^{-2}$
ξ^*	constant of compressibility correction

Subscripts

0	total condition
D	Downstream
edm	eddy dissipation model
F	fuel
f	fuel
∞	free stream
lam	no-model
O	oxidizer
P	product
tot	total condition
U	Upstream

Other Symbols

∇	Mathematical operator

Acronyms / Abbreviations

AUSMDV	Advection Upstream Splitting Method combining Difference and Vector splitting
BC	Boundary Condition
BK	Burrows and Kurkov
CCP	Combined Cycle Propulsion
CFD	Computational Fluid Dynamics
CFL	Courant Friedrichs Lewy number

CMME	Conserved mass / momentum / energy
CVP	Counter rotating vortex pair
DLR	German Aerospace Center
DNS	Direct Numerical Simulation
EASM	Explicit Algebraic Stress Model
EBU	Eddy Breakup model
EDM	Eddy Dissipation Model
EFM	Equilibrium Flux Method
ER	Equivalence Ratio
E-S	Evans-Schexnayder
FRC	Finite Rate Chemistry
HEG	High Enthalpy Shock Tunnel Göttingen
HIFiRE	Hypersonic International Flight Research Experimentation
JAXA	Japan Aerospace Exploration Agency
LEO	low Earth Orbit
LES	Large-Eddy Simulation
MDO	Multi-disciplinary Design Optimization
NASA	National Aeronautics and Space Administration
NASP	National AeroSpace Plane
ODE	Ordinary differential equation
PaSR	Partially Stirred Reactor
PDF	Probablity Density Function
PSR	Perfectly Stirred Reactor
QSS	Quasi-Steady-State

RANS	Reynolds-Averaged Navier-Stokes
RBCC	Rocket-Based Combined Cycle
REST	Rectangular-To-Elliptic Shape Transition
RHS	Right-Hand-Side
RNG	Renormalization Group
SA	Spalart-Allmaras
scramjet	supersonic combustion ramjet
SEI	SpaceWorks Entreprises Inc.
SERJ	Supercharged Ejector RamJet
SPARTAN	Scramjet Powered Accelerator for Reusable Technology AdvaNcement
SSTO	Single-Stage-To-Orbit
SST	Shear Stress Transport
STA	Stream-Thrust Averaging
SWBLI	Shock Wave Boundary Layer Interaction
TBCC	Turbine-Based Combined Cycle
TBE	Third-body efficiency
TCI	Turbulence chemistry interaction
TP	Thrust Potential, N
TRL	Technology Readiness Level
URANS	Unsteady RANS
WBS	Work breakdown structure

Chapter 1

Introduction

> *"Hypersonics is the future – and always will be."*
>
> - Mark J. Lewis (2016),

Over the past decade the satellites market has steadily grown driven by today's technological advances intensively relying on communication. Orbiting satellites enable everyday tasks from observing phenomena on Earth such as meteorological processes and bush fires, beaming phone and TV signals around the world and guiding an individual driving his car to a desired location through GPS. On top of these tasks, satellites allow scientists to explore part of the universe we cannot observe through ground telescopes. This is exemplified by the Hubble Space Telescope, brought into orbit by the National Aeronautics and Space Administration (NASA) in 1990. With the growth of the satellites market another trend has emerged in recent years: smaller satellites with a mass below 500 kg. Instead of designing a large satellite with a lot of functionalities another option is to design multiple smaller satellites with reduced but specific functionalities. These small satellites can then form a constellation in a low Earth orbit (LEO) [1, 2]. The IRIDIUM system [3] is an existing example of a satellite constellation in LEO which provides a worldwide personal communication network. Note that each satellite of the latter network weighs around 700 kg. The trend toward smaller satellites is partly due to the introduction of CubeSats originally intended for space research. CubeSats are a type of nano satellites with a mass of only a few kilograms. In 2015, SpaceWorks Enterprises Inc. (SEI) [4] published a survey on small satellites with a weight between 1 and 50 kg. The company projected around 550 launches by 2020 indicating a clear growth in the small satellites market [5] (in 2014, 158 of these type of satellites were launched). The main issue is that there is currently no dedicated launcher for small satellites. The smaller payloads are brought into orbit following a rideshare concept where they are tagged along as a secondary payload of a larger mission. The main customer of the mission has control on the launch date, orbit altitude and orbit inclination [5]. Efforts are undertaken in the development of rocket launchers such as Rocket Lab's Electron [6], however reusability is not the opted development path [5]. Another important issue is that rocket technology is operating close to theoretical limits [5, 7]. A viable option for reducing the launch cost of small satellites is to introduce a reusable airbreathing propulsion component. To achieve this goal scramjet technology could become key. In terms of payload mass fraction, Smart and Tetlow [8] indicated that a three-stage-to-orbit rocket-scramjet-rocket system, for delivery of small satellites ($\approx$ 150 kg) to LEO, could attain values of 1.47 %. In comparison, a rocket-based system of similar scale would be characterized by a payload mass fraction of 0.9 %. The above comparison is based on a 200 km circular orbit insertion. Other benefits of a scramjet vehicle are reusability, aircraft-like reliability and safety [9] and manoeuvrability. From an economical point of view, the reusability will reduce the cost providing that refurbishments between each flight can be kept to a minimum [5]. All these advantages can be exploited if and only if scramjet operation can be ensured over the broad range of Mach numbers ($\approx$ 6-12) [8] required for acceleration. Scramjet technology is currently not yet at this level [10].

In order to advance the understanding of scramjet propulsion, ground based high-speed wind tunnels are intensively used. However, these facilities are expensive to operate and limited in test times. They can therefore not be relied on to assess scramjet operation over the whole flight envelope. Computational Fluid Dynamics (CFD) is therefore attractive as a tool to aid in the design of scramjet powered hypersonic vehicles. Modeling choices in CFD, more specifically for turbulence-chemistry interaction, can rapidly increase the computational cost which is not desirable in early scramjet design phase. For this reason, low-fidelity models are the preferred numerical tools to characterize the scramjet propulsion when integrated as a subsystem in an hypersonic vehicle. Given the many assumptions made in low-fidelity models, a careful validation must be performed in different relevant conditions in order to gain confidence in their application and minimize the risks of erroneous predictions. It is the aim of this work to explore the use of CFD methods for the analysis and design of scramjet combustors with a particular attention on identifying and formulating the most appropriate approach balancing the computational cost and the consistency of the method with the physics characterizing such complex flows.

1.1 Scramjet Propulsion

1.1.1 Context

Over the years different design solutions have been proposed to realize reliable and cost-effective propulsion systems. Canonical solutions for access-to-space systems based on two-, or multi-stage-to-orbit designs improved efficiency while allowing for some degree of re-usability [11, 12]. The technology of combined cycle propulsion (CCP) systems allows switching between different propulsion technologies in a way to ensure the most efficient flight path as exemplified by Marquardt's conceptual design of the Supercharged Ejector RamJet (SERJ) engine [13]. A recent study conducted by NASA showed how rocket-based combined cycle (RBCC) and turbine-based combined cycle (TBCC) engines are technologies that could enable highly-efficient access to space and future airliner propulsion systems while preserving full re-usability [14].

The concept of combining together different propulsive systems to optimize the performance according to the operational regime is key to the development of future vehicles. Along this perspective, engineering optimized systems for the atmospheric high-Mach segment of the flight path is crucial. Ramjet and supersonic combustion ramjet (scramjet) technologies are constantly being studied to specifically target the supersonic and hypersonic regimes. Being airbreathing, a (sc)ramjet relies on the atmospheric oxygen to combust the fuel. Figure 1.1 sketches a comparison between a turbojet, a ramjet and scramjet concept. Unlike a conventional turbojet, a (sc)ramjet does not contain any rotating part to compress the flow but relies instead on shock waves to achieve the same goal (ram-compression). Above Mach 3 the thermal loads on rotating parts become too high, hence the need for an alternative found in the ramjet [15]. In a ramjet the incoming flow is decelerated to subsonic levels at the entrance of the combustion chamber. The flowpath remains supersonic throughout a scramjet with marginal decelerations. A (sc)ramjet is characterised by a much higher specific impulse than a rocket as illustrated by Figure 1.1 for hydrogen and hydrocarbon fuels. Ramjets are very efficient in the supersonic range of approximately Mach 3 to 5. As the flight Mach number increases into the hypersonic regime (above Mach 5), the pressures and temperatures inside a ramjet become so high that the efficiency drops rapidly. Moreover, from a manufacturing point of view, the high pressures and temperatures become problematic for pratical structures of reasonable mass [10, 16]. The flow should therefore remain supersonic which is achieved in a scramjet. A main disadvantage of (sc)ramjets is their inability to operate at low speeds. Consequently, they have to be integrated in CCP or multi-stage systems. Designs incorporating these advanced airbreathing concepts require a careful coupling with the flight vehicle to achieve the desired forebody compression before entering the engine. An engine-airframe integrated vehicle design is inherently more complex than a rocket propulsion system [5]. Nevertheless, in order to reach the near-orbital velocities for access to space, scramjet technology appears to be a viable option [16] with benefits in payload mass fraction for small satellites [8].

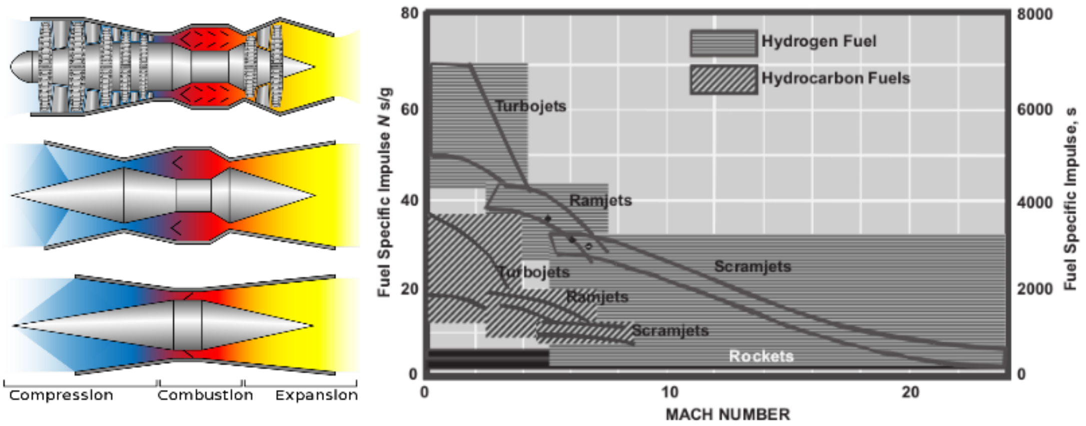

Figure 1.1: Left: turbojet (top), ramjet (center) and scramjet (bottom) designs [17]. Right: specific impulse of different propulsion concepts as a function of Mach number [18].

1.1.2 Challenges of Scramjets

Efforts in the development of high-speed airbreathing propulsion systems were initiated in the late 1950's [19, 20]. Following the pioneering work of, inter alia, Antonio Ferri [21], scramjets concepts were intensively studied with possible applications including hypersonic cruise vehicles [22, 23], missiles [16, 24] and access-to-space systems [5, 7, 16]. Measurements obtained from experimental facilities are intensively relied on in order to understand scramjet operation and the process of supersonic combustion. Disadvantages of experimental facilities include the high operating cost and the limited test time, in the order of milliseconds, when high Mach number (> 8) flows have to be generated [20]. In order to fill the gap, the development of computational tools was required. An historical overview about the evolution of numerical techniques to aid scramjet development is given by Drummond [20] in view of NASA's National AeroSpace Plane (NASP) and Hyper-X programs. In current scramjet research, Computational Fluid Dynamics (CFD) is intensively used in combination with experiments.

In order to verify the validity of observations made in ground-based facilities and validate the design tools and methods, several test flight programs were established. These include the HyShot test flight [25], the Hyper-X program with successful X-43 [26] and X-51 [27, 28] scramjet operation, and the HIFiRE program [29–31]. In the case of the HyShot, a post flight experimental campaign [32] has been performed in the High Enthalpy Shock Tunnel Göttingen (HEG) of the German Aerospace Center (DLR) . The aim was to provide a better set of comparison data by designing a test condition matching flight Pitot pressure measurements. The subsequent comparison sucessfully demonstrated a qualitatively good agreement between ground and flight test. In the X-43 program, CFD-based preflight propulsion expectations of the Mach 10 [33] test were in good agreement with the flight pressure measurements providing a validation of the numerical tools (CFD and low-fidelity cycle analysis). Similar observations were made regarding the comparison between ground and flight test [26]. Moreover, post-flight nose-to-tail CFD simulations showed excellent agreement with measured acceleration and decelerations.

Following the X-43 test flights, Mc Clinton [26] discussed the maturity of scramjet technology. The author adopted the Technology Readiness Level (TRL) which is a measurement system that assesses the maturity level of a particular technology [34]. It is a scale from TRL 1 to TRL 9 where the highest level is equivalent to “flight proven through a successful mission operation”. A vehicle-based work breakdown structure (WBS) is given for two possible applications incorporating scramjet technology. The first one consists of a fully air-breathing Single-Stage-To-Orbit (SSTO) vehicle accelerating till Mach 15. Bowcutt and Hatakeyema [35] identified critical aspects for the high-Mach segment which are included in the WBS. Scramjet propulsion is given a low TRL 3-4[1] which is explained by the fact that the technology is required to operate from Mach 4 to 15. This cannot be demonstrated with single flight tests at a certain Mach number realized in the X-43 or other program. Moreover, as mentioned previously, ground test facilities provide very limited test times for high Mach numbers. A second WBS is given for a low Mach air-breathing first stage with operation to Mach 7. In this

---

[1] TRL 3: Analytical and experimental critical function and/or characteristic proof-of-concept.
TRL 4:Component and/or breadboard validation in laboratory environment.

context, scramjet propulsion is characterised by a higher TRL 5-6[2]. A ramjet (TRL 9) could operate from Mach 2 to 5 whereafter the scramjet operation will take over. By setting a maximum operational Mach of 7, ground facilities, with longer test times, can be intensively relied on in order to achieve a higher TRL. This all demonstrates that there are still many hurdles to overcome. Several scramjet test flights have been conducted since the X-43 program which resulted in improved understanding of the technology but a TRL 9 is not yet achieved, at least publicly known. Future perspective will require cross validation of CFD tools, ground testing facilities and flight test [32].

With gained confidence in the validity of numerical tools and ground facilities, the research toward the realization of scramjet technology is an ongoing process. An inconsistent funding and incoherent research strategies [36] is one of the causes explaining that after almost 60 years of research the technology is not up to point yet. Many remaining challenges, and active topics of scramjet research, include [26] boundary layer transition (natural or forced) [37, 38], inlet design [19, 39, 40], shock-boundary layer interaction [41, 42], isolator shock train [43], cold wall heat transfer and cooling [44, 45], fuel injection [46], penetration and mixing [10, 47–52], fuel type [53, 54], turbulent combustion [20, 55], unstart [56] and high temperature materials [57]. Moreover, an aspect of growing importance is the quantification of the environmental impact at high altitude which is highly dependent on the fuel type and targeted technology (hypersonic cruise or access to space) [58]. This will play a major role in future formulation of regulations which are currently non-existent.

1.1.3 The Role of Numerical Tools in the Design Process of Scramjets

CFD has evolved over the years to become strongly embedded in scramjet studies. One of the principal reasons is the growth in available computational power. In spite of this advantage, numerical studies remain costly as more and more physics are being modeled with increased level of complexity. More detailed studies are required in order to understand the specifics of the turbulent mixing process for instance. However, sometimes this level of complexity is not required / practical in preliminary design studies such as in trajectory optimization processes[5, 7, 8, 59] . CFD is especially

---

[2] TRL 5: Component and/or breadboard validation in relevant environment.
TRL 6: System/subsystem model or prototype demonstration in a relevant environment (ground or space).

useful for studying the high Mach number regime as experimental pulse facilities can only provide a limited amount of information. Moreover, vehicle integrated concepts cannot be experimentaly tested [3]. Nose-to-tail CFD simulations [22, 61] can help in improving current understanding. A robust scramjet design need to be able to operate at off-design conditions and this can be evaluated by numerical tools. The high Mach ($\approx$ 7-12) operation is for instance targeted in the Australian SPARTAN program [62]. The hydrogen-fueled SPARTAN vehicle, shown in Figure 1.2, is a reusable scramjet second stage accelerator as part of a three-stage-to-orbit rocket-scramjet-rocket system for small payload delivery. An example trajectory for the scramjet powered vehicle is given in Figure 1.3 at a constant 50 kPa dynamic pressure. Current preliminary design procedure for this vehicle involves the use of a quasi-one dimensional solver [63, 64] in order to generate a propulsion database for adoption in the trajectory optimization tool [59]. One- or quasi-one dimensional tools can only provide a limited amount of information and require a careful validation. Section 2.1 will further discuss these low-fidelity solvers. Note that a preliminary design involves the study of many candidate configurations which imposes constraints on the computational time of the adopted numerical tools in order to advance the design at a reasonable pace set by project requirements. An ideal approach for improving the SPARTAN's vehicle design would require full nose-to-tail CFD simulations at every point of the trajectory. Ultimately, a coupling of the CFD solver with an adjoint solver [65] could furthermore enable to optimize the integration of the scramjet engine within the vehicle's body. Full nose-to-tail simulations are currently computationally too expensive to perform in a preliminary design context and a compromise could be found in selecting a limited amount of operation points from Figure 1.3 for CFD study. Even then, the state-of-the-art models for the combustion in propulsion flowpath analysis are expensive to run. The latter does as well limit the performance of an adjoint solver. In order to incorporate CFD in preminary design studies there is a need for a cheap description of the combustion process. It is the aim of this work to use CFD methods in the analysis and design of scramjet combustors. In a scenario such as the SPARTAN, a computationally effective combustion model (Eddy Dissipation Model) could be possible given the high Mach scramjet operation. Section 2.2 will further discuss this model as well as the CFD methods for scramjets found in the literature.

---

[3] Recent efforts at the Center for Hypersonics of the University of Queensland resulted in a full free-stream Mach 12 scramjet testing inside an expansion tube with demonstration of combustion [60] (private communication, Pierpaolo Toniato, 20th of May 2018).

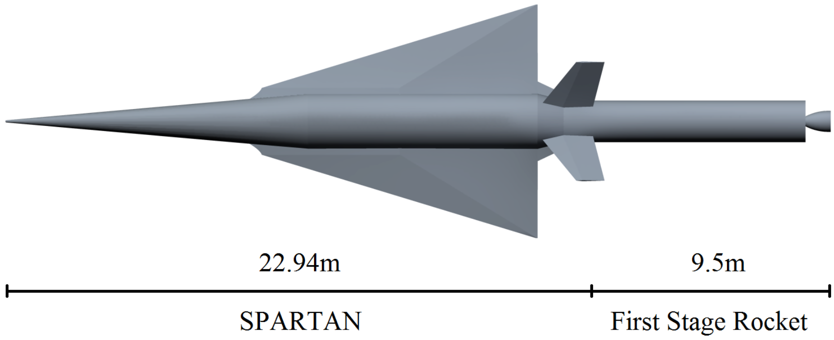

Figure 1.2: Illustration of the SPARTAN second stage vehicle and first stage rocket booster. Image provided by Sholto Forbes-Spyratos in private communication in advance of future journal publication.

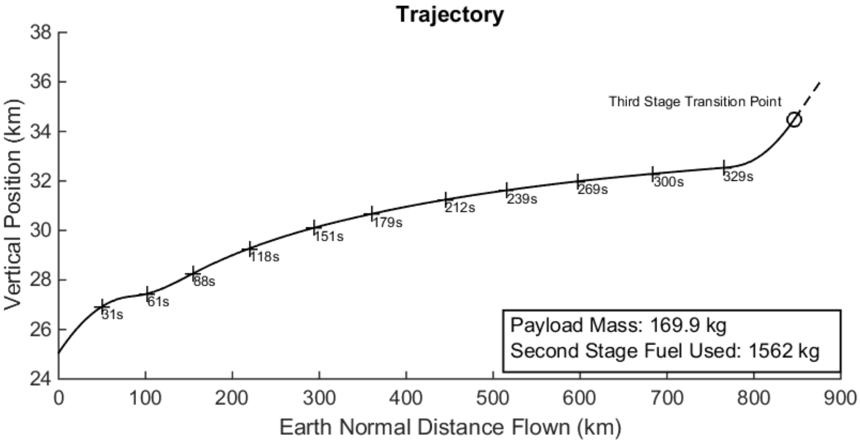

Figure 1.3: SPARTAN accelerator trajectory. Image provided by Sholto Forbes-Spyratos in private communication in advance of future journal publication

1.2 Objectives of the thesis

The main aim of this work is to:
formulate and implement a computationally affordable open-source CFD approach to describe scramjet combustion in an access-to-space scenario which can be relied on for cost effective preliminary design studies.

In pursuing the above stated objective, answers to the following research questions are sought:

- *Are RANS closures with linear eddy viscosity models appropriate to study scramjet flow paths? Is the turbulence model of the selected CFD solver accurate*

enough for further considerations?
Once a CFD solver is selected, its capability in providing accurate results for existing validation cases needs to be evaluated. Characterizing the behavior of the turbulence model is key in doing so.

- *Are compressibility corrections required in typical scramjet flow paths?*
  The aim of compressibility corrections is to account for reductions in the spreading rate of a mixing layer prevalent when the difference in velocity between fluid streams is high. The corrections are applied on the turbulence model under consideration.

- *What is the most appropriate setting for the EDM constant in a non-premixed configuration?*
  Following a review of the literature, the EDM (Eddy Dissipation Model) is selected to address the combustion modeling as its formulation is computationally affordable and its use valid for the conditions of interest. The EDM constant directly influences the fuel consumption rate and has a standard value which is derived from low-speed flame studies. No information on the most appropriate setting can be found in the literature on scramjet flows.

- *Should a kinetic limit be applied on the EDM in primarily mixing-limited scramjet flow paths?* The effect of chemical kinetics can be considered to limit the fuel consumption rate predicted by the EDM. It implies the use of the no-model approach with a single-step global reaction.

- *Can the use of the existing EDM formulation be improved when simulating scramjet combustion? Are there ways to make a better use of the EDM given a certain type of fuel injection mechanism or geometrical configuration?*

- *Can the use of the EDM be pushed to scramjets dominated by non-mixing limited combustion? Can the EDM still provide meaningful information when applied on a scramjet geometry which is dominated by kinetic effects?*

- *How can the fuel injection approach in a scamjet be optimized by applying the EDM? Given a scramjet configuration, what type of metrics can the EDM provide* *with enough accuracy in order to improve the design?*

1.3 Outline of the thesis

This thesis is organised in the following chapters with a roadmap of the core work presented in Figure 1.4.

Chapter 2 - A Literature Overview on Scramjet Design Tools This chapter discusses the state-of-the-art numerical tools applied to the study of scramjets at different stages of the design process. A candidate combustion model (the EDM) for study in this work is identified and its use in previous scramjet studies detailed.

Chapter 3 - The Governing Equations of Compressible Turbulent Reacting Flows This chapter briefly introduces the concept of turbulence and its description with the RANS approach. The different modeling choices specific to scramjet flow paths are detailed and the chapter concludes by a succinct discussion of the discretization of the governing equations.

Chapter 4 - Assessment of Eilmer for Scramjet Flow Paths In this chapter, the selected CFD solver (Eilmer), is applied to four scramjet configurations which are to be studied with the newly implemented combustion model in the following chapter. The validation task aims at ensuring the suitability and appropriate use of the turbulence model.

Chapter 5 - Assessment and Optimization of the EDM for Scramjet Flow Field Prediction This chapter provides a detailed description about the combustion model selected for study as part of this thesis. The newly implemented model is applied to the study of the four scramjets discussed in the previous chapter. This exercise is performed in order to evaluate the model settings and its predictive capability.

Chapter 6 - Application of RANS EDM to a Design Problem In this chapter, the HyShot II combustor is considered and several injection approaches are investigated with the EDM. An improvement to the current design is suggested. With this exercise, the final aim of this thesis has been realized.

Chapter 7 - Conclusions and Future Work This chapter concludes the thesis by summarizing the findings from Chapters 4 to 6. Answers to the research questions introduced in Section 1.2 are provided. Finally, recommendations for future work are given.

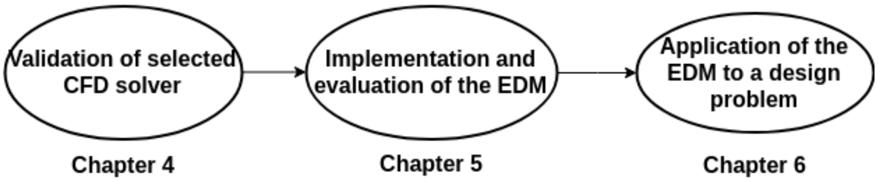

Figure 1.4: Roadmap of the PhD.

Chapter 2

A Literature Overview on Scramjet Design Tools

This chapter provides an overview on the numerical tools documented in the literature for the study of scramjets. The tools are classified as either low-fidelity or high-fidelity. Section 2.1 discusses the former class which is suitable for rapid analyses and integration in complete vehicle studies. The second class adopts computational fluid dynamics and is typically used for study of more detailed physics occurring inside scramjets. It is the subject of Section 2.2. Finally, a summary on the topics covered in this chapter is given in Section 2.3.

2.1 System Analysis Tools Used For Scramjet Propulsion

Hypersonic air-breathing propulsion systems have been intensively studied over the past decades with the aim of being introduced in access to space systems and high-speed airliners. The ramjet and supersonic combustion ramjet (scramjet) are considered as candidate engines for such systems. In the early years following the conceptual introduction of (sc)ramjet engines, experimental studies were mainly performed in order to gain insight in the physics occurring in these type of engines. Over time, the use of numerical simulations has gained popularity due to their availability and the limitations of experimental facilities; short test times (typically in the order of milliseconds), difficulty to recreate the high enthalpy flow conditions, high operating costs and limited amount of measurements that can be conducted per experimental shot.

Among the adopted numerical tools for the characterization of (sc)ramjet propulsion are the class of so-called low-fidelity models which do not solve the Navier-Stokes equations with Computational Fluid Dynamics (CFD). Nevertheless, CFD analyses are typically performed to validate other approaches or even provide information for improvements and / or tuning [66–68]. The popularity of low-fidelity models can be explained by the very low computational requirements which makes them attractive for integration as a subsystem in a complete vehicle analysis as well as in Multi-disciplinary Design Optimization (MDO) as exemplified by Wuilbercq et al. [69]. The complexity of the propulsion model in such tools can vary greatly.

A popular low-fidelity approach documented in the literature is the class of one-dimensional (no area change) or quasi-one dimensional (allows for area change in the direction of the flow) models. A set of fluid dynamics equations are formulated for the bulk propeties resulting in a system of, usually stiff, ordinary differential equations (ODE's) which have to be integrated. Additional physics can be accounted for such as friction / heat losses and mixing effects. The effect of shock reflections can be integrated through correlations of experimental data as explained by Smart [70]. Some examples of their use and validation relevant to scramjets are now covered. O'Brien et al. [24] developed a quasi-one dimensional analysis tool for high-speed engines which includes finite-rate chemistry effects with the use of the CHEMKIN II [71] package. Predictions from the code were validated with two hydrogen-fueled scramjet configurations. The ignition delay and experimental pressure traces along the wall were adequately reproduced. Furthermore, the scramjet mode of a rocket-based combined cycle (RBCC) engine (hydrogen fueled) and a hydrocarbon scramjet missile were studied as a demonstration of the model stating the importance of considering finite-rate effect instead of equilibrium chemistry assumptions. Birzer and Doolan [72] presented a quasi-one dimensional model for scramjets similar to O'brien et al. [24] with the assumption of either equilibrium or mixing limited combustion. The latter implies that as soon as fuel and air mix, the mixture goes immediately to an equilibrium state of fuel, air and combustion products [5, 8]. The authors introduce a supersonic mixing model relying on a proportionality constant which is found by use of CFD predictions from the literature. Three hydrogen-fueled scramjet test cases are studied for which experimental pressure data is available. They each use a different type of fuel injection. Pressure variations cannot be captured, however, mean pressure distributions are successfully reproduced by the solver. This characteristic makes the model suitable to predict performance of scramjet vehicles in a conceptual design phase. The Aerospace research group at the University of Michigan [73–76] has been steadily developing low-fidelity models in the past decade to study ramjet and scramjets propulsion systems and integrate them in an MDO framework. Efforts have been made to account for more detailed chemistry description within a quasi-one dimensional solver called MASIV [74]. The approach considers a steady laminar flamelet model in conjunction with a presumed probability distribution function (PDF) model to account for turbulence chemistry interaction (TCI). The formulation accounts for locally three-dimensional combustion and mixing which is then averaged to provide a one-dimensional input for the solver. The scramjet combustion is considered to be mixing-limited. Predictions of MASIV are compared to experimental data and CFD results of a direct-connect scramjet configuration. A good quantitative comparison is observed for different flow variables and it is concluded that the level of accuracy provided by MASIV is suitable for MDO applications. The solver has been used in a subsequent study of two scramjet configurations integrated into an x-43-like hypersonic vehicle [75]. The transition process modeling between ram and scram mode has as well been tackled by the authors. The approach presented by Torrez et al. [74] combines one-dimensional models with a three-dimensional model along the flow path. This idea of sequencing models with different dimension is also embodied in the SRGULL code from NASA Langley [77, 78]. The way the multi-dimensional information is reduced into one dimension has been examined by, inter alia, Baurle and Gaffney [79]. Edwards and Fulton [80] compared two-dimensional CFD simulations of a generic vehicle integrated scramjet with SRGULL. In the latter solver, the inlet flow field is obtained by stream-thrust averaging a two-dimensional Euler simulation and the combustor is modeled as one dimensional. The study concludes that SRGULL can capture the general wall pressure response but is incapable of reproducing the oscillations due to shock reflections. Nevertheless, performance parameters such as thrust and specific impulse were similarly predicted by SRGULL and the CFD. It is still to be shown if similar observations can be made with more complex geometries.

A very different approach than previously covered consist of using a zero-dimensional or "jump" solver. An engine flow path is discretized in several blocks and the analysis jumps from one block to the other. Each block contains the description of a particular physical process, e.g. injection, mixing, combustion. A great level of flexibility can be achieved and literally any type of engine can be composed from the basic building blocks, hence making it suitable for combined-cycle engine analysis. The method does not require an integration along the flow path resulting in tractable levels of computational cost. Such an approach is adopted by the HyPro solver [66–68] developed at the University of Strathclyde. Published work with the solver relies on a very simplified description of the combustion process, i.e. complete combustion with an efficiency. HyPro has been compared to CFD predictions of two scramjet configurations yielding a very good match with averaged quantities of pressure and Mach number from the CFD at the entrance and exit of the different blocks. The solver has recently been coupled with Cantera [81] and more sophisticated combustion models are being developed.

All of the above studies and methods demonstrate the general limitation of low-fidelity models which is the need for extensive validation. Many assumptions are made regarding the mixing and the combustion towards which a lot of efforts are directed in order to increase the fidelity through CFD. Pressure traces along the walls of a scramjet, commonly measured in experimental campaigns, are typically used as validation. Low-fidelity models are able to capture general trends in the latter quantity but variations coupled to shock reflections cannot be obtained. General trends could be sufficient in order to predict integrated quantities such as thrust with careful validation. In a combustor design context, the sole knowledge about trends is insufficient in order to study and improve the injection physics for instance. It is also worth noting as a general comment that the number of scramjet validation test cases available in the open literature is limited. It is therefore important to evolve towards modeling techniques which require little validation in order to gain confidence in their applicability to other configurations.

A practical example of the use of system analysis tools for scramjet design is the development of a three-stage-to-orbit rocket-scramjet-rocket system by the University of Queensland. The first and second stage are designed to be reusable. Figure 2.1 illustrates[1]the idea which should enable small payloads of the order of 100 kg to be put in sun-synchronous orbit [5]. The second stage (Figure 1.2) is known as the SPARTAN (Scramjet Powered Accelerator for Reusable Technology AdvaNcement) and is hydrogen fueled. In the generation of the trajectories, the trajectory program makes use of a propulsion module to obtain information on specific thrust, specific impulse, and equivalence ratio for a given flight velocity, angle of attack and altitude [8]. This propulsion database is generated a priori for the selected fixed geometry scramjet engine with a quasi-one-dimensional model. The latest scramjet configuration is called the C-RESTM10 (Rectangular-To-Elliptic Shape Transition) [5]. A mixing-limited fuel combustion is assumed. A mixing efficiency curve needs as well to provided in order to define the amount of fuel which is allowed to react with air at a given station along the combustor. Currently an empirical formula is used with the setting of a constant. See [8, 63] for more details about the different modeling choices. A schematic of the current design tools used at the different flow stations is given in Figure 2.2. No dimensions are given on the latter figure as it is shown purely as an illustrative example of a vehicle integrated scramjet. The design of the SPARTAN vehicle does already rely on CFD simulations for the forebody and inlet compression [8] (station 1 to 2 in Figure 2.2) and, more recently, for the aft-body expansion [5] (station 9 to 10 in Figure 2.2). CFD is however not yet relied on for the combustor which is due to the high computational cost associated with typical methods. The SPARTAN vehicle design process could really benefit from an increased level of fidelity if a computationally affordable CFD approach could be relied on. In a first step, the CFD can replace the quasi-one-dimensional model in order to generate a propulsion database for the trajectory optimization program. Doing so would remove the need for assumptions on, inter alia, mixing efficiency or a diffuser model to account for possible flow separation and the effect of the shock train upstream the point of injection [8, 70]. Moreover, more precise boundary conditions can be provided to the aft-body expansion CFD computation. An increased level of fidelity for the latter computations is of importance as it will affect the shape of the nozzle and tail-end of the vehicle. All of the above comments regarding the benefits of CFD for the scramjet are not limited to this illustrative example of the SPARTAN. Even in a situation where CFD is not desired, a computationally affordable description can still be relied on for improving the quasi-one dimensional models in analogy to the practice in MASIV [75].

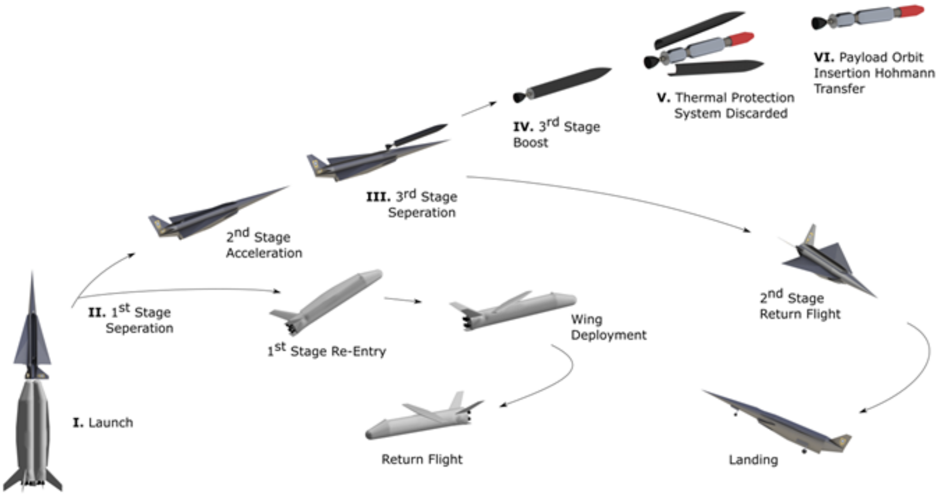

Figure 2.1: Illustration of the three-stage-to-orbit rocket-scramjet-rocket concept [82] .

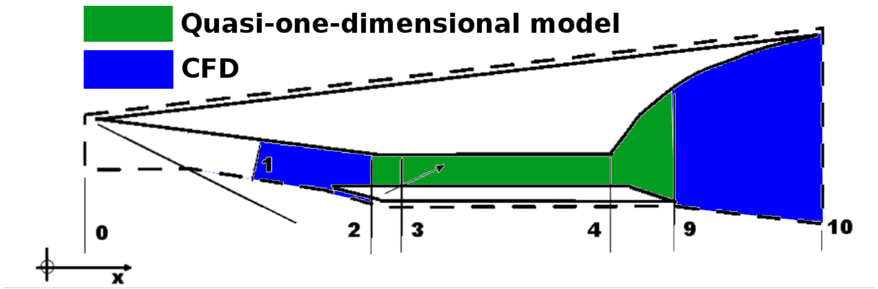

Figure 2.2: Tools used in the design of the different engine flow stations in a vehicle integrated scramjet. Image adapted from [8] .

2.2 High-Speed Reacting Flows Modeling with CFD

Today's technological advancements have rendered the use of Computational Fluid Dynamics (CFD) complementary to experimental studies [10, 52, 54, 83–91]. The main reason is that experiments can only provide a limited amount of information. Pressure and heat flux in a line along the wall are typically measured during a shot (one operation) in an impulse facility. To cover a wider area of the scramjet walls, an increased amount of probes are required or several shots with a fixed number of probes. It is also possible to use imaging techniques in order to get, for example, temperature or composition information in certain planes of interest. Obtaining data across several planes would require multiple shots to be performed which inherently introduces some differences coupled to the inability of exactly reproducing the same test conditions. The operational cost of impulse facilities will limit the number of shots performed. In conclusion, it is impossible to get a complete overview of what's going on everywhere within the test section which explains why experimental facilities provide a limited amount of information. Experimental data is required to validate CFD solvers whereafter CFD can be used in more detailed studies of scramjet combustion phenomena. While low fidelity tools are actively relied on for system analysis and in MDO approaches, CFD, with its higher fidelity, has gained its place in scramjet combustor design. Prior to building an experimental model for testing in a shock tunnel, multiple numerical simulations are performed as illustrated by Moura et al. [92]. Once the experimental campaign has been performed, a posteriori CFD computations are performed with improved boundary conditions matching more closely the facility conditions. This approach is adopted in [10, 52, 54, 84, 90] for instance. Within the

---

[1] Note that the web page from where the image is taken does not exist any more. It is however, possible to retrieve the information by using a web archive tool

possible CFD approaches, different levels of fidelity can be considered to describe the process of turbulence and the combustion. These topics are the subject of the following discussions.

2.2.1 Turbulence Modeling

Among the available CFD approaches, Reynolds-Averaged Navier-Stokes (RANS) remains the commonly adopted tool for design purposes in hypersonic propulsion flow paths [93, 94]. This status is a consequence of the high cost associated with more advanced descriptions of turbulence including Large-Eddy Simulations (LES) and Direct Numerical Simulations (DNS) . While LES starts to become more widespread, DNS remains at a level where canonical studies can be performed to further the understanding of, for instance, shock-turbulence interaction [95]. LES, which resolves large scale turbulent motions and models the smaller ones, is applied in situations where RANS cannot adequately enough capture the (unsteady) phenomena relevant to the turbulent supersonic combustion process in a scramjet. E.g. Larsson et al. [43] studied the unsteady shock-train motion inside the HyShot II scramjet combustor. Fureby et al. [96] applied LES on the same combustor in order to describe the self-ignition phenomenon. The authors explain that RANS is sufficient in capturing the main flow features, but LES results in significant improvements of detailed flow structures predictions. Genin and Menon [97] developed an LES description and demonstrated its use on the DLR combustor configuration [98]. Sometimes hybrid RANS/LES approaches are preferred to LES in order to keep the computational cost to tractable levels in the presence of physical walls. Potturi and Edwards [99] did for instance opt for the latter approach in the study of the DLR combustor. An extensive sensitivity study was performed considering different options for grid topology, reaction mechanism or subgrid scale model. The same hybrid approach was applied to the experiment of Burrows and Kurkov [100] by Edwards et al. [101] in order to study the supersonic flame characteristics. The increased level of detail obtained in LES or hybrid RANS/LES is coupled to higher computational cost which does not make the approach practical as an engineering design tool [93]. With respect to RANS, LES requires finer grids in order to resolve the energy of the large scales and a sufficient amount of simulation time is needed for statistically meaningful averaged quantities. Moreover, generating an initial turbulent field for the simulation is not trivial and it is common practice to start from a RANS result. Therefore, in a review paper published over a decade ago on the state-of-the-art in high speed reacting flows modeling, Baurle [93] mentioned that the developments of RANS methodologies does still have value and will remain in demand [93]. In a more recent review, Georgiadis et al. [94] confirmed that LES or hybrid RANS/LES techniques are still not mature enough for hypersonic propulsion flowpaths. The authors discuss the practical state-of-the-art RANS techniques used in tackling the challenging physics described in Subsection 1.1.2 based on their personal experience with the Wind-US CFD solver.

Within the RANS framework, linear eddy viscosity models are typically used which rely on Boussinesq assumption to address the Reynold stresses. One- and two-equation turbulence models are then introduced to close the system of governing equations and remain popular in supersonic flow paths. The two-equation model approach is commonly adopted for hypersonic propulsion CFD [94]. This trend follows from the larger range of applicability and suitability for complex geometries in comparison to e.g. one equation models without drastically increasing the computational cost. Among the one-equation turbulence models, the Spalart-Allmaras is mainly used in scramjet CFD studies [91, 94, 96, 102–105]. Popular two-equation models for supersonic flows include k-ε [87, 106–117], Wilcox' k-ω [102, 118–125] and Menter's k-ω Shear Stress Transport (SST) [49, 51, 80, 83, 84, 105, 112, 126–132]. The development of the SST model was motivated by the sensitivity of the k-ω 1998 model to freestream turbulence properties and the inability to predict separated flows [133]. Away from walls. the model uses a k-ε turbulence formulation, which does not depend on free stream turbulence quantities, and switches to k-ω when approaching physical boundaries. Over the years the free stream sensitivity limitation of the k-ω has been addressed and improvements have been made. The improvements in the 2006 version include: reduced free stream sensitivity, improved behavior for compression corners and hypersonic SWBLI (shock wave boundary layer interaction) and the capability to handle free shear flows [134]. For this latter model the importance of the stress limiter parameter in predicting separation was demonstrated by Wilcox [134] and confirmed by Chan et al. [123] and reasonable agreement with wall pressure data was observed. As part of the present work, this version has been proven capable of similar performances as Menter's SST model [135] in non-reacting scramjet propulsion flow paths. Some of the disadvantages of RANS include the strong sensitivity to constant values for turbulent Prandtl and Schmidt numbers or the inability to account for the anisotropy of large scale turbulence motions [93]. Moreover, compressibility corrections can be applied to the turbulence model in order to account for the reduction of shear layer growth [136]. Other approaches such as full Reynolds stress closures can offer a more precise description of the turbulent flow field but the superiority in accuracy over two-equation eddy viscosity models has not yet been proven to be sufficiently high to justify the increase in computational cost [94]. Another approach which has been explored is the use of nonlinear explicit algebraic stress models (EASMs) [93, 94]. The EASM is only slightly more computationally expensive than linear two-equation eddy viscosity models [93, 94] and do account for Reynolds stress anisotropies. Its use is however not widespread in the high speed propulsion community. Georgiadis et al. [94] concluded in their review paper that RANS turbulence modeling is still characterized by shortfalls which limit the predictive capability and there has not been a lot of focus on developments to improve the status in the last decade. Two-equation linear eddy viscosity turbulence models appear to remain the state-of-the-art for practical engineering calculations of hypersonic propulsion flow paths.

As part of this work an open-source CFD solver is selected and answers to the following questions related to the turbulence modeling are sought. Are RANS closures with linear eddy viscosity models appropriate to study scramjet flow paths? Is the turbulence model of the selected CFD solver accurate enough for further considerations? Furthermore, the need for compressibility corrections in typical scramjet flow paths is evaluated.

2.2.2 Combustion Modeling

In the simulations of scramjet combustors the CFD solver has, in addition to the Reynolds stresses, to deal with the chemical source term which is highly non-linear and cannot be directly related to mean flow properties. Turbulence can considerably affect the combustion process by either promoting or suppressing reactions. It is the role of the turbulence chemistry interaction (TCI) model to describe this effect through the chemical source term. In scramjet flow studies, the use of the “no-model” or Arrhenius approach is commonly adopted where the law of mass action is applied for a given reaction mechanism. In the latter approach, TCI is completely ignored which is acceptable when chemical time scales are larger than turbulent mixing scales [137].

In past research, RANS turbulence models have been validated by comparison with experimental data. Relevant to scramjet internal flows the standard test cases of Burrows-Kurkov, the DLR combustor, SCHOLAR, JAXA’s scramjet and the HyShot combustor are typically used. The CFD predictions can be compared with experimental data in non-reacting conditions, where only the turbulence model’s capability is evaluated, and reacting conditions, where the interaction between turbulence and combustion is addressed. Examples of supersonic combustion modeling with RANS and the no-model approach, for hydrogen as fuel, can be found in the literature for the experiments of Burrows- Kurkov [104, 107, 108, 112, 119, 127, 129], SCHOLAR [118, 138], JAXA's scramjet [139, 140] and the HyShot [91, 102, 126]. Depending on the test case, the no-model choice did provide satisfactory results, however other studies demonstrated the need to include the effect of turbulence on the chemistry which, in most cases, increases the computational cost. Studies adopting a TCI model such as Probability Density Functions (PDF), a flamelet model or Eddy Dissipation Concept / Model can be found applied to the experiments of Burrows-Kurkov [141, 142], SCHOLAR [143], DLR [111, 115, 117, 131, 144, 145] and the HyShot [102, 103, 146]. Karl [86] and Bouheraoua [15] provide a basic description of several TCI models and the underlying assumptions to which the interested reader is referred to. For even more details the reference book of Poinsot and Veynante [137] can be consulted.

Whether or not a TCI model is required is still the subject of ongoing studies. Gonzalez-Juez et al. [55] published in 2017 a review on the advances and remaining challenges in the modeling of high-speed turbulent combustion for propulsion flow paths. The authors performed a thorough investigation of studies from the literature on several scramjet test cases or representative supersonic flames. Selected literature predictions were obtained with different descriptions of turbulence (LES, RANS, hybrid RANS/LES) and turbulent combustion modeling (no-model, flamelet, PDF etc). One of the questions of interest in [55] related to the debate on the need for a TCI model. An important comment pointed out by the authors is the difficulty for objective comparisons between different studies from the literature. This is illustrated with predictions of Cheng's [147] supersonic burner by two LES studies. Figure 2.3 presents one of the results. One study uses the no-model approach on a mesh containing 6.6M tetrahedral cells (Boivin et al. in Figure 2.3) while another study applies the Partially Stirred Reactor (PaSR) on a mesh with 31M cells predominantly hexahedral (Present study in Figure 2.3). The latter result demonstrated an overall improvement of the predictive capability but it is arguable whether this is because of the TCI model or the finer mesh. With a finer mesh, the LES does resolve a larger range of scales which impacts the turbulent combustion process.

In another example, considering the UV-A scramjet [148], a no-model study resulted in better predictions of wall pressure trace in comparison to a flamelet approach. However, a comparison to the experimental mean temperature map demonstrates that the flamelet model is more appropriate than the no-model. Following these observa-

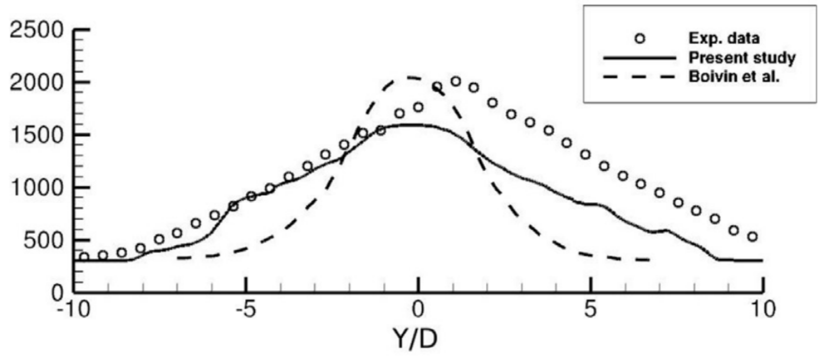

Figure 2.3: Spatial variation of mean temperature in Cheng's burner predicted by two LES studies. Image reproduced from [55] .

tions, Gonzalez-Juez et al. [55] adviced to be careful in drawing conclusions on the superiority of a model based on the sole comparison of wall pressure data. In further comparisons, transported (or evolution) PDF (TPDF) simulations results were more accurate than the no-model approach for three out of five test cases. It must be noted that a TPDF TCI model is very expensive, possibly up to a factor 10 with respect to the no-model description [93]. Based on the considered literature studies, no general conclusion on the need for a TCI model can be drawn. In some cases better predictive capability is obtained while in others not, depending on the comparison data.

While the search for the most accurate combustion model(s) is ongoing, the practical engineering side needs as well to be considered. If one has to design the length of a combustion chamber, trends indicated by a less sophisticated model could be sufficient in answering, for instance, the questions “How much fuel do I burn? Do I need to have a longer combustor or can it be shortened?”. Even if the need for a TCI model is disproven, the use of a detailed mechanism of reaction remains a costly option. Consider for example the Mach 12 REST engine (half-scale model) computations performed by Landsberg et al. [51]. The authors performed RANS simulations of the isolator-combustor-nozzle with mesh size of approximately 20M cells and the no-model approach with the 13-species, 33-reaction mechanism of Jachimowski [149]. This choice results in the addition of 13 species equations which have to be solved in every cell and an increase in overall stiffness of the system due to chemical time scales. While a flow field solution can be obtained in a relatively acceptable amount of time, with large computational capacity, the approach could strongly benefit from a decrease in complexity of the combustion modeling. That is, at the cost of a reduced level of detail in flow physics. Such a possible path could be explored for scramjet flow paths where the combustion is primarily mixing-limited.

2.2.3 Mixing-limited Scramjet Combustion

The combustion process inside a scramjet can be categorized in two extreme cases. One extreme is a kinetically controlled combustion. In this case the chemical kinetics dominate the behavior inside the combustor and turbulence does not play a significant role. This is for example prevalent in radical farming scramjet concepts [84]. The latter concept is illustrated in Figure 2.4 reproduced from the work of Odam and Paull [150]. By ingesting the leading edge shocks a pattern of interacting shock waves and expansion fans is obtained. This in turn induces regions of elevated pressure and temperature where radicals are formed in the combustion process, hence the term radical farms. Note that fuel is injected in the intake as to maximise the effectiveness of the concept. The radical farming technique can be relied on to ignite the flow at milder combustor entrance conditions with mean static temperatures below the auto-ignition temperature of the fuel ($\approx$ 1000 K for hydrogen). A lower mean combustor temperature is the result of a reduced intake compression which can be targeted to minimize shock wave induced intake losses as pointed out by Lorrain [84]. For a kinetically controlled combustion, in terms of numerical modeling, no TCI is modeled and the chemical source term is described by the no-model approach. The choice of the mechanism of reaction is however very important as pointed out by Gonzalez-Juez et al. [55]. The second extreme case is the mixing-limited combustion where chemistry is very fast and the turbulence controls

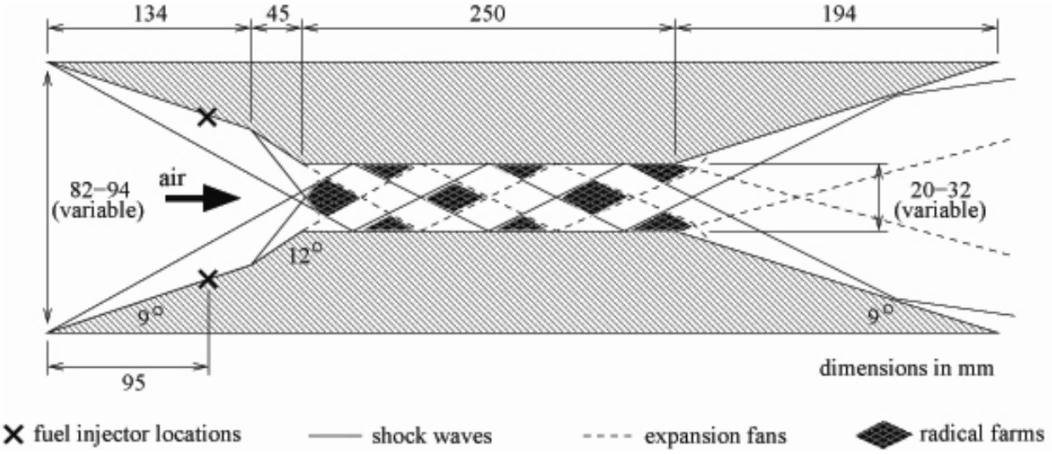

Figure 2.4: The concept of radical farming. Image reproduced from [150].

the reaction rates. A TCI model is required to account for the turbulence dominated combustion. A single-step global reaction can be considered, with a reduced number of species, instead of a detailed reaction mechanism. The supersonic combustion process inside an actual scramjet lies somewhere in between those two extremes. A lot of efforts are being undertaken in identifying the exact regime(s) of turbulent combustion which will guide the direction of modeling [15]. Considering a scramjet powered vehicle operating as an accelerator for access-to-space such as the SPARTAN. The combustor entrance conditions will be characterized by [151] Mach numbers $\approx$ 1-3 and static temperatures above 1000 K. At the latter conditions it can be assumed that hydrogen/air chemistry is fast. The combustion process could therefore be considered to be mainly mixing limited [49, 151, 152]. As an approximation, a single-step global reaction can be used [151] which will considerably reduce the computational cost of the simulations. Adopting a TCI model relying on such an approach could be a viable option to improve the design process of the SPARTAN vehicle. Moreover, several quasi-one dimensional models covered in Section 2.1 do already assume a mixing-limited combustion. Relying on the assumption of mixing-limited combustion, the Eddy Dissipation Model (EDM) , introduced by Magnussen and Hjertager [153], could be a viable option in the context of scramjet combustor design or replacing the low-fidelity model in the generation of a propulsion database (see Figure 2.2). An overview on its use for scramjet propulsion is the subject of Subsection 2.2.5. The combustion process is not only influenced by the intake compression, which sets the combustor entrance conditions, but also by the combustor design and more specifically the fuel injection mechanism. This topic is briefly discussed in Subsection 2.2.4.

2.2.4 Fuel Injection in Scramjets

Fuel injection high speed propulsion flow paths remains an active topic of study with no clear superiority of one mechanism over another. A recent comprehensive overview on the challenges of fuel injection in high-speed flow paths is given by Lee et al. [46]. A discussion on common injection approaches in scramjets and coupled ignition physics can be found in the review paper of Urzay [154]. Ideally, a fuel injection mechanism should "achieve ignition, maintain a stable flame zone, enhance rapid flame spread into the core airflow, and achieve fuel/air mixing necessary for efficient combustion" [46]. It is out of the scope of the present work to go in detail over the different injection approaches documented in the literature. Instead, some details about fuel injection configurations in experimental studies commonly adopted for numerical validation are given. Figure 2.5 presents a schematic of several injection strategies with two main categories: wall-based (step, cavity, porthole, film, ramp) and strut injection [155]. The strut injector has been used in the DLR combustor experiment of Waidmann et al. [98] that has been the subject of many numerical studies with RANS and LES. The physical presence of a strut in the middle of a flow path introduces downstream recirculation regions where fuel and air are able to mix. Moreover, fuel is introduced into the core air stream as shown in Figure 2.5 which avoids fuel penetration problems encountered in wall-based injection [155]. The strut does however obstruct the flow resulting in the generation of shock waves inducing losses and severe heating is experienced, especially near the leading edge. Appropriate cooling must be ensured. A strut without fuel injection behind its base can also be used to generate vortical structures in order to enhance mixing and is adopted in JAXA's scramjet configuration [156]. In the latter scramjet, fuel is injected normal to the flow through portholes located at the sidewalls behind two steps. It is a combination of the "step" and "porthole" scheme shown in Figure 2.5. The porthole injection strategy has been used in multiple experimental studies including the HyShot II combustor [102], the SCHOLAR setup [118] or the REST-type engine [10, 155]. Porthole injection does not physically obstruct the flow and is easy to implement. However, this injection type can induce shock losses and boundary layer separation. Moreover, fuel penetration into the core flow is a main issue and is highly dependent on the injection angle. A ramp injection is implemented in the UV-A scramjet [148] or derived configuration [157]. It induces extra vorticity into the flow which improves mixing but does as well introduce flow losses [155]. A popular experiment for CFD validation studies is that of Burrows and Kurkov [100] which is characterized by a step injection. The parallel injection of fuel with respect to the air stream does result in long combustion chambers in order to achieve high mixing and combustion efficiencies. They are therefore not very practical for actual scramjet designs. Cavity based injection is typical for hydrocarbon fuels in order to allow more time for fuel/air mixing through recirculation (flameholding). It is used in the HIFiRE 2 scramjet [158] as well as on the Mach 8 REST engine with hydrocarbon fuels [54]. The test cases selected for numerical study in the present work are characterized by different fuel injection strategies: step, strut and porthole.

2.2.5 Literature Review on the Eddy Dissipation Model

The use of the Eddy Dissipation Model (EDM) for scramjets has been reported by several authors. It has been both applied on hydrogen and hydrocarbon fueled configurations. The reaction rate predicted by the EDM is given in Equation 2.1 and will be

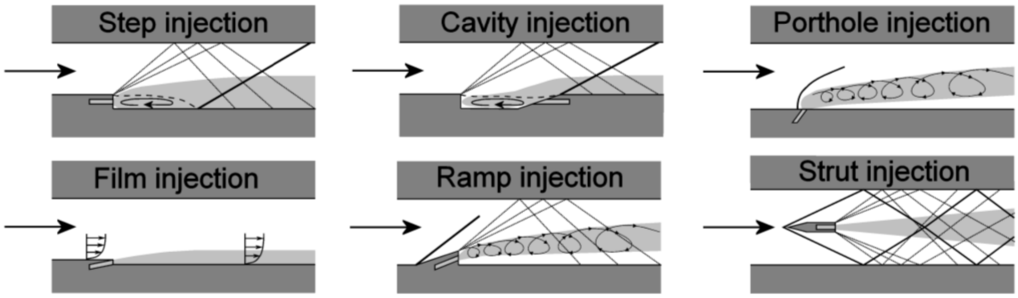

Figure 2.5: Commonly adopted fuel injection strategies. Image reproduced from [155].

discussed in further details in Chapter 5. Note however the presence of two modeling constants, $\mathrm{A_{edm}}$ and $\mathrm{B_{edm}}$, which have standard values derived from low-speed flame studies [153]. These constants have a direct impact on the computation of the reaction rate. In the literature, only a limited number of studies with the EDM report the setting of one ($\mathrm{A_{edm}}$) or both constants. Unless otherwise stated, the following discussion implies that the details on the above constant(s) are not reported. Note that the latter term on the right-hand-side of Equation 2.1 is often omitted in numerical scramjet studies where the combustion is mainly premixed.

$$\bar{\dot{\omega}}_F = -A_{\mathrm{edm}}\,\bar{\rho}\beta^*\omega\,\min\left[\tilde{Y}_F, \frac{\tilde{Y}_O}{s}, B_{\mathrm{edm}}\frac{\tilde{Y}_P}{s+1}\right] \tag{2.1}$$

With regard to the use of hydrogen fuel, the following studies have been performed. Abdel-Salam et al. [159] adopted the EDM in conjunction with the renormalization group (RNG) k-ε turbulence model for study of the mixing process in a scramjet engine with commercial software. A raised and relieved ramp configuration was considered but no comparison with experimental data is performed. Mohieldin and Tiwari [160] studied a dual-mode scramjet configuration with Mach 2.5 vitiated air stream. Note that a dual-mode scramjet can combine both subsonic and supersonic combustion operation as to allow flight over a broader range of Mach numbers. Above a flight Mach of approximately 8, the geometry operates in what is called pure scram mode (supersonic combustion dominates) [63]. Between flight Mach of 5 and 8 the transition between ram and scram-mode operation occurs and is termed dual-mode. The computational domain considered by Mohieldin and Tiwari [160] was a direct connect rectangular combustor with backward facing steps on upper and lower walls. Fuel is injected through portholes located at the base, behind those steps (5 lower wall, 4 upper wall). The Mach 2.5 vitiated air stream is representative of a 7.5 flight Mach. The inlet total temperature is 2000 K which resulted in a static temperature of 1055 K. Commercial software was used to perform the CFD simulations with the RNG k-ε turbulence model. The chemical source term was computed as the minimum between the EDM and the no-model approach with a single-step global reaction. From here onward this will be referred to as “EDM with kinetic limit”. A comparison to experimental wall pressure measurements is performed with an overall satisfactory agreement and most of the important features were well resolved. In a subsequent study, Luetke et al. [161] considered a simplified version of the dual-mode scramjet discussed above. The aim of the study is to compare steady-state and unsteady results as well as the effect of the discretization order in view of the highly asymmetric upstream interaction. A purely numerical study with commercial software is reported with the RNG k-ε turbulence model. The EDM with kinetic limit is adopted. Note that when no details on the EDM are given for a commercial software, it could be assumed that standard values for the model constants are used as reported in the user guide of Fluent [162] for instance. Belmrabet et al. [163] applied the EDM with the Spalart-Allmaras turbulence model for purely numerical study of the transverse fuel injection over a flat plate. Chakraborty [164] applied the EDM with commercial software on two hydrogen-fueled scramjet configurations. Reasonable agreement is observed in comparison with experimental pressure data. Several other RANS studies have been performed with commercial software for the experiments of Burrows and Kurkov [142], SCHOLAR [143, 165], the DLR combustor [117] and Cheng’s burner [166]. The aim of these different studies was to validate the EDM’s capability in predicting overall characteristics of mixing and combustion by comparison with experimental data. The main motivation of the authors for considering the EDM is its simple kinetic and simple TCI formulation which would be suitable as an engineering analysis tool. While the latter goal is understandable, no details on the model constants (except for [166] which documents the standard values) are given, nor any sensitivity study has been performed in order to understand the most appropriate use of the model given a certain injection type. Kummitha et al. [167–170] published a series of work where the EDM, with commercial software, is used in order to investigate the effect of changes in the DLR combustor configuration. These changes include the use of cavities, inserts and multiple struts. Jindala and Kumar [171] did as well consider the DLR combustor geometry to study the effect of a change in symmetry angle or an asymmetric strut on the flow field with EDM and commercial software. Edwards and Fulton [80] implemented the non-premixed EDM formulation in the REACTMB in-house CFD solver as part of the development of tools for testing and evaluation (T&E) of high-speed flight vehicles. Instead of applying a kinetic limit, an ignition temperature is defined which has to be locally exceeded in order for reactions to occur. The threshold was set to 900 K for hydrogen and ethylene fuel. The authors mention that the EDM constant (A_{edm}) is usually selected between 1 and 4 and that careful calibration is required. The EDM is compared to a 9-species finite rate chemistry no-model computation on a scramjet model similar to the SCHOLAR configuration. Flame structure and overall heat release were very similar between both approaches but the EDM predicted higher peak temperatures. No experimental data was available for further study. Drozda et al. [172] studied several fuel injection devices mounted on a flat plate at an equivalent flight Mach number of 15 (combustor inflow Mach = 6) at 37 km altitude. NASA's VULCAN CFD solver is used for RANS simulations. The authors motivate the use of the EDM with kinetic limit as their interest lies in the on the impact of heat release on the mixing.

The EDM has as well been considered in several hydrocarbon-fueled scramjet studies. Li et al. [173] studied the ignition characteristics inside a direct-connect dual-mode scramjet experimentally investigated at the Air Force Research Laboratory. Menter's k-ω SST model was used in conjunction with a two-step global kinetics mechanism (Westbrook and Dryer, 5-species) for ethylene / air combustion. The EDM with standard model settings is applied with a kinetic limit. Simulations were representative of a Mach 5 flight. No comparison with experimental data is presented and the emphasis of the discussion is put on the effect of air-throttling on the ignition process mechanism. The same geometry and combustion modeling choices were considered for study of the effect of fuel staging on the ignition process and combustion stability by Zhang et al. [174]. Simulated steady state predictions did agree well with experimental wall pressure measurements for two different equivalence ratio's. Manna et al. [175] investigated liquid kerosene combustion in a scramjet designed for future airframe integrated flight demonstration at Mach 6.5 and altitude of 32.5 km. Parametric studies are performed with commercial software which include the change of strut configuration. The k-ε turbulence model is selected with the EDM and a single-step global reaction. The use of this combustion model is motivated by its simplicity and robustness. In a following work, Manna et al. [176] further optimized the fuel injection and strut arrangement for the combustor discussed above. The same combustion modeling approach is adopted. Dharavath et al. [61] integrated the previously optimized scramjet combustor [176] on an hypersonic test vehicle and performed full nose-to-tail CFD simulations with commercial software at two angles of attack. Standard settings for the EDM constants were adopted. Chakraborty [164] investigated two kerosene-fueled scramjet configurations with the EDM and a single-step global reaction. Trends in experimental surface pressure were predicted with commercial software, especially in the divergent section of the combustors. Bynum and Baurle [177] performed a design of experiments study on the HIFiRE 2, hydrocarbon-fueled scramjet. The aim was to determine the effects of the Arc-Heated Scramjet Test Facility variations on the results. VULCAN was used for the CFD simulations with Menter's SST model and the EDM. Motivation of the latter is the mixing-limited combustion valid for the geometry under investigation at nominal flight Mach number of 5.84. No details on the model setting were given. Storch et al. [158] compared VULCAN CFD predictions with experimental data obtained from ground-testing of the same HIFiRE 2, hydrocarbon-fueled scramjet at simulated enthalpies of four different flight Mach numbers. The hydrocarbon fuel, binary mixture of ethylene and methane, combustion is modeled with the EDM. The CFD solutions were one-dimensionalised as to enable comparison with superimposed pressure data collected at the four walls. Simulations with CFD++ were as well performed with no-model finite-rate chemistry (22-species). One-dimensional pressure traces for both solvers were in good agreement, especially in dual-mode operation. Borghi et al. [178, 179] studied the HIFiRE 2 scramjet flowpath with the Wind-US solver. Two single-step forward reactions are considered for the methane / ethylene mixture. The EDM reaction rate (non-premixed) was obtained with standard setting of the model constant. A kinetic limit on the EDM was considered by the authors. Overall good agreement with experimental pressure traces were observed with more pronounced discrepancies in the downstream end of the cavity. Dharavath et al. [180] performed numerical simulations of an ethylene-fueled scramjet combustor ground tested at conditions equivalent to Mach 6 flight at 30 km altitude. The EDM with kinetic limit is selected for the combustion treatment and standard settings for the model constants. A comparison with experimental wall pressure trace demonstrated a reasonable agreement of the commercial software predictions. Note that the extend of the experimental data set is very limited. Edwards and Fulton [80] applied the EDM to study the ethylene / air combustion inside an axisymmetric dual-mode scramjet combustor. They considered the REACTMB solver with RANS and 7-species, 3-step mechanism for the EDM which requires case specific calibration. However, no details are given on the final values used. A comparison with experimental wall pressure traces is presented for two equivalence ratio's with an overall reasonable agreement.

All of the above studies apply the EDM either with or without kinetic limit. No attempt is made in improving the use of or modifying the model. This includes improving the selection of the model constant(s). To the best of the author's knowledge, Norris

[181] is the only author whom discussed a methodology which could be used in order to specify a-priori the modeling constants of the EDM. The approach enables to specify an upper kinetic limit to the reaction rate. It relies on the use of a Perfectly Stirred Reactor (PSR) and Partially Stirred Reactor (PaSR) which are zero dimensional models. More precisely, the EDM used in the PSR is compared to finite-rate chemistry with detailed reaction mechanism in the PaSR for several residence and mixing times. It requires the specification of inflow fuel and air properties which are representative for the problem under consideration. Note that this does not imply the use of the inflow properties of the considered scramjet combustor for instance but instead conditions representative for the combustion process. The EDM constants are then tuned as to get a better agreement with the PaSR results. Moreover, in order to account for blow-out, a limit to the maximum mixing time scale is introduced. The author illustrates this methodology with a subsonic JP7 / air combustion considering 16-species and 45 reactions. The latter mechanism is representative of an hydrocarbon scramjet combustion. While the method has a lot of merit, it remains to be seen how the approach would perform in supersonic reacting flows in the presence of shock and expansions. Moreover, the paper discusses the tuning methodology but no practical problem is presented and is subject to future work of the author.

The problem remains that when given a certain scramjet configuration, based on the work in the literature, it is not possible to know which value of the EDM constant(s) would be the most appropriate. This open question is considered in the present work and an attempt in answering it is made for hydrogen combustion. The benefits of the EDM in terms of reduction in computational cost for hydrocarbon fuels is much larger (many more species and reactions) than for hydrogen but is subject to future possible considerations. Furthemore, other questions with regard to the EDM are considered for study in this thesis. Is there a need to apply a kinetic limit on the EDM in primary mixing-limited scramjet flow paths? Can the use of the EDM be improved for scramjet simulations given a type of fuel injection? Is the EDM still valid when the scramjet combustion is mainly kinetically controlled? What type of metrics can the EDM provide with enough accuracy in order to optimize the fuel injection in a given scramjet?

2.3 Summary of Chapter

An overview of the numerical tools adopted in scramjet related studies has been given. It can be concluded that when scramjet propulsion is considered as a subsystem in MDO or vehicle analyses, low fidelity models are primarily used. Attempts are made in introducing CFD as to improve the predictive capability of these low fidelity models but the overall expense associated with the process inhibits its use as a replacement. When scramjet combustor designs are considered, a higher fidelity is preferred through the use of CFD. This allows a more detailed investigation and understanding of the physics in parametric studies. In terms of CFD approaches, RANS remains the state-of-the-art for design purposes in hypersonic propulsion flow paths. The need for a TCI model in the combustion modeling is an ongoing topic of research. For the high Mach ($\approx$ 8-12) operation regime of a scramjet, the EDM was identified as a viable candidate for combustion modeling offering a balance between computational cost and predictive accuracy. Whilst the EDM has been adopted in several scramjet related studies, there are still some open questions regarding its use.

Chapter 3

The Governing Equations of Compressible Turbulent Reacting Flows

This Chapter provides a summary of the governing equations for compressible turbulent reacting flows to be solved with Computational Fluid Dynamics (CFD). A special emphasis is placed on the specification of modeling choices relevant to simulating scramjet type flows as used in this work. In a first section (3.1), the basic idea of turbulence is explained including the implication of the known approaches to describe the phenomenon. The second section (3.2) introduces the Reynolds-Averaged Navier-Stokes equations and all modeling choices for turbulent supersonic reacting flows. A solver is selected in a third section (3.3) followed by a description of the finite volume method and the numerical methods adopted to solve the governing equations (3.4). The final section (3.5) provides a summary of the chapter.

3.1 Turbulence

"Big whirls have little whirls, that feed on their velocity; and little whirls have lesser whirls, and so on to viscosity - in the molecular sense." These famous words expressed by Richardson in 1922 were an early attempt in the description of the physical process that is turbulence [182]. More specifically, the concept of the energy cascade in a fully developed turbulent flow is being introduced. In view of Richardson, turbulence is composed of so-called "eddies" of different sizes. The term eddy has no exact definition but a formulation is given by Pope [183]; an eddy represents a turbulent motion, localized within a region of size l, that is at least moderately coherent over this region. On top of a charecteristic size or length scale l, eddies have a characteristic velocity $u(l)$ and timescale $\tau(l) = l/u(l)$. A turbulent flow is composed of many eddies of different sizes and life times interacting with each other. Considering L and U, respectively the characteristic length scale and velocity of a fully turbulent flow. The largest eddies have a characteristic length scale l_0 on the order of L and characteristic velocity u_0 on the order of U. This scale is also referred to as the integral length scale. In the energy cascade process, the unstable largest eddies (l_0) break up due to vortex stretching and tilting, transferring their energy to smaller eddies. The break up process repeats itself on eddies with smaller size until the local Reynolds number ($Re(l)$) becomes small enough so that a stable eddy motion is possible and the kinetic energy of the smaller eddies is dissipated into heat due to viscous forces (molecular viscosity). It is however only in 1941 that a mathematically supported description of this cascade process was introduced by Kolmogorov [184] also known as the K41 theory. In his work two similarity hypotheses were formulated to describe the statistical behavior of eddies in locally isotropic turbulence. The term local isotropy refers to isotropy at scales smaller than the largest eddies ($l << l_0$) and is assumed to be the case in turbulent flows with sufficiently high Reynolds numbers. The hypotheses state that the motion of the smaller scales ($l << l_0$) depend only upon the rate at which the larger eddies transfer their energy (ε) and the kinematic viscosity (ν). It is convenient to represent the implications of Kolmogorov's theory in terms of a spectral distribution of the energy. Figure 3.1 presents this result with on the vertical axis the turbulent kinetic energy ($E(\kappa)$) and on the horizontal axis the wavenumber (κ) of the different eddies. The wavenumber is inversely proportional to the characteristic size of an eddy as $\kappa = 2\pi/l$. On the horizontal axis, l represents the integral length scale which is the characteristic length associated with the largest eddies ($l = l_0$). Integrating the energy spectrum over all wavenumbers results in the turbulent kinetic energy which represents the kinetic energy due to the fluctuating turbulent velocity of all eddies present in the flow, at a given time [136]. The K41 theory (second similarity hypothesis) stipulates the existence of a region where the eddy motion, and so $E(\kappa)$, does only depend on ε and κ, and not on viscosity. This region is indicated as the inertial subrange and the law governing the region is known as Kolmogorov's -5/3 law. It must be noted that there exist some controversy about the validity of this law, more specifically the -5/3 exponent, as the internal intermittent character of turbulence is not accounted for. This subject is however, out of the scope of this work and does not impact further discussions. The interested reader is referred to the work of Jou [185] for further details.

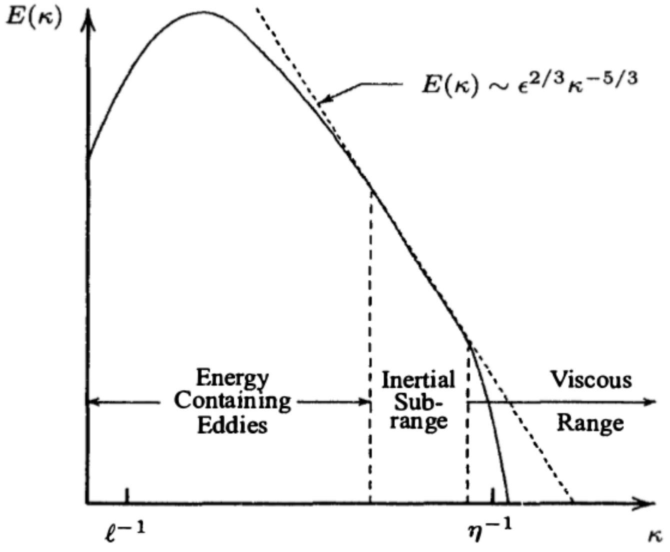

Figure 3.1: The energy spectrum in a turbulent flow on a log-log scale. Reproduced from Wilcox [136].

The energy spectrum and the idea of the energy cascade is of importance in the field of Computational Fluid Dynamics (CFD). It is exactly this process of eddies interacting with each other that need to be described in some way by CFD in order to predict numerically turbulent flows. To do so, three main approaches are used: Direct Numerical Simulation (DNS), Large Eddy Simulation (LES) and Reynolds Averaged Navier-Stokes (RANS) simulations. It is not the intention of this work to go into an in depth discussion of each approach but to give the reader a basic idea of the implications. Figure 3.2, taken from the reference book of Poinsot and Veynante [137], illustrates this with the combustion of a premixed flame inside a rectangular region. The temperature inside the latter region is monitored over a time period. DNS does not include any modeling assumptions and captures all oscillations in the temperature signal. The oscillations are influenced by interaction of all turbulent eddies. LES, which does model smaller scales and resolves the larger ones, is able to capture the large scale motions in the signal but not the smaller ones. RANS, where every interaction between eddies is modeled, is only capable of predicting a mean behavior of the temperature signal over time. In the literature discussion in Section 2.2, it was concluded that in order to keep the computational costs at a moderate level, the RANS approach has to be considered. The following section introduces the equations of fluid motions in a RANS framework.

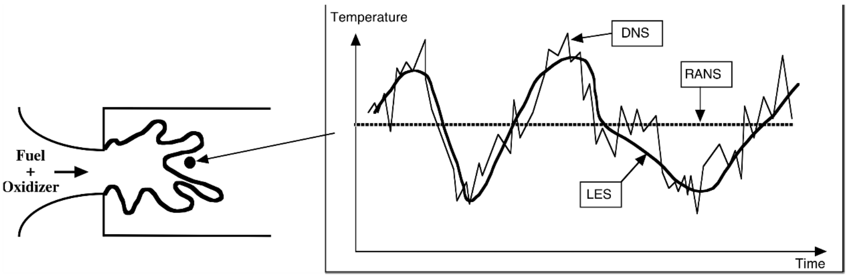

Figure 3.2: The implications of DNS, LES and RANS on the time evolution of the temperature. Reproduced from Poinsot and Veynante [137].

3.2 Reynolds/Favre-Averaged Navier Stokes

The instantaneous governing equations for fluid flows can be modified to represent a time-averaged state of the flow field described in terms of mean flow quantities by means of averaging. In the case of stationary turbulence, a quantity $\phi(t)$ can at any point in time be statistically described by the sum of a mean value and a fluctuating part as

$$\phi(t) = \bar{\phi} + \phi^{'}, \quad \bar{\phi} = \lim_{T\to\infty} \frac{1}{T} \int_{t}^{t+T} \phi(t) dt \tag{3.1}$$

This decomposition makes use of the time average also known as Reynolds averaging. Figure 3.3 illustrates the idea for the velocity components [136]. The time averaged mean is indicated by U_i in this representation. In compressible flows it is also useful to consider the mass-weighted or Favre average. The decomposition of a quantity is similar to Equation 3.1 with a mean and fluctuating part.

$$\phi(t) = \tilde{\phi} + \phi^{''}, \quad \tilde{\phi} = \frac{1}{\bar{\rho}} \lim_{T\to\infty} \frac{1}{T} \int_{t}^{t+T} \rho \phi(t) dt \tag{3.2}$$

Finally, the following combination of Reynolds and Favre averages are introduced into the instantaneous governing equations.

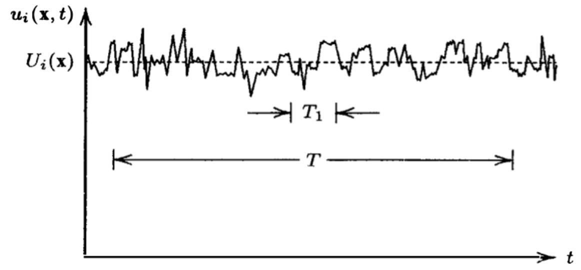

Figure 3.3: Time averaging in the case of stationary turbulence. Reproduced from Wilcox [136].

$$
\begin{aligned}
&\rho = \bar{\rho} + \rho^{'} \quad u_i = \tilde{u}_i + u_i^{''} \quad p = \bar{p} + p^{'} \quad h = \tilde{h} + h^{''} \\
&e = \tilde{e} + e^{''} \quad T = \tilde{T} + T^{''} \quad q_i = \bar{q}_i + q_i^{''} \quad Y_s = \tilde{Y}_s + Y_s^{''} \\
&\tau_{ij} = \bar{\tau}_{ij} + \tau_{ij}^{'} \quad \dot{\omega}_s = \bar{\dot{\omega}}_s + \dot{\omega}_s^{'}
\end{aligned}
\tag{3.3}
$$

The choice of combining both averaging approaches minimizes the number of unknown correlations that would appear [93, 137]. Introducing Favre averaging eliminates density fluctuations from the averaged equations [136]. The governing equations for turbulent reacting flows can now be written following the notation of Baurle [93] as:

Mass Conservation:

$$
\frac{\partial \bar{\rho}}{\partial t} + \frac{\partial}{\partial x_i}\left(\bar{\rho}\tilde{u}_i\right) = 0 \tag{3.4}
$$

Momentum Conservation:

$$
\frac{\partial}{\partial t}\left(\bar{\rho}\tilde{u}_i\right) + \frac{\partial}{\partial x_j}\left(\bar{\rho}\tilde{u}_j\tilde{u}_i + \delta_{ij}\bar{p}\right) = \frac{\partial}{\partial x_j}\left(\bar{\tau}_{ji} - \bar{\rho}\widetilde{u_i^{''}u_j^{''}}\right) \tag{3.5}
$$

Energy Conservation:

$$
\frac{\partial}{\partial t}\left(\bar{\rho}\tilde{E}\right) + \frac{\partial}{\partial x_j}\left(\bar{\rho}\tilde{u}_j\tilde{H}\right) = \frac{\partial}{\partial x_j}\left(\bar{\tau}_{ij}\tilde{u}_i + \overline{\tau_{ij}u_i^{''}} - \bar{q}_j - \bar{\rho}\widetilde{H^{''}u_j^{''}}\right) \tag{3.6}
$$

Species Conservation:

$$
\frac{\partial(\bar{\rho}\tilde{Y}_s)}{\partial t} + \frac{\partial(\bar{\rho}\tilde{Y}_s\tilde{u}_j)}{\partial x_j} = \bar{\dot{\omega}}_s - \frac{\partial}{\partial x_j}\left(\bar{J}_{s_j} + \bar{\rho}\widetilde{Y_s^{''}u_j^{''}}\right) \tag{3.7}
$$

with conserved variables $\bar{\rho}$, $\bar{\rho}\tilde{u}_j$, $\bar{\rho}\tilde{E}$, $\bar{\rho}\tilde{Y}_s$ representing density, momentum, total energy per unit volume and partial densities of the species s (s=1,...,N). Throughout this work, the above set of equations will be referred to as the Reynolds Averaged Navier-Stokes equations (RANS). Equations 3.4 to 3.7 are written in such a way that those terms which require modeling are indicated on the right-hand side. The system of conservation equations for a turbulent chemically reacting flow needs extensive modeling. The common practice for scramjet simulations is now detailed.

In Equation 3.6, the total energy and enthalpy are defined as

$$\tilde{E} = \tilde{e} + \frac{1}{2}\tilde{u}_i\tilde{u}_i + k \qquad \tilde{H} = \tilde{h} + \frac{1}{2}\tilde{u}_i\tilde{u}_i + k \tag{3.8}$$

where $\tilde{e}$ and $\tilde{h}$ are respectively the specific internal energy and specific enthalpy in J/kg. In above equation the turbulent kinetic energy k has also been introduced which for compressible flows is defined in Equation 3.9 [136]. Therefore, some modeling assumptions have already been made which will be covered later on.

$$k = \frac{1}{2}\widetilde{u_i'' u_i''} \tag{3.9}$$

For scramjet type flows a thermally perfect gas is typically assumed. The thermal equation of state ($p-\rho-T$) is then given by (neglecting effect of composition fluctuations)

$$p = \bar{\rho}R\tilde{T} \ , \qquad\qquad R = R_u \sum_{s=1}^{N} \frac{\tilde{Y}_s}{W_s} \tag{3.10}$$

and the caloric equation of state ($p-\rho-e$) as [186]:

$$\tilde{e} = \frac{p}{\bar{\rho}(\gamma-1)} \tag{3.11}$$

The mean molecular stress tensor $\bar{\tau}_{ij} = \bar{\tau}_{ji}$ is modeled neglecting the effect of turbulence fluctuations on the molecular viscosity and assuming equality between conventional and mass-weighted averaged velocities:

$$\bar{\tau}_{ij} = 2\mu\tilde{S}_{ij} + \lambda\tilde{u}_{k,k}\delta_{ij} \tag{3.12}$$

with $\tilde{S}_{ij}$ the strain-rate tensor [137, 187] as a function of mass-weighted velocities defined in Equation 3.13 and the secondary viscosity coefficient λ is written as a function of the mixture molecular viscosity μ following Stokes' hypothesis in Equation

3.14. This latter is true for monoatomic gases but is still used for all gases in CFD [136]. In Equation 3.12 δ_{ij} is the Kronecker delta symbol which takes a value of 1 when i=j and 0 otherwise.

$$\tilde{S}_{ij} = \frac{1}{2}(\tilde{u}_{i,j} + \tilde{u}_{j,i}) \tag{3.13}$$

$$\lambda = -\frac{2}{3}\mu \tag{3.14}$$

The momentum equation contains a term which is called the Reynolds Stress tensor $\bar{\rho}\widetilde{u_i''u_j''}$. This second order tensor is symmetric and contains consequently 6 unknowns which have to be dealt with by the turbulence model. The most common approach in RANS of turbulent reacting scramjet flow paths is to rely on Boussinesq assumption. The assumption is given in Equation 3.15 and mimics the molecular gradient diffusion process (Equation 3.12) by introducing an eddy or turbulent viscosity μ_t. Therefore, turbulence models relying on Boussinesq' assumption are referred to as linear eddy viscosity models. The latter assumption does as well include the turbulent kinetic energy which is consistent with its definition in Equation 3.9.

$$-\bar{\rho}\widetilde{u_i''u_j''} = 2\mu_t\tilde{S}_{ij} - \frac{2}{3}\delta_{ij}(\mu_t\tilde{u}_{k,k} + \bar{\rho}k) \tag{3.15}$$

An important consequence of Boussinesq assumption, and a limitation in the current work, is that Reynolds stress anisotropies are not accounted which are responsible for secondary flow motions. See Baurle [93] or Poinsot and Veynante (p153)[137] for more details about this and possible modeling improvements to correct the issue. Boussinesq assumption introduces a new unknown which has to be specified by the modeler: the eddy viscosity. Several approaches are possible to do so and for scramjet flows, the one-equation or two-equation approach is commonly adopted. Among the one-equation options, the Spalart-Allmaras turbulence model is popular as it introduces a transport equation for a quantity directly related to the eddy viscosity [93, 188]. However, a problem arises with one-equation models: how do we obtain the turbulent kinetic energy appearing in Boussinesq assumption? To avoid the issue, the last term in Equation 3.15 is generally ignored [86, 188]. In general, the two-equation models approach is commonly adopted for hypersonic propulsion CFD [94]. This trend follows from the larger range of applicability and suitability for complex geometries in comparison to e.g. one equation models without drastically increasing the computational cost [93]. Two-equation turbulence models typically introduce a transport equation for the turbulent kinetic energy k (m^2/s^2) and another transport equation for either the dissipation rate of turbulent kinetic energy ε (m^2/s^3) or its specific dissipation rate ω ($1/s$). Consequently, through the chosen variables, the turbulence model includes the energy cascade process discussed in Section 3.1. More specifically, the value of k predicted by the CFD in every cell of the mesh does represent the sum of the energy of all eddies contained within the cell as illustrated in Figure 3.1. The same is true for ε or ω which represents an average behavior of the transfer of energy between the eddies of different sizes in each cell of the domain. As the present work only considers Wilcox' 2006 $k-\omega$ model [134, 136], the equations for this model are introduced in this section. The following discussions remain valid for the k-ε or the k-ω Shear Stress Transport (SST) as only the transport equations for the turbulent quantities will differ. In Wilcox' 2006 $k-\omega$ model, Equations 3.16 and 3.17 are used to model turbulence. With the knowledge of k and ω, the eddy viscosity is then obtained through Equation 3.18. Note the use of a stress limiter on the value of ω which does limit the ratio of production to dissipation of turbulent kinetic energy. The different closure coefficients are given in Equation 3.19.

Turbulence Kinetic Energy:

$$\frac{\partial}{\partial t}(\bar{\rho}k)+\frac{\partial}{\partial x_j}\left(\bar{\rho}\tilde{u}_j k\right)=\bar{\rho}\widetilde{u_i''u_j''}\frac{\partial \tilde{u}_i}{\partial x_j}-\beta^*\bar{\rho}k\omega+\frac{\partial}{\partial x_j}\left[\left(\mu+\sigma^*\frac{\bar{\rho}k}{\omega}\right)\frac{\partial k}{\partial x_j}\right] \tag{3.16}$$

Specific Dissipation Rate:

$$\frac{\partial}{\partial t}(\bar{\rho}\omega)+\frac{\partial}{\partial x_j}\left(\bar{\rho}\tilde{u}_j\omega\right)=\alpha\frac{\omega}{k}\bar{\rho}\widetilde{u_i''u_j''}\frac{\partial \tilde{u}_i}{\partial x_j}-\beta\bar{\rho}\omega^2+\sigma_d\frac{\bar{\rho}}{\omega}\frac{\partial k}{\partial x_j}\frac{\partial \omega}{\partial x_j}+$$
$$\frac{\partial}{\partial x_j}\left[\left(\mu+\sigma\frac{\bar{\rho}k}{\omega}\right)\frac{\partial \omega}{\partial x_j}\right] \tag{3.17}$$

Eddy Viscosity:

$$\mu_t=\frac{\bar{\rho}k}{\tilde{\omega}} \qquad \tilde{\omega}=\max\left\{\omega,\ C_{lim}\sqrt{\frac{2\bar{S}_{ij}\bar{S}_{ij}}{\beta^*}}\right\} \qquad C_{lim}=\frac{7}{8} \tag{3.18}$$

Closure Coefficients:

$$\alpha=\frac{13}{25} \qquad \beta=\beta_o f_\beta \qquad \beta^*=\frac{9}{100} \qquad \sigma=\frac{1}{2} \qquad \sigma^*=\frac{3}{5} \qquad \sigma_{do}=\frac{1}{8}$$

$$\beta_o=0.0708 \qquad Pr_t=\frac{8}{9} \qquad \sigma_d=\begin{cases}0, & \frac{\partial k}{\partial x_j}\frac{\partial \omega}{\partial x_j}\leq 0\\ \sigma_{do}, & \frac{\partial k}{\partial x_j}\frac{\partial \omega}{\partial x_j}>0\end{cases}$$

$$f_\beta = \frac{1+85\chi_\omega}{1+100\chi_\omega} \qquad \chi_\omega = \left|\frac{\Omega_{ij}\Omega_{jk}\hat{S}_{ki}}{(\beta^*\omega)^3}\right| \qquad \hat{S}_{ki} = \tilde{S}_{ki} - \frac{1}{2}\frac{\partial \tilde{u}_m}{\partial x_m}\delta_{ki} \tag{3.19}$$

In the expression for the stress limiter the quantity $\bar{S}_{ij}$ is related to the mean rate of strain tensor as

$$\bar{S}_{ij} = \tilde{S}_{ij} - \frac{1}{3}\frac{\partial \tilde{u}_k}{\partial x_k}\delta_{ij} \tag{3.20}$$

In addition, the k-ω 2006 version considered in this work does include an extra production limiter in the equation for turbulent kinetic energy, namely:

$$min(P, 25\beta^*\rho k\omega) \qquad P = \bar{\rho}\widetilde{u_i^{''}u_j^{''}}\tilde{u}_{i,j} \tag{3.21}$$

This addition follows in the steps of the k-ω SST model but appears to not result in a significant difference [189].

A compressibility correction for the model exist known as the dilatation-dissipation correction which improves the behavior of the model in predicting compressible shear layer growth, albeit for the wrong reasons [190]. An explanation of the latter statement and further details behind the correction can be found in Appendix B. The correction relies on the value of the turbulent Mach number and has been added in the turbulence model as part of this work

$$M_t = \sqrt{\frac{2k}{a^2}} \tag{3.22}$$

The correction for the k-ω equation is obtained by making the destruction terms in Equations 3.16 and 3.17 dependent on the turbulent Mach number as:

$$\beta^* = \beta_i^*(1+\xi^* F(M_t)) \tag{3.23}$$

and

$$\beta = \beta_i - \beta_i^*\xi^* F(M_t) \tag{3.24}$$

where β_i^* is the incompressible model constant equal to 0.09 and $\beta_i = \beta_o f_\beta$ from the turbulence model [136, 134]. In Wilcox' version of the dilatation-dissipation correction the following function is defined

$$F(M_t) = (M_t^2 - M_{t_o}^2)\mathscr{H}(M_t - M_{t_o}) \tag{3.25}$$

where $\mathscr{H}$ is the Heavyside function (0 if argument smaller than 0 and 1 if greater or equal). The constant ξ^* is set to 2 and M_{t_o} to 0.25 in accordance with Wilcox [136].

In order to continue the description of the modeling approach for the conservation equations it is convenient to rewrite the energy equation (Equation 3.6) by replacing the total enthalpy fluctuation on the right-hand-side (RHS) by the different contributions as given in Equation 3.26 [93].

$$H'' = h'' + \tilde{u}_i u_i'' + k'' \tag{3.26}$$

Doing this yields the following form of the energy conservation equation

$$\frac{\partial}{\partial t}\left(\bar{\rho}\tilde{E}\right) + \frac{\partial}{\partial x_j}\left(\bar{\rho}\tilde{u}_j\tilde{H}\right) = \frac{\partial}{\partial x_j}\left(\bar{\tau}_{ij}\tilde{u}_i + \overline{\tau_{ij}u_i''} - \bar{q}_j - \bar{\rho}\widetilde{h''u_j''} - \bar{\rho}\tilde{u}_i\widetilde{u_i''u_j''} - \bar{\rho}\widetilde{k''u_j''}\right) \tag{3.27}$$

The last term in this equation represents the turbulent transport of turbulent kinetic energy and is typically approximated by a gradient diffusion relation:

$$\bar{\rho}\widetilde{k''u_j''} = -\frac{\mu_t}{\sigma_k}\frac{\partial k}{\partial x_j} \tag{3.28}$$

where σ_k is a closure coefficient of the selected turbulence model [93]. In the case of the $k-\omega$ 2006 model [134], $\sigma_k = 1/\sigma^*$.

The second term from the right contains the Reynold stresses and has previously being defined in Equation 3.15. The third term is referred to as the Reynolds heat flux vector and is as well approximated by a gradient diffusion hypothesis:

$$\bar{\rho}\widetilde{h''u_j''} = -\frac{\mu_t}{Pr_t}\frac{\partial \tilde{h}}{\partial x_j} \tag{3.29}$$

The second term on the RHS is a molecular diffusion term and is approximated by

$$\overline{\tau_{ij}u_i''} \approx \frac{\partial}{\partial x_j}\left(\mu\frac{\partial \tilde{k}}{\partial x_j}\right) \tag{3.30}$$

This assumption comes from incompressible flows but it is assumed that this remains valid for compressible flows [93]. The only term left to model is the averaged total heat flux $\bar{q}_i$ which is the sum of contribution from heat conduction and the energy flux created by inter-species diffusion. Fourier law is used for the former and yields:

$$\bar{q}_j = \overline{\kappa \frac{\partial T}{\partial x_j}} + \sum_{s=1}^{N} \overline{J_{s_j} h_s(T)} \tag{3.31}$$

Similarly to molecular stresses, the effect of turbulent fluctuations on the heat conduction are neglected yielding

$$\overline{\kappa \frac{\partial T}{\partial x_j}} \approx \kappa \frac{\partial \tilde{T}}{\partial x_j} = \frac{c_p \mu}{Pr} \frac{\partial (c_p \tilde{T}/c_p)}{\partial x_j} \approx \frac{\mu}{Pr} \frac{\partial \tilde{h}}{\partial x_j} \tag{3.32}$$

where κ is the coefficient of thermal conductivity ($W/(mK)$). The second term in Equation 3.31 (laminar diffusion fluxes) can be neglected if high enough Reynolds numbers are encountered or modeled with a gradient law introducing laminar diffusion fluxes as will be seen further below. This second effect is called the Dufour effect (heat flux due to species mass fraction gradients). The components of the diffusion flux J_{s_j} of species s is defined as a function of the species diffusion velocity V_{s_j} [93, 137] as

$$J_{s_j} = \rho Y_s V_{s_j} \tag{3.33}$$

Fick's law is commonly used to define the diffusion velocities and yields for species s:

$$V_{s_j} = -\frac{D_s}{Y_s} \frac{\partial Y_s}{\partial x_j} \tag{3.34}$$

where D_s is a mean species molecular diffusion coefficient (mass diffusion). It expresses the mass diffusivity of species "s" relative to the mixture. The Soret effect is neglected (molecular species diffusion due to temperature gradients) [137]. Applying Fick's law gives the following expression for the mean species diffusion fluxes

$$\bar{J}_{s_j} = \overline{\rho Y_s V_{s_j}} \approx \bar{\rho} D_s \frac{\partial \tilde{Y}_s}{\partial x_j} \tag{3.35}$$

where the last expression is obtained by again neglecting the effect of turbulent fluctuations on the mass diffusivity and equating conventional averages to mass-weighted averages. In scramjet flows one typically assume a single constant Lewis number for all the species. Even though it is not valid in e.g. the case of hydrogen, turbulent diffusion is much higher than the laminar counterpart [105]. The laminar diffusion is sometimes not considered in scramjet simulations. This implies the following relation for the mass diffusivities [137]:

$$D_s = \frac{\nu}{Sc_s} = \frac{\nu}{PrLe_s} \tag{3.36}$$

with Pr the Prandtl number and Sc_s the Schmidt number. The last term on the RHS of the species conservation (Equation 3.7) is called the Reynolds mass flux and is obtained through a gradient law:

$$\bar{\rho}\widetilde{Y_s'' u_j''} = -\frac{\mu_t}{Sc_t}\frac{\partial \tilde{Y}_s}{\partial x_j} \tag{3.37}$$

Turbulent Prandtl Pr_t (Equation 3.28) and Schmidt numbers Sc_t (Equation 3.37) are usually assumed constant in simulations and need to be tuned depending on the problem. One combination for one problem does not imply the best performance for another. Approaches to vary them based on the flow solution do exist [93, 113, 191, 192] but are not considered in this work as they require solving additional equation and thus increasing the computational cost.

The inter-species diffusion energy flux in Equation 3.31 can be rewritten as a function of the mass diffusivity D_s, neglecting turbulent fluctuations on mixture diffusivities and ensemble average equals mass averages, as (making use of Equation 3.35)

$$\sum_{s=1}^{N} \overline{J_{s_j} h_s(T)} \approx \sum_{s=1}^{N} \bar{\rho} D_s h_s(\tilde{T}) \frac{\partial \tilde{Y}_s}{\partial x_j} \tag{3.38}$$

Finally, a new form of the energy (Equations 3.6 and 3.27) is obtained:

$$\begin{gathered}\frac{\partial}{\partial t}\left(\bar{\rho}\tilde{E}\right) + \frac{\partial}{\partial x_j}\left(\bar{\rho}\tilde{u}_j\tilde{H}\right) = \\ \frac{\partial}{\partial x_j}\left[\left(\frac{\mu}{Pr} + \frac{\mu_t}{Pr_t}\right)\frac{\partial \tilde{h}}{\partial x_j} + \left(\mu + \sigma^* \frac{\bar{\rho} k}{\omega}\right)\frac{\partial k}{\partial x_j}\right] + \frac{\partial}{\partial x_j}\left[\tilde{u}_i\left(\bar{\tau}_{ij} - \bar{\rho}\widetilde{u_i'' u_j''}\right)\right]\end{gathered} \tag{3.39}$$

Note that in specifying the diffusion of the turbulent kinetic energy, Equation 3.28 has been applied by replacing μ_t without applying the stress limiter of Equation 3.18 and is consistent with [134].

The remaining term to be specified in order to simulate compressible turbulent reacting flows is the species mean reaction rate $\bar{\dot{\omega}}_s$ ($kg/(m^3 s)$) in Equation 3.7. The scramjet simulation community is still in debate on how to model this term appropriately. The major issue is that this term is highly non-linear and cannot be directly related to mean flow properties, i.e. $\bar{\dot{\omega}}_s \neq \dot{\omega}_s(\tilde{T}, \bar{\rho}, \tilde{Y}_s)$. The idea can be illustrated with a simplified example taken from the online lecture notes of Bakker [193] (Lecture 10, p11). A single step methane reaction is considered for a turbulent fluid which has a constant species concentration at all times but does spend one third of its time at respectively 300K, 1000K and 1700K. In this example, computing the reaction rate with Arrhenius law yields $\bar{\dot{\omega}}_s = 4.8e4 \neq \dot{\omega}_s(\tilde{T}) = 7.12$. In other words, a very significant difference in reaction rate is observed and the effect of turbulence (temperature fluctuations) needs to be accounted for in this specific example. Similar observations are reported in [181, 194] with possibly orders of magnitude differences in mean reaction rate predictions. For scramjet flows, some authors reported satisfactory results in some comparisons with experimental data by neglecting the effect of turbulence, while for other configurations this is not the case any more. The topic of turbulence / chemistry interaction (TCI) will be covered in Chapter 5. The following description in Subsection 3.2.1 does not include TCI and is referred to as the "Arrhenius" or the "no-model" approach [137]. The latter modeling choice has been selected for some validation studies in Chapter 4 and is therefore briefly covered.

3.2.1 The no-model approach

Following the notation of Poinsot and Veynante, [137] a chemical system of N species s reacting through M reactions can be written as

$$\sum_{s=1}^{N} \nu'_{sj}\mathscr{M}_s \rightleftharpoons \sum_{s=1}^{N} \nu''_{sj}\mathscr{M}_s \quad , \qquad j = 1, M \tag{3.40}$$

where $\mathscr{M}_s$ represents species s and ν'_{sj} and ν''_{sj} are the molar stochiometric coefficients of species s in reaction j. Mass conservation implies that

$$\sum_{s=1}^{N} \nu'_{sj}W_s = \sum_{s=1}^{N} \nu''_{sj}W_s \quad , \qquad j = 1, M \tag{3.41}$$

The chemical source term in Equation 3.7 is expressed as the sum of all the rates $\dot{\omega}_{sj}$ (j=1,...,M) produced by the reactions in which species s participates by

$$\bar{\dot{\omega}}_s = \sum_{j=1}^{M} \bar{\dot{\omega}}_{sj} = W_s \overline{\frac{d[\tilde{X}_s]}{dt}} = W_s \sum_{j=1}^{M} \nu_{sj}\tilde{\Gamma}_j \left[k_{fj} \prod_{k=1}^{N} [\tilde{X}_k]^{\nu'_{kj}} - k_{rj} \prod_{k=1}^{N} [\tilde{X}_k]^{\nu''_{kj}} \right] \tag{3.42}$$

in which ν_{sj} is defined as

$$\nu_{sj} = \nu''_{sj} - \nu'_{sj} \tag{3.43}$$

Equation 3.42 is known as the law of mass action in which k_{fs} and k_{rs} are respectively the forward and reverse rates of reaction j. They are usually evaluated by Arrhenius empirical law given in Equation 3.44. The molar concentrations $[\tilde{X}_s]$ are expressed as a function of the species partial density $\bar{\rho}_s$ and the atomic weight of species s, W_s, or the mole fractions $\tilde{X}_s$ and the mean mean molecular weight W, by Equation 3.45. The term $\tilde{\Gamma}_j$ is introduced to account for the third bodies and is defined in Equation 3.46 [195] introducing the third body efficiencies γ_{sj}.

$$k_{fj} = A_{fj} T^{\beta_j} exp\left(-\frac{E_j}{R_u T}\right) = A_{fj} T^{\beta_j} exp\left(-\frac{T_{aj}}{T}\right) \tag{3.44}$$

$$[\tilde{X}_s] = \frac{\bar{\rho}\tilde{Y}_s}{W_s} = \frac{\bar{\rho}_s}{W_s} = \bar{\rho}\frac{\tilde{X}_s}{W} \tag{3.45}$$

$$\tilde{\Gamma}_j = \sum_s^N \gamma_{sj}[\tilde{X}_s] = \sum_s^N \gamma_{sj}\frac{\bar{\rho}\tilde{Y}_s}{W_s} \tag{3.46}$$

Solving Equation 3.44 requires knowledge of the pre-exponential constants A_{fj}, the temperature exponents β_j and the activation energies E_j (or activation temperatures $T_{aj} = E_j/R_u$). R_u is the universal gas constant with a value of 8.314 J/(mole K). A similar equation can be formulated for the reverse reaction rates k_{rj} or can be computed through the forward rates through equilibrium constants (see [137] or [196]). Note that the sum of all the species reaction rates equals zero ($\sum_{s=1}^N \dot{\omega}_s = 0$) following mass conservation. It is convenient for certain integration schemes, such as the alpha-QSS applied in this work (see Section 3.4), to write $\frac{d[\tilde{X}_s]}{dt}$ as a function of production (q_s) and loss (L_s) rates. This is obtained for every species "s" as [197]:

$$\frac{d[\tilde{X}_s]}{dt} = q_s - L_s = \sum_{j=1}^M \dot{\omega}_{app_{s,j}} - \sum_{j=1}^M \dot{\omega}_{va_{s,j}} \tag{3.47}$$

The terms $\dot{\omega}_{app_{s,j}}$ and $\dot{\omega}_{va_{s,j}}$ are dependent on the value of ν_{sj} as shown in Table 3.1.

All the modeling required to represent the physics of compressible turbulent reacting flows has been covered. The next step is the selection of a solver to solve those equations with a numerical approach and is the subject of the following section.

Table 3.1: The form of the chemical production and loss terms based on the value of ν_{sj}

	$\nu_{sj} > 0$	$\nu_{sj} < 0$
$\dot{\omega}_{app_s}$	$\nu_{sj} k_{fj} \prod_k [\tilde{X}_k]^{\nu'_{kj}}$	$-\nu_{sj} k_{bj} \prod_k [\tilde{X}_k]^{\nu''_{kj}}$
$\dot{\omega}_{va_s}$	$-\nu_{sj} k_{bj} \prod_k [\tilde{X}_k]^{\nu''_{kj}}$	$\nu_{sj} k_{fj} \prod_k [\tilde{X}_k]^{\nu'_{kj}}$

3.3 Selection of a CFD Solver

It is the author's and institution's aim to work with open-source software which offers transparency and facilitates the reproducibility of the presented results. Among the available open-source CFD software, Eilmer [196, 198] was considered throughout this work. It is a solver developed at the University of Queensland with development origins in 1991 with the intent to be like SPARK [120, 199, 200] but with new technology. Eilmer specifically targets hypersonic type flows. The solver has seen many features added in recent years which allow it to tackle scramjet type flows.

The Eilmer CFD package has evolved over the years and at the time of this study, the matured Eilmer3 release was readily available [201]. It is written in C / C++ with a Python interface for pre- and post-processing as well as some Lua scripting. Gollan and Jacobs [196] discussed the main features of Eilmer and validated the solver with several test cases. Chan et al. [123] presented the validation of the implemented k-ω model in Eilmer with test cases representative for parts of the flow fields inside scramjet engines. Other studies with Eilmer for non-reacting conditions include supersonic cavity flows [202, 203], hypersonic shock wave boundary layer interation (SWBLI) [204] and scramjet combustors [125]. In reacting conditions the solver has been used for combustion in narrow channels by Kang et al. [205].

Since June 2015 a new project has started named Eilmer4 [198, 206, 207]. The project intends to give the solver a new face starting from new foundations written in the D programming language and interacting with Lua omitting the use of Python. The solver benefits, for example, from new and improved thermochemistry modules and a wider range of applicability through the use of unstructured grids. A steady-state solver is under development making use of a Jacobian-free Newton-Krylov [208] approach as well as an adjoint solver [65]. A full list of the features can be consulted on the repository [209]. The solver has proven to be highly portable by adopting the D language.

In this work, the Eilmer3 solver is selected as Eilmer4 did not benefit from all the capabilities of the former version at the time of performing the simulations. Some weak points about the Eilmer3 solver specific to the present work include the unsteady character and mesh generation. Steady-state problems are studied in this thesis which is computationally intensive with an unsteady solver. More specifically, the chemical time scales are typically a few orders of magnitude smaller than the turbulence time scales which results in a stiff set of governing equations to be solved. In the solver, the time step is set through the Courant Friedrichs Lewy (CFL) number. With the no-model approach described in Subsection 3.2.1, sub-iterations with respect to the CFL based time step are required, increasing the computational time. Eilmer3 is characterized by a block-structured meshing approach which in turn influences the effectiveness of the parallel runs. A small block required by geometrical constraints can detrimentally affect the simulation time. The use of a mesh partitioner would improve the parallelization and is considered in Eilmer4.

3.4 The Finite Volume Method

To understand the way to solve the governing equations introduced in Section 3.2, it is more convenient to rewrite them in another form. For simplicity, the two-dimensional form is considered here. The unsteady compressible equations governing fluid flows can be written in conservative form accounting for source terms through an array Q as

$$\frac{\partial U}{\partial t} + \nabla.\vec{F}(U,\nabla U) = \frac{\partial U}{\partial t} + \nabla.[\vec{F}_{inv}(U) - \vec{F}_{vis}(U,\nabla U)] = Q \tag{3.48}$$

or in integral form:

$$\frac{\partial}{\partial t}\int_V U dV = -\oint_S \left(\vec{F}_{inv} - \vec{F}_{vis}\right)\cdot \hat{n}\, dA + \int_V Q dV \ , \tag{3.49}$$

with U, the array of conserved variables and $\vec{F}$, the total flux vector consisting of an inviscid flux part $\vec{F}_{inv}$ and a viscous flux part $\vec{F}_{vis}$. The array of conserved variables for thermal equilibrium in turbulent reacting flows is expressed by :

$$U = (\bar{\rho}, \bar{\rho}\tilde{u}, \bar{\rho}\tilde{v}, \bar{\rho}\tilde{E}, \bar{\rho}\tilde{Y}_s, \bar{\rho}k, \bar{\rho}\omega)^T \tag{3.50}$$

with conserved quantities in order of appearance being density, momentum components per unit volume, total energy per unit volume, mass density of species *s* (s=1,...,N), turbulent kinetic energy and its dissipation rate.

$$\vec{F}_{inv} = \begin{pmatrix} \bar{\rho}\tilde{u}_j \\ \bar{\rho}\tilde{u}_j\tilde{u} + \bar{p}\delta_{j1} \\ \bar{\rho}\tilde{u}_j\tilde{v} + \bar{p}\delta_{j2} \\ \bar{\rho}\tilde{u}_j\tilde{H} \\ \bar{\rho}\tilde{Y}_s\tilde{u}_j \\ \bar{\rho}k\tilde{u}_j \\ \bar{\rho}\omega\tilde{u}_j \end{pmatrix} \tag{3.51}$$

$$\vec{F}_{vis} = \begin{pmatrix} 0 \\ \bar{\tau}_{1j} - \bar{\rho}\widetilde{u''u''_j} \\ \bar{\tau}_{2j} - \bar{\rho}\widetilde{v''u''_j} \\ \left(\frac{\mu}{Pr} + \frac{\mu_T}{Pr_t}\right)\tilde{h}_{,j} + \left(\mu + \sigma^* \frac{\bar{\rho}k}{\omega}\right)k_{,j} + \tilde{u}_i\left(\bar{\tau}_{ij} - \bar{\rho}\widetilde{u''_i u''_j}\right) \\ -(\bar{\rho}D + \frac{\mu_t}{Sc_t})\tilde{Y}_{s,j} \\ \left(\mu + \sigma^* \frac{\bar{\rho}k}{\omega}\right)k_{,j} \\ \left(\mu + \sigma \frac{\bar{\rho}k}{\omega}\right)\omega_{,j} \end{pmatrix} \tag{3.52}$$

$$Q = \begin{pmatrix} 0 \\ 0 \\ 0 \\ 0 \\ \bar{\dot{\omega}}_s \\ \bar{\rho}\widetilde{u''_i u''_j}\tilde{u}_{i,j} - \beta^*\bar{\rho}k\omega \\ \alpha\frac{\omega}{k}\bar{\rho}\widetilde{u''_i u''_j}\tilde{u}_{i,j} - \beta\bar{\rho}\omega^2 + \sigma_d\frac{\bar{\rho}}{\omega}k_{,j}\,\omega_{,j} \end{pmatrix} \tag{3.53}$$

The integral form of the governing equation of the finite volume method is approximated as

$$\frac{dU}{dt} = -\frac{1}{V}\sum_{cell-surface}\left(\vec{F}_{inv} - \vec{F}_{vis}\right)\cdot\vec{n}\,dA + Q\,, \tag{3.54}$$

with U and Q being cell averages. The fluxes are typically estimated at the midpoints of the cell interfaces. Following the methodology in the Eilmer CFD solver [197], the latter source term is split in different contributions. For the type of flows studied in this work it is only relevant to split it in a contribution from the turbulence and from the chemistry as $Q = Q_{turb} + Q_{chem}$. Note that for axisymmetric simulations there is an addition geometrical source term not represented here. The solver adopts an operator-splitting approach recommended by Oran and Boris [210]. Doing so decouples the application of the physical mechanisms. Consequently, the following approximation of the Ordinary Differential Equation (ODE) (3.54) is obtained for the time integration.

$$\begin{aligned} \int_{\Delta t} \frac{dU}{dt} dt &= \int_{\Delta t} \left(\frac{dU}{dt} \right)_{\text{inv.}} dt + \int_{\Delta t} \left(\frac{dU}{dt} \right)_{\text{visc.}} dt \\ &+ \sum_{N_c} \left[\int_{\Delta t_c} \left(\frac{dU}{dt} \right)_{\text{chem.}} dt \right] , \end{aligned} \tag{3.55}$$

where,

$$\left(\frac{dU}{dt} \right)_{\text{inv.}} = -\frac{1}{V} \sum_{cell-surface} \left(\vec{F}_{inv} \right) \cdot \vec{n} \, dA \, , \tag{3.56}$$

$$\left(\frac{dU}{dt} \right)_{\text{visc.}} = -\frac{1}{V} \sum_{cell-surface} \left(-\vec{F}_{vis} \right) \cdot \vec{n} \, dA \, , \; + Q_{\text{turb.}} \tag{3.57}$$

$$\left(\frac{dU}{dt} \right)_{\text{chem.}} = Q_{\text{chem.}} \, , \tag{3.58}$$

Now that the operator-splitting approach has been described, the solution method is briefly discussed with references to more detailed elaborations by other authors.

In order to get a flow state update in Eilmer [197] the following steps are applied. Firstly, the inviscid fluxes (Equation 3.56) are computed. Shock capturing is ensured by treating the inviscid fluxes with an adaptive method switching between Macrossan's Equilibrium Flux Method (EFM)[211] and Liou and Wada's Advection Upstream Splitting Method combining difference and vector splitting (AUSMDV) [212]. With its more diffusive character, the former is active in regions with strong gradients in normal velocity component (tunable parameter) while the latter is used elsewhere. Secondly, the viscous fluxes are computed by means of Gauss' theorem as well as the turbulent source term (Equation 3.56). The third step consists of a time integration of the combined Equations 3.56 and 3.57. This work considered three possible update schemes for the time integration: the forward Euler (1st order accurate), Heun's predictor corrector scheme [213] (2nd order accurate) and the three-stage Runge-Kutta (2nd order accurate). A new set of conserved quantities are obtained at this point. The final step consists of computing the chemical source term (Equation 3.58) and integrate in time. The system of ODEs given by Equation 3.42 is typically very stiff and requires special methods to be efficiently solved. The stiffness is a consequence of dealing with chemical time scales which are typically orders of magnitude smaller than the turbulent time scales. In this work the alpha-QSS (quasi-steady-state) approach of Mott [197, 214] is adopted when required to use the no-model combustion method. Note that the option exists of integrating Equations 3.56 and 3.57 separately in time but has not been considered in the current work. It could be argued that performing separate time integrations and performing successive computations with updated state variables does influence the final result. However, this effect should not be significant as the time steps are very low. A typical Δt for a turbulent simulation with the flow solver is $<$ 1e-9s.

3.5 Summary of Chapter

This chapter started with a brief description of turbulence and the general ability of a numerical description in describing the phenomenon. It is shown in an example that RANS does not capture fluctuations in time of a given quantity and it is a known limitation of the approach. Subsequently, the chemically reactive RANS equations were introduced as well as the modeling assumptions specific to scramjet simulations. The importance of the specification of the values for $\mathrm{Pr_t}$ and $\mathrm{Sc_t}$ was pointed out. The RANS turbulence model adopted in this work is detailed and the implication of the compressibility correction on its form was covered. The Eilmer CFD solver was selected for further studies in this work as it is developed specifically for hypersonic flows and has the basic capabilities to tackle supersonic turbulent reacting flows. Finally, the discretization methods adopted by the latter solver were briefly detailed. Eilmer has not yet been intensively applied to hypersonic propulsion flow paths and has not been applied in such flows with reactions. A validation study is therefore required and is the subject of Chapter 4.

Chapter 4

Assessment of Eilmer for Scramjet Flow Paths

This chapter investigates the predictive capability of Eilmer specifically for scramjet internal flow paths. A combination of non-reacting and reacting studies are performed for the configurations selected for further study with the EDM in Chapter 5. A key aim of the present investigations is to assess the behavior of the k-ω 2006 turbulence model which has very limited validation in the open literature. Another aim of this chapter is to evaluate whether or not a compressibility correction is required for typical scramjet simulations. Section 4.1 discusses the studies considering the presently selected turbulence model found in the literature. Sections 4.2 to 4.5 present the validation of the turbulence model on four scramjet geometries. The suitability of the model is evaluated based on available experimental data and / or reference CFD. A brief summary of the observations is provided in Section 4.6.

4.1 Wilcox' k-ω 2006 Model Applied to Scramjets

It was pointed out in Section 2.2 that prior versions of Wilcox' k-ω turbulence model had some limitations in predictive capability which include strong sensitivity to free stream turbulence properties and inability to adequately capture separated flows. Significant changes [134] in the modeling have been made to obtain the updated version used in the present work, i.e. the k-ω 2006. There is however, very limited validation of the improved model relevant to physics inside supersonic propulsion flow paths. Rumsey [190] adopted it in a comparative study with other turbulence models for hypersonic boundary layer applications. The effect of using compressibility corrections (dilatation-dissipation and pressure-dilatation), typically developed for improved predictions of free shear flows, is explored on adiabatic, hot and cold flat plates. It was shown that omitting a compressibility correction at Mach numbers below 5 works reasonably well in predicting skin friction coefficients. Chan et al. [123] applied Wilcox' 2006 model to test cases representative for parts of the flow fields inside scramjet engines: a flat plate , an axisymmetric cylinder, a backward-facing step, the mixing of two coaxial jets and a 3D SWBLI. The former two geometries were chosen for study of turbulent boundary layer predictions and good agreement was observed with experimental measurements. The flat plate simulations demonstrated that, despite the k-ω 2006 model's sensitivity to freestream turbulence boundary conditions (BC's), it is suitable to predict skin friction coefficients. The cylinder test case showed the more severe grid requirements for adequate predictions of wall heat transfer compared to wall pressure. In the backward facing step simulations a good prediction of the expansion fan, recompression shock and separation region size was observed. The experimental boundary layer profiles of pressure, velocity and temperature, at different axial locations behind the step, are well predicted with some local under-or overestimations outside of the measurement uncertainty. Simulations of the coflow jet in ambient air demonstrated a good agreement with experiments up to a certain point where the numerical interaction between these streams deviated by up to 15 % from the experiment. The importance of matching turbulence intensities at the nozzle exit plane was demonstrated. In the 3D SWBLI simulations, induced by the interaction between a fin and a flat plate, the stress limiter in Wilcox' 2006 model captured well the measured wall pressure further away from the fin with overestimations in the near fin region. Yentsch et al. [124] used the k-ω 2006 to simulated the HIFiRE-1 flight test geometry. The experiment was designed to collect information on laminar-to-turbulent boundary layer transition (cone), SWBLI (flare) and mass flow capture (open channel). Results from the study showed the need for flow dependent tailoring of the k-ω 2006 model to match as closely as possible experimental trends of wall pressure and heat transfer coefficients. Their study demonstrate the difficulty of numerically recreating flight data compared to tunnel data characterised by an improved control over the boundary conditions.

However, the above studies did not consider confined, nor reacting test cases which are more relevant to a supersonic air-breathing propulsion flow path. To the author's knowledge only Chan et al. [125, 215] applied the model to a scramjet combustor in non-reacting conditions with and without fuel injection. In their comparison with experimental wall pressure data a good agreement was obtained at the majority of the measurement locations without fuel injection. With fuel injection into a N_2 stream, from a specific position with respect to the fuel injection plane, the CFD predictions underpredict the experimental wall pressure values. The aim of the present work is to share insight on the application of Wilcox' k-ω 2006 model specific to supersonic internal flow paths typical of scramjet engines. This is achieved by investigating multiple scramjet configurations available in the open literature. Relevant geometries for further study with the Eddy Dissipation Model (EDM) in Chapter 5 have been selected. The turbulence model is carefully applied in this work and sensitivity studies have been performed. The investigations in this chapter will ensure that the results with the EDM are not affected by limitations, or an inappropriate use, of the turbulence model.

In the present and following chapters, in order to keep the computational cost at tractable levels, when no wall functions are activated, values for the non-dimensional first wall distance are slightly relaxed above the typical requirement of $y^+ < 1$ for turbulent boundary layers [216]. In scramjet propulsion flow paths, $y^+ < 1$, is typically achieved with a first cell distance normal to the wall below 1e-6 m [10, 49, 51, 123]. Such an approach is suitable for heat flux predictions as it ensures several cells to be located inside the viscous sublayer. Heat flux predictions are not of primary interest in this work and therefore the adopted approach ensures that the first cell is located inside the viscous sublayer, i.e. $y^+ = u^+$. This is achieved for $y^+ < 5$ [47, 216] or more practically with a wall normal first cell distance below 5e-6 m [101]. Such a setting should be acceptable [216] and has proven to be true from the experience acquired in the present work.

4.2 The Experiment of Burrows and Kurkov

A commonly used test case in CFD code validation studies for supersonic combustion is the experiment of Burrows and Kurkov [100, 217] (BK). Figure 4.1 shows the original set up and Figure 4.2 the computational domain considered in this work. The experiment is characterized by the availability of an extensive set of comparison data in pure mixing and reacting conditions. The setup consists of the sonic injection of hydrogen from a backward-facing step, parallel to a vitiated air stream. Many authors have performed RANS studies of the geometry over the last three decades [104, 106–108, 112, 113, 119, 127, 129, 141, 142, 191, 192]. The test case is known to be very sensitive to the the values of turbulent Prandtl (Pr_t) and Schmidt (Sc_t) numbers. A table summarizing some of the literature simulating the BK configuration is given in

Appendix A.1. Information about the turbulence model, values for $\mathrm{Pr_t}$ and $\mathrm{Sc_t}$ as well as details on the combustion setting are listed in the latter table. The BK configuration was designed for the study of supersonic mixing and combustion at flight Mach numbers above 6 [100]. A Mach 2.44 vitiated airflow with static temperature above 1000 K are supplied to the test section. Such combustor entrance values are representative for a flight Mach number $\approx$ 8 [102, 151]. The combustor inflow conditions are in accordance with the basic requirements for a mixing-limited dominated combustion process which motivates the selection of the BK test case for study in this work.

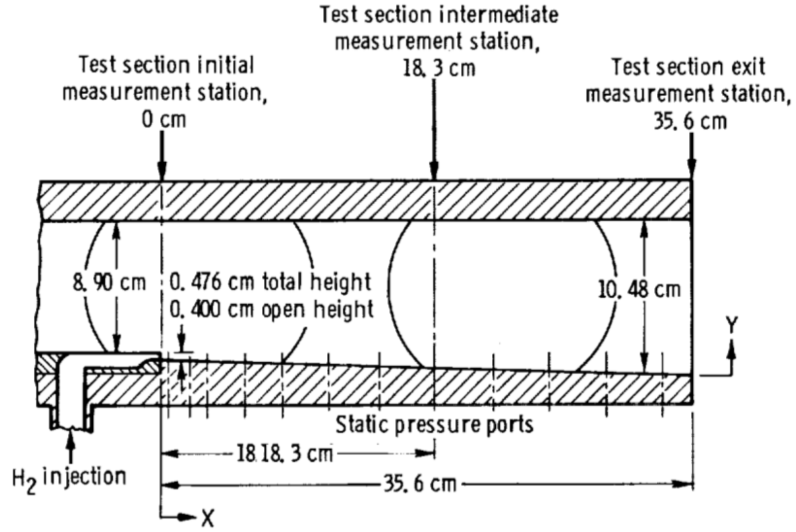

Figure 4.1: The supersonic combustion experiment of Burrows-Kurkov. Image reproduced from [217].

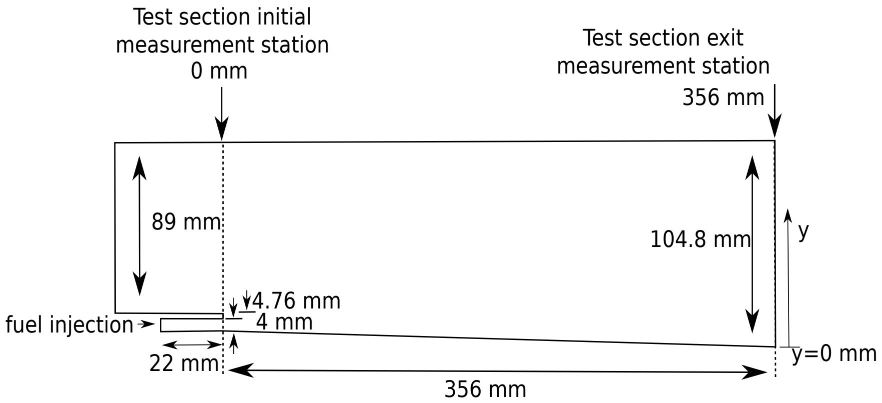

Figure 4.2: Schematic of the Burrows-Kurkov supersonic combustion experiment [217]. Not to scale.

The subsequent discussions are structured as follow. Firstly, the computational approach is explained including the boundary conditions for the pure mixing and reacting experimental setting. Secondly, a grid independence study is performed. The third study is dedicated to the non-reacting, pure mixing conditions with a sensitivity study on the values of $\mathrm{Pr_t}$ and $\mathrm{Sc_t}$. This is followed by an investigation of the compressibility correction for the k-ω 2006 turbulence model. Finally, the reacting setting is simulated with the no-model approach.

4.2.1 Problem Formulation

The experimental setup in Figure 4.2 has been simulated in two stages. In the first stage, a boundary layer section (BLS) of 65 cm is considered using the supersonic inflow conditions listed in Table 4.1. Values for turbulence intensity (I) and the ratio of turbulent to laminar viscosity (μ_t/μ) are set to 5 % and 10 respectively. The exit profile of the first stage is used as an inflow condition for the second stage which considered the geometry depicted in Figure 4.2 with a BLS of 2 cm. The inflow quantities are listed in Tables A.2 and A.3 in Appendix A.1 for half of the symmetric channel. The injector is simulated as a constant area channel of 2.2 cm. Turbulence boundary conditions for the injector are the same as for the separate BLS simulations. Walls are treated isothermal at a temperature of 300 K and a supersonic outflow is prescribed where values from the interior of the domain are extrapolated.

Table 4.1: Inflow and injector flow conditions for Burrow-Kurkov' experiment.

	pure mixing		**reacting**	
	inflow	injector	inflow	injector
u (m/s)	1733.4	BC1: 1217 BC2: 1231	1741.4	1217
T (K)	1150.0	BC1: 254 BC2: 260	1237.9	254
p (Pa)	101350.0	BC1: 101350.0 BC2: 113964.0	96000.0	101350.0
$\mathrm{Y_{H_2}}$	0.001	1.0	0.0	1.0
$\mathrm{Y_{O_2}}$	0.0	0.0	0.258	0.0
$\mathrm{Y_{H_2O}}$	0.233	0.0	0.256	0.0
$\mathrm{Y_{N_2}}$	0.766	0.0	0.486	0.0

Two sets of injector boundary conditions (BC's) are explored in the inert-gas / pure mixing setting. The set denoted as BC1 is typically encountered in the open-literature for simulating this test case [104, 108, 113, 127, 129]. The second set of conditions, denoted as BC2, are taken from the work of Edwards et al. [101] which demonstrated a very good agreement overall with experiments in their work. These conditions correspond to total values for temperature and pressure of 314.0 K and 216675.0 Pa, respectively. Figure 4.3 shows the resulting profiles of Pitot pressure (p_{pitot}) at the entrance of the combustor (x = 0 cm) and composition at the exit of the combustor (x = 35.6 cm) for both sets of BC's. The horizontal axis represents the distance from the respective lower walls. Results are shown for $\mathrm{Pr_t} = \mathrm{Sc_t} = 0.5$. Also represented are the experimentally obtained values for the different variables. Adopting BC1 does match the experimental data of Pitot pressure at the exit of the injector while BC2 overpredicts these values. The same injector exit conditions as Edwards et al. [101] are obtained by Eilmer but the curves do differ towards the air stream which is explained by the different inflow conditions adopted by the above mentioned authors. The BC2 setting results in an improved penetration depth of hydrogen into the air flow which is in better agreement with experimental measurements (Figure 4.3 (b)). However, the influence is very limited and highly probably within the experimental error. Therefore, the injector flow conditions in the reacting simulations are taken equal to BC1. However, the same vitiated air flow as Edwards et al. [101] are considered in the reacting conditions. This approach results in the profile of total temperature at the injection step shown in Figure 4.4. The profiles are compared to the experimental data collected at the first section (x = 0 cm) as well as to the CFD of Edwards et al. [101] obtained with an hybrid RANS / LES approach. An overall satisfactory prediction of the inflow conditions are observed with a boundary layer thickness at the entrance of the combustor around 1 cm.

4.2.2 Grid Independence

A mesh independence study has been performed with structured grids containing 185 920 (mesh 1) and 267 456 (mesh 2) cells. In both cases, the maximum first cell distance to physical walls was below 5e-6 m ensuring that the first cell is located inside the viscous sublayer. The numerical predictions are presented for the finite-rate chemistry simulations relying on the 7 species, 8 reactions mechanism of Evans-Schexnayder [107] with modified third-body efficiencies (TBE's) in accordance with Bhagwandin et al. [127]. Details of the reaction mechanism are given in Table 4.2. Third-bodies are denoted with "M" in the reactions. The different terms allowing to compute the forward and reverse reaction rates with Equation 3.44 are also listed. Turbulence settings are set as $\mathrm{Pr_t} = \mathrm{Sc_t} = 0.5$. The result of the mesh refinement study on the total

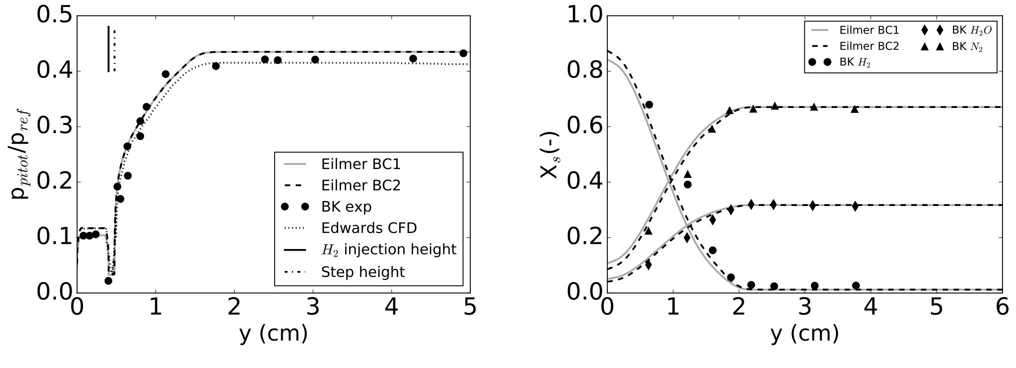

(a) (b)

Figure 4.3: Inert-gas mixing: effect of injector BC on pitot pressure at x=0 cm (a) and exit composition (b), p_{ref} = 18.5e5 Pa, Pr_t=Sc_t = 0.5

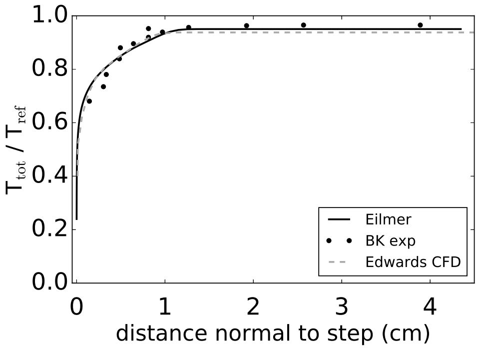

Figure 4.4: Vitiated air flow total temperature at the entrance of the combustor; T_{ref}=2380 K.

temperature (T_0) at the exit of the combustor (x = 35.6 cm) is shown in Figure 4.5. The horizontal axis represents the distance from the lower wall. No visible differences in predictions are observed indicating mesh independent results. The same is valid for the combustion efficiency along the combustor. This paramater has been computed according to Kim et al. [218] as :

$$\eta_c(x) = 1 - \frac{\int \rho u Y_F dA}{(\int \rho u Y_F dA)_{x=0}} = 1 - \frac{\dot{m}_F}{(\dot{m}_F)_{x=0}} \tag{4.1}$$

Equation 4.1 evaluates the mass flow rate of fuel ($\dot{m}_F$) at any position with respect to the injected amount. The profiles of η_c obtained by both meshes are very similar and a mesh independent result is achieved. In the following discussions the coarser mesh is

Table 4.2: Modified H_2/air mechanism of Evans and Schexnayder with 7 species, 8 reactions.

Reaction	A_f A_r	β_f β_r	$T_{a,f}$ $T_{a,r}$	**TBE**
$H_2 + M <=> H + H + M'$	5.5e18 1.8e18	-1 -1	51987.0 0.0	$H_2 = 2.5$, $H_2O = 16.25$ all other = 1.0
$O_2 + M <=> O + O + M'$	7.2e18 4.0e17	-1 -1	59340.0 0.0	$H_2 = 2.5$, $H_2O = 16.25$ all other = 1.0
$H_2O + M <=> OH + H + M'$	5.2e21 4.4e20	-1.5 -1.5	59386.0 0.0	$H_2 = 2.5$, $H_2O = 16.25$ all other = 1.0
$OH + M <=> O + H + M'$	8.5e18 7.1e18	-1.0 -1.0	50830.0 0.0	$H_2 = 2.5$, $H_2O = 16.25$ all other = 1.0
$H_2O + O <=> OH + OH$	5.8e13 5.3e12	0.0 0.0	9059.0 503.0	
$H_2O + H <=> OH + H_2$	8.4e13 2.0e13	0.0 0.0	10116.0 2600.0	
$O_2 + H <=> OH + O$	2.2e14 1.5e13	0.0 0.0	8455.0 0.0	
$H_2 + O <=> OH + H$	7.5e13 3.0e13	0.0 0.0	5586.0 4429.0	

considered.

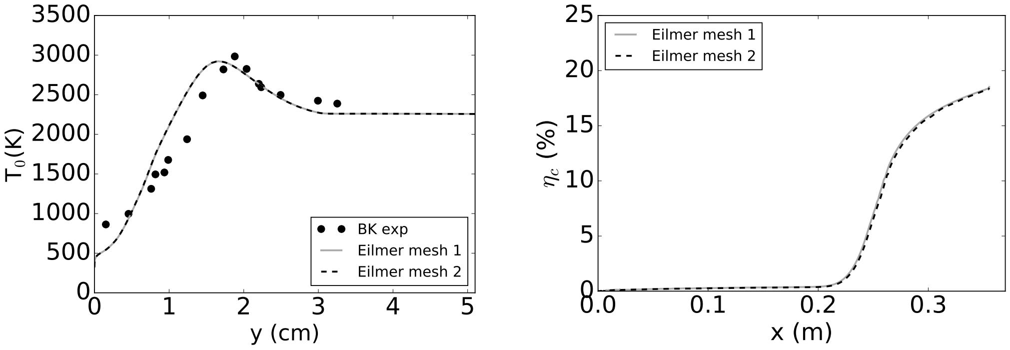

(a) (b)

Figure 4.5: Predictions of total temperature at x=35.6 cm (a) and combustion efficiency (b) obtained with different mesh sizes.

4.2.3 Inert Mixing Conditions

Figure 4.6 (a) and (b) presents the result of the simulations with Eilmer at the exit plane (x = 35.6 cm) in the case of fuel injection without reactions (no O_2 in air stream). Two different settings for the combination of $\mathrm{Pr_t}$, $\mathrm{Sc_t}$ are considered as to evaluate the sensitivity of the result to these turbulence model parameters. Parent and Sislian [119] demonstrated some sensitivity to these parameters for the same test case with the k-ω 1998 turbulence model. A similar study needs to be performed with the k-ω 2006 model. With regard to the composition, Figure 4.6 (a), the setting $\mathrm{Pr_t} = \mathrm{Sc_t} = 0.5$ seem to capture more accurately the experimental slope than a value of 0.7. In terms of Pitot pressure, Figure 4.6 (b), no setting appear to be better over the complete set of measurement locations. Note that Parent and Sislian [119] also obtained a better match with a value of 0.5 for the above turbulence parameters. However, the CFD predictions between y = 1.5 and 2.2 cm are in much better agreement in this work. This is the effect of the cross-diffusion term in Equation 3.17 which improves the performance of the k-ω model in shear layers [134]. Overall, the influence of $\mathrm{Pr_t}$ and $\mathrm{Sc_t}$ is rather limited in the inert mixing conditions. It will be shown later on that these parameters have a much bigger influence once combustion is considered.

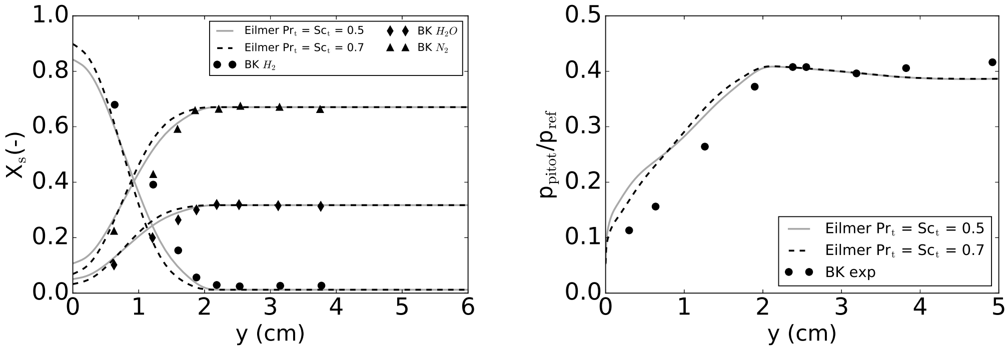

(a) (b)

Figure 4.6: Inert-gas mixing: Composition (a) and Pitot pressure (b) at x=35.6 cm obtained with different settings of $\mathrm{Pr_t}$, $\mathrm{Sc_t}$. p_{ref} = 18.5e5 Pa.

4.2.4 Compressibility Correction

Based on the mass flux weigthed averaged quantities [79] of both streams just before the step, a convective Mach number of 0.21 is obtained for the experiment of Burrows and Kurkov with density ratio of 2.63 . At such a low value, the shear layer spreading rate should not be affected by any compressibility effect [219, 220]. Figure 4.7 confirms this with the profiles of x-velocity component and hydrogen mass fraction. Profiles are given for two locations downstream the point of injection as illustrated in Figure 4.8. The numerical predictions are presented for the finite-rate chemistry simulations (no TCI) relying on the 7 species, 8 reactions mechanism of Evans-Schexnayder [107] with modified third-body efficiencies in accordance with Bhagwandin et al. [127]. Turbulence settings are set as $\mathrm{Pr_t} = \mathrm{Sc_t} = 0.5$. The differences in velocity predictions were in the order of a few m/s. Investigating the contour of $\mathrm{M_t}$ in Figure 4.8 shows very low values (< 0.3) for this parameter of interest driving the compressibility correction (Equations 3.23 and 3.24). This observation is in accordance with the expectations for the convective Mach number computed above and confirms the adequate behavior of the correction for the BK combustor.

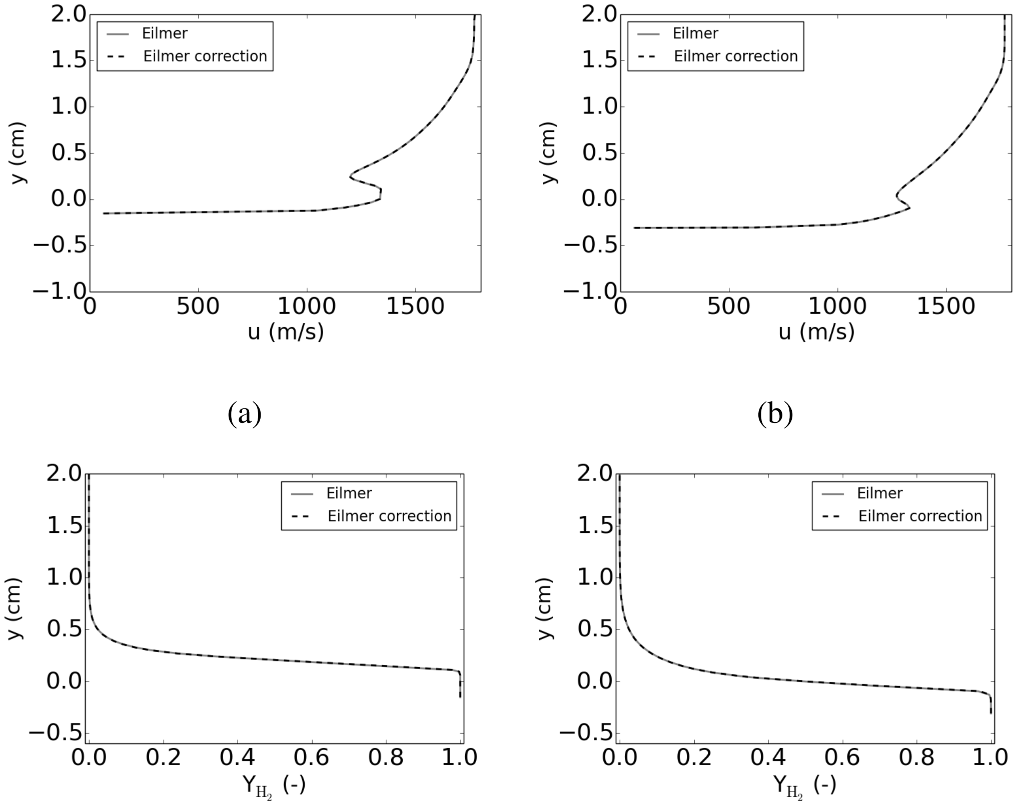

(a) (b)

(c) (d)

Figure 4.7: Effect of applying the compressibility correction on x-velocity component at (a) x = 50 mm, (b) x = 100 mm and the hydrogen mass fraction Y_{H_2}(c) x = 50 mm, (d) x = 100 mm with $\mathrm{Pr_t} = \mathrm{Sc_t} = 0.5$.

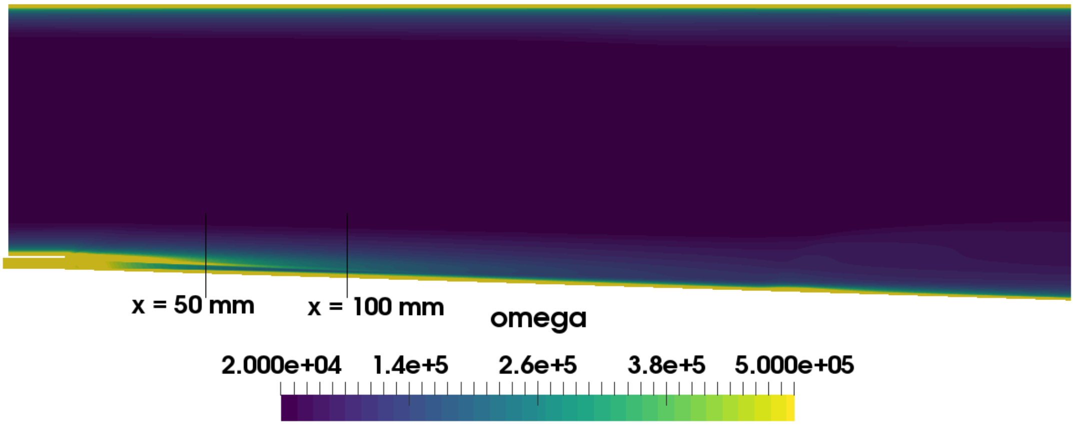

Figure 4.8: Contour of turbulent Mach number for the Burrows-Kurkov test case with $\mathrm{Pr_t} = \mathrm{Sc_t} = 0.5$.

4.2.5 Reacting Conditions

In subsequent studies, the reacting conditions of the BK experiment are considered. The suitability of the k-ω 2006 model is evaluated as well as the sensitivity to $\mathrm{Pr_t}$ and $\mathrm{Sc_t}$. In order to ensure the predictions are within certain expectations this study is performed with a finite-rate chemistry simulations (no TCI) relying on the 7 species, 8 reactions mechanism of Evans-Schexnayder [107] with modified third-body efficiencies (see Table 4.2). Bhagwandin et al. [127] demonstrated that the latter mechanism captured quite well the ignition delay and reported an onset location at x = 25 cm downstream the point of fuel injection. The result was obtained with the k-ω SST turbulence model and a setting of $\mathrm{Pr_t} = \mathrm{Sc_t} = 0.7$. When available, the predictions of Eilmer are compared to the CFD of Bhagwandin et al. [127] denoted as “Ref”. In the reference CFD, a boundary layer (BL) is prescribed at the entrance of the combustor based on digitized experimental profiles.

Figures 4.9 to 4.11 show the predictions of Eilmer for different flow quantities with several settings of $\mathrm{Pr_t}$, $\mathrm{Sc_t}$ at the exit of the combustor (x = 35.6 cm). The horizontal axis represents the vertical distance from the lower wall. The Eilmer predictions with similar settings (black dashed lines) of the turbulent parameters as the reference CFD solution are quite different. A possible explanation for the difference could be the vitiated inflow properties as the prescribed BL profile in the present work is obtained in another way. The present simulations show a localized maximum near the wall. In order to ensure that the reaction mechanism is correctly applied, a comparison has been made with and without the use of modified third-body efficiencies. The result of this investigation is shown in Figure 4.12 for the Mach number and total temperature. The effect of the difference in reaction mechanism is clearly visible. Without the modification, the experimental peak in total temperature cannot be captured. The bump in Mach number near the wall is slightly affected by the change in mechanism, but not as pronounced as in the reference CFD in Figure 4.9. Nevertheless, Figure 4.12 demonstrates the effectiveness of the modified third-body efficiencies. Assuming the grid independence of the reference CFD solution (the authors do not demonstrate grid independence), the only explanation for the observed difference in Mach number is the applied turbulence model. The latter does as well explain the discrepancies in other flow quantities. A strong sensitivity to the setting of $\mathrm{Pr_t}$ and $\mathrm{Sc_t}$ is observed and confirms the requirement of case dependent calibration. The sensitivity is more pronounced than in the inert mixing case studied previously (compare $\mathrm{Pr_t} = \mathrm{Sc_t} = 0.5$ and 0.7 in Figure 4.6) . This can be explained by the presence of reactions which induce strong gradients in species mass fractions and temperature and are consequently influenced by the setting of $\mathrm{Pr_t}$ and $\mathrm{Sc_t}$ (see Equation 3.52). In terms of the species mole fractions, the combinations $\mathrm{Pr_t} = 0.9$, 0.5 and $\mathrm{Sc_t} = 0.5$ are not affecting the results. The same combinations do result overall in the best agreement with the experimental data. The combination $\mathrm{Pr_t} = \mathrm{Sc_t} = 0.5$ is selected for further comparison. An onset of ignition located at x = 23 cm is observed with the latter setting. Experimentally [100] an ignition delay is observed between 18 (wall pressure trace) and 25 cm (photographs of OH radiation).

In conclusion, the k-ω 2006 turbulence model is characterized by a similar predictive behavior as the k-ω SST for the same reaction mechanism. It must be noted that Parent and Sislian [119] were unable to obtain similar profiles of composition with the older version of the standard k-ω model and the same setting for $\mathrm{Pr_t}$ and $\mathrm{Sc_t}$. The latter authors used a more detailed mechanism of reaction than in the present work. The fact that the presently predicted ignition delay is within the bounds of experimental measurements (between 18 and 25 cm downstream the injection location) demonstrates that the k-ω 2006 yields reasonable predictions of the flow field. The same observation is made for different flow quantities at the exit plane. Therefore, the model appears to be suitable for the study of similar scramjet configurations after calibration of the $\mathrm{Pr_t}$ and $\mathrm{Sc_t}$ parameters.

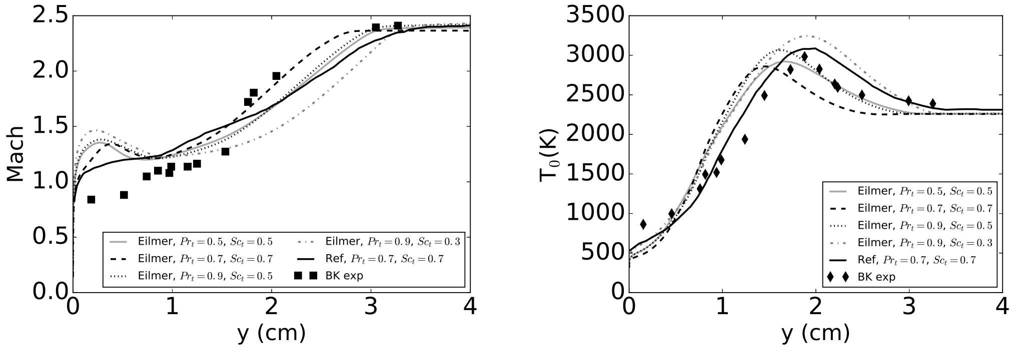

(a) (b)

Figure 4.9: Predictions of Mach (a) and total temperature (b) at x=35.6 cm obtained with several settings of $\mathrm{Pr_t}$ and $\mathrm{Sc_t}$.

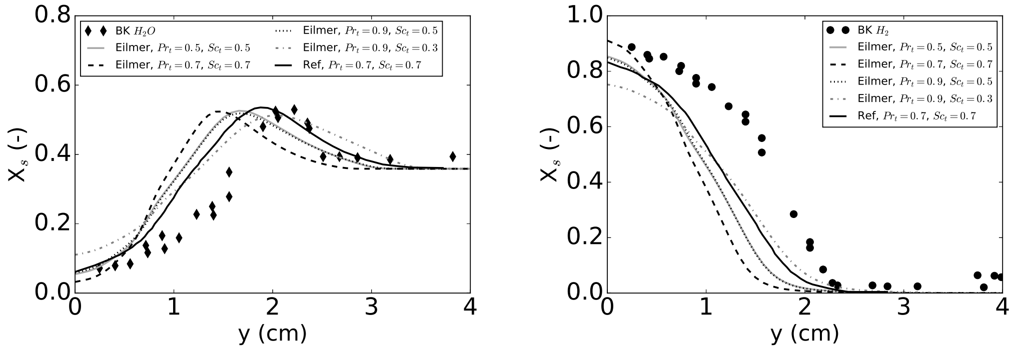

(a) (b)

Figure 4.10: Predictions of H_2O (a) and H_2 (b) mole fraction at x=35.6 cm obtained with several settings of $\mathrm{Pr_t}$ and $\mathrm{Sc_t}$.

4.3 The DLR Combustor Experiment

The DLR combustor experiment of Waidmann et al. [98] is depicted in Figure 4.13 and a schematic of the computational domain considered in this work in Figure 4.14. A Mach 2 vitiated air stream is supplied to the test chamber with cold temperature ($<$ 1000 K) due to limitations of the facility. Similarly to the Burrows-Kurkov experiment, measurements have been taken in both a pure mixing and a combusting setting, enabling a vaste amount of experimental comparison data. The main geometry is notionally two-dimensional, however the use of porthole injectors on the rear of the strut sets up an inherently three-dimensional flow field. Several two-and three-dimensional RANS

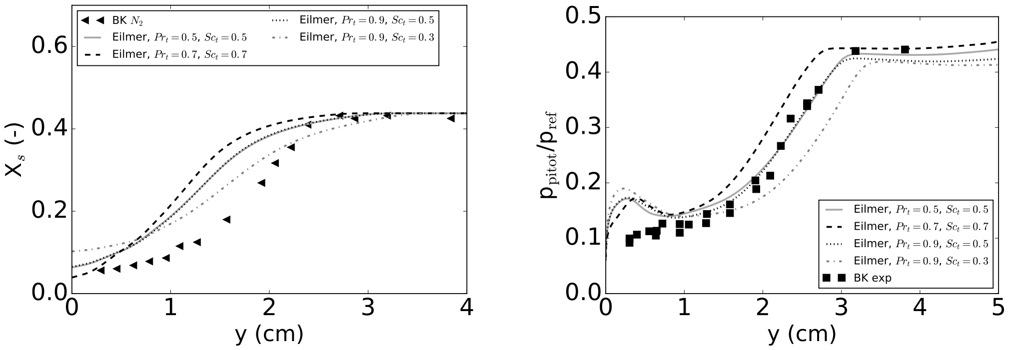

(a) (b)

Figure 4.11: Predictions of H_2 (a) mole fraction and Pitot pressure (b) at x=35.6 cm obtained with several settings of $\mathrm{Pr_t}$ and $\mathrm{Sc_t}$. $\mathrm{p_{ref}}$ = 17.1e5 Pa.

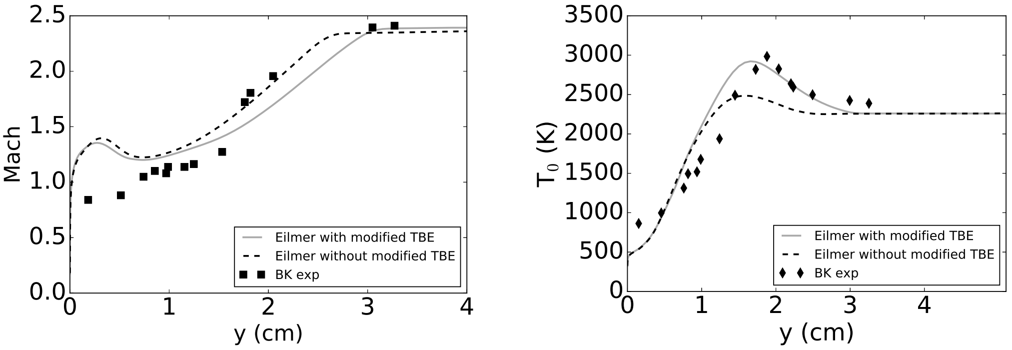

(a) (b)

Figure 4.12: Predictions of Mach (a) and total temperature (b) at x=35.6 cm with and without modified third-body efficiencies $\mathrm{Pr_t} = \mathrm{Sc_t} = 0.5$.

studies of this combustor test case can be found in the literature [111, 115, 117, 131, 144, 145] where each author introduces a TCI model. A table summarizing some of the literature simulating the DLR combustor is given in Appendix A.2. Information about the turbulence model, values for $\mathrm{Pr_t}$ and $\mathrm{Sc_t}$, wall boundary conditions as well as details on the combustion setting are listed in the latter table. Most of the studies reported in Appendix A.2 adopt a TCI model which assumes that turbulent time scales are larger than chemical time scales (flamelet, EDM). Waidmann et al. [98] identified the combustion mode to be situated in the flamelet regime. This an indication that, in spite of the cold vitiated air stream conditions, the combustion process is primarily mixing limited. The flamelet and EDM commonly rely on the assumption of fast chemistry.

The DLR combustor is therefore expected to be adequate for study of the EDM in this work. In spite of the three-dimensionality of the configuration, two-dimensional studies are useful as a proof of concept for modeling techniques. Oevermann [111] and Mura et al. [115] obtained reasonable results in their two dimensional studies. Following this approach, the present work considers the application of EDM on a two-dimensional domain with single slot injector. It is expected that the two-dimensional assumption will introduce a certain degree of error when making direct comparison to experiment.

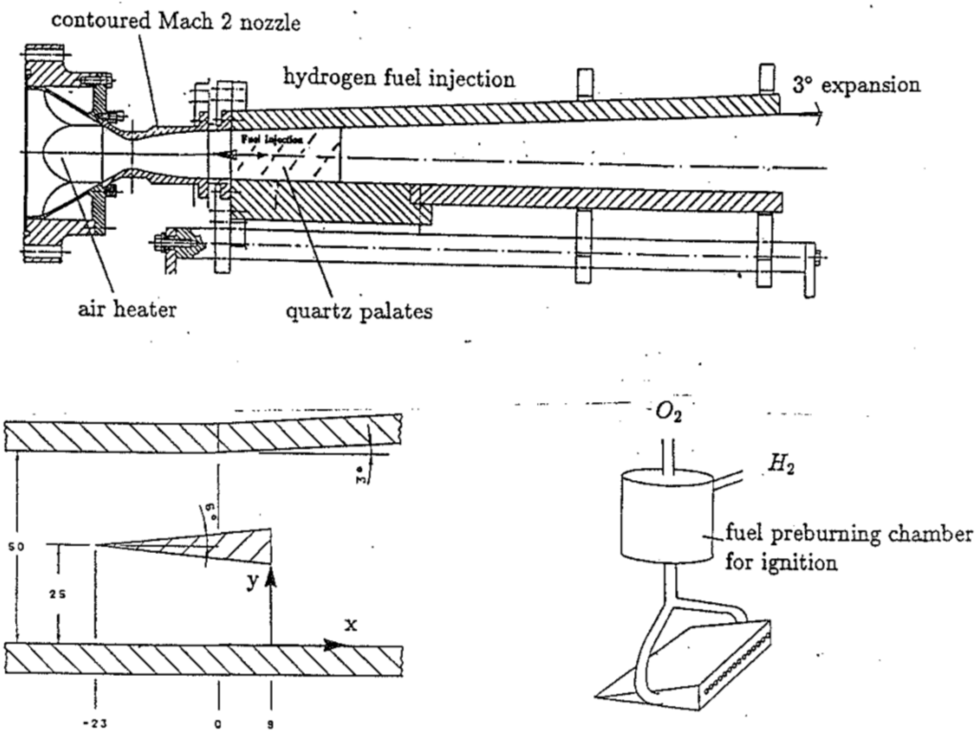

Figure 4.13: The DLR combustor experiment. Image reproduced from [98].

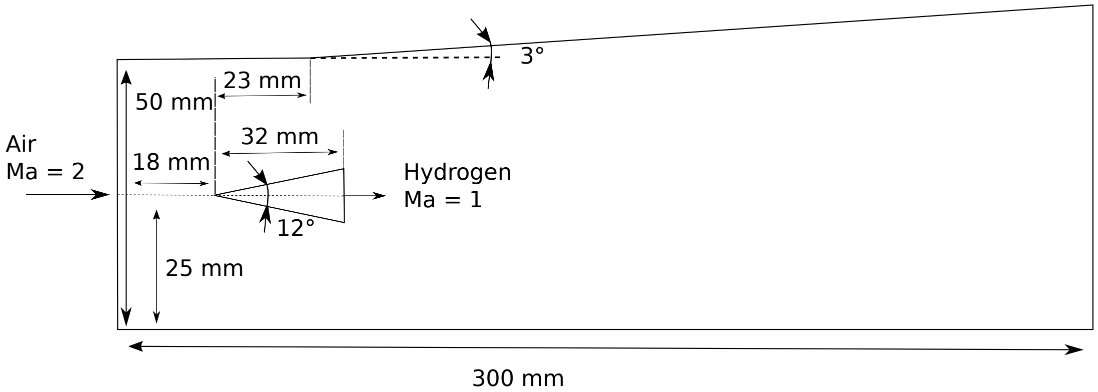

Figure 4.14: Schematic of the DLR combustor experiment [98]. Not to scale.

4.3.1 Problem Formulation

A structured grid has been generated for the domain shown in Figure 4.14. The distance between the supersonic inlet, with conditions given in Table 4.3, and the start of the strut is taken as 18 mm and the total combustor length as 300 mm. The vitiated air stream corresponds to total conditions: T_0 = 600 K, p_0 = 7.8 bar. Upper and lower walls are treated as inviscid which is an acceptable choice given the distant location with respect to the reaction zone. The strut walls are defined as adiabatic and supersonic outflow is assumed. Given the relatively low stream temperatures in the combustor and the location of the reaction zone further downstream of the strut, the heat transfer to the strut walls is expected to be small supporting the adiabatic wall boundary condition setting. Turbulence quantities are taken similar to Oevermann [111] and Mura et al. [115]: for the free stream inflow $I = 0.3\%$, $\mu_t/\mu = 675$ and for the injector $I = 3.3\%$, $\mu_t/\mu = 63$.

Table 4.3: Inflow and injector flow conditions for the DLR combustor experiment.

	inflow	injector
u (m/s)	730.0	1200.0
T (K)	340.0	250.0
p (Pa)	100000.0	100000.0
Y_{H_2} (-)	0.0	1.0
Y_{O_2} (-)	0.232	0.0
Y_{H_2O} (-)	0.032	0.0
Y_{N_2} (-)	0.736	0.0

Grid Independence

A mesh independence study has been performed with structured grids containing 117 000 (mesh 1) and 276 432 (mesh 2) cells. This study has been performed with the EDM (A_{edm}=4) and a combination Pr_t = Sc_t = 0.9 was adopted. This result is solely considered to demonstrate mesh independence as the EDM will be covered in more details in Chapter 5. Simulations of the DLR scramjet with the no-model combustion approach have not been performed as part of this work for two reasons. Firstly, previous work from the literature without considering TCI identified its inability in dealing with the DLR combustor test case. Secondly, applying a detailed reaction mechanism with a no-model approach requires a lot of computational effort with the unsteady solver that is Eilmer. As the no-model approach is not expected to yield good results it is discarded as a possible point of comparison for the EDM. The result of the mesh independence study is shown in Figure 4.15 for the horizontal velocity component along a line superimposing the symmetry axis of the strut. In the following discussions the term centerline velocity will be used instead. Some small differences are observed in the recirculation regions behind the strut (x $\approx$ 70 mm) as well as further downstream in the combustor. However, for most of the profile both meshes predict the same centerline velocity. Also shown in Figure 4.15 is the combustion efficiency computed with Equation 4.1. The profiles are very similar with a maximum difference of 1.5 % between the grids. Given the limited effect of the refinement ($\approx$ factor 2) on the solution, the coarser mesh is suitable to study the application of the EDM on the combustor. Therefore the following discussion considers the first mesh.

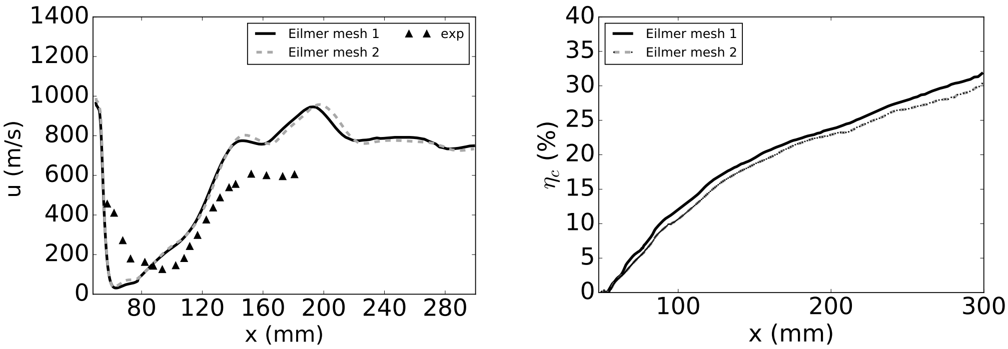

(a) (b)

Figure 4.15: Predictions of centerline velocity (a) and combustion efficiency (b) obtained with different mesh sizes.

4.3.2 Inert Mixing Conditions

In a first step, the DLR combustor has been studied without combustion. It is the aim to assess the suitability of the turbulence model prior activating reactions for the specific investigation of the EDM in Chapter 5. Figure 4.16 presents a qualitative comparison of Eilmer and the experimental Schlieren (shadowgraph). The CFD prediction is shown for a setting $\mathrm{Pr_t} = \mathrm{Sc_t} = 0.5$. The setting of the latter parameter has an influence on the shock structure as will be shown on the wall pressure trace in a subsequent discussion. Nevertheless, Figure 4.16 allows a meaningful comparison on the flow feature that should be predicted by the CFD. Similar shock patterns are observed with differences in the reflection locations at the wall and shear layer. Due to the slightly diverging upper wall, the reflected shock wave on the upper wall (caused by the strut's leading edge) interacts further downstream with the shear layer (x $\approx$ 90 mm) compared to the lower wall counterpart (x $\approx$ 82 mm). This is as well visible in the experiment. At (x $\approx$ 155 mm), such shock wave reflection do not occur anymore. This is because the flow is completely supersonic while it is subsonic till x $\approx$ 125 mm as shown in Figure 4.17. The expansion fans originating at the trailing edge corners of the strut are as well visible. Note that, as reported by Overmann [111], the shadowgraph shows shock structures originating from the base of the wedge which are attributed to irregularities in the geometry. Such features are not captured by the CFD.

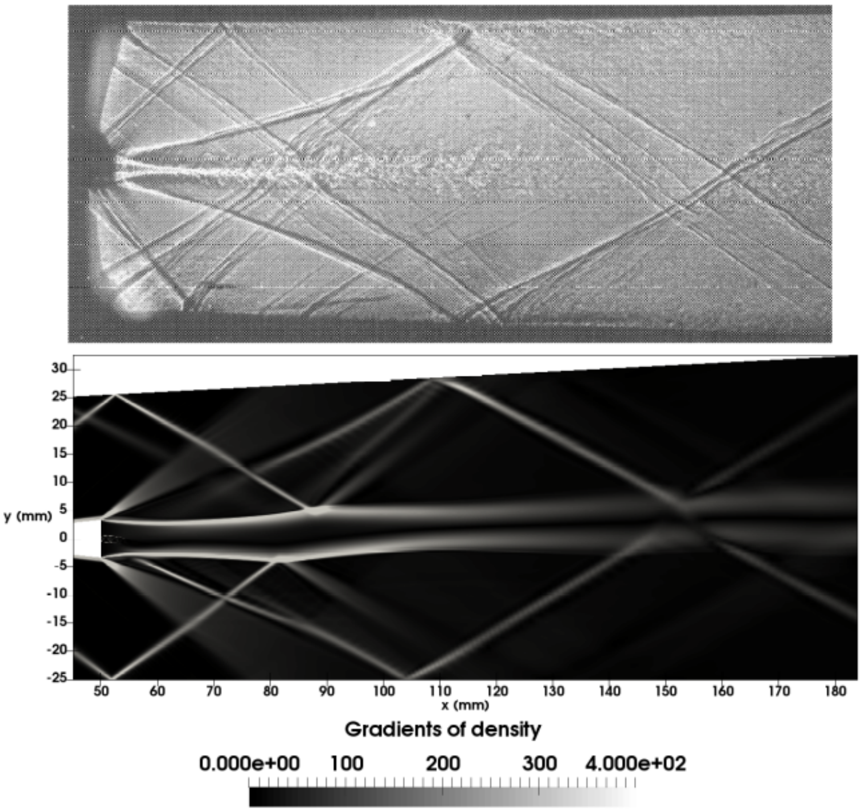

Figure 4.16: Comparison of experimental (taken from [111]) and numerical (Pr_t = Sc_t = 0.5) Schlieren image for the non-reacting conditions.

The effect of varying values for Pr_t and Sc_t is assessed with the wall pressure trace (Figure 4.18) and the velocity profiles at several axial locations (Figure 4.19). Simulations have been performed with a value of 0.5 and 0.9 for both parameters. Also

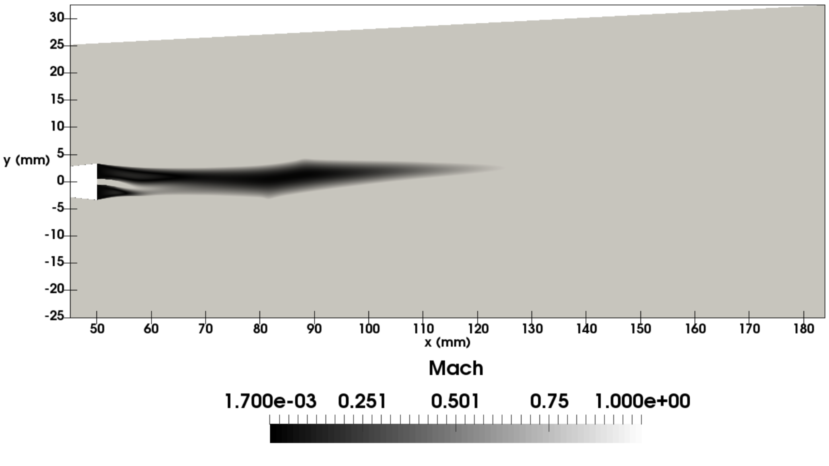

Figure 4.17: Subsonic hydrogen jet predicted with $Pr_t = Sc_t = 0.5$ for the non-reacting conditions.

represented are the numerical predictions of Oevermann [111] obtained with $Pr_t = Sc_t = 0.7$ in conjunction with the k-ε model. Figure 4.18 shows that a better agreement with experimental wall pressure measurements is obtained with a lower value for both parameters (black lines). This is shown at the location of the second shock reflection on the lower wall ($x \approx 105$ mm). Overmann's [111] pressure trace captures more accurately the reflection at the lower wall (black dotted) with turbulence setting in between the ones selected in this work. It is surprising that the curve does not lay between the Eilmer predictions. Given that the same boundary conditions were used, and assuming the appropriateness of selected grids and numerical approach, the difference is attributed to the selected turbulence model. The peak in pressure at $x \approx 130$ mm is underestimated by the different CFD approaches. Oevermann [111] states that accounting for wall boundary layers and / or three-dimensional effects could explain the behavior but Gao et al. [144] demonstrated that this is not the case. Moreover, current observations are in accordance with more advanced CFD predictions of Genin and Menon [97] (LES) and Potturi and Edwards [221]. This demonstrates the challenging nature of the test case, even in non-reacting conditions. Similar results are obtained for the centerline pressure and are given in Figure A.2 of Appendix A.2.

The streamwise velocity traces predicted by Eilmer agree qualitatively well with experimental meaurements obtained with Laser Doppler Velocimetry (LDV) at several axial locations along the combustor in Figure 4.19. At the first measurement location,

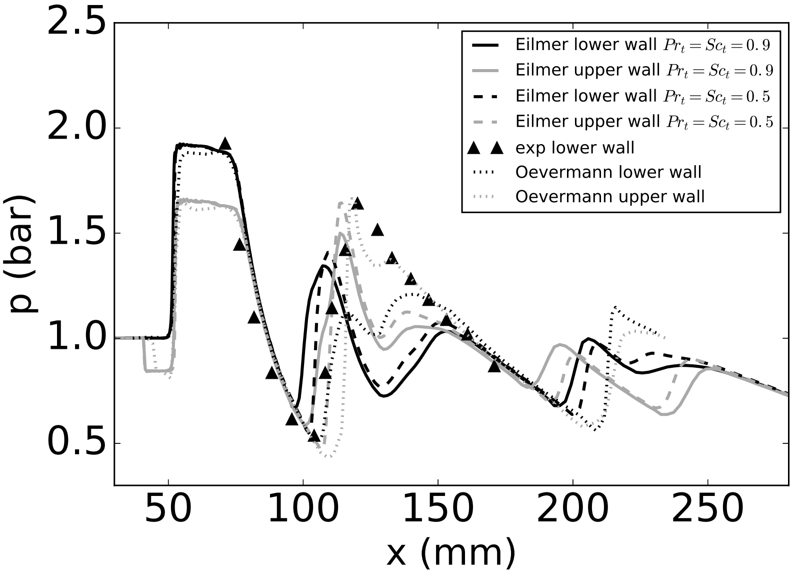

Figure 4.18: Pressure distribution along upper and lower combustor walls for the non-reacting conditions.

close to the point of injection behind the strut, the choice of $\mathrm{Pr_t}$ and $\mathrm{Sc_t}$ combination affects the profile at y $\approx$ 25 mm. The upper recirculation zone behind the strut does extend further dowsntream for a value of 0.5 compared to the 0.9 setting. At the other downstream axial locations, differences in profiles are not so pronounced. Based on the available experimental data it is not possible to state one choice as being superior to the other. In all cases, peak values presently obtained are larger than the CFD of Oevermann [111] and are attributed to the difference in adopted turbulence model. The upward shift of the minima inside the jet at positions (a), (c) and (d) are as well reported by several authors [97, 111, 115, 144, 221, 222] without explanation of the possible cause.

In conclusion, the k-ω 2006 turbulence model is able to capture the essential features from the combustor (Figure 4.16). The wall pressure trace is slightly better predicted with a combination $\mathrm{Pr_t}$ = $\mathrm{Sc_t}$ = 0.5 (Figure 4.18) and different results are observed with respect to other turbulence models. The latter comment is also valid for the profiles of streamwise velocity at several axial locations inside the combustor (Figure 4.19). The trends do however agree well with other results reported in the literature which shows that there is no clear superiority of one turbulence modeling approach over the other based on available experimental data. Consequently, the k-ω

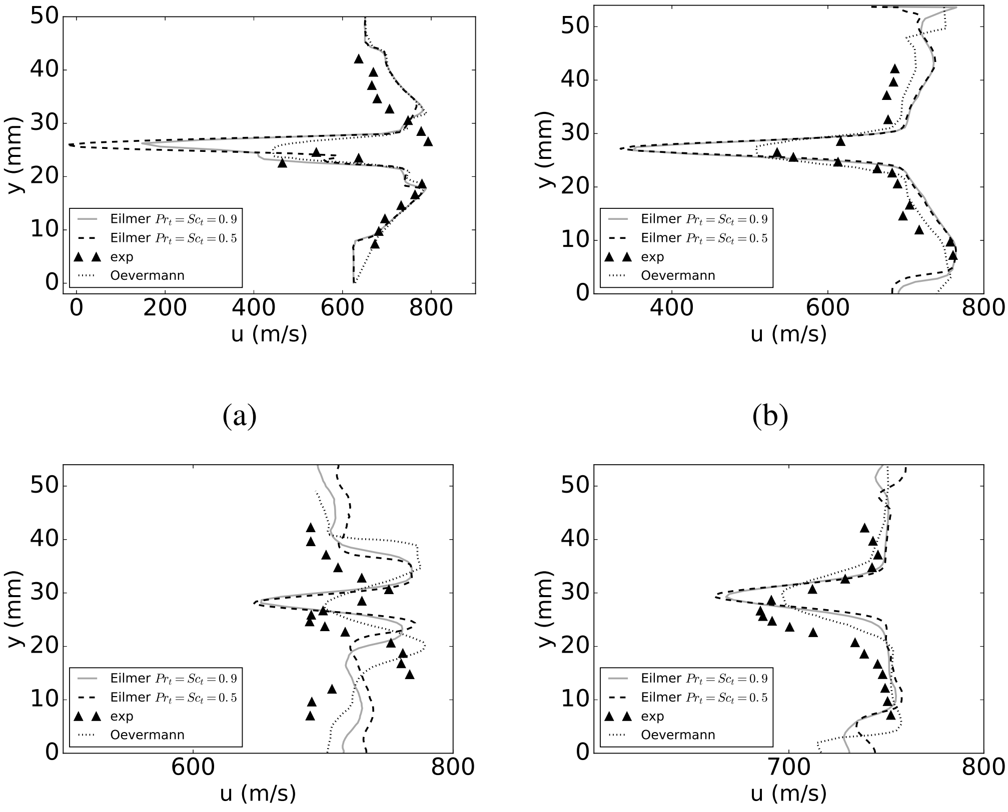

(a) (b)

(c) (d)

Figure 4.19: Profiles of velocity at axial locations (a) x = 64 mm , (b) x = 111 mm, (c) x = 143 mm, (d) x = 219 mm in non-reacting conditions.

2006 model is shown to be capable of simulating the non-reacting flow field inside the DLR combustor. Moreover, there is no preferred setting for the values of $\mathrm{Pr_t}$ and $\mathrm{Sc_t}$.

4.3.3 Compressibility Correction

Similarly as in 4.2.4, the effect of Wilcox' [136] compressibility correction is evaluated. In their work on the DLR combustor, Waidmann et al. [98] mention that compressibility leads to a great suppression of shear layer growth. The convective Mach number in this case is equal to 0.30 based on the stream properties listed in Table 4.3. From the discussion in Appendix B, the correction is not expected to have a great impact on the flow field. Figures 4.20 and 4.21 show, respectively, the effect of the compressibility correction on the streamwise velocity component and hydrogen mass fraction at three axial locations. A setting $\mathrm{Pr_t} = \mathrm{Sc_t} = 0.5$ is adopted for the simulations. The correction only slightly affect the velocity profiles with the most discernible differences in (b) and (c) which are located in the supersonic region (see Figure 4.17). The differences are however not observed in the shear layer growth but instead in the shock structures. In order to visualize what happens in these regions it is convenient to compute the gradient of the streamwise velocity component in the flow field and look at the vertical component of this variable. Figure A.3 in Appendix A.2 shows the resulting contour which yields more information than the shadowgraph in Figure 4.16. Three vertical lines are indicating the axial locations considered in Figure 4.20. The shock structures, explaining the behavior in the latter figure can be clearly visualised. The representation can be interpreted as follow. Moving along a vertical line from bottom to top, when crossing a light (positive) region the streamwise velocity component will increase and when crossing a dark (negative) region it will decrease. Performing this exercise explains the observations at the three locations of interest in Figure 4.20. In terms of the hydrogen mass fraction in Figure 4.21, the shear layer growth is very slightly reduced which confirms the desired effect of the correction. The small variations can be explained by the low values of the turbulent Mach number in Figure 4.22. The magnitude levels of M_t are higher for the present combustor than in the Burrows-Kurkov test case. Nevertheless, the limited effect of the correction is in accordance with the low value of the convective Mach number. Therefore, the compressibility correction is not considered in the following simulations.

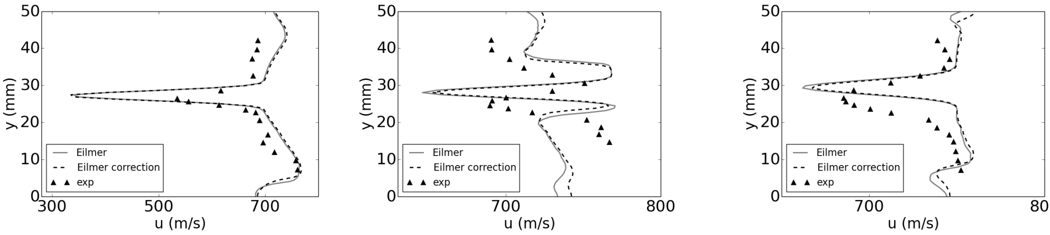

(a) (b) (c)

Figure 4.20: Effect of applying the compressibility correction on the x-velocity component at (a) x = 111 mm, (b) x = 143 mm and (c) x = 219 mm with Pr_t=Sc_t=0.5.

4.4 The HyShot II Combustor (HEG ground test)

The HyShot II scramjet configuration is sketched in Figure 4.23 and a photograph of the model installed in the test section is given in Figure 4.24. It consists of an

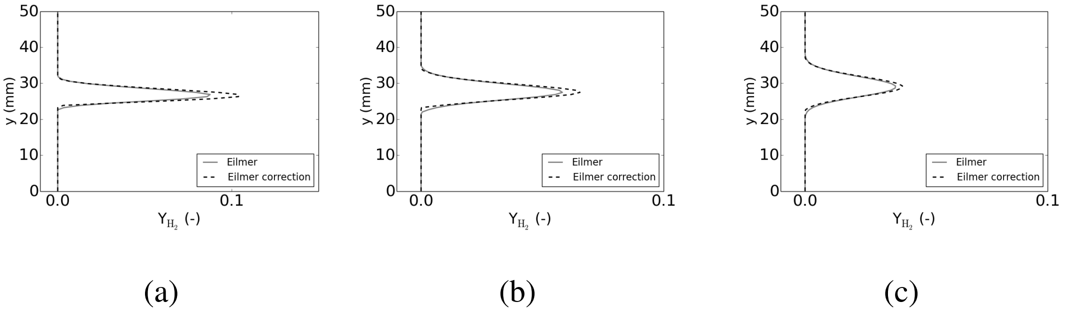

(a) (b) (c)

Figure 4.21: Effect of applying the compressibility correction on the hydrogen mass fraction (Y_{H_2}) component at (a) x = 111 mm, (b) x = 143 mm and (c) x = 219 mm with Pr_t=Sc_t=0.5.

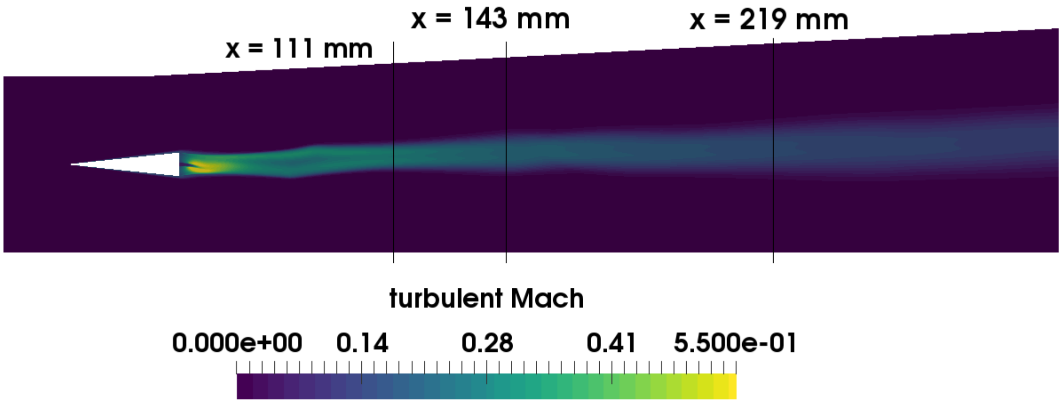

Figure 4.22: Contour of turbulent Mach number for the DLR test case with Pr_t=Sc_t=0.5.

intake ramp, representing a vehicle forebody compression, leading to a constant area combustion chamber followed by a nozzle. The configuration contains a bleed channel which swallows completely the intake boundary layer. Fuel is injected perpendicular to the incoming flow inside the constant area combustor. The width of the intake ramp is larger than the combustor as to provide a two-dimensional inflow condition for the three-dimensional combustion chamber. The HyShot II combustor was designed for an actual flight test aiming to provide benchmark data on hydrogen combustion at Mach 8 flight conditions. It was as well considered in experimental campaigns inside the HEG shock tunnel at the DLR with a 1:1 scale copy. Even though this configuration was developed for a flight experiment it is considered in this section as a generic test case given the fact that it was not designed to generate thrust [86]. The configuration is however, much closer to an actual scramjet compared to the Burrows-Kurkov and DLR combustors. Note that the available set of comparison data for this test case is not as extensive as for the latter two. The ground test conditions have been considered in several RANS studies in the literature [86, 96, 102, 105, 146, 223]. Table A.5 summarizes some of the literature simulating the HyShot II configuration in Appendix A.3. Information about the turbulence model, values for $\mathrm{Pr_t}$ and $\mathrm{Sc_t}$ as well as details on the combustion setting are listed in the latter table. The experimental test conditions considered here represent a Mach 8 flight at an altitude of 27 km (HEG condition XIII). A very detailed description of this ground test experiment is given by Karl [86]. It was demonstrated in several RANS studies [86, 105] that the combustion is primarily mixing limited. Moreover, the same comment was made by Larsson et al. [43] in their numerical study of the combustor with LES. The HyShot II combustor is therefore a suitable candidate for study with the EDM.

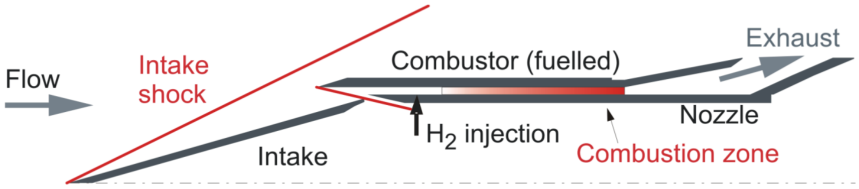

Figure 4.23: Schematic of the HyShot II combustor. Image reproduced from [56].

4.4.1 Problem Formulation

In the present work, the intake part (Figure 4.23) is not considered. Instead, the combustor CFD inflow conditions documented in the literature [86, 102, 56] are used. These conditions are given at a cross section 5 mm downstream from the body side's leading

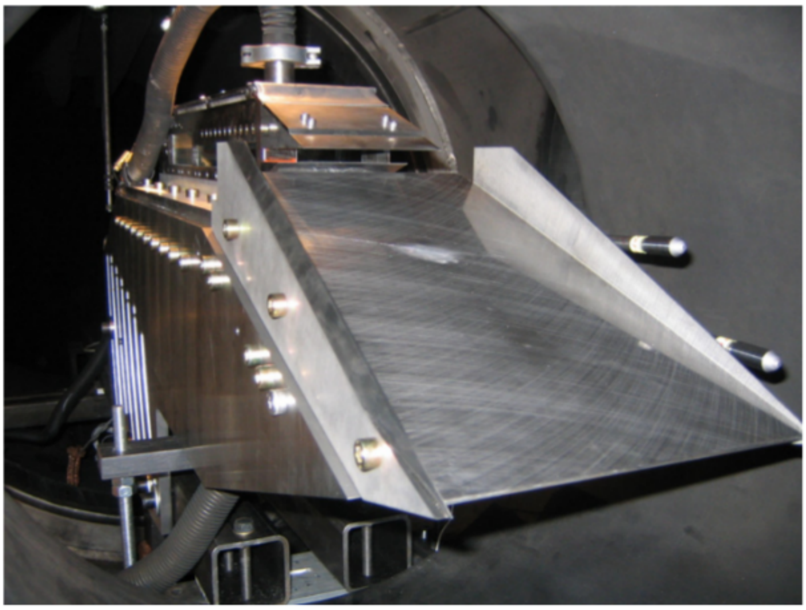

Figure 4.24: HyShot II installed in test section of HEG. Image reproduced from [56].

edge. The CFD data, obtained with the k-ω SST, has been kindly provided by Sebastian Karl from the DLR and is shown in Figure 4.25. Interpolated quantities for the wall normal cells used in Eilmer are also shown. The profiles in Figure 4.25 are prescribed at the inlet of the three-dimensional domain considered in this work (same inflow for each lateral cell location) and correspond to averaged conditions listed in Table 4.4.

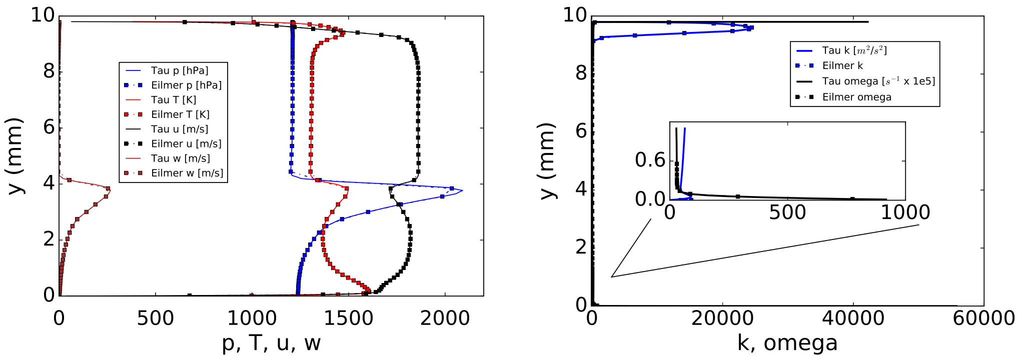

(a) (b)

Figure 4.25: Prescribed inflow conditions for (a) pressure, temperature and velocity (b) turbulence.

Table 4.4: Inflow (averaged) and injector flow conditions for the HyShot II combustor.

	inflow (averaged)	injector
u (m/s)	1720	1206.7 (tranverse)
T (K)	1300	249
p (Pa)	130000	263720
Mach (-)	2.4	1.0
Y_{H_2} (-)	0.0	1.0
Y_{O_2} (-)	0.233	0.0
Y_{H_2O} (-)	0.00	0.0
Y_{N_2} (-)	0.767	0.0

Figure 4.26 shows the computational domain considered in this work. It consists of half an injector and two symmetry planes and represents one-eigth of the total span. Note the combustor length considered in this work is 2 cm shorter than the original geometry. The injector is modeled as a supersonic inflow boundary with conditions listed in Table 4.4. The resulting equivalence ratio is 0.29. Turbulence injector flow conditions are set as I = 5 %, μ_t/μ = 10. The upper and lower boundaries (z coordinates) are treated as viscous isothermal walls at a temperature of 300 K. A supersonic outflow is prescribed at the exit of the geometry. The boundary layer (BL) along the upper wall (cowl side) is assumed to be fully turbulent while a transition from laminar to turbulent takes place at the lower wall (injector side) around x = 45 mm (see [86]). This is accounted for in Eilmer by generating two turbulent zones across the width of the domain as illustrated in Figure 4.26. Outside these zones the turbulent quantities (k,ω) are purely transported and do not affect the other governing equations. Compressible wall functions of Nichols and Nelson [224] are adopted as to reduce the computational cost of the simulations due to grid requirements. An O-grid topology is adopted for the injector. Inviscid fluxes are treated with the AUSMDV and time stepping with a predictor-corrector scheme. Values for turbulent Prantl and Schmidt numbers are set to 0.9 and 0.7 respectively. Sensitivity studies to these parameters have been reported by Karl [86] and Pecnik et al. [105] with the Spalart-Allmaras and the k-ω SST turbulence model respectively. It was observed by both authors that the resulting pressure traces with different combination remain between the experimental uncertainty of the measurements. Therefore, such a sensitivity with the k-ω 2006 model is not considered in the present work. Instead, the standard setting for these parameters is selected.

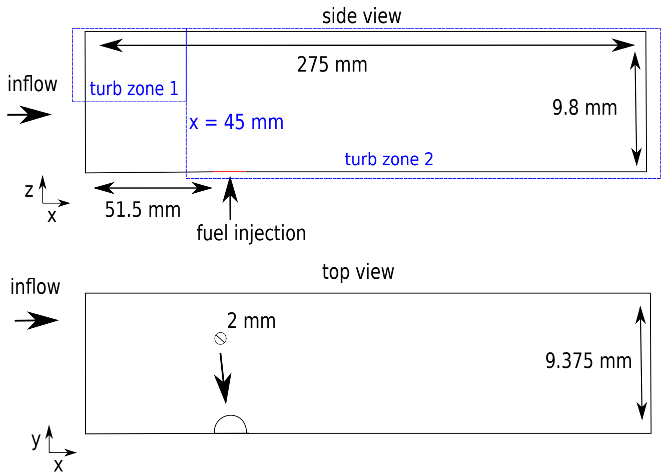

Figure 4.26: Computational domain of the HyShot II combustor. Not to scale.

4.4.2 Grid Independence and Compressibility Correction

A mesh size containing 1.3M structured cells was generated for the non-reacting conditions without fuel injection. For the reacting conditions (Chapter 5), a finer mesh was generated resulting in 2.8M cells. No grid independence study has been performed for this test case. Pecnik et al. [105] obtained satisfactory reacting wall pressure traces with a structured grid consisting of 2.6M cells. Moreover, the injector was modeled as part of the computational domain which extended to include a part of the nozzle. This indicates that the current mesh size of 2.8M cells is a good starting point. In order to ascertain the suitability of the grid for the Eilmer CFD solver, future work should include a mesh independence study.

The effect of the turbulence compressibility correction on the HyShot II combustor has not been considered in the present test case. Previous investigations with the Burrows-Kurkov and DLR test case demonstrated its very limited influence. Moreover, Karl [86] showed no effect of its use on the wall pressure trace, nor the heat flux. Similar results are expected to follow from such study with the Eilmer CFD solver and Wilcox'k-ω 2006 model.

4.4.3 Non-reacting Conditions

Figure 4.27 compares the wall pressure predictions with experimental data and another CFD solution. Pressure traces are shown for the body and the cowl side. The reference solution has been obtained with the TAU code [86] and the Spalart-Allmaras (SA) turbulence model. No wall functions were used in the reference results. A similar setting for Pr_t has been used as in the present work. Predictions with Eilmer demonstrate overall a very good agreement with the experimental data. In comparison with the TAU SA results, current predictions appear to have lower peak pressure values at several locations. This can be explained by the use of wall functions with Eilmer. Nevertheless, similar shock reflection locations are captured and the suitability of the k-ω 2006 turbulence model demonstrated. In this work, the no-model approach with detailed reaction mechanism has not been considered for the HyShot II combustor as it would have resulted in an intensive use of available computational resources. As the emphasize of this thesis is on the EDM, the resources have been used to its study instead.

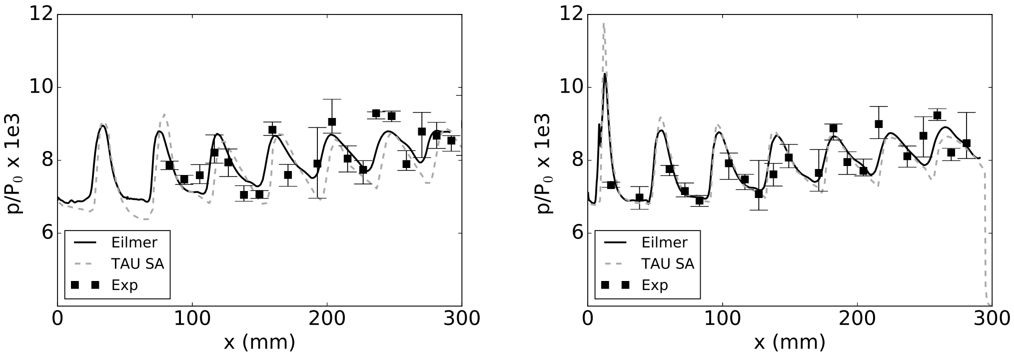

(a) (b)

Figure 4.27: Non-reacting wall pressure trace in the HyShot II combustor with (a) injector / body side, (b) cowl side. P_0 = 17.73e6 Pa.

4.5 The Scramjet of Lorrain

This scramjet geometry is a test case investigated by Lorrain et al. [84, 225, 226] in the University of Queensland's T4 hypersonic piston-driven shock tunnel. It is a specific type of scramjet engine which relies on the concept of radical farming and has been introduced within the SCRAMSPACE I project [227]. This scramjet test case is selected in order to answer the question of whether or not the application of the EDM can be pushed to scramjets where the combustion is mainly kinetically limited. The latter is prevalent in radical farming scramjets. The no-model approach with detailed reaction mechanism has proven to be adequate in simulating this type of configuration

[84]. Therefore, as a means of comparison, a no-model simulation with Eilmer will be used as a reference for assessing the behavior of the EDM in Chapter 5.

4.5.1 Problem formulation

Figure 4.28 gives a schematic of Lorrain's experimental setup while Figure 4.29 shows the geometry and boundary conditions used by Lorrain et al. [225] for study of the finite-rate chemistry mechanisms governing the combustion process with CFD++ [228]. As it can be seen in the upper representation, the full geometry consists of an inlet (sharp leading edge) with two ramps leading to the constant area combustor which terminates in an exit nozzle. As a numerical demonstration, a premixed configuration (lower representation) was also studied. Lorrain aimed at investigating shock and expansion wave structures as well as boundary layer viscous heating effects. The test case has been simulated in three different conditions [225] which are reproduced in the present work:

a. A full geometry (upper part of Figure 4.29) with only air as a working fluid.

b. A frozen hydrogen fueled simulation with only the combustor and nozzle (lower part of Figure 4.29).

c. A reacting hydrogen fueled simulation with only the combustor and nozzle (lower part of Figure 4.29).

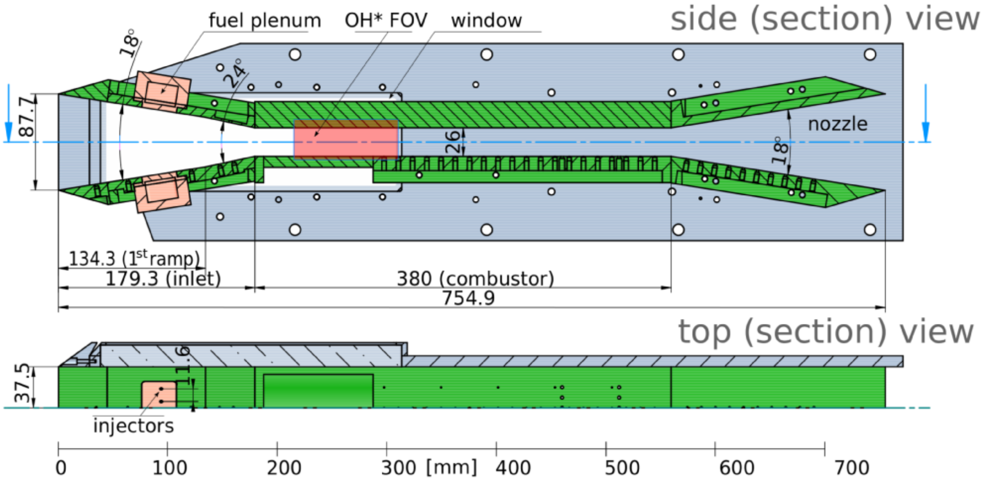

Figure 4.28: Experimental scramjet configuration of Lorrain. Image reproduced from [225]

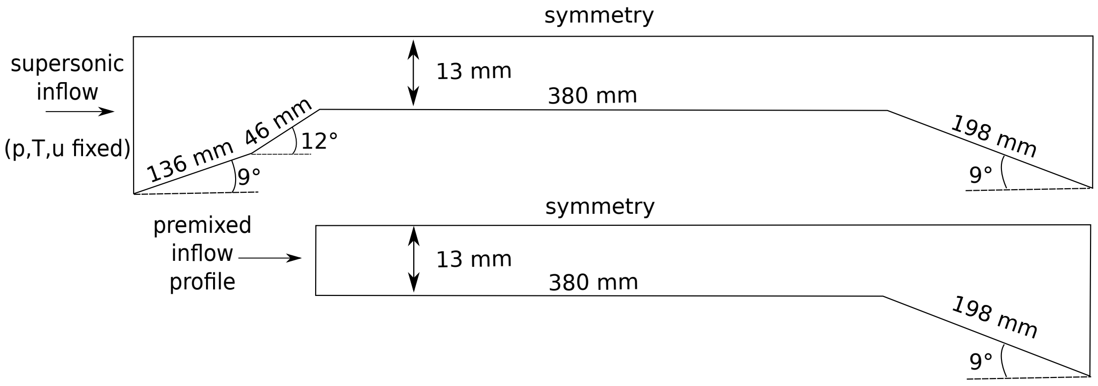

Figure 4.29: The geometry considered for scramjet CFD simulations [225] with top: for fuel-off case, bottom: for frozen and combusting case

Table 4.5 summarizes the supersonic inflow conditions of Lorrain's experimental and numerical study for the fuel-off case with u, p, T and X being respectively the velocity, static pressure, static temperature and mole fractions. Turbulent inlet quantities were set with an intensity I of 2 % and a ratio of viscosities μ_t/μ equal to 5. The symmetry of the geometry was exploited in the simulations and the walls are considered isothermal at a temperature of 300 K. This assumption is acceptable considering the very short experimental test time, on the order of milliseconds, which is not sufficient to cause significant temperature elevations. A turbulent Prandtl number of 0.89 was specified in both solvers for the presented results and for the reacting simulation the turbulent Schmidt number is set to 0.7.

Table 4.5: Flow conditions at the inlet of Lorrain's scramjet geometry for the different simulations [225].

	u (m/s)	p (Pa)	T (K)	$X_{O_2}(-)$	$X_{N_2}(-)$	$X_{H_2}(-)$
fuel-off	2830	4100	370	0.21	0.79	0.0
frozen / reacting	u(y)	p(y)	T(y)	0.157	0.593	0.25

4.5.2 Grid Independence

In all simulations, the maximum first cell distance to physical walls was below 5e-6 m ensuring that the first cell is located inside the viscous sublayer. The non-reacting configuration in Figure 4.29 has been simulated with 322 080 cells. Frozen and reacting simulations considering only the combustor and nozzle were studied with a mesh size of 354 640 cells. The latter setting has proven to be adequate following a grid independence study. The result of this study is shown in Figure 4.30 for two grids containing respectively 233 750 (mesh 1) and 354 640 (mesh 2) cells. The EDM with setting A_{edm}=1 and the kinetic limit was adopted for the grid independence study. This result is solely considered to demonstrate mesh independence as the EDM will be covered in more details in Chapter 5. Figure 4.30 presents the pressure along the wall and the combustion efficiency (Equation 4.1) obtained with both grids. The curves indicate the achievement of mesh independence as no difference in predictions are observed.

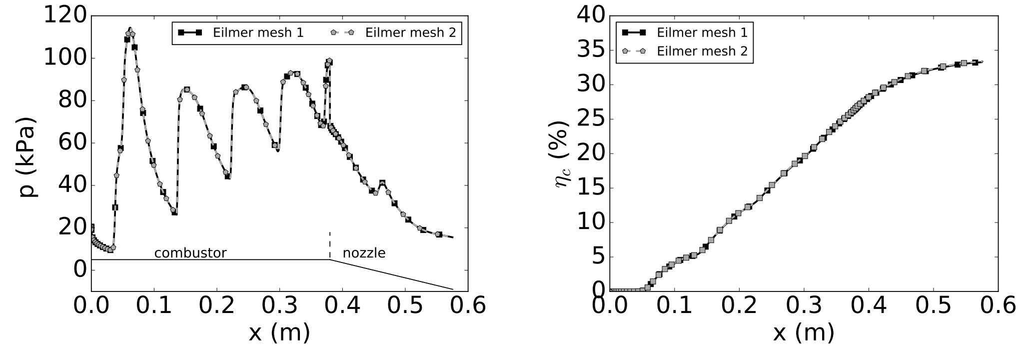

(a) (b)

Figure 4.30: Effect of grid size on (a) wall pressure and (b) combustion efficiency for Lorrain's scramjet. $A_{\mathrm{edm}} = 1$, kinetic limit.

4.5.3 Non-reacting Conditions

Firstly, results for the non-reacting simulation (case a) are presented. Figure 4.31 compares the experimental wall pressure coefficient [225] with the CFD. The simulation seems to underestimate pressure values such as the first peak inside the combustor. Nevertheless, the location is estimated in a fair manner. This single peak is the result of a very close reflection of the two intake ramps shocks which then propagate as a single shock. The Schlieren observations discussed further below will make this more clear. The combustor profile does follow the trend of the experimental data but from the second peak onwards a shift in position is observed. The nozzle section predictions seem to miss some fundamental behavior. Observe as well the discrepancy between the CFD and the experiment near the entrance of the combustor. Connecting the third, fourth and fifth data point suggests the presence of a smaller peak. This has been further investigated by consulting Lorrain's more complete work [84] In the latter reference, Lorrain mentions that during the testing some of the pressure sensors gave false readings following electrical connection problems. Based on a different set of experimental data points (see Figure 6.7 p 98 of [84]), no smaller peak is observed. This suggests the possibility that the fourth data point in Figure 4.31 results from a false reading.

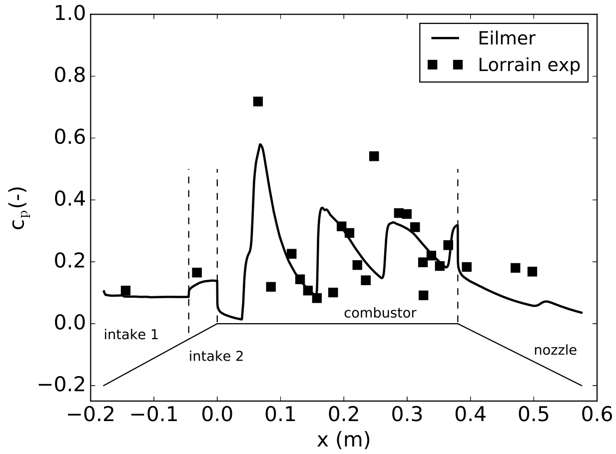

Figure 4.31: Wall pressure coefficient for the fuel-off test case of Lorrain, comparison with experimental values.

Figure 4.32 presents the experimental Schlieren of intake regions and combustor entrance as well as the CFD gradient of density. The different flow features shown experimentally are visible in the numerics with the two shocks of the intake ramps as well as the expansion wave at the combustor entrance corner which is consistent with the previously observed wall pressure profile. It must be noted that, when looking at the experimental Schlieren further downstream in the combustor, the reflected shocks do not cross at the center of the geometry. This suggests an asymmetry in the geometry which was later confirmed [84]. Consequently the pressure data also captured this asymmetry which is not accounted for in the present simulation. This could explain the mismatch between experimental data and CFD observed in Figure 4.31.

For the simulations in frozen conditions (case b) the profiles of the flow variables at the entrance of the combustor are extracted from the fuel-off results (case a) and prescribed as inlet boundary conditions. In order to account for the presence of hydrogen the pressure profile was altered as $p_{frozen} = p_{fuel-off}/(1 - X_{H_2})$. For the frozen condition, CFD data of pressure is available from Lorrain et al. [225] along

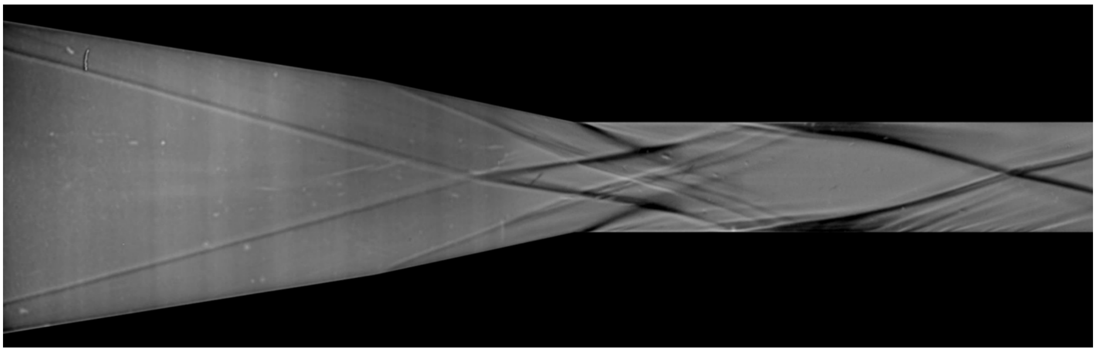

(a) Experiment [225]

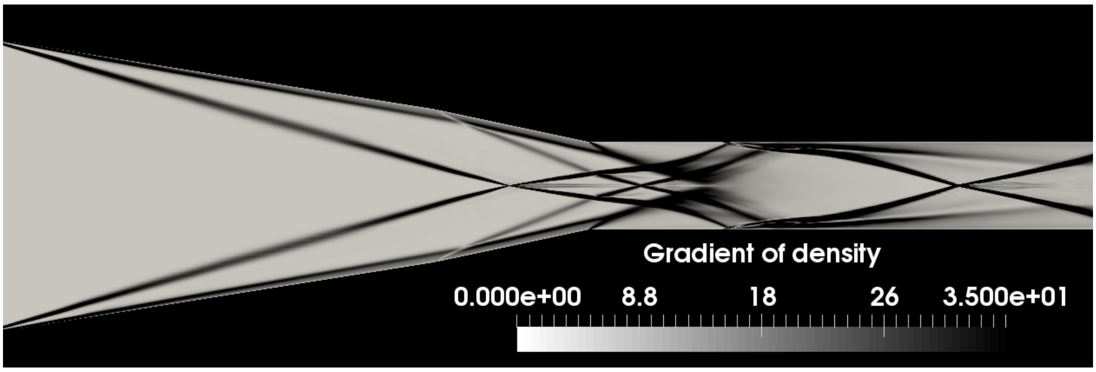

(b) CFD

Figure 4.32: A qualitative comparison of the experimental Schlieren and CFD for Lorrain's fuel-off conditions. Note that the scales do not perfectly match.

a streamline originating 1.5 mm from the lower wall at the combustor entrance as shown in Figure 4.33. In the first part of the combustor both CFD results do predict similar shock positions. It is only toward the end of the combustor and the nozzle that the simulations start to differ. Lorrain's simulation were obtained with the k-ω SST turbulence model which is believed to explain partly the difference in observations. Moreover, the fact that a comparison is made along a streamline introduces a degree of error given the flow field dependency of such a process. Overall, the predictions with the k-ω 2006 in present work are similar to the k-ω SST of Lorrain.

4.5.4 Reacting Conditions

The CFD prediction of Eilmer with no-model, finite-rate chemistry and the 13 species, 33 reactions mechanism of Jachimowski [149] is compared to the predictions of Lorrain [225] adopting the same settings. Figure 4.34 presents the comparison of the pressure along a streamline originating 1.5 mm from the wall at the entrance of the combustor. The position of the shocks in the combustor and the shock induced

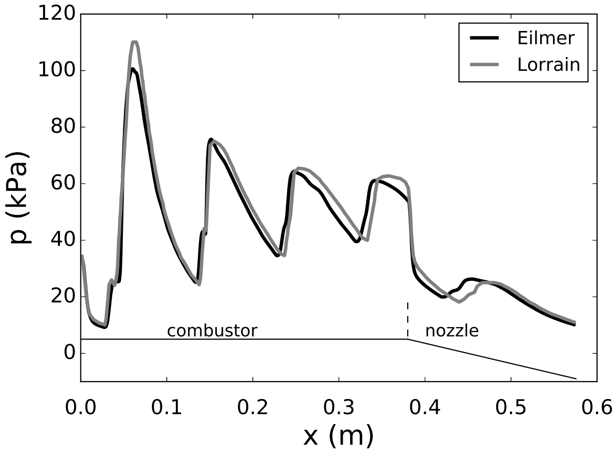

Figure 4.33: Static pressure along a streamline starting 1.5 mm from the combustor's entrance wall of Lorrain in frozen conditions.

boundary layer separation bubble (x $\approx$ 0.04 m) are in agreement between both solvers. Some discrepancies are observed in the nozzle and in the strengths of the shocks. Similar observations were made in frozen conditions and the cause was attributed to the difference in turbulence model. Moreover, the fact that a comparison is made along a streamline introduces a degree of error given the flow field dependency of such a process. Lorrain performed a more in depth three-dimensional CFD study considering the complete scramjet [84]. A good qualitative and quantitative agreement in wall pressure trace is observed in comparison with experimental measurements. The CFD methodology with the no-model approach for combustion is therefore deemed suitable for this type of scramjet. The comparison in Figure 4.34 demonstrates that the no-model results of Eilmer, which are similar to Lorrain, are adequate to be used as a reference for further comparison with the EDM in a subsequent study.

4.6 Summary of Chapter

This chapter discussed the numerical study of four scramjet test cases. The aim was to validate the selected solver in relevant scramjet conditions with a special emphasis on the behavior of the turbulence model and the combustion without TCI. It is pointed out that the k-ω 2006 turbulence model has limited validation in the literature. Consequently, the results in this chapter contribute to the general validation of the latter model. The test cases were selected with respect to this thesis final objective and are further studied with the EDM in Chapter 5. The first three configurations (Burrows-

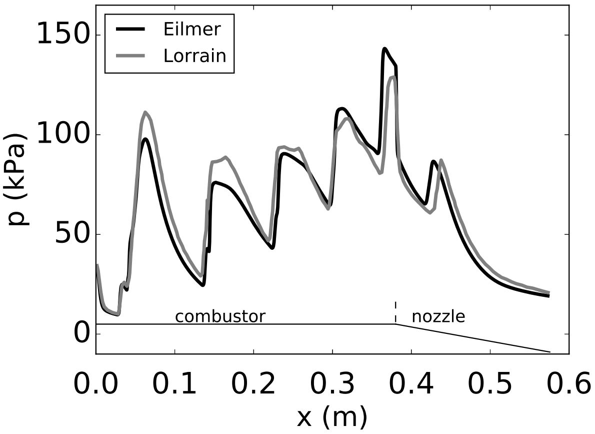

Figure 4.34: Static pressure along a streamline starting 1.5 mm from the combustor's entrance wall of Lorrain in reacting conditions.

Kurkov, DLR and HyShot II) are representative for the high flight Mach number experienced by scramjets where the combustion is believed to be mainly mixing-limited. The EDM should therefore be a valid model for study of the combustion. The latter test case (Lorrain) is a scramjet where the combustion is dominated by kinetic effects. It is considered in this work in order to assess if the EDM can still provide reasonable results when the underlying assumptions of the model are not valid anymore. Predictions of the experiment of Burrows and Kurkov demonstrated the strong sensitivity to values of $\mathrm{Pr_t}$ and $\mathrm{Sc_t}$. This observation is even more pronounced in reacting conditions. Overall, a good predictive behavior of the selected CFD solver was observed by comparison with experimental data and reference CFD results. The k-ω 2006 model is deemed suitable for study of this type of scramjet configurations and demonstrated a clear improvement to prior versions of the model. In the study of the DLR combustor in inert conditions, the sensitivity to values of $\mathrm{Pr_t}$ and $\mathrm{Sc_t}$ was further demonstrated. Comparing with experimental data and reference CFD showed that the essential features of the flow field were reasonably well captured by the present solver. In both the experiment of Burrows and Kurkov and the DLR combustor, the use of a compressibility correction has not shown signficant changes. The non-reacting experimental pressure traces inside the HyShot II combustor were well predicted by the CFD. Finally, the numerical study of Lorrain's scramjet showed some differences in predictions with respect to a reference CFD solution obtained with the k-ω SST turbulence model in frozen and reacting conditions. Nevertheless, the overall trends predicted by Eilmer in reacting conditions are similar to the premixed CFD of Lorrain.

Therefore, the no-model results of Eilmer are considered as a reference for further study in Chapter 5.

Chapter 5

Assessment and Optimization of the EDM for Scramjet Flow Field Prediction

This chapter presents the work performed by considering the Eddy Dissipation Model (EDM) to tackle the combustion modeling within the RANS framework. Section 5.1 discusses the theory and numerics of the EDM including the different formulations. The most appropriate setting for the model constant is studied in Section 5.2 with three generic scramjet combustors for which experimental data is available. This includes the investigation of possible ways to make a better use of the model. In Section 5.3, the EDM is applied to a scramjet configuration where the combustion is dominated by chemical kinetics. The aim is to understand if the use of the EDM could be extended beyond its original scope. Finally, Section 5.4 provides a summary of the findings. The work in this chapter has been partially presented at two conferences [229, 230]

5.1 The Eddy Dissipation Model (EDM)

In Chapter 2, a computationally affordable model for turbulence chemistry interaction (TCI) description was identified: the Eddy Dissipation Model (EDM). The model is used to specify the chemical source term in Equation 3.7 and is considered in the present work for the study of scramjet combustion. This section is dedicated to the EDM and is structured as follows. Firstly, a description of the physical assumption of the EDM is given (5.1.1) followed by the numerical formulation (5.1.2). Then, the modeling constants used in the description of the model are discussed (5.1.3).

Afterwards options to limit the reaction rate predicted with EDM are introduced (5.1.4) followed by a brief discussion on the computational cost of the model (5.1.5).

5.1.1 Physical Interpretation of the EDM

The Eddy Dissipation Model (EDM) introduced by Magnussen and Hjertager[153, 137] is closely related to the Eddy Breakup Model (EBU) of Spalding. It assumes that fuel and oxidizer are carried by separate eddies in diffusion flames. Furthermore, chemical reactions are fast so that fuel and oxidizer will react as soon as they mix on a molecular scale. Assuming this fast chemistry limit in the EDM, the rate at which reactions occur is then dependent on the rate at which turbulent eddies carrying fuel and oxidizer are brought together. In other words, the mean reaction rate is mainly controlled by a turbulent mixing time. On dimensional basis, this mixing time is estimated from the integral length scales by using the turbulence model parameters which describe the energy cascade process in turbulent flows [182, 184]. Consequently, the mixing on a molecular level is dependent on the rate at which the eddies dissipate. From this description, the model can be also be referred to as “mixed-is-burned".

5.1.2 Numerical Implementation of the EDM

Basic formulation

The EDM is numerically implemented by assuming a single-step irreversible reaction of the form

$$\nu_F^{'}F+\nu_O^{'}O\rightarrow\nu_P^{''}P \tag{5.1}$$

where ν_s are the stoichiometric coefficients of Fuel (F), Oxidizer (O) and Products (P). Such a form is consistent with the model’s physical description of fast-occurring chemical reactions. The use of a single-step irreversible reaction instead of a reaction mechanism reduces the computational cost and makes it useful for design.
In the case of hydrogen combustion, the reaction is :

$$2H_2+O_2\rightarrow 2H_2O \tag{5.2}$$

and N_2 acting as an inert species. This results in four species equations. Species conservation presented previously as Equation 3.7 is repeated here as Equation 5.3.

$$\frac{\partial(\bar{\rho}\tilde{Y}_s)}{\partial t}+\frac{\partial(\bar{\rho}\tilde{Y}_s\tilde{u}_j)}{\partial x_j}=\bar{\dot{\omega}}_s-\frac{\partial}{\partial x_j}\left(\bar{J}_{s_j}+\bar{\rho}\widetilde{Y_s^{''}u_j^{''}}\right) \tag{5.3}$$

The reaction rate of fuel predicted by EDM is defined as (previously presented as equation 2.1):

$$\bar{\dot{\omega}}_F = -A_{\text{edm}}\ \bar{\rho}\beta^*\omega\ \min\left[\tilde{Y}_F, \frac{\tilde{Y}_O}{s}, B_{\text{edm}}\frac{\tilde{Y}_P}{s+1}\right] \tag{5.4}$$

The oxidizer and product reaction rates can then be obtained as:

$$\bar{\dot{\omega}}_O = s\ \bar{\dot{\omega}}_F \ \ , \quad \bar{\dot{\omega}}_P = -(s+1)\bar{\dot{\omega}}_F \tag{5.5}$$

In the above equation s is the mass stoichiometric ratio defined as

$$s = \frac{\nu_O' W_O}{\nu_F' W_F} \tag{5.6}$$

and equals 8 for H_2-air combustion. W_s is the molar mass in kg/mole and Y_s the mass fraction. In Equation 5.4, β^* is a turbulence model constant [134] with a value of 0.09 and ω (1/s) is the specific dissipation of turbulent kinetic energy obtained through the turbulence model. The underlying physical assumption regarding the dissipation of turbulent eddies in the model is accounted for through the latter parameter.

Note that the EDM works in conjunction with two equation turbulence models. This can be the k-ω, the k-ε or the k-ω Shear Stress Transport (SST) model. If the model does not compute ω, its value can be obtained from k and ε as

$$\omega = \frac{\varepsilon}{\beta^* k} \tag{5.7}$$

A one equation turbulence model such as Spalart-Allmaras (SA), also adopted in hypersonic propulsion flow path simulations (see Section 2.2), does not directly provide enough integral turbulence quantities to specify the turbulent mixing times scale required in Equation 5.4. The SA provides a transport equation for a quantity $\tilde{\nu}$ which is directly related to the eddy viscosity [188]. A possibility consists of deriving a turbulent kinetic energy (k_{SA}) and dissipation rate (ε_{SA}) as [231]:

$$k_{SA} = \frac{\tilde{\nu}}{l_t} \tag{5.8}$$

and

$$\varepsilon_{SA} = C_\mu \frac{k_{SA}}{d^2/\tilde{\nu}} \tag{5.9}$$

with $\mathrm{l_t}$ the integral length scale (= $\mathrm{l_0}$, see Section 3.1), C_μ a model constant usually taken as 0.09 [137] and d is the distance to the closest wall. Equation 5.8 requires the specification of the integral length scale which is a flow dependent quantity. The above method is therefore not the most suitable when the SA turbulence model is adopted with the EDM. However, research looking at improving the formulation of values for values for $\mathrm{k_{SA}}$ and $\varepsilon_{\mathrm{SA}}$ is currently being undertaken at the University of Sydney (Dr Ben Thornber, personal communication, 22 January, 2018). Belmrabet et al. [163] did use another approach to apply EDM to an hydrogen-fueled scramjet in conjunction with the SA turbulence model. The authors rely on the hypothesis of local equilibrium between production and dissipation of turbulent kinetic energy in order to provide a value for the ratio ε/k which depends on the turbulent Reynolds number.

Generalised formulation

The form of the EDM outlined previously assumes that there are only 2 reactants and 1 type of product formed. What if more species are involved in the considered single step global reaction? Take for example the following reaction for methane:

$$C_2H_4 + 3O_2 \to 2CO_2 + 2H_2O \tag{5.10}$$

A more general form of the EDM can be formulated to address such cases. Consider again a chemical system of N species s reacting through M reactions [137]

$$\sum_{s=1}^{N} \nu'_{sj}\mathscr{M}_s \rightleftharpoons \sum_{s=1}^{N} \nu''_{sj}\mathscr{M}_s \quad , \qquad j = 1, M \tag{5.11}$$

where $\mathscr{M}_s$ represents species s and ν'_{sj} and ν''_{sj} are the molar stochiometric coefficients of species s in reaction j. Mass conservation implies that

$$\sum_{s=1}^{N} \nu'_{sj}W_s = \sum_{s=1}^{N} \nu''_{sj}W_s \quad , \qquad j = 1, M \tag{5.12}$$

As the EDM works with a single reaction the index j is equal to 1. The reaction rate for a specific species is then given by the general form of the EDM as

$$\bar{\dot{\omega}}_k = W_k(\nu''_k - \nu'_k)\frac{A_{\mathrm{edm}}}{\tau}min\left[\frac{\bar{\rho}_F}{\nu'_F W_F}, \frac{\bar{\rho}_O}{\nu'_O W_O}, B_{\mathrm{edm}}\frac{\bar{\rho}_P}{\nu''_P W_P}\right] \tag{5.13}$$

With the chemical time scale $\tau = k/\varepsilon$ or with Equation 5.7, $\tau = 1/(\beta^*\omega)$. The above equation can be rewritten by making use of Equation 5.6 as:

$$\bar{\dot{\omega}}_k = \frac{W_k(\nu_k'' - \nu_k')}{\nu_F' W_F} \left(\frac{A_{\text{edm}}}{\tau} \bar{\rho} \;\; min \left[\tilde{Y}_F, \frac{\tilde{Y}_O}{s}, B_{\text{edm}} \frac{\tilde{Y}_P}{1+s} \right] \right) \tag{5.14}$$

It can be seen that the term between brackets equals the fuel reaction rate of Equation 5.4 (opposite sign). Consequently, this property can be used in order to obtain the reaction rates for more than 3 species in a single step reaction.

Multi-Step Reactions

Some research in the literature (see Section 2.2) report the application of EDM in conjunction with a multi-step reaction mechanism for ethylene - air combustion [80, 173, 174]. This approach requires to evaluate Equation 5.14 for every reaction of the mechanism. Moreover, the kinetic limit (see Equation 5.15 in 5.1.4) can as well be invoked for each reaction. Note however that the number of reactions should be kept to a minimum as erroneous results could readily arise. This is explained by the fact that the development of a mechanism of reaction is based on Arrhenius rates which differ for each reaction. The EDM applies the same turbulent rate (ω) for each reaction and can therefore not predict species [162] that are kinetically controlled, e.g. intermediate radicals.

5.1.3 Specification of the Model Constants

A_{edm} and B_{edm} are model constants which have standard values of 4.0 and 0.5. This combination of values follows from the work of Magnussen and Hjertager [153]. In the study of six different low-speed flame simulations, in conjunction with the k-ε turbulence model, satisfactory results in comparison with experimental data were obtained by adopting the above settings. However, this combination might not be the most appropriate for the desired type of flow fields under study. E.g. for scramjets, Edwards et al. [80] suggest a value for A_{edm} between 1 and 4. The physical effect of increasing this constant's value is the promotion of the turbulent eddy dissipation process in the flow field which, where available, brings fuel and oxidizer together on a molecular level. In summary, the mean fuel reaction rate of EDM, $\bar{\dot{\omega}}_F(kg/(m^3.s))$, is a function of turbulence (ω), and the mass fractions of fuel ($\tilde{Y}_F$), oxidizer ($\tilde{Y}_O$) and products ($\tilde{Y}_P$) in every cell of the domain. Note that the latter term in the minimum evaluation of Equation 5.4 is intended to account for the effect of hot (or cold) products in a premixed turbulent flame situation where both fuel and oxidizer are contained within the same eddies [153]. The importance of the products on the combustion process can be controlled through the parameter B$_{\text{edm}}$. An increase in value of B$_{\text{edm}}$ will promote the reaction between fuel and oxidizer as more hot products are present to ignite the premixed mixture. The premixed situation is not very common in scramjet flows except for the case of oxygen enrichment. Moreover, the inclusion of the product term implies that for reactions to occur an initial product mass fraction is required. This value is usually taken as 0.01 (see Fluent user guide for example [162]). Care must be taken if the product term is considered for numerical study of experimental scramjet combustors as the inflow conditions typically contain vitiated products such as water vapor for instance. These vitiation products shouldn't be considered in the product mass fraction of Equation 5.4 as they are not the result of combustion.

5.1.4 Limiting the Reaction Rate within EDM

The EDM does not include any effect of chemical kinetics. Equation 5.4 does not account for the temperature on the formation of products. Consequently, the EDM has a tendency to over-predict the fuel consumption as well as peak temperatures. The way to mitigate these disadvantages is by limiting $\bar{\dot{\omega}}_F$ with a kinetic reaction rate. This can be done by use of the reaction rate obtained with the "no-model" or Arrhenius approach (law of mass action), given by Equation 3.42, and a single step global reaction [93]:

$$\bar{\dot{\omega}}_F = \min(\bar{\dot{\omega}}_{F,\text{edm}}, \bar{\dot{\omega}}_{F,\text{lam}}) \tag{5.15}$$

where $\bar{\dot{\omega}}_{F,\text{lam}}$ is given by:

$$\bar{\dot{\omega}}_{F,\text{lam}} = -\nu_F^{'} W_F \ [k_f [X_F]^{\nu_F^{'}} [X_O]^{\nu_O^{'}} - k_r [X_P]^{\nu_P^{'}}] \tag{5.16}$$

The kinetic limit allows the extension of the EDM's applicability to test cases where the combustion is not purely mixing limited but where ignition delay effects are present. However, the trade-off is the introduction of two reaction rate parameters which are not universally defined: the forward reaction rate k_f and the backward or reverse reaction rate k_r. The former is obtained with Arrhenius law by defining a pre-exponential constant A and an activation temperature T$_A$ for a single step global reaction of the hydrogen-air combustion. Several options are available in the open-literature for the Arrhenius law constants and this work will adopt the values A=1.1e19 and T$_A$ = 8052

K as proposed by Chandra Murty and Chakraborty [143]. These values have been obtained for hydrogen combustion by requiring that the flame speed of the single step kinetics match with those from full chemistry as pointed out by Sekar and Mukunda [232]. The k_r is obtained from the forward rate and equilibrium constant. The use of Equation 5.15 will be referred to as "EDM with kinetic limit". Another approach to reduce the over-predictions in fuel consumption is by specifying an “ignition temperature" that has to be exceeded in every cell in order for combustion to occur. Edwards and Fulton [80] applied this for scramjet internal flow paths with a threshold of 900 K for hydrogen and ethylene.

As pointed out by Baurle [93], the use of EDM does alleviate the stiffness of the governing equations as turbulent time scales are driving the reactions. This characteristic makes the use of EDM beneficial for design purposes. In the case of non-premixed scramjet flow path simulations with EDM, on top of the model constant $\mathrm{A}_{\mathrm{edm}}$, values for turbulent Prandtl (Pr_t) and Schmidt number (Sc_t) have to be specified. Including the possibility to limit reaction rates with a kinetic limit, this leaves the user to specify a combination of 3 (or 4) parameters per simulation. Details about the settings and effect of parameter values choices are presented in Sections 5.2 and 5.3.

5.1.5 Computational advantage of the EDM

It has been pointed out at multiple occasions in this work that the EDM has the advantage of being a computationally cheap model for TCI. The reason relates to the fact that turbulence controls the reaction rates and not the chemical kinetics. Therefore, a less stiff set of governing equations is solved. An attempt in quantifying the computational advantage of the EDM with respect to the no-model approach is now made. Note that the following discussion is based on the Eilmer flow solver and is thus coupled to its numerical description. In other words, the difference in combustion modeling will affect the description and integration of the chemical source term in Equation 3.58.

The chemical increment for the EDM with or without kinetic limit is schematized in Figure 5.1. The reaction rate is denoted as RR for simplicity. The overall procedure is self-explanatory. The integration of Equation 3.58 is performed with a simple forward Euler scheme. Based on the CFL criterion a flow time step, Δt_{flow}, is obtained to which the time step for the chemical increment is set equal to. In other words $\Delta t_{chem} = \Delta t_{flow}$ which is the great advantage of the EDM. Note that integrating Equation 3.58 results in an update of the species mass fractions but not in the other variables. Therefore an update of the gas state is necessary as shown in the flowchart. All of the steps in Figure 5.1 have to be performed for every cell.

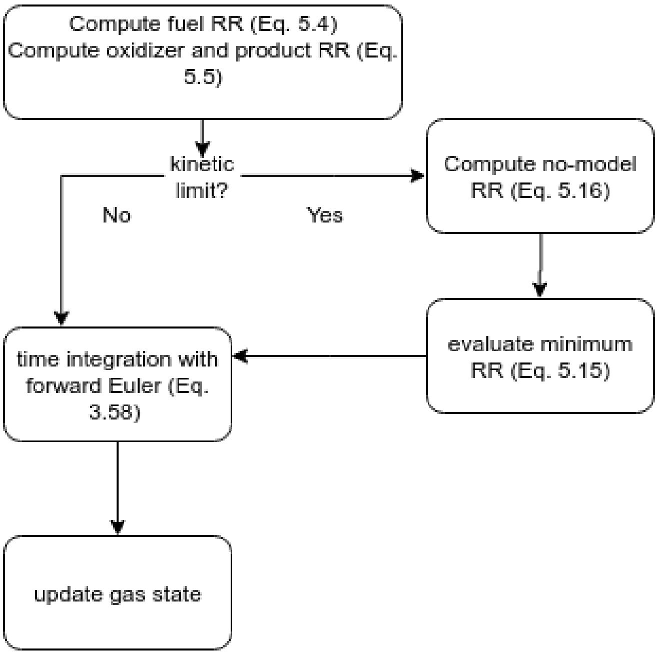

Figure 5.1: Flowchart of the EDM chemical increment.

A very simplistic representation of the chemical increment procedure for the no-model approach is given in Figure 5.2. Some explanations are required in order to understand the diagram. When starting the chemical increment over a time Δt_{flow}, an initial chemistry time step (Δt_{chem}) must be defined and cannot be larger than the flow time step. At the initial iteration of the solver there is no Δt_{chem} and an evaluation is made based on a formula of Young and Boris [197, 233]:

$$\Delta t_{chem} = \varepsilon_1 \ min \left(\frac{[X_s]}{[\dot{X}_s]} \right) \tag{5.17}$$

with ε_1 taken as 1.0e-3 in Eilmer [197]. Evaluating Equation 5.17 requires knowledge of the rate of change of the species concentration through Equation 3.42. The latter operation is as costly as computing the no-model reaction rates when the kinetic limit is activated for the EDM (see Figure 5.1). It must be performed only once. When the chemistry problem is not solved for the first time, the old chemistry time step is used as an initial candidate step to solve the system of ODE's. The latter is solved with the α-QSS method which is detailed in [197]. It is applied to integrate Equation 3.58 in steps determined by Δt_{chem} until a time Δt_{flow} is elapsed. A new composition is then obtained and the other quantities are subsequently updated. The flowchart representation is simplistic given that solving the ODE system is not trivial and failures are commonly encountered resulting in multiple attempts and adaptations of the chemistry time step. As pointed out by Jacobs et al. [197], it is not uncommon to have simulations where the chemistry time step is 100-1000 times smaller than the flow time step which means that 100-1000 subcycles are required in order to solve the chemistry problem. In other words, repeating the α-QSS method 100-1000 times. Moreover, the α-QSS is a predictor-corrector method in which the corrector is iterated upon until a desired convergence is achieved [197]. In both the predictor and corrector step the production and loss terms (see Equation 3.47) are evaluated. The above is repeated for every cell of the computational domain. It can now be understood that the EDM is very advantageous in terms of computational steps which in theory does as well result in much less computational time to solve the chemistry problem.

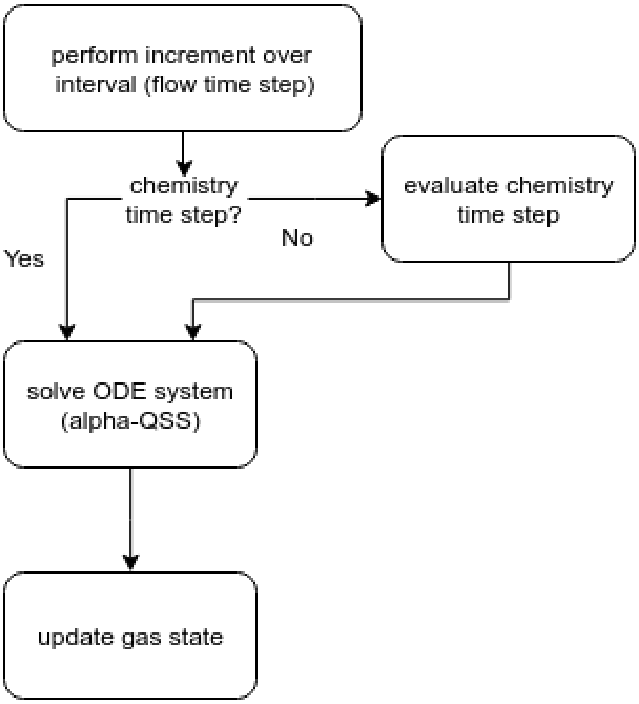

Figure 5.2: Flowchart of the chemical increment for no-model approach.

It is not trivial to quantify the advantage of the EDM over the no-model approach as the number of subcyles in the latter is dependent on the problem under study (grid, flow physics) and the selected reaction mechanism in an unsteady fashion. As a measure of comparison the hydrogen / air combustion experiment of Burrows and Kurkov (see Section 4.2) is considered with a mesh containing 185 920 cells. Simulations are run for 200 time steps with the forward Euler global integration scheme and a CFL value of 0.5. Runs are performed on two CPU cores (Intel(R) Pentium(R) CPU B950). A summary of the different runs is given in Table 5.1. The EDM with kinetic limit is only slightly more expensive than the standard EDM. No-model simulations are performed with the reaction mechanism of Evans and Schexnayder (ES) (see Table 4.2) as well as with a single-step reaction (SSR) using the values for Arrhenius law's constants of Chandra Murty and Chakraborty [143] given in Subsection 5.1.4. Both mechanisms do result in a simulation time more than double than that of the EDM. This demonstrates the computational advantage of the latter model. It is as well shown that the SSR takes longer to finish 200 time steps than the more detailed mechanism of ES. With less species participating in the combustion process, the SSR makes the problem very stiff which results in even more subcycles to solve the chemical system. Care should therefore be taken in drawing conclusions solely based on the number of species and reactions prior a simulation.

Table 5.1: Computational cost comparison of the EDM and no-model approach.

model	**wall clock time**
EDM	22 m 14 s
EDM + kinetic limit	23 m 50 s
no-model, 7 sp, 8 reac modified Evans-Schexnayder	52 m 48 s
no-model, 4 sp, 1 reac	64 m 42 s

5.2 Study of the EDM with Generic Mixing-limited Scramjet Configurations

When given a scramjet combustor there are no guidelines or detailed information available in the literature which tells the user which setting of the EDM is the most appropriate. Some research mentions that the EDM requires tuning without providing the result of that process [80]. In some other cases the value for the A_{edm} constant is set to the standard value of 4 which is a setting derived from subsonic flame studies. There is a clear lack of knowledge about the use of the EDM for scramjet flows. In this section, in order to understand the effect of varying the A_{edm} constant on the supersonic combustion process, three generic scramjet test cases are selected: the experiment of Burrows and Kurkov, the DLR combustor and the HyShot II combustor. The aim is to provide the user, if possible, with an approach on how to select the model constant. The three scramjet configurations have been experimentally studied, providing evaluation data for the numerical simulation. Moreover, the configurations rely on fundamentally different injection mechanisms allowing to explore the EDM on a broader range of scramjets. The conditions inside the selected test cases are characteristic for a mixing-limited combustion process which motivates their selection for study of the EDM. Chapter 4 presented the validation study of the three scramjet combustors selected in this section in non-reacting (and reacting with no-model approach) conditions. This study ensured that the solver is correctly applied to the test cases in order to isolate as much as possible the effect of the EDM on the flow solution.

5.2.1 The experiment of Burrows and Kurkov

A detailed description of the test case was given in 4.2. The computational domain is shown again in Figure 5.3.

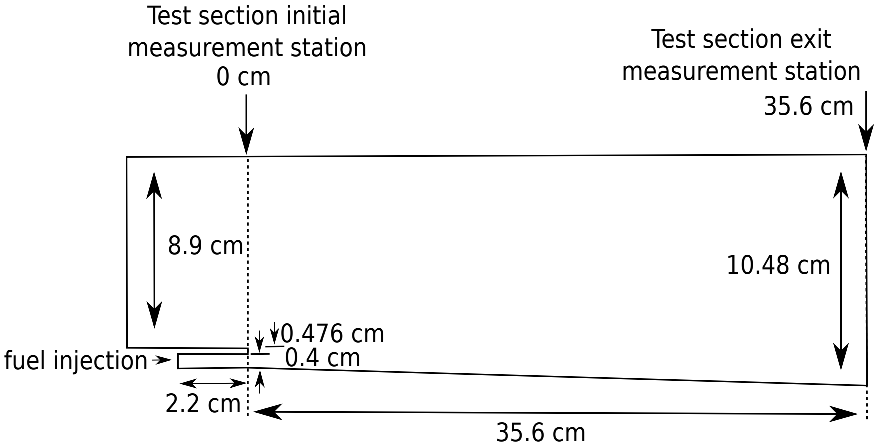

Figure 5.3: Schematic of the Burrows-Kurkov supersonic combustion experiment [217]. Not to scale.

The influence of the A_{edm} parameter (Equation 5.4) is assessed through comparison with the available experimental data measured at the exit plane (x= 35.6 cm) in Figures 5.4 to 5.7. The horizontal axis represents the vertical distance from the lower wall. Simulations have been performed with several values of the A_{edm}. No kinetic limit (Equation 5.15) has been used in these results. It will be shown hereafter that it did not influence the different profiles at the exit of the test section.

The effect of varying A_{edm} is observed in the profile of total temperature (T_0) in Figure 5.4. A higher peak value is coupled to a higher A_{edm} setting. This behavior is a direct consequence of the model (Equation 5.4) as more products are allowed to be formed, if enough reactants available, which in turn relates to an increased mean temperature. A value of 6 results in a peak value comparable to experiments, however the location is closer to the lower wall by $\approx$ 0.44 cm (4.2 % of the exit height). An increase of the standard setting of $A_{edm} = 4$ does not demonstrate drastic changes which suggests the presence of an asymptotic limit. This can be explained by the scarce presence of reactants, due to a lack of mixing, still available for reaction at that location predicted by the EDM (Figure 5.7, $y \approx 1.5$ cm). Experimentally this situation occurs further away from the wall. Adopting a lower value of the model constant ($A_{edm} = 1$) results in a consistent under-prediction of the peak total temperature. Regarding the profiles of Mach number, a higher A_{edm} setting is in better agreement with the experimental data. Overall a good match with experiment is observed for Mach number. The prediction obtained with finite-rate chemistry discussed in a previous step, denoted as "E-S" are as well shown in Figure 5.4. Regarding the Mach number exit profiles, the EDM results are in much better agreement with the experiment trace than finite rate result. In terms of the total temperature, the experimental peak location is more adequately predicted by the latter approach. The same observation is made with regard to the composition and is therefore not shown. Note however that thickness of the reaction zone as predicted by the EDM (A_{edm} = 4 , 6) appears to represent better the experimental trace. As pointed out in 5.1.2, results with EDM required much less computational effort compared to the finite-rate no-model approach. Starting from a converged solution it takes the EDM simulation about 16 h to advance one flow length in time. The same result with finite rate chemistry and the E-S reaction mechanism takes 81 h. One flow length is based on the distance from the entrance of the combustor and the mass flux weighted averaged velocity of the vitiated air just before the step and is about 0.21 ms. This comparison has been made on 72 CPU cores on the Tinaroo HPC system of the University of Queensland with a CFL setting of 0.5. Figure 5.5, showing pitot pressure (p_{pitot}) and mass flow, confirms the need for a higher value of the EDM constant in order to get an improved agreement with experiments. The influence is, however, contained to the region closer to the wall ($y < 2$ cm).

Figures 5.6 and 5.7 show the exit profiles of species mole fractions. The observations on the effect of A_{edm} on the H_2O mole fraction are in agreement with the total temperature curves discussed previously. A higher setting predicts peak values comparable to experiment but an offset in peak position is present. The different EDM results under-predict the penetration depth of hydrogen into the vitiated airflow. The

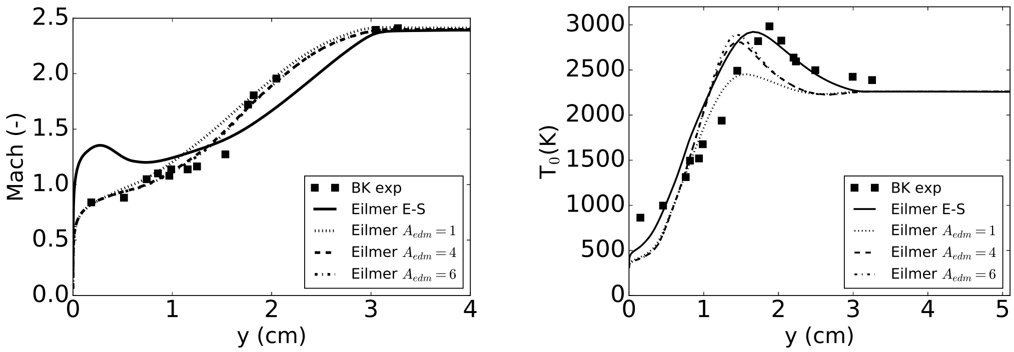

(a) (b)

Figure 5.4: Predictions of Mach (a) and total temperature (b) at x=35.6 cm obtained with EDM compared with experimental values of Burrows and Kurkov.

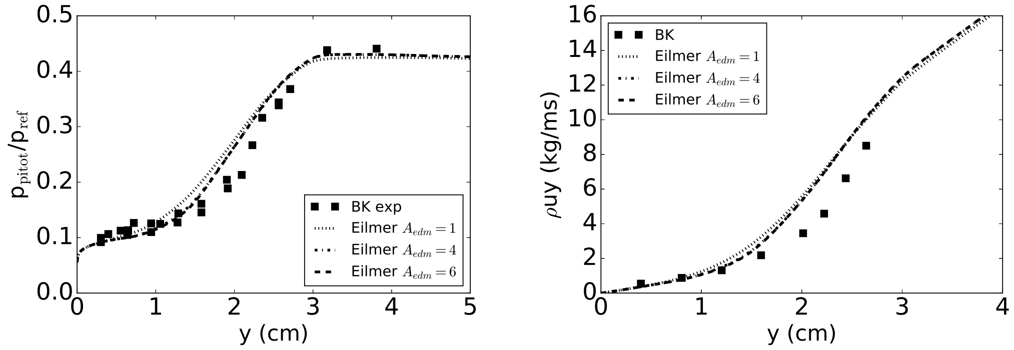

(a) (b)

Figure 5.5: Predictions of pitot pressure (a) and mass flow (b) at x=35.6 cm obtained with EDM compared with experimental values of Burrows and Kurkov. P_{ref}=17.1e5 Pa

X_{O_2} profiles show that the experimental slope is better captured by a higher value of the EDM constant. Based on the current comparisons, the EDM is capable of giving reasonable results at the exit of the combustor.

Overall the best results with EDM are obtained by prescribing $A_{edm} = 6$. The explanation for this can be understood by studying the contour of product mass fraction $Y_P = Y_{H_2O}$ (or mean temperature) and ω. Figure 5.8 shows the product mass fraction contour predicted by the EDM (upper representation). The contour is in accordance with what would be obtained with a single-step reaction (see [127]) except for the fact that combustion occurs very close to the injection point. This behavior, which is

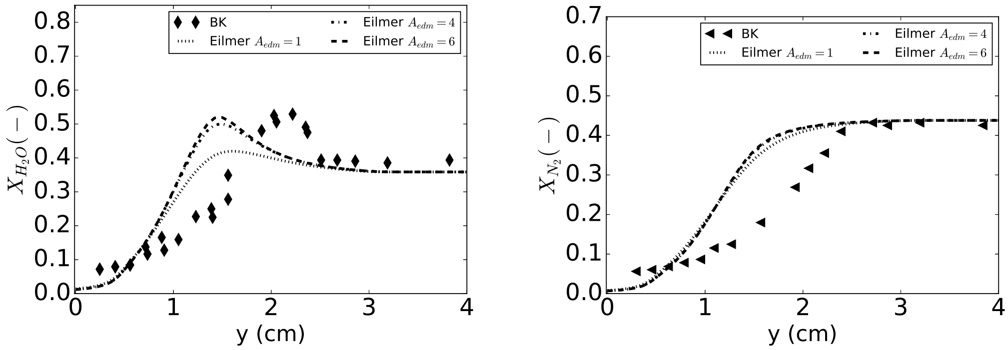

(a) (b)

Figure 5.6: Predictions of H_2O (a) and N_2 (b) mole fraction at x=35.6 cm obtained with EDM compared with experimental values of Burrows and Kurkov.

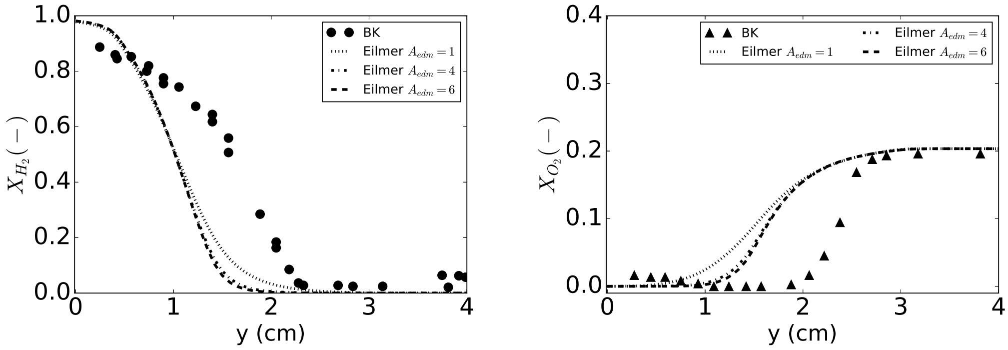

(a) (b)

Figure 5.7: Predictions of H_2 (a) and O_2 (b) mole fraction at x=35.6 cm obtained with EDM compared with experimental values of Burrows and Kurkov.

unphysical, is expected as the EDM allows products to be formed as soon as fuel and oxidizer mix. Introducing the kinetic limit (Equation 5.15) does mitigate this effect as can be seen in the bottom contour. It was mentioned earlier that applying this limit does not affect the CFD predictions at the exit of the combustor. This statement is confirmed by observing the profiles of Mach number and total temperature in Figure 5.9. The same observations are valid for the other quantities and are therefore not shown in this work. The kinetic limit only affects a very small region near the injector and the length of the combustor is long enough so as to allow the EDM to compensate this localized effect near the injector. The minimal influence of the kinetic limit is explained by the high vitiated air-stream temperature. In the experiments, ignition onset is indicated by a rise in wall static pressure 18 cm downstream the injection point [100]. With the kinetic limit this occurs at $\approx$ 1 cm downstream the same injection point. Figure 5.8 demonstrates that the kinetic limit is perhaps not the most adequate way of introducing an ignition delay in a shear layer environment with high free stream temperature. A possible approach that could be explored is to not allow reactions to occurr when the mass fraction of fuel is above a certain threshold value. This would allow for a longer induction zone than presently obtained with a kinetic limit. It will be shown in 5.2.1 that the use of the EDM can be greatly improved with a simple approach.

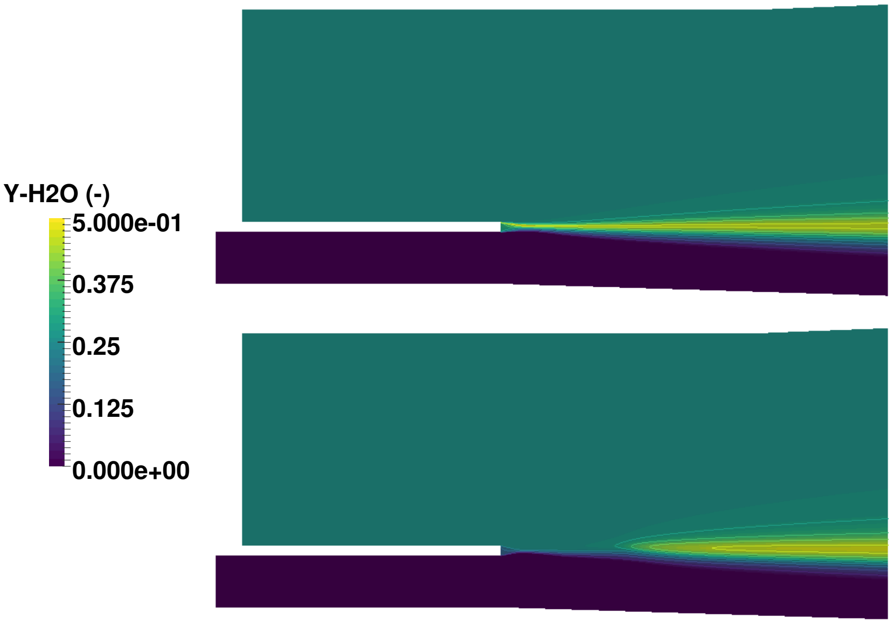

Figure 5.8: Mass fraction contours of H_2O close to the injection point with from top to bottom: EDM, EDM with kinetic limit.

The EDM assumes that a high rate of mixing is characterized by a high value of ω. This assumption is not valid near the injector where no combustion is taking place but where very high values of ω are predicted by the turbulence model in Figure 5.10. Moving further away from this point a decrease in ω is observed which is coupled to a decay in the strength of the turbulence inside the combustor. The high local values in the shear layer near the injector is the cause for an early product formation given the direct influence of ω in Equation 5.4 and the availability of both fuel and oxidizer. In reality the combustion should start after some ignition delay, i.e. kinetically limited. The location for ignition onset is downstream of the injection point where the value

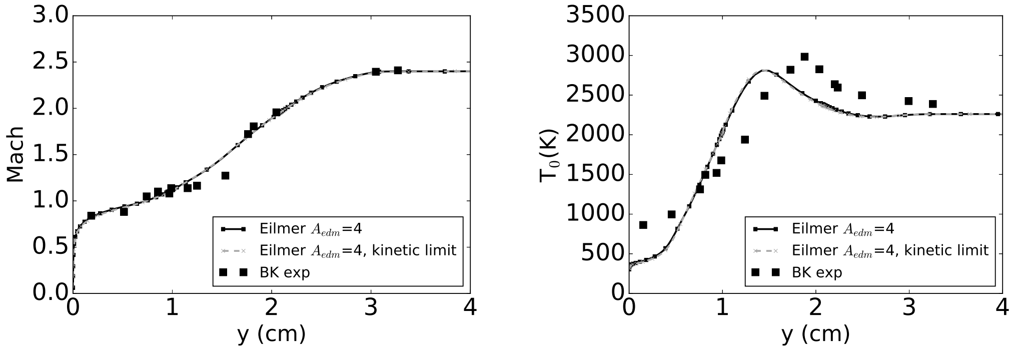

(a) (b)

Figure 5.9: Comparison of EDM with and without kinetic limit on Mach (a) and total temperature (b) at the exit of the combustor (x = 35.6 cm)

of omega decreases. Consequently, an increase in the A_{edm} constant is required as a compensation. Values much higher than 6 have no strong influence as there are not enough reactants at stochiometric ratio left to burn at the interface between the fuel stream and the vitiated air stream.

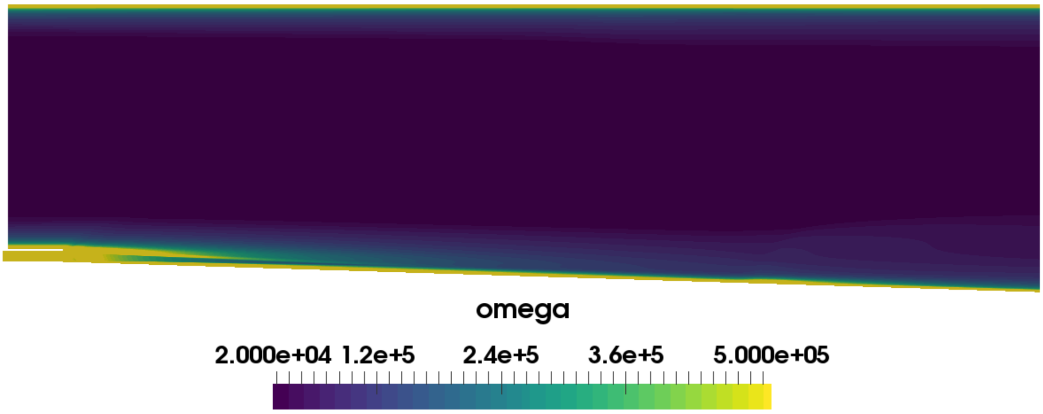

Figure 5.10: Contour of ω for the experiment of Burrows and Kurkov

Ignition Delay with Zonal EDM

The reference work of Burrow and Kurkov [217] mentions that it is possible to rely on a one-dimensional kinetics program to obtain an estimate of the expected ignition delay. Such an approach can prove very beneficial for the use of the EDM which has shown to lack the ability to account for ignition delay in a parallel injection setting with high free stream temperatures (above the autoignition temperature of hydrogen).

Based on a freestream temperature of 1270 K, an H_2/O_2 ratio of 0.013 and a free stream mixture containing N_2, O_2, H_2O and NO, an induction time (or ignition delay or runaway length) of 90e-6 s was obtained [217] with the one-dimensional kinetics program developed by Bittker and Scullin [234]. Using an averaged vitiated air stream velocity at the entrance of the combustor of 1689 m/s (obtained from CFD), a flow length equal to 2.1e-4 s is obtained. The latter value yields an estimate of a fluid element residence time inside the combustor. From this value and the previously calculated induction time, the ignition location inside the combustor is estimated to be at x = 0.153 m. Note that this approach only gives a rough estimate of the induction process. It does for example not account for the low fuel stream temperature near the wall which can have a significant influence as indicated by Burrows and Kurkov [217]. Nevertheless, this information can be relied on for a better use of the EDM. A simulation has been performed relying on the above estimate where no combustion is allowed at any axial location before that point, hence the terminology "zone". Recall that experimentally [100] an ignition delay is observed between 18 (wall pressure trace) and 25 cm (photographs of OH radiation). The no-model simulation with modified Evans-Schexnayder (E-S) mechanism predicted an onset of ignition at a position of 23 cm. Note that it is also possible to obtain an estimate of the ignition delay from a correlation provided by Pergament [235]:

$$\tau_R = \frac{8 \times 10^{-3}}{p} e^{9600/T_o} \tag{5.18}$$

where T_o is an initial temperature and p, the ambient pressure prior to reaction. The formulation is obtained by data correlation for equivalence ratio's (ER) between 0.4 and 2.0. As the present ER is 0.4122, the formula could be used and with a pressure of 1 atm and T_o of 1270 K an ignition delay of 8.77e-5 s is obtained. Consequently, the onset of ignition is computed at 14.87 cm which is very close from the 15.3 cm previously estimated. Only simulation with the latter value have been considered in this work. Note the definition of the ER (ϕ) for hydrogen as [137]

$$\phi = \frac{8\dot{m}_{H_2}}{\dot{m}_{O_2}} \tag{5.19}$$

The above formula represents the ratio between the actual amount of hydrogen injected and the oxygen supplied divided by the stochiometric ratio. The latter equals 8 for H_2/O_2 combustion.

Figure 5.11 compares the different approaches with experimental values of Mach number and total temperature (T_0) at the combustor exit. The classical EDM is shown for a constant value A_{edm} = 6 following the parametric study discussed previously. The zonal EDM is denoted as "zone 15.3 cm". The profiles of T_0 show that the use of the EDM can be greatly improved with an estimate of ignition onset. A very good agreement with experimental T_0 values is observed near the wall with the zonal use of the EDM. The E-S does perform better than the classic EDM but slightly less than the zonal EDM. This is explained by the fact that the combustion process is kinetically limited until the onset of ignition whereafter it becomes mixing limited. The same observation was made by Kirchhartz et al. [236] in an axisymmetric scramjet combustor with similar fuel injection mechanism. The EDM assumes a mixing limited combustion and is therefore more appropriate once the flow is ignited. In terms of the Mach number profile, a lesser agreement with experimental data is observed for the zonal EDM compared to the curve without. Nevertheless, it remains superior to the E-S CFD prediction in the vicinity of the wall. Figure 5.12 shows the resulting Mach number flow field with the different approaches. The onset of ignition is indicated by a combustion induced shock wave in the bottom two contours. The flow field of the standard EDM is very similar to that of a single-step reaction and does not have any downstream shocks. If the combustor would be longer, the latter approach would not be able to account for possible interactions between reflected shocks and the reaction zone. It is therefore not recommended for use in the design of similar geometries, i.e. parallel injection of fuel with respect to air stream. Because of the difference in induction zone between E-S and the zonal EDM, the possible downstream shock reflections would occur at different locations. A subsonic zone is clearly observed near the ignition location in the case of the zonal EDM. It is coupled with a small recirculation zone and induced by the strength of the combustion. Similar observations have been reported in the literature by Engblom et al. [112] with the temperature contour (Figure 4, p11) and by Bhagwandin et al. [127] with the total temperature. The temperature contours obtained in this work are given in Figure A.1 of Appendix A.1. The E-S does predict as well a small subsonic zone (without recirculation).

In conclusion, even though the estimated induction length from the one-dimensional program does not agree with experimental observations [1], it proves to be very useful information for an improved use of the EDM. The observations in Figure 5.11 demon-

---

[1] It must be noted that the BK test case is very sensitive to the selected turbulence model [112], inflow conditions [112] and reaction mechanism [127]. Moreover, there is some uncertainty regarding the onset of ignition.

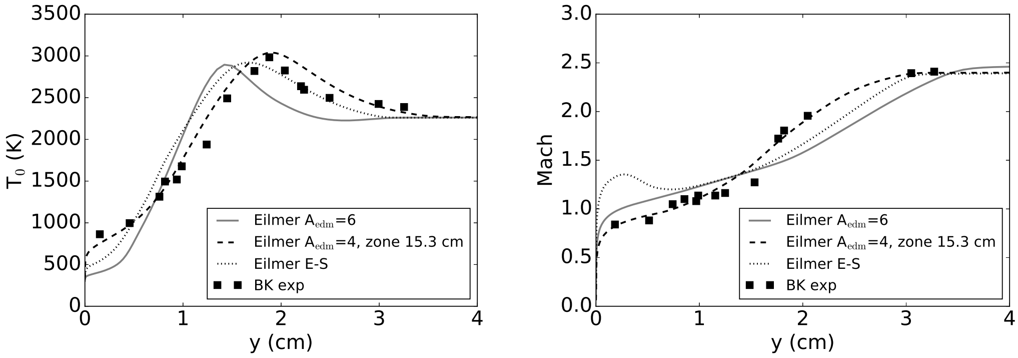

(a) (b)

Figure 5.11: Comparison of EDM with and without zone on total temperature (a) and Mach number (b) at the exit of the combustor (x = 35.6 cm). E-S = Evans-Schexnayder

strate that the zonal EDM provides a good estimate of the reaction zone. Therefore, relying on an ignition delay estimate proves to be a viable approach to design scramjet combustors with fuel injection parallel to the air stream using the EDM approach.

5.2.2 The DLR combustor experiment

A detailed description of the test case was given in 4.3. The computational domain is shown again in Figure 5.13.

The reacting flow field is now considered. Simulations with a no-model approach, for comparison purposes, have not been considered for this test case in the present work. It was demonstrated by Gao et al. [144] and Potturi et al. [221] that the temperature flow field is not captured accurately enough without TCI. As the free stream temperature (Table 4.3) is too low to allow auto-ignition, experimentally some pre-burned hydrogen is injected to ignite the flow. Numerically some "tricks" exist to ignite the flow field such as the definition of a zone where hot products are introduced [115]. Such an approach is however not required for the standard EDM as the model does not depend on the temperature (see Equation 5.4).

Firstly the effect of introducing a kinetic limit on the EDM reaction rate has been explored. Figure 5.14 shows its influence compared with some of the available experimental data for the EDM setting, $A_{\mathrm{edm}} = 4$, and a turbulent setting in accordance with Gao et al. [144] of $Pr_t = Sc_t = 0.9$. Simulations with kinetic limit were initiated from the converged EDM result without limit as to avoid the need for a source of ignition

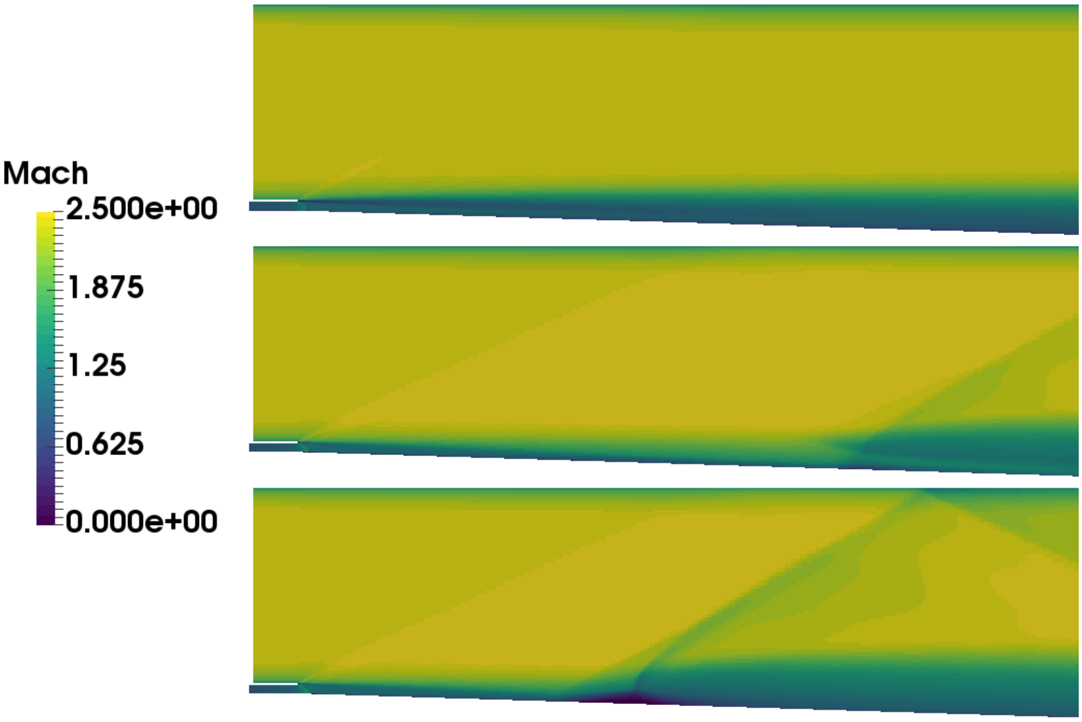

Figure 5.12: Mach number contour with from top to bottom: EDM (A_{edm} = 6), E-S, EDM zone (A_{edm} = 4)

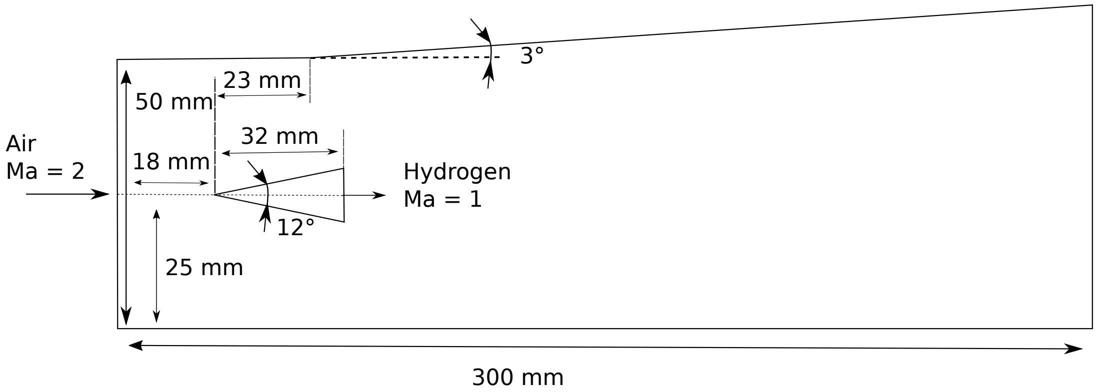

Figure 5.13: Schematic of the DLR combustor experiment [98]. Not to scale.

given the low free-stream temperatures.

Profiles of axial velocity did not show significant differences however the static temperature profiles did. This behavior can be observed in Figure 5.14 (b) where the axial velocity is presented at the second measurement location of Figure 5.15 (x = 111 mm). Profiles of axial velocity and temperature at other locations not discussed here are given in Appendix A.2, Figure A.4. Applying the kinetic limit mostly affected the local minimum in axial velocity between the two shear layers but its position is not influenced by the modeling option. According to the experimental measurements, the minimum around 180 m/s with kinetic limit is an under-prediction of the expected value. On the other hand, the minimum value without any limiting factor slightly over-predicts the experimental observations. Despite of having similar minimum locations, the velocity profiles of Eilmer are not aligned with experimental trend. It must be noted that even the more advanced CFD models [97, 99, 237] do not yield a good agreement with this particular set of experimental data which demonstrates the challenging nature of the test case.

The numerical results of the axial temperature profile are strongly influenced by the kinetic limit. Predictions at the first measurement station shown in Figure 5.15 are presented in Figure 5.14 (a). Applying the kinetic limit does suppress combustion in the lower recirculation region just downstream of the strut (see bottom of Figure 5.15). This in turn results in a single temperature peak and is not in agreement with the experimental data. The observation is explained by the low free stream temperature and the asymmetry in the geometry. The temperature contour (Figure 5.15) shows the extent of the supression. The EDM results in peak temperature locations similar

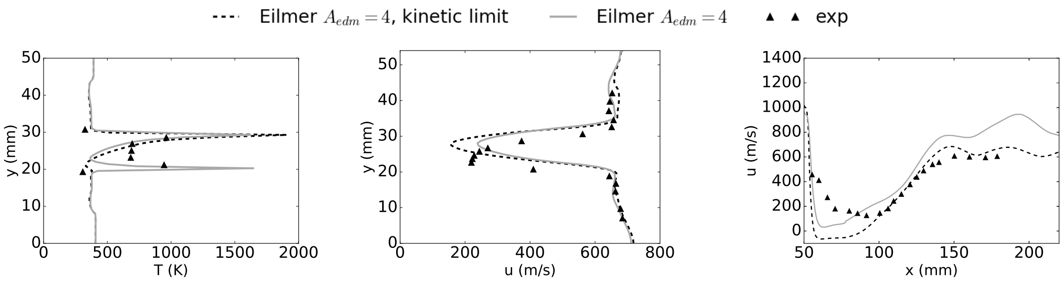

(a) (b) (c)

Figure 5.14: Effect of applying the kinetic limit on the temperature at axial location 1 (a), the velocity at axial location 2 (b), the centerline velocity (c). $A_{edm} = 4$, $Pr_t = Sc_t = 0.9$.

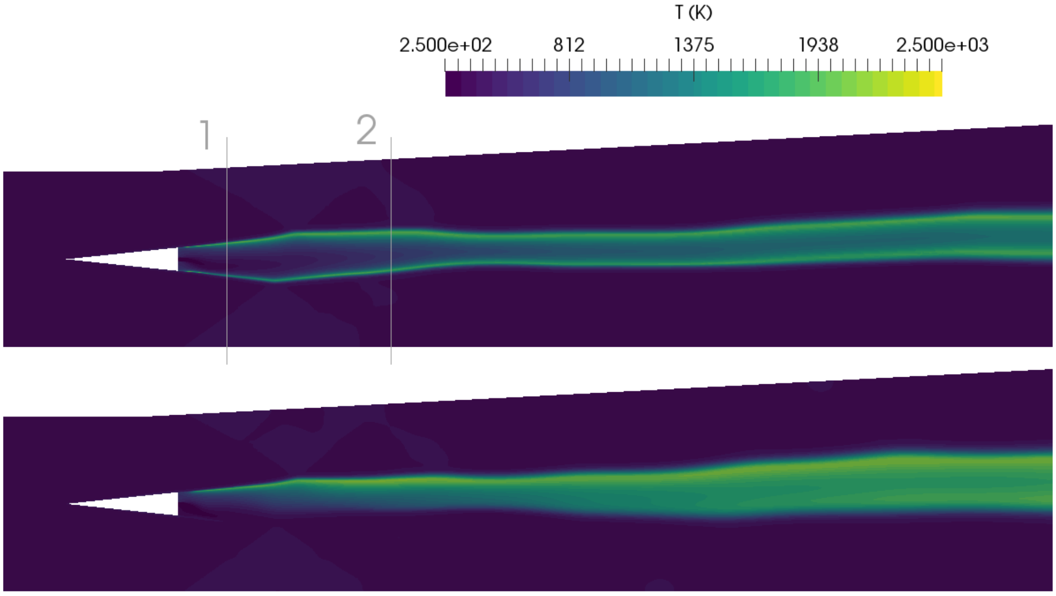

Figure 5.15: Temperature contour ($A_{edm} = 4$, $Pr_t = Sc_t = 0.9$) with indication of the axial measurement locations considered in the present work. Top: EDM, Bottom: EDM with kinetic limit.

to experiments. The structure of the recirculation regions is however different in the numerical simulation. Figure 5.14 (c) shows the centerline velocity. As mentioned above, the structure of the recirculation regions behind the strut is different depending on whether EDM is used with a kinetic limit or not. The upper recirculation zone does extend down to the centerline which is not experimentally observed, neither predicted by the standard EDM. Further downstream inside the combustor, the profile of velocity of the EDM with kinetic limit is in better agreement with the experimental data than the other profiles. Note the difference with the experiment of Burrows and Kurkov (Figure 5.8) where the kinetic limit had a very limited influence on the result due to the high free stream temperature. Recall that the kinetic limit relies on a single-step reaction with a no-model combustion description. The methodology therefore considers a very limited number of species. In the experiment of Burrows and Kurkov it was observed that, once the static temperature of the air stream exceeds the autoignition value of the fuel, combustion occurs almost instantaneously with the single-step reaction. Instead, the DLR combustor has a very cold inflow air stream temperature which result in a suppressed combustion region due to the effect of the kinetic limit.

The influence on the kinetic limit is further evaluated with the combustion efficiency along the combustor which is a parameter of interest in scramjet design. Figure 5.16 shows the profiles of the combustion efficiency. Computing the latter value with the formula adopted by Kim et al. [218], i.e. Equation 4.1, does result in negative values near the point of injection. This is due to the presence of the recirculation regions behind the strut where injected hydrogen is present, hence a larger mass fraction of fuel than injected is found at those axial locations. Other formulations exist for the combustion efficiency which relies on the amount of water vapour formed and is e.g. used by Moura et al. [238]:

$$\eta_c = \frac{0.1119\dot{m}_{\mathrm{H_2O}}}{\dot{m}_{\mathrm{H_2,injected}}} \tag{5.20}$$

The resulting profile is as well shown in Figure 5.16 with values remaining positive along the combustor. At the exit, x = 300 mm, the formulations used by Kim et al. [218] and Moura et al. [238] differ by only ≈ 3 %. This indicates that both definitions could be applied for design assessments. Equation 5.20 is considered in all of the following discussions and graphical representations of the combustion efficiency. Note that the water vapour mass flow rate from the vitiated air stream, $\dot{m}_{\mathrm{H_2O},\infty}$ = 1.17 kg/s, has to be acounted for in the computation. This means that its value must be substracted from the computed mass flux in every plane to obtain the amount of H_2O formed as the result of combustion. Applying the kinetic limit does result in a lower combustion efficiency near the strut and is in accordance with the temperature contour of Figure 5.15. Nevertheless, at the exit of the combustor the difference with the standard EDM is only about 2 %. This can be explained by a lack of mixing between the hydrogen stream and air stream along the combustor. By the end of the domain, almost all the fuel and oxidizer that can mix have been consumed. In conclusion, both approaches provide a similar answer to the question “ How much do I burn inside the combustor" and could therefore be considered. The lower wall pressure trace is another parameter of interest in scramjet design and is given in Figure A.5 of Appendix A.2. It is shown that peak pressure locations are better captured whitout kinetic limit and is a direct consequence of the suppressed combustion near the strut observed previously. Given the fact that the approach with kinetic limit did not capture a double temperature peak near the point of injection, the standard EDM is considered for further simulations.

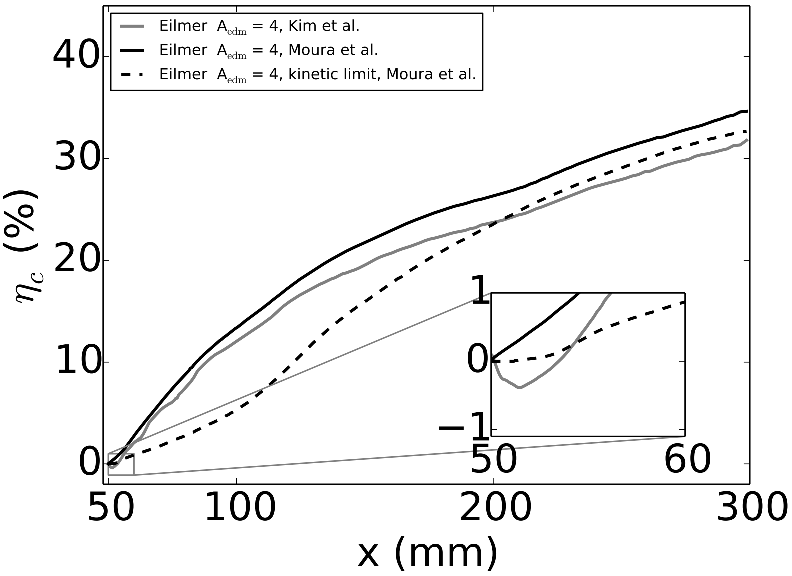

Figure 5.16: Combustion efficiency for the DLR combustor experiment of Waidmann et al. [98] with different formulations and effect of kinetic limit

Secondly, the most appropriate setting for the A_{edm} constant is now investigated. From the observations in the Burrows-Kurkov test case, the configuration is expected to have very high values of ω in the shear layers induced by the strut with decreasing strength towards the end of the combustor. Figure 5.17 confirms this statement. Moreover, the higher ω values are as well present near the fuel injector. Experimentally, the flame is located in the vicinity of the injection point behind the strut. In contrast to Burrows-Kurkov, there is no significant runaway length. In terms of the EDM, given the high ω values behind the strut, a relatively low value of A_{edm} should be an appropriate choice. A too low value would however negatively influence the combustion zone further downstream characterized by lower ω values.

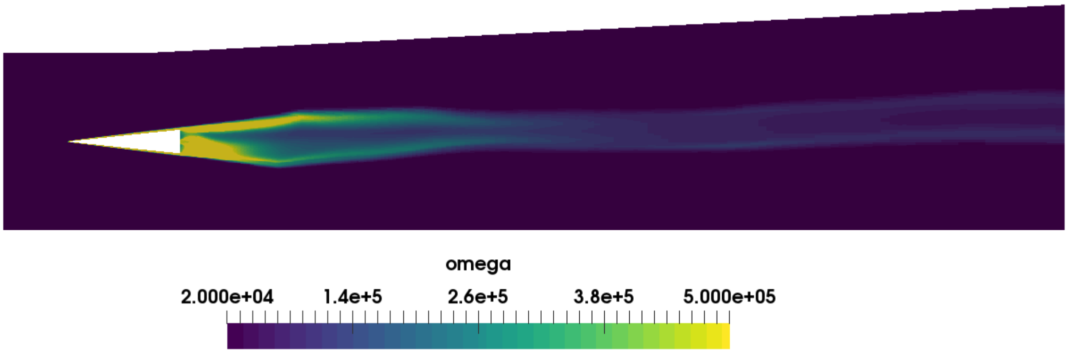

Figure 5.17: Contour of ω for the DLR combustor experiment of Waidmann et al. [98]

Figure 5.18 shows the mean temperature at locations 1 and 2 depicted in Figure 5.15 as well as along the lower combustor wall obtained with the same three settings of the EDM as in Burrows-Kurkov, namely A_{edm}= 1, 4 and 6. Figure 5.19 presents the velocity at the same locations 1 and 2 as above as well as the centerline velocity. In this discussion, turbulence settings are set to $Pr_t = Sc_t = 0.9$. Profiles for other quantities not discussed here, and for which experimental data is avalaible, are given in Figure A.6 of Appendix A.2. The influence of A_{edm} on the velocity is very limited: minimal at the axial measurement locations and slightly more pronounced along the centerline. There is an influence on the size of the upper recirculation zone directly behind the strut. Regarding the lower wall pressure, a different EDM setting does not strongly affect the profile. This can be understood from the fact that the width of the reaction zone along the combustor is not influenced by the combustion model which is shown in the temperature profiles. It is however influenced by the interaction between the shock waves and the turbulent shear layers, and consequently by the turbulence model. The wall pressure trends are similar to some of the results reported in the literature by Potturi and Edwards [99]. The width of the reaction zone predicted by Eilmer with different EDM settings is in good agreement with the experiment.

At the first measurement location, the mean temperature follows the experimental trend well. Peak values in the two shear layers are strongly influenced by the A_{edm} setting. It is difficult to state which setting is more appropriate as not enough experimental data points are available in the shear layer to shed light on the observed peak temperature values. It can be inferred that a value for A_{edm} higher than 1 and below 4 is required. Adopting $A_{edm} = 1$ results in an under-prediction of the peak mean temperature in the lower shear layer at the first measurement location. At the second

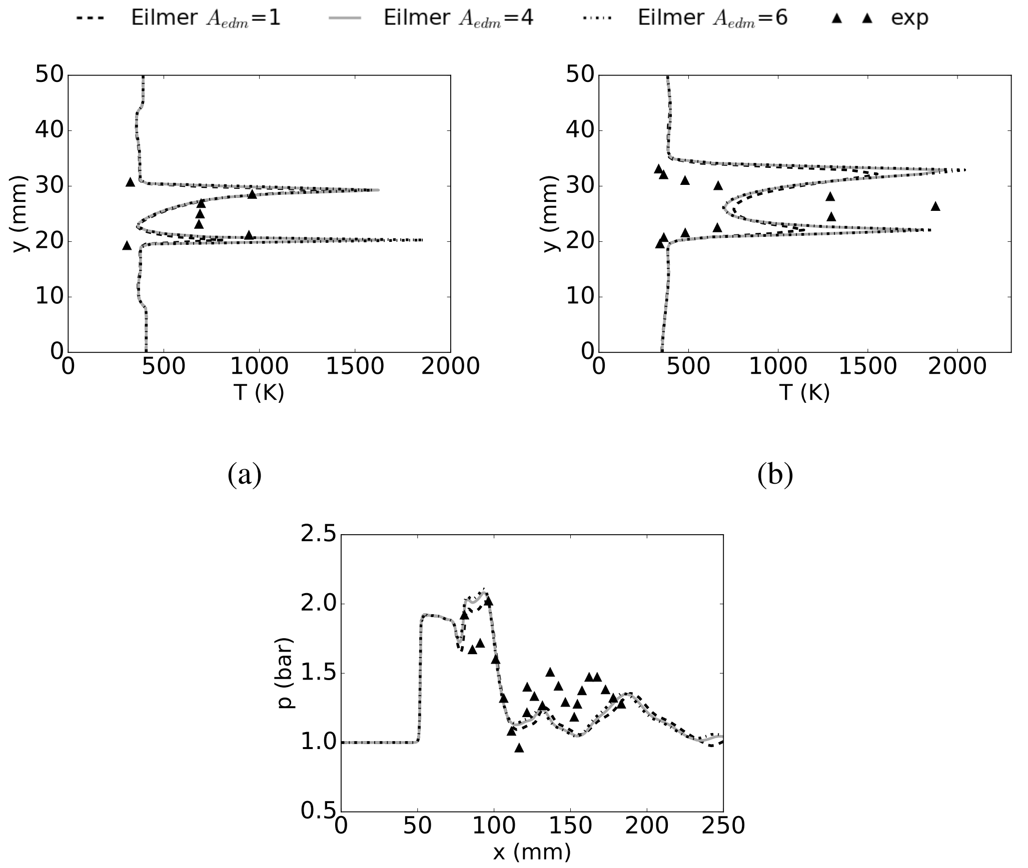

(a)

(b)

(c)

Figure 5.18: Effect of the model constant A_{edm} on the temperature at axial locations 1 (a) and 2 (b), and on the wall pressure (c). Results obtained with $Pr_t = Sc_t = 0.9$.

location the same effect of the EDM setting is observed: higher value coupled with increased peak temperature. In order to match the experimental peak, A_{edm} should be set to ≈ 4. However, a double peak profile is predicted by the CFD which is not experimentally observed. Ignition of fresh gases occurs at the interface between the fuel rich wake and the air stream [98] which is correctly predicted by the EDM in the vicinity of the strut. This behavior is however sustained by the model in the downstream region with similar observations reported in the literature for different scramjet configurations [143, 80, 171] (see temperature contours). There is a lack of heat conduction and / or species diffusion toward the center of the geometry. Adapting the values of Pr_t and Sc_t could improve the predictions. However, in contrast to the configurations of Burrows-Kurkov, a stronger coupling between the turbulence and the combustion model is observed, i.e. it is difficult to uncouple the settings of the turbulence model from the ones of the EDM. A sensitivity study to the values of Pr_t, Sc_t and A_{edm} has been performed. It was however not possible to find a conclusive setting which agrees well with experimental trends at all locations along the combustor. A few results of this study are given in Appendix A.2, Figures A.7 and A.8. The CFD predictions of Oevermann [111] with a flamelet TCI model are as well displayed for reference. Further investigations about the above mentioned coupling are out of the scope of the present work where the aim is to identify the most appropriate use of the EDM by understanding its relation to the physics in different scramjet configurations. Nevertheless, the observations are in accordance with the above stated expectations of the EDM: in the vicinity of the strut (a region with higher values of ω) a lower A_{edm} setting is more appropriate while further away (a region with lower values of ω) a higher A_{edm} setting performs better. Based on the comparison with experimental data, overall the standard setting of 4 is a good compromise for the DLR combustor.

Figure 5.20 presents the combustion efficiency, based on formed water vapour (Equation 5.20), along the DLR combustor predicted with the different A_{edm} settings. The latter parameter does not appear to have a significant influence on this quantity integrated at each axial location. This is especially true for the settings of 4 and 6 which is in accordance with previous observations in Figures 5.18 and 5.19. A difference in combustion efficiency at the exit plane of 5 % is obtained between $A_{edm} = 1$ and $A_{edm} = 6$. The trace of combustion efficiency confirms the overall appropriateness of the standard EDM setting. If the aim of the designer is to improve the combustion efficiency inside the combustor, the EDM could be relied on with $A_{edm} = 4$.

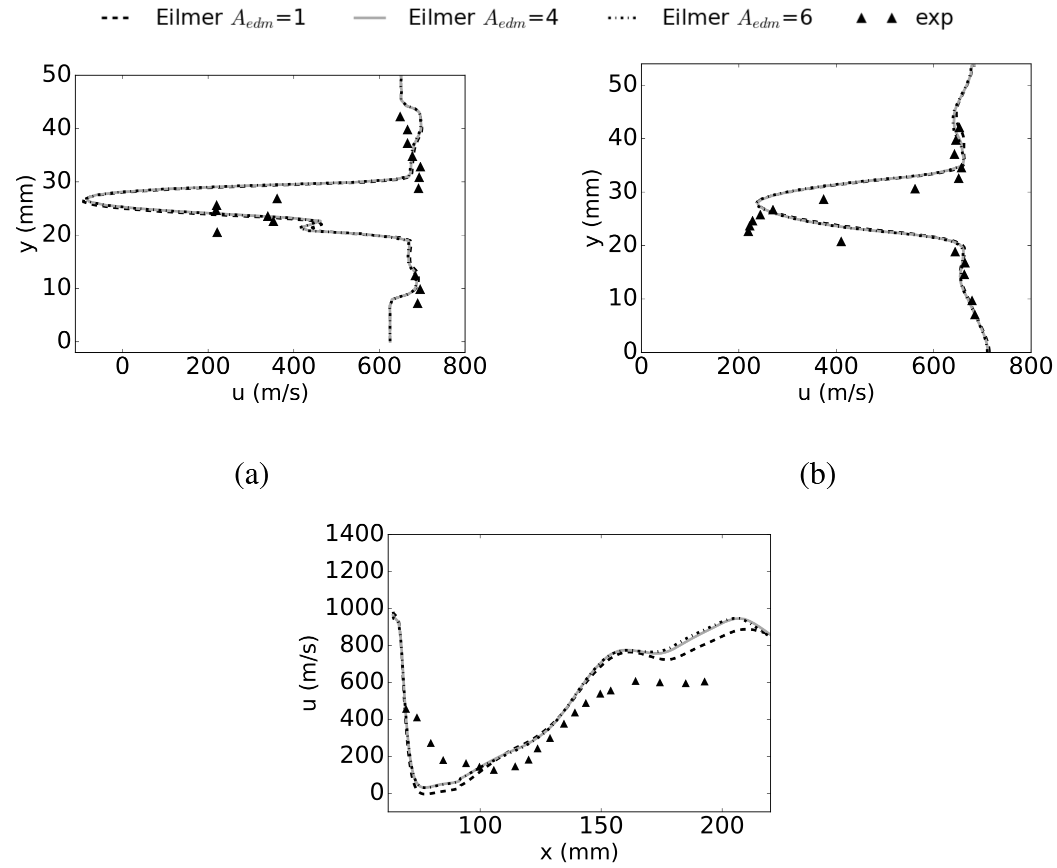

(a)

(b)

(c)

Figure 5.19: Effect of the model constant A_{edm} on the velocity at axial locations 1 (a) and 2 (b), and on the centerline velocity (c). Results obtained with $Pr_t = Sc_t = 0.9$.

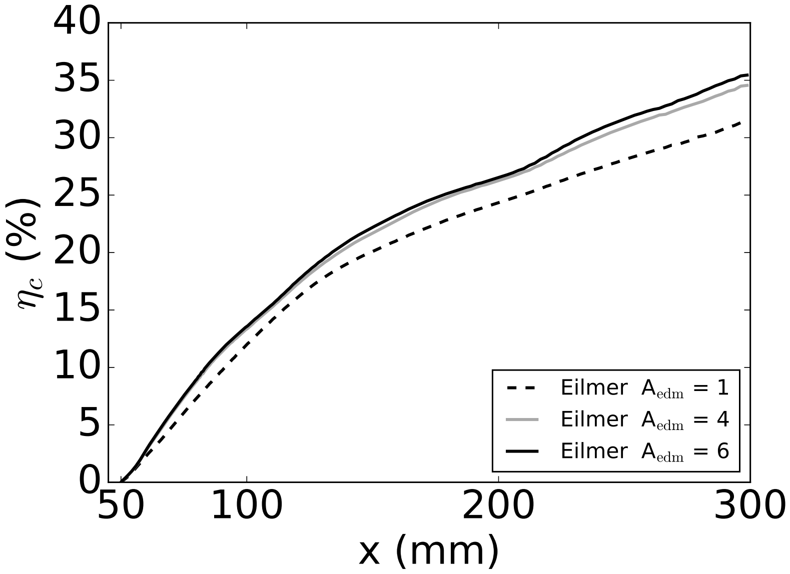

Figure 5.20: Effect of the model constant A_{edm} on the combustion efficiency for the DLR combustor experiment of Waidmann et al. [98] with $Pr_t = Sc_t = 0.9$.

Based on the numerical results of the DLR combustor with the EDM a suggestion for a modification could be made. Namely, the introduction of a zonal dependency of the A_{edm} value. Close to the point of injection a lower ($\approx$ 1-4) setting of the A_{edm} constant could be used and further downstream a higher value ($>$ 4). Waidmann et al. [98] discussed the main features inside a configuration such as the DLR combustor. The authors explain the presence of three distinct zones dominated by fundamentally different physics and is shown in Figure 5.21. Firstly there is an induction zone, just behind the strut, where the combustion is dominated by a diffusion process between the injected fuel and vitiated air stream. It is followed by a transitional zone where large scale structures are developing. These structures originate in the shear layers between the air and fuel stream due to the velocity difference and vorticity is produced. They are responsible for the entrainment of the oxidizer inside the reaction zone. In this zone, the combustion is dominated by convection instead of diffusion. Further downstream, a third zone can be discerned where the turbulent eddies break down and the flow becomes more chaotic. Such information can be used for a better application of the EDM and the idea of a zonal EDM could relate to the different flow characteristics discussed in Figure 5.21. The extend of the three zones would have to be estimated and the A_{edm} setting adapted. It was shown in the experiment of Burrows and Kurkov that even an estimate of the ignition delay is good enough in order to draw design conclusions with the EDM. The same comment can be made for the DLR combustor. Moreover, the zonal approach could as well be applied to the values of $\mathrm{Pr_t}$ and $\mathrm{Sc_t}$. Another possibility would consist of a variable $\mathrm{Pr_t}$ and $\mathrm{Sc_t}$ formulation [191, 192] which would require two extra transport equations. This would increase the computational cost but could be viable option in conjunction with the EDM as the advantage of a less stiff set of governing equations can still be exploited. The idea of a zonal modification should be valid for similar type of configuration. However, such an approach has to be further explored before drawing definitive conclusions on its feasibility and could be the subject of future work. The JAXA combustor [139, 156] could be a good test case for study of the EDM as it includes a strut and has proven to have a mixing-limited mode of combustion. Note that RANS might not be the most appropriate description for the turbulence inside the second (and third zone) in Figure 5.21 as capturing accurately such vortical structures would require LES instead.

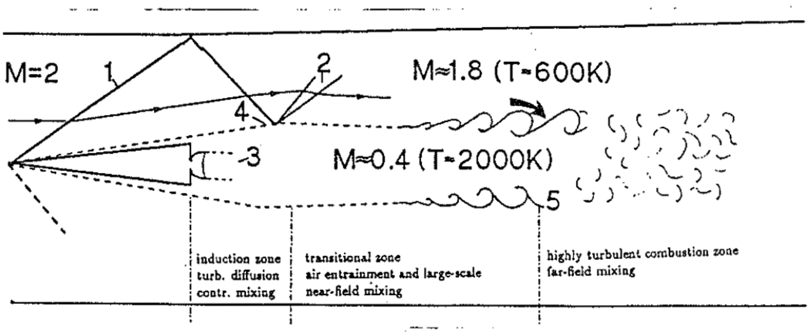

Figure 5.21: Sketch of the flow field inside the DLR combustor experiment of Waidmann et al. [98]. 1: attached shock, 2: expansion, 3: sonic hydrogen jet, 4: shear layer reflection, 5: uniform velocity in both zones.

5.2.3 The HyShot II Combustor (HEG ground test)

A detailed description of the test case was given in 4.4. The computational domain is shown again in Figure 5.22. Reacting simulations of the HyShot II combustor have been performed with the EDM. It was not possible to converge toward a steady-state. It is likely there is inherent unsteadiness in the flow that has been resolved by the time-accurate explicit stepping, hence it is an unsteady (URANS) simulation [239, 240]. URANS requires small enough time steps in order to capture variations in mean flow properties due to the largest turbulent fluctuations. Karl et al. [56] reported a study

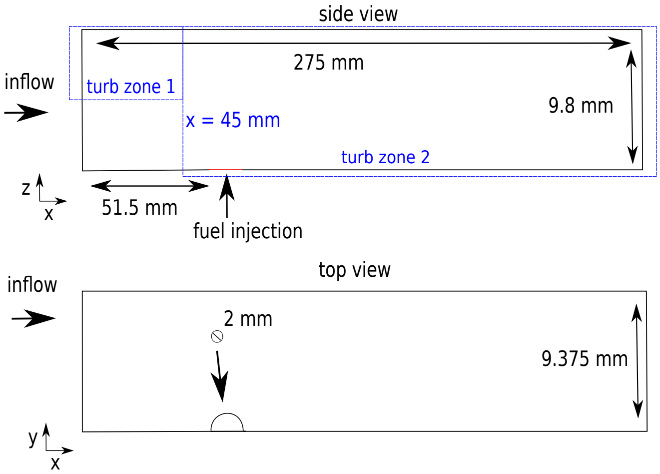

Figure 5.22: Computational domain of the HyShot II combustor. Not to scale.

of the unsteady shock train inside the HyShot II combustor. The latter work applied URANS with a second order accurate temporal discretization scheme and physical time steps of 1e-7s. The predictor-corrector scheme used in Eilmer is second order accurate [213] and time steps in current HyShot simulations were below 4e-9 s. It can therefore be concluded that URANS is performed in the present work, hence explaining the unsteadiness of the solutions. Note that the non-reacting simulations in Subsection 4.4.3 did converge to a steady state. It can therefore be inferred that the unsteadiness originates due to the injection of fuel (shear driven instability) and / or the combustion process.

In order to compare the URANS solutions to the experimental data, time-averaging is applied. Figures 5.23 and 5.24 present the result of this averaging process for the pressure along the cowl and injector walls at the symmetry plane y = 9.375 mm. The simulations are presented for an A_{edm} = 4 setting. The arrow indicates the point of fuel injection. The experimental data is obtained by averaging nine HEG measurements with an ER between 0.266 and 0.351 [86]. Three curves are presented taken at three distinct times within one flow length (t1 = start,t2 = center and t3 = end) as well as the averaged trace. As expected, the latter curve lies between the former three time instants demonstrating the adequateness of the sampling interval. Overall a good agreement with experimental measurements is observed, especially for the cowl side. Looking at the instantaneous pressures, the unsteady behavior is visible after ≈ 100 mm. Figure 5.25 shows an instantaneous contour of hydrogen mass fraction at the injector symmetry plane. Upon injection, the hydrogen jet (centered at x = 52.5 mm) induces a separation of the upstream boundary layer. A portion of the injected hydrogen can therefore penetrate this recirculation region (see ≈ x = 50 mm). The unsteady character of the flow is clearly visible from the wavy variation in this mean quantity downstream. Similarly to the DLR combustor experiment (see Figure 5.21), the combustion zone is characterized by an induction region where the combustion is diffusion dominated. After x ≈ 90 mm large turbulent structures are able to develop and the combustion becomes convection dominated. This explains the character of the unsteady wall pressure traces discussed previously.

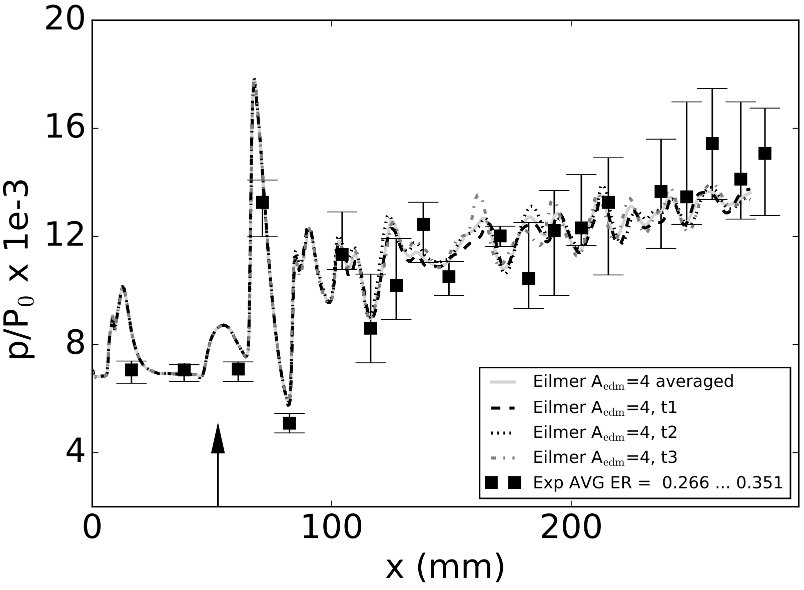

Figure 5.23: Instantaneous and time averaged pressure traces along the cowl wall at y = 9.375 mm with A_{edm} = 4 and P_0 = 17.73 MPa.

The effect of varying the value of A_{edm} on the wall pressure is investigated in Figures 5.26 and 5.27. Increasing the value does result in increased pressure values and an overall vertical shift of the profile. This effect is more pronounced when comparing the curves of A_{edm} = 4 and 6 with respect to the curves of A_{edm} = 2 and 4. On the injector side in Figure 5.27, an upstream shift of the shock reflection positions is induced by an increased A_{edm} value. The cowl wall pressure trace is in good agreement with the experimental data for the different curves. On the injector side, the pressure traces are within the experimental uncertainty for most of the combustor length. Close to the axial injection location (≈ 52.5 - 120 mm), the EDM is unable to account for the experimental pressure variation. A similar observation is made for the CFD predictions obtained by Karl [86] which is shown in Figure 5.28 (b). The reference CFD results

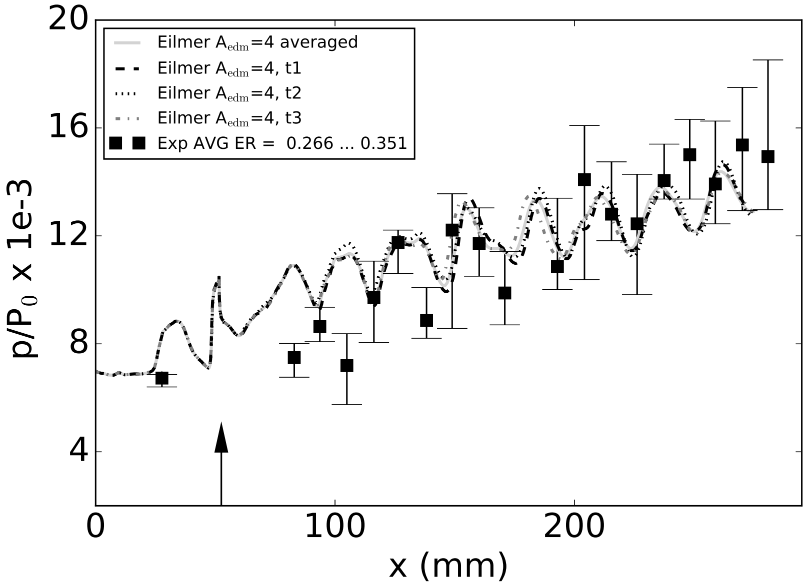

Figure 5.24: Instantaneous and time averaged pressure traces along the injector wall at y = 9.375 mm with A_{edm} = 4 and P_0 = 17.73 MPa.

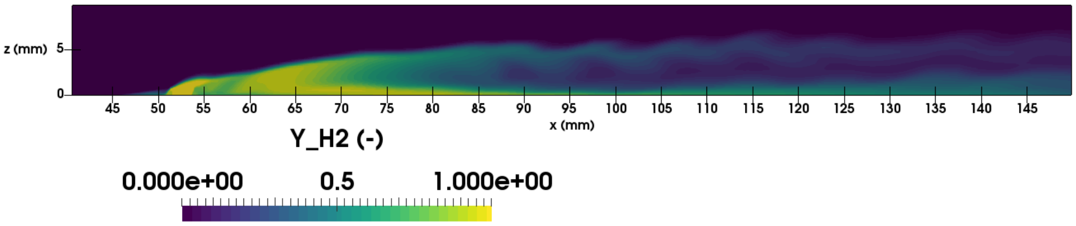

Figure 5.25: Instantaneous contour of Y_{H_2} at the injector symmetry plane (y = 0 mm) with A_{edm} = 4

are predicted by the DLR Tau code with the Spalart-Allmaras turbulence model in conjunction with a no-model chemistry (modified Jachimowski mechanism) approach. The same settings for Pr_t and Sc_t as in the present work were used. Note that Pecnik et al. [105] showed more success in capturing the injector side wall pressure trace with a flamelet TCI model. On the cowl side (Figure 5.28 (a)), the EDM pressure trace demonstrates a similar trend as the reference CFD. In terms of shock strength, A_{edm} = 6 agrees better with the Tau computation. The pressure profiles in Figures 5.26 and 5.27 have been integrated as to obtain the pressure force and averaged pressure. The same has been performed for the experimental values with results shown in Table 5.2. Given the limited amount of experimental measurements, the latter quantities should be seen as an indication more than an absolute reference point. In Table 5.2,

$\mathrm{Exp}_{\mathrm{avg}}$ is calculated by considering the experimental wall pressure averaged over the different ER's. $\mathrm{Exp}_{\mathrm{min}}$ is computed based on the minimum experimental values and $\mathrm{Exp}_{\mathrm{max}}$ based on the maximum. On the injector side, the pressure force calculated with the different EDM simulations overpredict the experimental maximum. This result is probably due to the pressure prediction between $\approx$ 52.5 - 120 mm and the lack of experimental data in this region. Nevertheless, in terms of averaged pressure, simulations with different A_{edm} settings are within the experimental bounds. On the cowl side, the same observation is made as for the injector side with regard to the averaged pressure values. The pressure force computed for A_{edm} = 2 and 4 are within the experimental bounds while it is overestimated for A_{edm} = 6.

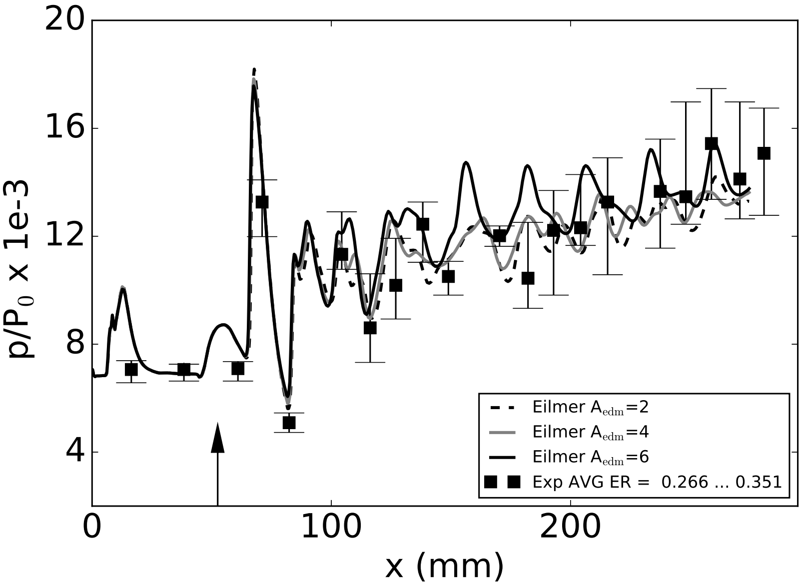

Figure 5.26: Effect of A_{edm} on the pressure traces along the cowl wall at y = 9.375 mm with P_0 = 17.73 MPa.

Figure 5.29 presents a comparison of the stream-thrust-averaged (STA) values for temperature and pressure along the combustor length. Stream-thrust-averaging is a way to extract one-dimensional flow properties from a multi-dimensional data set. Its use has been reported in the literature for scramjet combustor analysis [19, 80, 86]. The procedure detailed by Baurle and Gaffney [79] has been applied in order to obtain the STA values. Note that the latter authors refer to the method as the conserved mass/momentum/energy or CMME method. STA predictions from the reference CFD [86] at the exit of the constant area combustor are presented in Figure 5.29. Recall that

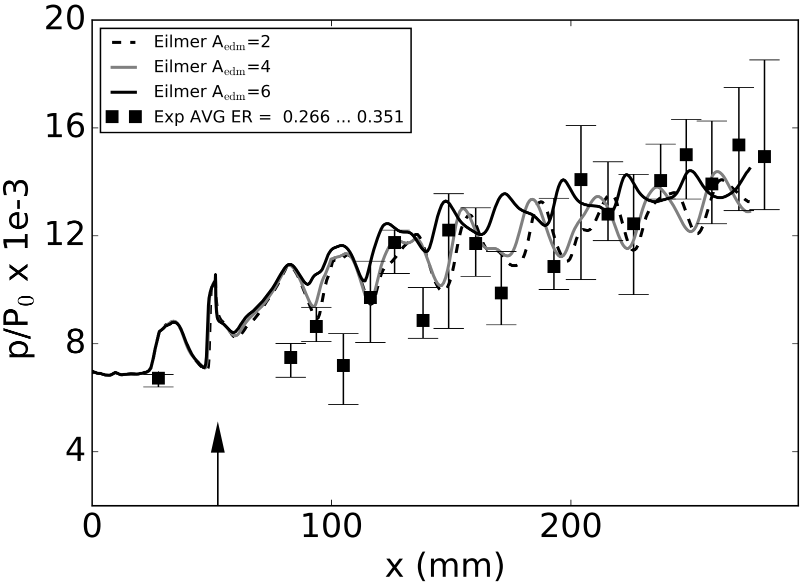

Figure 5.27: Effect of A_{edm} on the pressure traces along the injector wall at y = 9.375 mm and P_0 = 17.73 MPa.

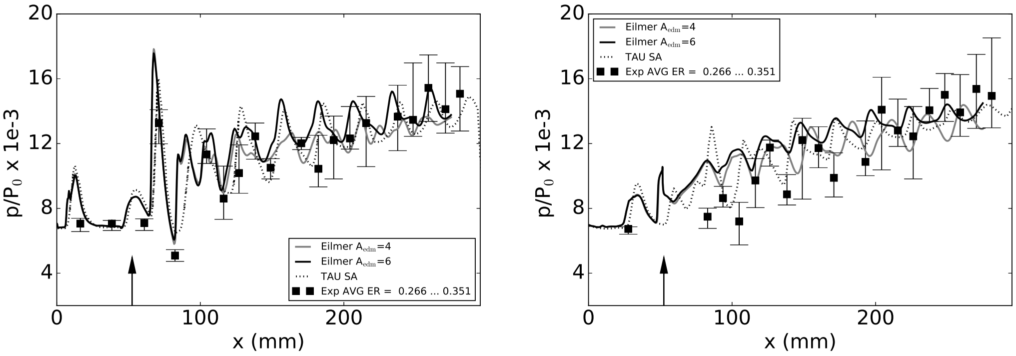

(a) (b)

Figure 5.28: Pressure along the wall at y = 9.375 mm with EDM and no-model reference CFD: (a) cowl side, (b) injector side. P_0 = 17.73 MPa.

the current computational domain is slightly shorter than the orginal geometry. The arrow indicates the point of fuel injection. Temperature and pressure values are scaled by the combustor entrance state. STA averaged temperature and pressure profiles do barely differ for A_{edm} = 2 or 4 with very similar combustor exit values. This observation is in agreement with the wall pressure traces discussed previously in Figures 5.26 and 5.27. The STA temperature at x = 275 mm is higher than the reference CFD at x = 295

Table 5.2: Averaged pressure and pressure force predicted by the EDM for the HyShot II combustor.

	$\mathbf{Exp_{min}}$	$\mathbf{Exp_{avg}}$	$\mathbf{Exp_{max}}$	$\mathbf{A_{edm} = 2}$	$\mathbf{A_{edm} = 4}$	$\mathbf{A_{edm} = 6}$
Injector wall						
pressure force (kN)	39.4	45.0	50.4	52.5	53.0	54.5
averaged pressure (kPa)	162.5	185.7	207.9	190.1	192.7	198.2
Cowl wall						
pressure force (kN)	43.3	48.3	53.9	52.7	53.1	54.7
averaged pressure (kPa)	170.1	189.7	211.9	191.5	193.1	198.8

mm. Based on this observation it could be inferred that A_{edm} should be kept equal to or lower than 4. The STA pressure trace demonstrates that the effect of A_{edm} on the combustion is localized between x $\approx$ 100 and the exit of the domain where the values seem to converge to a single one. No definitive conclusion on the best EDM constant setting can be formulated based on the pressure.

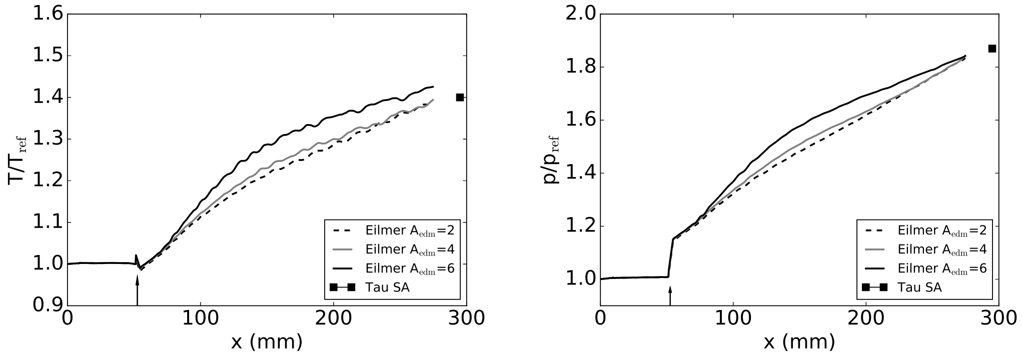

(a) (b)

Figure 5.29: Effect of A_{edm} on the STA value of (a) temperature and (b) pressure. Combustor entrance values are taken as reference for scaling.

The last value considered in order to evaluate the most appropriate setting for A_{edm} is the percentage of unburned hydrogen at the combustor exit. In case of the EDM this values is readily obtained from the water vapor based combustion efficiency (Equation 5.20) as an irreversible global single-step reaction describes the combustion process. Table 5.3 lists these values as well as the percentage documented by Karl [86]. Recall that the reference CFD value is taken 2 cm downstream of the current combustor exit. However, it is not expected that the EDM predictions will drastically increase over that short distance. Moreover, Karl [86] demonstrated that the value is highly dependent on the choice of turbulence model (up to 10 %) and the turbulent Schmidt number (up to 5 %). The author mentions that the quantity of injected hydrogen that does not react inside the constant area combustor varies between 6 % and 27 % depending on the combination of turbulence model and Schmidt number. The variation is significant and no experimental measurements are available to confirm the value. Furthermore, based on [86] it can be inferred that the amount of unburned hydrogen is evaluated based on the hydrogen mass fraction. This does not imply that products are formed as intermediate species containing atomic or molecular hydrogen are present in the flow. The latter possibility is not accounted for by the EDM which can result in some discrepancies. The reference CFD result should therefore be taken as an indication but not an absolute reference. In comparison to the reference value, the EDM underpredicts the efficiency of the combustion process. The difference in percentage of unburned hydrogen between $A_{edm} = 2$ and $A_{edm} = 6$ is only 7 %. From this observation, it can be inferred that each of the A_{edm} settings are appropriate to perform a design operation on the HyShot II combustor. That is, the different values indicate that the combustor performance can be improved by, for instance, changing the location or topology of the injector. Such a demonstration study is the subject of Chapter 6.

Table 5.3: Percentage of unburned hydrogen at the exit of the HyShot II combustor with different A_{edm} settings .

	Tau SA	**A_{edm} = 2**	**A_{edm} = 4**	**A_{edm} = 6**
unburned H_2 (%)	21*	39	36	32
*Value for Tau evaluated at combustor exit which is x = 295 mm. Eilmer domain extends only until x = 275 mm.				

Regarding the use of the EDM for the HyShot II combustor the following conclusions can be drawn. Based on the comparison in Table 5.2, it could be inferred that the value of A_{edm} should be kept below 6. The wall pressure traces in Figures 5.26 and 5.27 do confirm this statement. A higher setting would result in even higher peak values which would not agree with experimental measurements until $\approx$ 200 mm downstream inside the combustor. Further downstream the strength of the combustion is less intense and the CFD predictions are near the lower part of the experimental uncertainty interval, especially on the cowl side. The observation can be explained with the contour of ω in Figure 5.30. The turbulent dissipation rate is strong inside the barrel shock induced by fuel injection. This is shown in the different cross planes.

However, moving downstream, the strength reduces considerably (see locations x = 0.15, 0.2 and 0.275 m). In analogy with the Burrows-Kurkov and DLR configurations, a possibility would be to split the combustor in two zones with a higher A_{edm} value in the more downstream region. This approach will result in an increased percentage of unburned hydrogen which would be more in agreement with the reference CFD of Karl [86] in Table 5.3. The STA profile of temperature (Figure 5.29) did as well confirm that the EDM constant should be kept below 6. Overall, a setting A_{edm} between 4 and 6 is adviced for the HyShot II combustor.

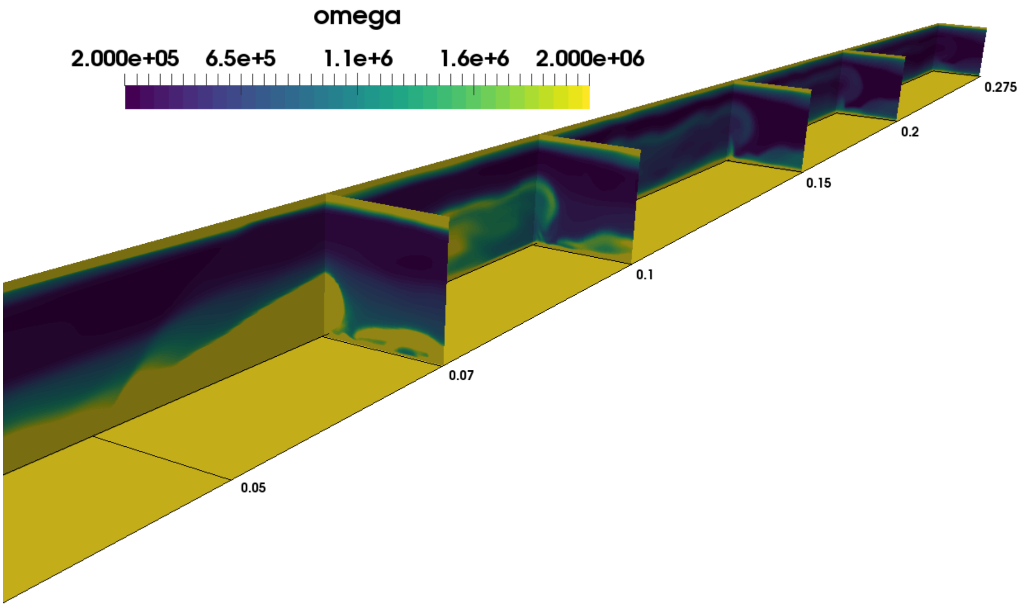

Figure 5.30: Contour of ω for the HyShot II scramjet combustor.

5.3 Application of the EDM to a Non-Mixing Limited Scramjet

The assumptions in the formulation of the EDM (see 5.1.1) are such that the model is suitable for mixing-limited combustion. What happens when the combustion is kinetically limited? Can the computationally cheap EDM (with kinetic limit) still be relied on in such conditions? This is the subject of this section's investigation.

In order to answer the question of whether or not the EDM's applicability can be pushed to scramjets designed with kinetic effects, the test case of Lorrain et al. [225, 226] is considered. Figure 5.31 shows the computational domain for study. The design of this scramjet relies on the concept of radical farming and as a consequence milder combustor entrance conditions are encountered, i.e. averaged temperature below 1000 K. The combustion is therefore expected to be mainly kinetically limited. In this study, the EDM is compared to a no-model finite-rate chemistry approach with detailed reaction mechanism. The latter description of the combustion is expected to be more approriate for a kinetically limited scramjet. Lorrain [84] did confirm this with a good comparison of three-dimensional simulations with experimental data. The no-model simulation used for comparison here has been discussed in Section 4.5 and is considered as the adequate or target solution. Given the premixed character of the simulation, the product term in Equation 5.4 is included in the EDM computations for correctness. However, this did not influence the steady state result: the product term acts as a transient. An initial product (H_2O) mass fraction of 0.01 is uniformly specified in the domain and the value of $\mathrm{B_{edm}}$ is set to the default value of 0.5.

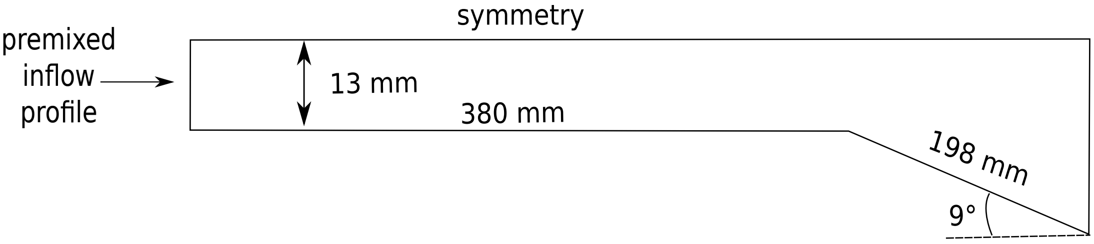

Figure 5.31: The premixed scramjet geometry [225] considered for study of the EDM.

The knowledge about the use of the EDM gained in the Burrows-Kurkov, the DLR and the HyShot II test case is used here. Given the geometry, high values of ω are expected near the wall. Figure 5.32 confirms this. Note that the contour is obtained from a combusting simulation, however the same observations are made in the frozen simulations. A viable approach in the specification of the $\mathrm{A_{edm}}$ constant could be to simulate a desired configuration without combustion. The resulting contour of ω will then give an indication of its order of magnitude in reacting conditions. Based on this, an appropriate value of the constant can be chosen. In the present scramjet a low value of $\mathrm{A_{edm}}$ should be appropriate. The scramjet design relies on a specific shock wave pattern to ignite the mixture of fuel and oxidizer in accordance with the concept of radical farming. The origin of the ignition is located in the near wall region around the second shock impingement [225]. The high values of ω in that region explains the choice for a reduced EDM constant. Simulations with $A_{edm} = 1$ and $A_{edm} = 2$ have been performed for comparison with the no-model, finite-rate chemistry CFD. As Lorrain's scramjet has an ignition delay the EDM results presented here were obtained with the kinetic limit (Equation 5.15). The test case demonstrated the importance of introducing a limit on the reaction rates predicted by the EDM as the unlimited simulations resulted in nonphysically high peak temperatures coupled with an unstart behavior where the shock-induced boundary layer separation bubble at the first shock impingement inside the combustor was continuously growing in the upstream direction.

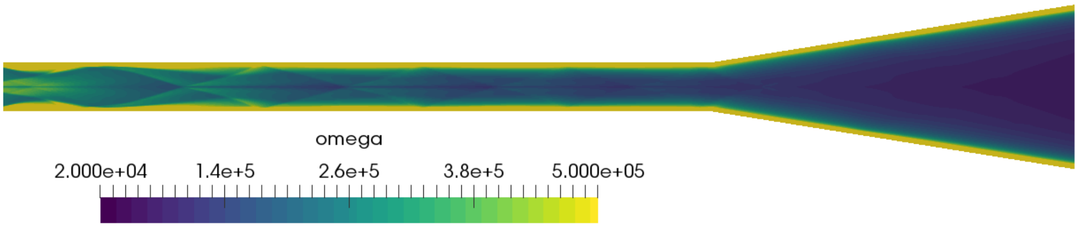

Figure 5.32: Contour of ω for the scramjet of Lorrain

In a first investigation the effect of the A_{edm} model constant has been quantified. Figure 5.33 shows the mean temperature (lower half) and product mass fraction (Y_{H_2O}, upper half) contour predicted with Eilmer and A_{edm} settings equal to 1 and 2. Also visible is the no-model, finite-rate numerical simulation with Jachimoswki's mechanism. The onset of ignition in the EDM contours is located closely after the first shock reflection. In the finite-rate simulation ignition occurs in the vicinity of the second shock reflection. The limited ignition delay in the case of EDM is a direct consequence of a single-step reaction kinetic limit and high near wall temperatures as pointed out in an earlier discussion with Figure 5.8. A setting $A_{edm} = 2$ results in an increased production of H_2O, in accordance to Equation 5.4, which in turn results in higher temperatures. The combustion is localized (see Y_{H_2O} contour) in the region near the wall where the turbulence dissipation (ω) is very intense. A higher A_{edm} constant enables product formation toward the center of the geometry. In comparison to the EDM results, the no-model contour shows the gradual formation of products from the walls toward the center. By the end of the combustor reactions are occuring over the complete width of the geometry. In the latter case, the temperatures are lower than for the EDM in the first half of the combustor. In the second half of the combustor and in the nozzle, temperatures are lower than for the EDM in the proximity of the wall but higher toward the centerline of the scramjet. It is possible to obtain product formation toward the center of the geometry with a higher value of A_{edm}. Doing so does however significantly increase the temperature values above physically achievable values. Therefore, in order to keep the predicted peak temperature values below a maximum physically achievable threshold, a lower setting, $A_{\mathrm{edm}} = 1-2$ should be selected to simulate Lorrain's scramjet.

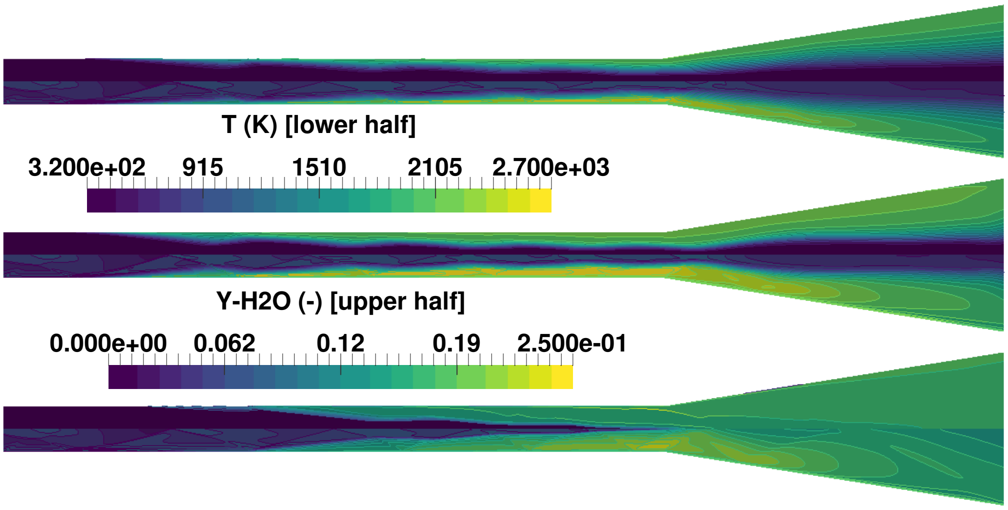

Figure 5.33: Temperature (lower half) and Y_{H_2O} (upper half) contours comparing the effect of the A_{edm} constant with no-model finite-rate chemistry results using Jachimowski's [149] reaction mechanism. From top to bottom: $A_{\mathrm{edm}} = 1$, $A_{\mathrm{edm}} = 2$ and Jachimowski.

The wall pressure obtained with EDM is compared to the no-model finite-rate chemistry in Figure 5.34. The simulation with $A_{\mathrm{edm}} = 1$ predicts the same shock locations inside the combustor as the no-model with Jachimowski's reaction mechanism. This is not the case anymore inside the nozzle. In the first half of the combustor the combustion is more intensively predicted by the low EDM setting. Thereafter the finite-rate chemistry demonstrates much stronger combustion. The observation is in accordance with the temperature and Y_{H_2O} contour, Figure 5.33, discussed above. The $A_{\mathrm{edm}} = 2$ profile differs from the other setting after the first shock reflection. In this case, the combustion is initiated slightly earlier and the size of the shock induced boundary layer separation bubble is larger than in the case $A_{\mathrm{edm}} = 1$. As expected the higher EDM value results in more intense combustion which is coupled to the higher peak pressure values. With respect to finite-rate chemistry the pressure along the wall with $A_{edm} = 2$ is consistently higher for most of the combustor section. Near the end of the combustor and in the nozzle section the opposite behavior is observed. In the case of finite-rate chemistry, intermediate species are formed which delays the formation of H_2O to the end of the combustor. This explains the difference with the EDM. By the end of the combustor H_2O is produced over the width of the scramjet which is not the case for EDM (see Figure 5.33). Consequently the flow in the nozzle is very different. The wall pressure is as well shown for A_{edm}=4 in the representation. A different shock pattern to the other EDM curves is observed toward the end of the combustor. The pressure in the nozzle section is in closer agreement to the no-model simulation.

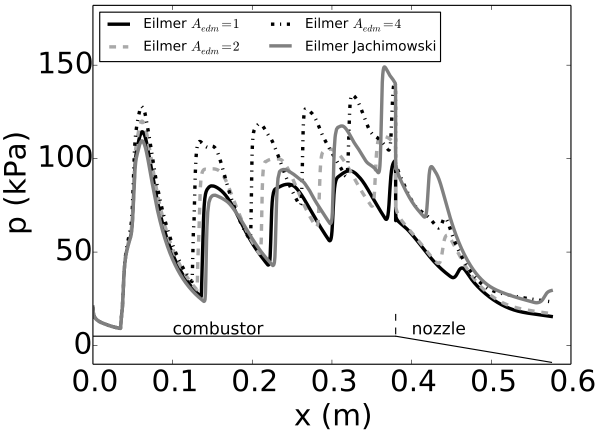

Figure 5.34: Wall pressure predicted with EDM and the no-model approach with detailed reaction mechanism.

The thrust predicted by the different CFD simulations is given in Table 5.4. The equivalence ratio for the conditions in Table 4.5 equals 0.81. A lower thrust is obtained with the EDM compared to the no-model approach. This is mainly explained by the differences in combustion strength toward the end of the combustor and the nozzle discussed above. The difference in thrust between Jachimowski and A_{edm} = 4 is equal to 83 N. The same order of magnitude is obtained with the EDM at a much reduced computational cost. Therefore, the latter model can be a viable option to predict thrust for preliminary design purposes by adopting a value A_{edm} = 4.

Table 5.4: Thrust predicted for Lorrain's scramjet by different CFD approaches.

	thrust (N)
A_{edm}=1	1149
A_{edm}=2	1245
A_{edm}=4	1567
Jachimowski	1650

The combustion efficiency is compared in Figure 5.35. The observations are in accordance with the discussions on the temperature / composition contours and the wall pressure curves. As more combustion is allowed to occur with a higher value of the EDM constant the combustion efficiency is consequently higher. The no-model result predicts a much higher combustion efficiency than the EDM, starting from x = 0.25 m. It must be noted that the higher setting for the EDM results in increased temperature values.The onset of ignition does not change which indicates the effectiveness of the kinetic limit. The amount of products formed after ignition strongly differs as shown by the different settings of the A_{edm}. The no-model approach with detailed reaction mechanism has an extra kinetic effect which is in accordance with the discussion of Figure 5.33. The EDM demonstrates as well considerable burning in the nozzle section which is not as pronounced in the no-model results. From Figure 5.35, the EDM appears not to be adequate enough to predict the combustion efficiency, along the combustor, in scramjet designs with strong kinetic effects.

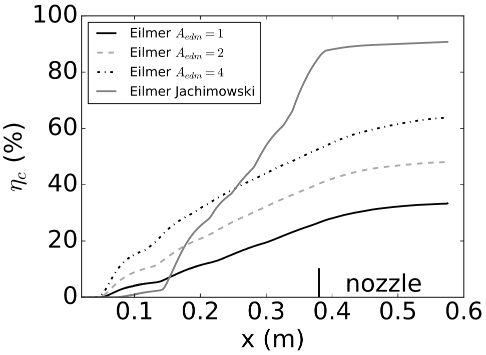

Figure 5.35: Combustion efficiency predicted with EDM and the no-model approach with detailed reaction mechanism for Lorrain's scramjet.

Figure 5.36 shows the stream-thrust averaged [79] profiles of temperature, pressure and Mach number along the geometry. The former two variables are scaled by the combustor entrance values which are respectively T_2 = 782 K and p_2 = 42 163 Pa. The subscript "2" is selected following the convention of Heiser and Pratt [241, 63, 19] and represents the inlet throat. The evolution of the profiles with Jachimowski's mechanism are overall very different than with the EDM. This is in accordance with the combustion efficiency previously discussed. The different profiles of the no-model and A_{edm} = 1 simulations are almost identical until $\approx$ 150 mm inside the combustor, shortly after the second shock reflection. The same observation was made with the wall pressure trace in Figure 5.34. This confirms that the lower setting for the EDM is the most appropriate in order to capture the ignition delay. The evolution downstream x = $\approx$ 150 mm is completely different as the lower setting for A_{edm} does not burn as much fuel. Even the higher value A_{edm} = 4 does not predict as high a temperature or pressure at the exit of the combustor (x = 380 mm). In the nozzle section, the temperature and Mach number do significantly differ. However, the averaged pressure drop by the exit of the nozzle is quite similarly predicted by the different CFD approaches. This explains the same order of magnitude of the thrust values in Table 5.4. The use of a zonal EDM (cfr DLR combustor) could be a viable option for this scramjet combustor. The zonal approach should be applied both horizontally and vertically in this case. Horizontally as to account for the ignition delay with a first region where A_{edm} is set to 1 and a second region with a higher value. Vertically as low ω values are obtained by the turbulence model in the center of the geometry, therefore a higher A_{edm} would be more appropriate in that region.

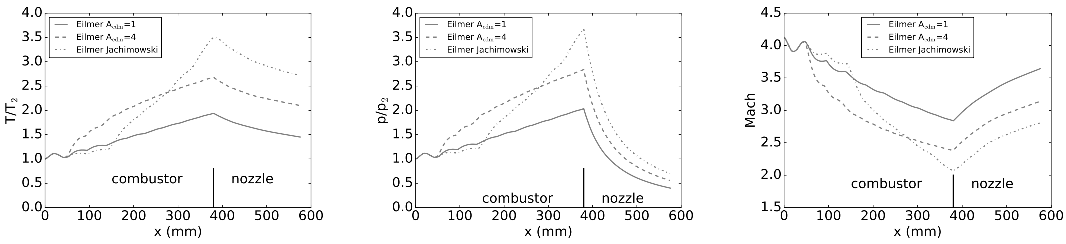

(a) (b) (c)

Figure 5.36: Stream-thrust averaged profiles of (a) temperature, (b) pressure and (c) Mach.

The following can be concluded regarding the use of the EDM on a scramjet design which is primarily kinetically limited.

- In order to keep the peak temperature physical, a low setting of the EDM constant (A_{edm} = 1-2) should be chosen.

- In order to correctly capture the ignition delay, A_{edm} = 1 should be adopted.
- In order to adequately predict the shock reflections inside the combustor (wall pressure trace), A_{edm} = 1-2 should be selected.
- In order to correctly predict the thrust, a higher value ($A_{edm} \geq 4$) should be considered.
- In order to obtain averaged quantities at the exit of the combustor similar to a no-model simulation result with detailed reaction mechanism, a high value ($A_{edm} \geq 4$) must be chosen.
- The combustion efficiency cannot be predicted accurately enough by the EDM.

The above statements indicate that for this test case it is not possible to get a good agreement for all quantities with a single value of the EDM constant. For a specific variable of interest it is possible to obtain reasonable results with the EDM.

5.4 Summary of Chapter

In this chapter, the EDM has been introduced and applied to four scramjet test cases. Three of the configurations were dominated by combustion physics for which the EDM is expected to yield reasonable results. The EDM relies on a model constant (A_{edm}) and it is shown, based on the previously mentioned three test case, that overall a setting A_{edm} = 4 provides reasonable results in comparison with the available experimental data. In the case of parallel injection of fuel with respect to the air stream it is shown that relying on an estimate of the ignition delay improves the predictive capability of the model. This zonal approach was as well identified as a viable methodology for improvement of the model's application for transverse fuel injection as well as for fuel injection behind a strut. It is subject to future work. Furthermore, the last test case investigated if the EDM could still be relied on in a combustor design where the chemical kinetics play an important role. The result of this study demonstrated that a single value for the model constant cannot provide a good agreement with all flow quantities. Instead, for a specific quantity of interest the EDM is capable of a good predictive behavior. A summary of the findings for the different test cases are listed in Table 5.5. The best setting for the model constant(s) for the performed simulations are given. Finally, the best modeling approach is underlined for each scramjet combustor. Now that the use of the EDM has been thoroughly investigated and characterised, the model is applied to a combustor design exercise in Chapter 6.

Table 5.5: Summary of EDM simulation settings for scramjet test cases in this work

Test case	**Modeling approach**	$\mathbf{A}_{\text{edm}}$	$\mathbf{B}_{\text{edm}}$	**Comments**
Burrows and Kurkov	Standard EDM	4 - 6	/	no ignition delay
	EDM + kinetic limit	4 - 6	/	limited ignition delay
	Zonal EDM	4	/	accounts for ignition delay
DLR	Standard EDM	4	/	zonal could improve the predictions
	EDM + kinetic limit	4	/	suppressed combustion in recirculation region
HyShot II	Standard EDM	4	/	zonal could improve the predictions
Lorrain	Standard EDM	1 - 4	0.5	unstart
	EDM + kinetic limit	1 - 2	0.5	peak static temperature, wall pressure, ignition delay
	EDM + kinetic limit	4	0.5	thrust, averaged exit quantities

Chapter 6

Application of RANS EDM to a Design Problem

The main objective of this thesis is to provide a computationally affordable CFD modeling approach to help in the design of scramjet flow paths. This includes the possibility to generate a propulsion database with a higher fidelity compared to conventional quasi-one dimensional approaches (see Section 2.1). It also includes, for instance, the study of a scramjet combustor with the aim of improving the fuel injector location or injector type (see Subsection 2.2.4). Up to this point, an open-source CFD solver has been selected, its use for scramjet flow paths validated (Chapter 4) and the selection of the EDM constants investigated (Chapter 5). The EDM has not yet been used in the context of drawing design conclusions. This aspect is tackled in the present chapter.

6.1 Selected Injection Approaches for the HyShot II Combustor

The HyShot II combustor geometry, discussed in Section 4.4 and Subsection 5.2.3, is considered for further study. The effect of varying the injector location and topology is investigated with the EDM. This task will give a demonstration of how design decisions could benefit from a computationally more affordable tool such as the EDM. In this chapter, the injection mechanism is kept to the category of porthole injection (see Figure 2.5). The EDM is applied with $\mathrm{A}_{\mathrm{edm}} = 4$ which proves to be an overall good compromise for the test case in Subsection 5.2.3. It must be noted that the HyShot II combustor was designed as an experiment to demonstrate supersonic combustion and not tailored for thrust generation. Nevertheless, this scramjet combustor is well characterised by previous research performed in the literature and is therefore a good starting point towards the demonstration of using the EDM for design decisions.

The EDM simulations (Subsection 5.2.3) indicated that a significant portion of hydrogen is unburned at the exit of the combustor. The current aim is to decrease this value, or in other words, to increase the combustion efficiency at the combustor exit. Only a limited amount of configurations are considered as to keep the use of the computational resources to a reasonable level. A first possibility consists of moving the injector upstream to the current location. By doing so, for a given ER, the residence time of fuel inside the combustor will be longer and should result in increased fraction of products. However, where should the injector ideally be located? Schetz et al. [242] demonstrated in an experimental study that shock impingement near the injection station does increase the mixing due to increased vorticity. This effect is more pronounced when the shock impinges downstream the point of injection. A drawback of the shock impingement is a reduced penetration depth of the fuel jet. The idea is illustrated in Figure 6.2 (a). Figure 6.1 illustrates the baseline porthole injection flow structures without an impinging shock wave.

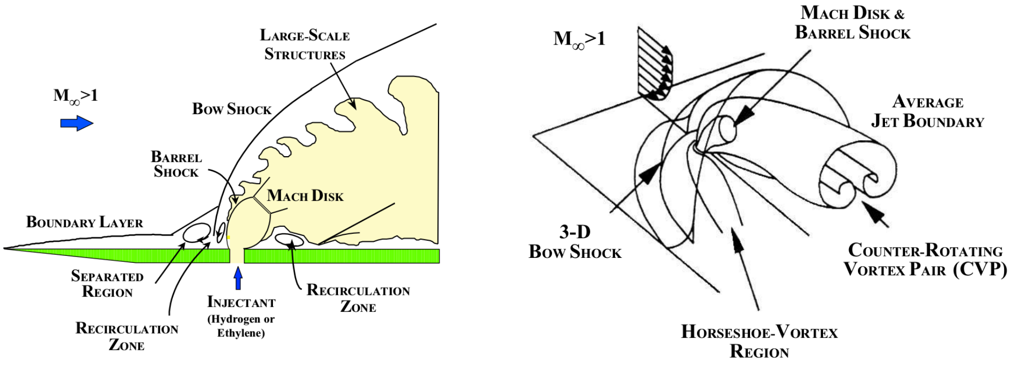

(a) (b)

Figure 6.1: Flow structures induced by sonic fuel injection through a porthole with (a) side view, (b) top view. Reproduced from Ben-Yakar [243]

Following the observations of Schetz et al. [242], the injector has been moved to an upstream location where the oblique shock (reflected on cowl wall) impinges downstream the point of injection. The new location for study has an injector leading edge located at x = 0.019 and is identified in Figure 6.3, showing the non-reacting pressure contour. It could be argued that locating the injector even further upstream of this point would improve the combustion efficiency as the residence time is even

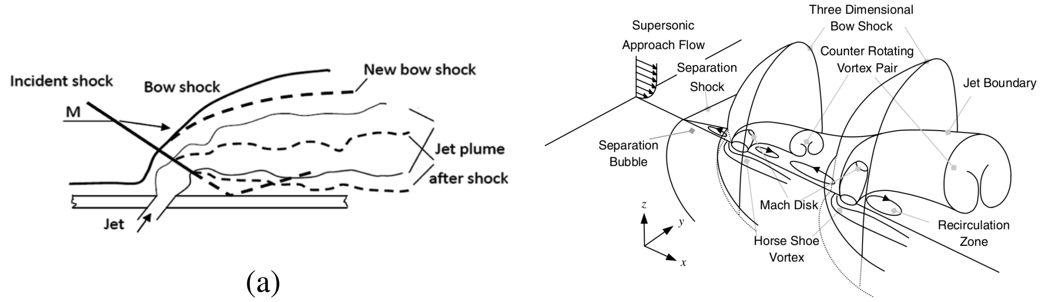

(a)

(b)

Figure 6.2: Flow structures induced by sonic fuel injection through a porthole with (a) shock impingement, (b) additional porthole injector. Reproduced from Schetz et al. [242] and Lee [47].

higher. This path has however not been explored in the present work and is subject to future investigations.

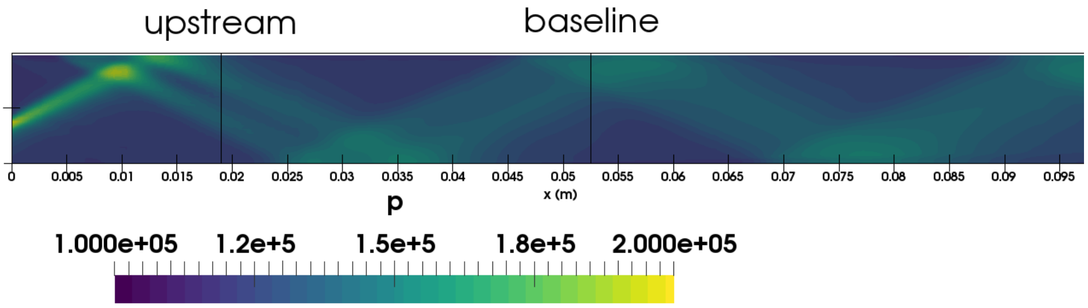

Figure 6.3: Non-reacting wall pressure contour with indication of injector locations inside the HyShot II combustor for study of the EDM.

A second injection strategy considered for study is the use of cascade or dual transverse fuel injectors. Lee [47, 48] (non-reacting and reacting) and more recently Landsberg et al. [49] (non-reacting) numerically investigated the latter approach. Figure 6.2 (b) illustrates the idea. Lee [47, 48] demonstrated that the results are highly dependent on the combination of jet to-cross-flow momentum flux ratio, J, and the distance between the injectors. The former parameter is defined as

$$J = \frac{(\rho V^2)_f}{(\rho V^2)_\infty} = \frac{(\gamma p M^2)_f}{(\gamma p M^2)_\infty} \tag{6.1}$$

and the latter distance is related to the area-equivalent total jet diameter $D_t = \sqrt{D_U^2 + D_D^2}$ [49]. For instance, $2D_t$ indicates that the injectors are separated by a distance of twice the value of D_t. D_U and D_D are the upstream and downstream injector diameters. Lee [47, 48] considered values of J equal to 1 and 2 at a single inflow condition, while Landsberg et al. [49] adopted J = 1 for study at different inflow conditions with angular porthole injection (45 deg to the wall). In reacting conditions, Lee [48] showed that for J = 1, the combustion efficiency improved greatly for a distance between injectors equal to $6D_t$ with respect to a single injector. It did however also result in increased total pressure losses (1 % in terms of $p_{0,exit}/p_{0,in}$) which where smaller in the case $2D_t$. With J = 2, the highest combustion efficiency was achieved with $8D_t$ but the total pressure losses were significantly higher too. In their non-reacting study with J = 1, Landsberg et al. [49] concluded that spacings between 4 and $6D_t$ provided optimal improvements over the range of Mach numbers considered. The HyShot II combustor is characterized by J = 0.35 [244] for an ER = 0.29. This value is much lower than considered in the previously discussed studies. From the observation of Lee [48] that D_t should increase with increased J, D_t is decreased in the present work. The distance between the injectors is set to $4D_t$ which is the minimum distance suggested by Landsberg et al. [49]. Lee [48] demonstrated, with no-model simulations, that the production rate of water vapor is almost the same as the consumption of hydrogen which indicates fast chemistry. It can therefore be interpreted that the EDM would be appropriate in studying the dual transverse injection. Figure 6.4 summarizes the injection strategies considered in the present chapter.

In a scramjet combustor design, the aim is to burn as much fuel as possible over the smallest length possible. The former condition ensures that the full potential of the combustion can be exploited in order to accelerate the flow and generate thrust. The combustion efficiency is the typical measure which is considered for this and is given by Equation 5.20. Reducing the length of the combustor aims at keeping friction and pressure losses to a minimum. A common measure is the total pressure loss across the combustor. The total pressure loss is computed as $(1- p_{0,exit} / p_{0,in})*100$, with $p_{0,in}$ equal to 2.41MPa. Another performance measure is the thrust potential (TP) [172] also known as the combustor effectiveness concept [245]. It is obtained by expanding one-dimensional flow quantities at a given streamwise location through an ideal (reversible), isentropic and adiabatic nozzle. As such, the TP is an indicator of the thrust that you could ideally generate by truncating the combustor. The TP is influenced by the losses in total pressure as well as by the chemical reactions. The

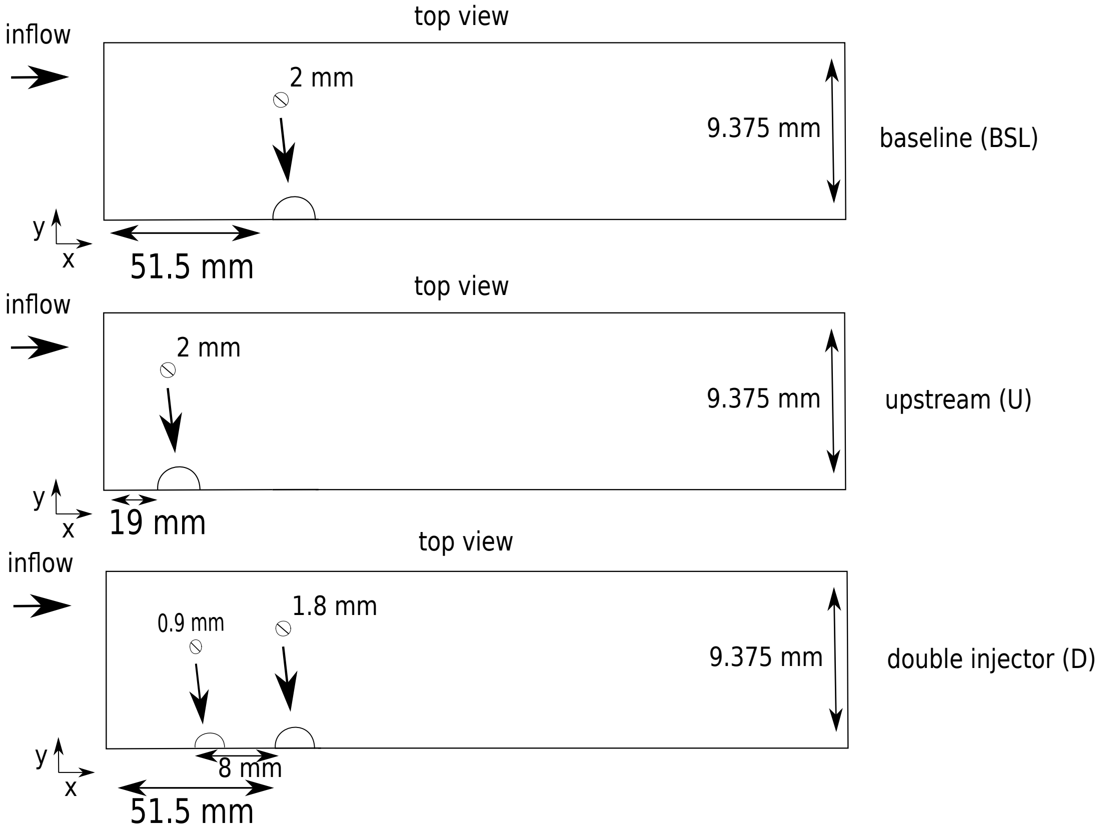

Figure 6.4: Sketch of the injection approaches inside the HyShot II combustor for study of the EDM. Not to scale.

former decreases its value while the latter can increase its value. The thrust potential at a given streamwise location is obtained with the following formula [172]:

$$\mathrm{TP} = \dot{m}u_{exit} + (p_{exit} - p_{\infty})A_{exit} \tag{6.2}$$

In this work, the flow is expanded to the free stream static pressure so that the last term on the right-hand side is exactly zero. The value of p_{∞} is taken equal to 2 kPa (see Karl [86] Table 4.2 or Larsson et al. [43]). The value obtained with Equation 6.2 is multiplied by eight as the present work does only consider one-eight of the computational domain. In the following study of different injectors, the combustion efficiency (water vapor based), total pressure loss and thrust potential are considered as the main metrics for comparison.

6.2 Effects of Injection Approaches on HyShot II Combustor

Firstly, the original injector (cf. Figure 6.1) is considered with an increased equivalence ratio (ER) of 0.35. The latter value is the highest ER for which experimental wall pressure measurements have been collected. The resulting wall pressure traces are compared with the experimental data and the lower ER CFD predictions in Figure 6.5. The increase in ER does result in an overall higher wall pressure on both the injector and cowl wall and is due to the larger heat release induced by an increase in available fuel [86]. The ER = 0.35 curves do confirm that from x $\approx$ 200 mm, a higher value of the EDM constant could be more appropriate. This should result, on average, in wall pressure predictions located toward the upper experimental uncertainty interval. The amount of unburned hydrogen is equal to 55 % for the higher ER value. Karl [86] predicted 25 % for the same value at the exit of his constant area combustor domain (2 cm downstream of current simulations). Recall the strong influence of turbulence model and reaction mechanism on this value. While the presently obtained result differs significantly from the CFD of Karl [86], in both cases an increase in unburned hydrogen is reflected, and consequently a decrease in combustion efficiency. Table 6.1 lists the latter parameter as well as the total pressure loss and thrust potential at the exit of the computational domain. The notation BSL29 represents the baseline injector location with ER = 0.29. In terms of total pressure loss, there is barely any effect of an increased ER. The total pressure is mass flux weighted averaged [79].

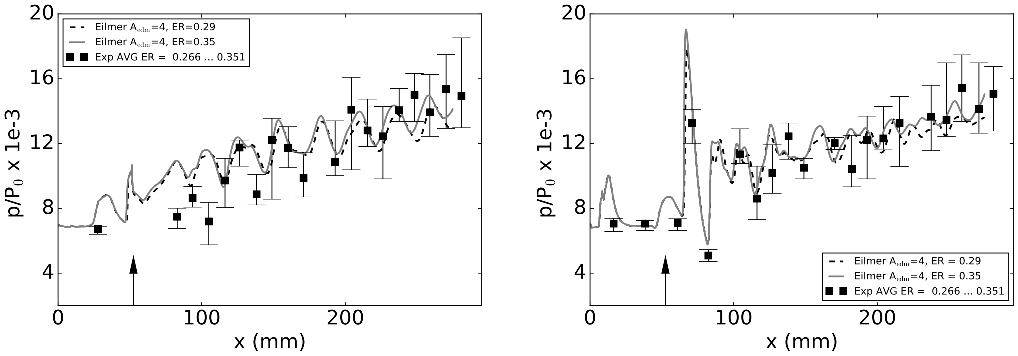

(a) (b)

Figure 6.5: Effect of ER on the pressure along the (a) injector wall and (b) cowl wall of the HyShot II combustor. P_0= 17.73 MPa.

Secondly, the influence of an upstream injection approach is evaluated. Figure 6.6 compares the instantaneous pressure contour of BSL29 (upper half) and the upstream injection (lower half) for the same equivalence ratio and is referred to as U29. The contours are shown at the injection symmetry plane and the injectors have been shifted to the same axial position. The interaction of the shock impingement on the fuel stream results in a slight bending of the injection bow shock similarly to the sketch in Figure 6.2 (a). Nevertheless, the reflection location of the bow shock on the cowl wall is very similar. A noteworthy difference can be seen in the boundary layer (BL) separation at the injector wall, just upstream the injection bow shock. For BSL29, this region extends more upstream than the U29 simulation and can be attributed to the thickness of the boundary layer. Investigating the contour of water vapor mass fraction does illustrate this more clearly in Figure 6.7. In the U29 case, as the injector is located very close to the combustor inlet, the BL does not grow as thick as in the BSL29 case. This does affect the transport of fuel / products through the horseshoe vortex (see Figure 6.1 (b)). This indicates that the interaction of the fuel jet with the BL can have an important effect on the flow field and should be kept in mind. In terms of combustion efficiency, the extra mixing / combustion length in the U29 case results in a much higher value by the combustor exit as seen in Table 6.1. With respect to BSL29, a 33 % improvement is observed. Locating the injector further upstream does result in higher total pressure losses (10 % increase with respect to BSL29), which is a direct consequence of the longer mixing / combustion region.

The same comparison with an ER of 0.35 resulted in a 32 % increase in combustion efficiency which is almost identical to the increase observed for the lower ER conditions.

The total pressure losses increased by 7 % between BSL35 and U35. In conclusion, for both ER's, the gain in combustion efficiency is higher than the loss in total pressure which indicate that locating the injector upstream the baseline design is a viable option for improving the HyShot II combustor's performance.

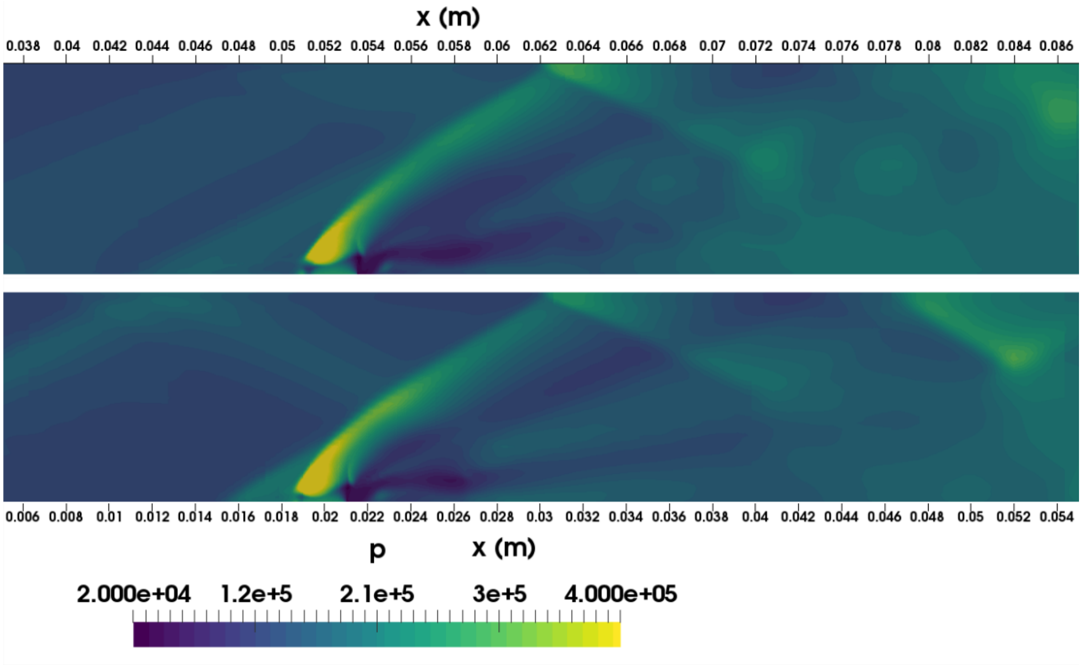

Figure 6.6: Instantaneous pressure contours showing the effect of shock impingement on injection inside the HyShot II combustor. Top: baseline, Bottom: upstream injector. $A_{edm} = 4$, $Pr_t = 0.9$, $Sc_t = 0.7$, ER = 0.29.

Table 6.1: Summary of combustion efficiency, total pressure loss and thrust potential for the different injector simulations at the exit plane of the HyShot II combustor.

	η_c (%)	Δp_0 (%)	TP (N)
BSL29	63	37	13
BSL35	55	38	12
U29	96	47	11
U35	87	45	11
D29	71	40	12

Lastly, the effect of adopting a cascade injector topology on the baseline configuration is investigated. The original injector has a diameter of 2 mm and is equal to D_t introduced in Section 6.1. Similarly to Landsberg et al. [49], a 1:2 ratio of injector

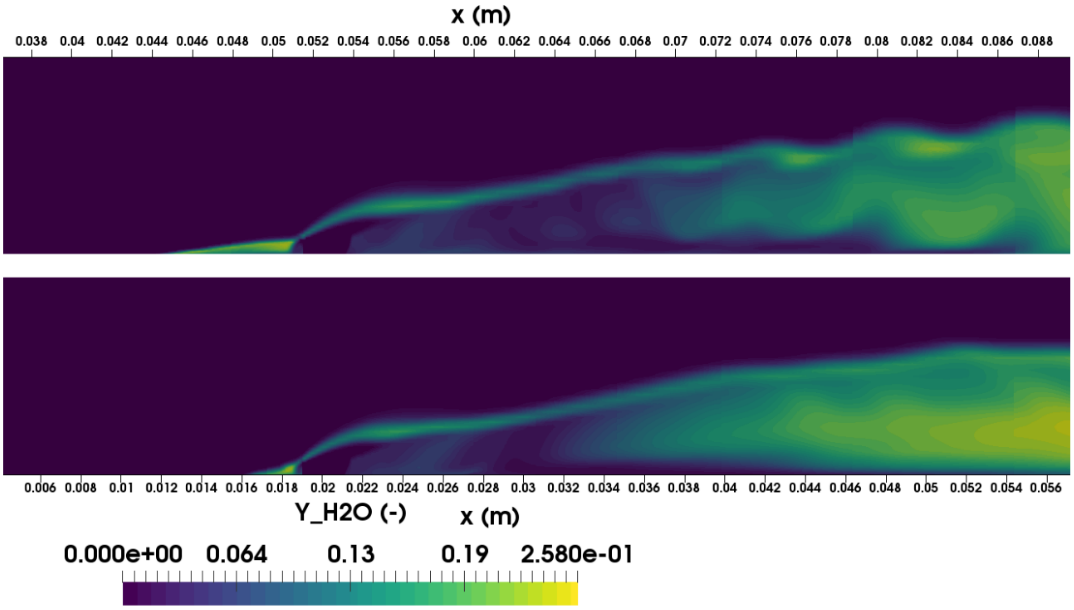

Figure 6.7: Instantaneous Y_{H_2O} contours showing the effect of shock impingement on injection inside the HyShot II combustor. Top: baseline, Bottom: upstream injector. $A_{edm} = 4$, $Pr_t = 0.9$, $Sc_t = 0.7$, ER = 0.29.

diameters is selected, yielding $D_U = 0.9$ mm and $D_D = 1.8$ mm. This ensures the same overall ER of 0.29. The injectors are seperated by $4D_t$ and the center of the downstream injector is located at the baseline axial position. Figure 6.8 compares the pressure contour of the baseline simulation and the cascade injector prediction, from here on, referred to as D29. Lee [47] demonstrated that due to a blockage effect of the front injector, the rear injection flow expands more strongly. This characteristic is less clear in the present case due to shock reflections on the cowl wall which add more complexity to the flow field. Such reflections were not accounted for in the study of Lee [47, 48] or Landsberg et al. [49]. In terms of exit combustion efficiency, Table 6.1 shows an increase of 8 % with respect to BSL29. Lee [48] did also document an increase in the production of water vapor with a cascade fuel injection at the exit of his computational domain, regardless of the chosen distance between injectors. The present study confirms the increased combustion efficiency in a more realistic combustor setting. The total pressure losses are 3 % higher for D29 with respect to BSL29. The gain in combustion efficiency is only slightly higher than the total pressure losses. Adopting a different distance between injectors might improve even further the performance. It is however only considered as future work.

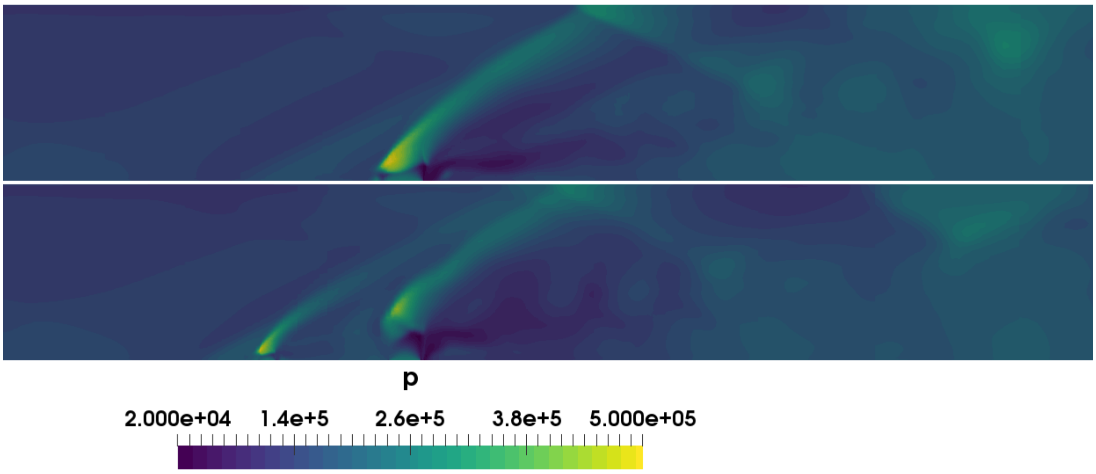

Figure 6.8: Instantaneous pressure contours inside the HyShot II combustor with top: baseline, bottom: cascade injector. $A_{edm} = 4$, $Pr_t = 0.9$, $Sc_t = 0.7$, ER = 0.29.

Figure 6.9 summarizes the results of the different simulations by showing the combustion efficiency and total pressure along the combustor. The small oscillations in the former profile are a consequence of the time averaging and can be remedied with an increased number of samples. The overall behavior will however not change and the curves are therefore representing the effect of the different simulations. The behavior of configuration D29 stands out from the rest. Unlike the BSL29 case, products are formed less rapidly till x $\approx$ 225 mm, whereafter the opposite is seen. Regarding the total pressure drop, the D29 curve is very similar to the BSL29 till x $\approx$ 190 mm whereafter the losses increase in the former case. The larger drop in total pressure for D29 is due to increased mixing and combustion (heat release) and is as well reflected in the combustion efficiency curve.

Investigating the Y_{H_2O} contour in Figure 6.10 shows that from x $\approx$ 175 mm, the combustion in the BSL29 simulation does seem to remain at a given distance from the cowl wall. Instead, in the D29 solution the reaction zone reaches even further and by the end of the combustor, combustion is observed very close to the cowl wall. The penetration depth in the transverse direction is consequently higher for D29 than BSL29 and is a characteristic of a cascade fuel injection system [47]. The larger penetration depth in the transverse direction is also shown at different slices in Figure 6.11. Having combustion occuring very close to the cowl wall can as well contribute to the drop in total pressure due to an increase in viscous losses. Figure 6.11 does show other differences between the BSL29 and D29 simulations. Firstly, the vortex structures

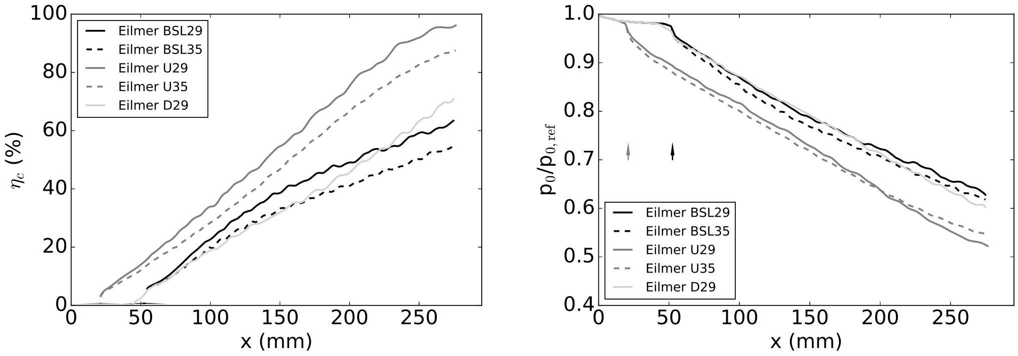

(a) (b)

Figure 6.9: Profiles of (a) combustion efficiency and (b) total pressure along the HyShot II combustor predicted with different injections.

near the point of injection. You et al. [244] presented a schematic of these structures for a low J flow field such as for the BSL29 and is reproduced in Figure 6.12. The representation will help in understanding the presently obtained results. In the BSL29 case (Figure 6.11), products (and fuel) are transported through both the horseshoe vortex and the upstream separated region. The latter extends spanwise till the symmetry plane. Due to this behavior, combustion occurs near the latter symmetry plane as can be seen at the x = 100 mm axial plane. In comparison, the D29 flow field shows that the separated region does not extend as far which is a consequence of the lower momentum of the upstream jet in comparison to the single jet of the BSL29. The latter does induce a stronger upstream disturbance. Moreover, at x = 100 mm, combustion near the symmetry plane is much less intense than for the BSL29. This observation explains why the combustion efficiency in Figure 6.9 for BSL29 is increasing more rapidly at first. In terms of the counter rotating vortex pair (CVP, only one shown), at x = 100 mm, the spanwise penetration is very similar and some differences can be seen at the base (referred to as near-field entrainment in Figure 6.12). In the BSL29 result, the horseshoe vortex is located further away from the injection symmetry plane than the structure resulting from the interaction between the two horseshoe vortices in the D29 simulation. It is again a direct consequence of the disturbance induced by the upstream jet for D29 which has a lower momentum than the BSL29 jet. This finally explains the difference in base structure at x = 100 mm. When moving further downstream (x = 175 mm), the D29 result shows a larger spanwise penetration of the reaction zone coupled to the growth in the size of the CVP. The near-field entrainment observed at x = 100 mm is barely present. In comparison, the BSL29 case still shows a strong interaction between the base and the CVP. From x $\approx$ 225 mm, the contact surface between fuel and oxidizer is larger for D29 which explains why the combustion efficiency curve in Figure 6.9 exceeds the BSL29 from around that point.

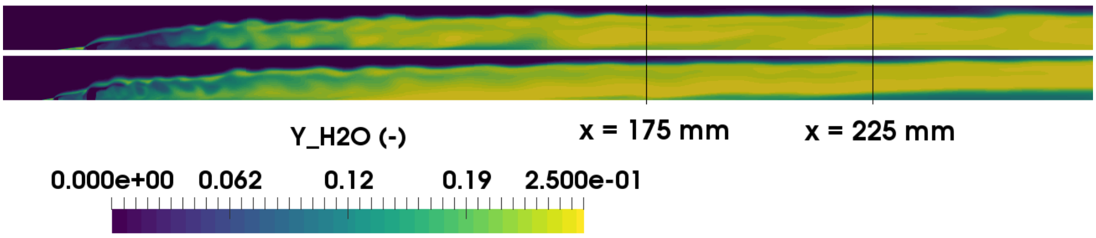

Figure 6.10: Instantaneous Y_{H_2O} contours inside the HyShot II combustor at injector symmetry plane with top: baseline, bottom: cascade injector. A_{edm} = 4, Pr_t = 0.9, Sc_t = 0.7, ER = 0.29.

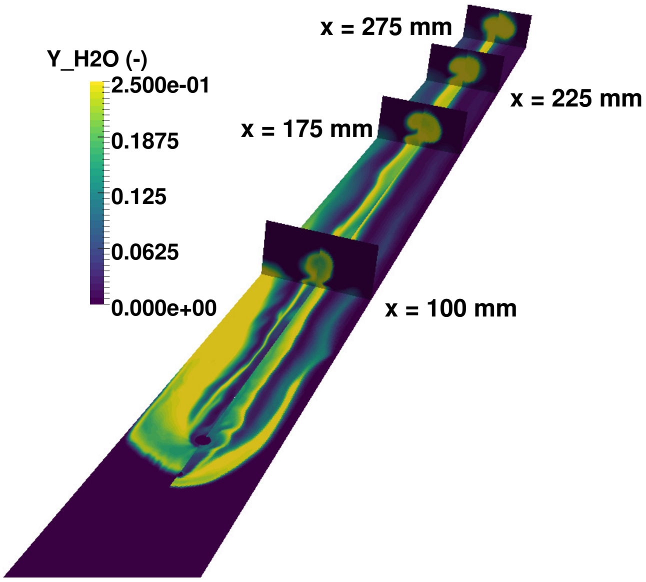

Figure 6.11: Instantaneous Y_{H_2O} contours for the HyShot II combustor at several axial locations with left: BSL29 and right: D29. A_{edm} = 4, Pr_t = 0.9, Sc_t = 0.7.

In terms of thrust potential, Table 6.1 indicates that there is barely any change in value at the combustor exit between the different simulations. This implies that the increase in combustion efficiency (heat release) observed for the upstream injection location is balanced by an increase in viscous and shock induced losses (total pressure). This also confirms that the HyShot II combustor is not well designed as a thrust

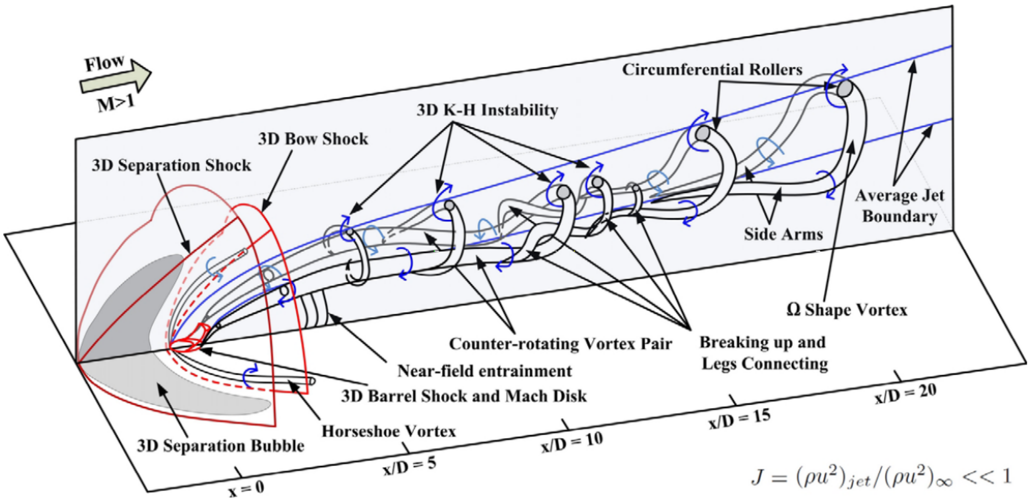

Figure 6.12: Shematic of vortex structures in a low J transverse jet. Reproduced from You et al. [244]

generating scramjet engine given the very low values of TP. A viable possibility to increase heat release whilst reducing the total pressure losses could consist of angular fuel injection instead (still with porthole mechanism). This should be looked at as part of future work. Figure 6.13 shows the TP along the combustor. The profiles for a given injector location do not drastically vary by changing the equivalence ratio.

In conclusion, locating the injector upstream (U29 and U35) results in the largest increase in performance, i.e. increase in combustion efficiency which is significantly larger than the increase in pressure losses. This has been demonstrated for two different ER's. However, the variation in thrust potential between the configurations is insignificant. Based solely on the latter metric, no topology can be considered superior to the others. This discussion concludes the demonstration of the EDM's capability in providing useful information inside a scramjet combustor which can be relied on for improving an existing scramjet combustor design.

6.3 Summary of Chapter

In this chapter the EDM is considered to improve the design of the HyShot II combustor. The injection strategy is varied for two different equivalence ratio's. Combustion efficiency, total pressure loss and thrust potential are considered as the metrics of

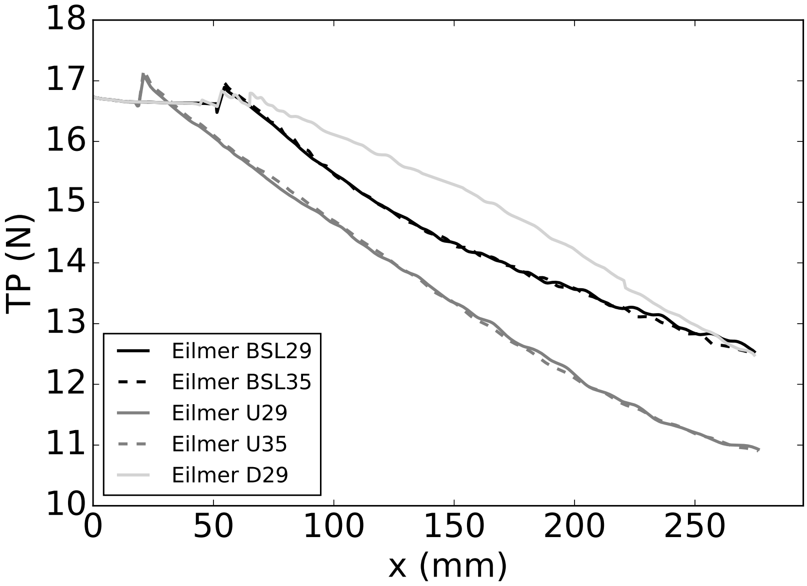

Figure 6.13: Thrust potential along the HyShot II combustor predicted with different injections.

interest for this design exercise. The former parameter can be increased with simple passive injection approaches. In terms of thrust potential it is however shown that the overall combustor performance does not vary much. The latter observation could be attributed to the test case itself as it was never intended to generate thrust.

Chapter 7

Conclusions and Future Work

7.1 Contributions

The design of scramjet propulsion systems for operation over a broad range of flight Mach numbers remains a challenging task. Advancements will require the combination of flight tests, ground tests and numerical models. Among the possible numerical methods, CFD plays a major role in furthering current understanding. Tackling turbulent compressible and chemically reacting flows inside a scramjet can be a computationally demanding task. This characteristic renders typical CFD approaches unusable for rapid design analyses of scramjets, let alone, complete vehicle analyses. Within this context, the overall aim of this thesis was to:
formulate and implement a computationally affordable open-source CFD approach to describe scramjet combustion in an access-to-space scenario which can be relied on for cost effective preliminary design studies.
Several research questions were formulated in order to identify different tasks toward the realization of the above stated goal. A summary on the realized tasks and answers to these different questions is now given.

The compressible flow solver Eilmer was selected for the numerical studies in the present work. Its use was assessed in non-reacting and reacting conditions in Chapter 4. The turbulence model adopted by the solver, Wilcox' k-ω 2006 model, has not been extensively used within the scramjet simulation community. It was therefore important to assess the suitability of the model in conditions relevant to this thesis' final aim. Four scramjet combustor test cases were selected for study in: the experiment of Burrows and Kurkov, the DLR combustor, the HyShot II combustor and Lorrain's scramjet simulations. Predictions with Eilmer were compared to experimental data and reference CFD solutions. The study displayed an overall good performance of Wilcox' k-ω 2006 turbulence model and validated its adequateness for scramjet internal flow paths with and without reactions. Sensitivity studies to the values of turbulent Prandtl and Schmidt numbers were performed in order to find the optimal combination for further considerations.

Furthermore, Wilcox' dilatation dissipation correction was implemented in Eilmer. Its influence on the flow field was investigated for the experiment of Burrows and Kurkov and the DLR combustor. The simulations in Chapter 4 showed a very limited influence of the correction on the overall flow field and was consequently not considered in subsequent studies.

The EDM was selected to describe the combustion process in scramjets operating at high flight Mach numbers typical of an access-to-space scenario. The model assumes a mixing-limited combustion process and is computationally cheap, hence showing the potential for design considerations. It has therefore been implemented in the Eilmer flow solver. The EDM relies on the specification of a constant A_{edm} for which no consistent guidelines are available in the literature. A sensitivity study on the EDM constant has been performed in Chapter 5 for the experiment of Burrows and Kurkov, the DLR combustor and the HyShot II combustor. The configurations were chosen because the flow conditions are representative for a primarily mixing-limited combustion process. Moreover, each of the test cases is characterized by a different fuel injection type. The experimental setting of Burrows and Kurkov studied the supersonic combustion between parallel streams of hydrogen and vitiated air. Fuel is injected behind a wedge in the DLR combustor and transversely from a porthole injector in the HyShot II combustor. For the experiment of Burrows and Kurkov, results with $A_{edm} = 4$ and 6 were very similar. In the DLR test case, the EDM formulation has proven to have difficulties in capturing the general trends in the combustion process with enough accuracy. The strong influence of the turbulence setting (turbulence Prandtl and Schmidt) on the test case and the limitations of RANS in simulating shear layer flows is thought to be the cause for the observations. Overall a setting $A_{edm} = 4$ is adviced. The same model constant setting resulted in a good agreement with experimental wall pressure traces in the HyShot II combustor.

Simulations with the EDM and a kinetic limit have been performed on the experiment of Burrows and Kurkov and on the DLR combustor. When activating the kinetic limit, the flow solver evaluates the reaction rate with the EDM and with the no-model approach and a single-step global reaction. The minimum of both is then considered to provide the fuel reaction rate. The effect of the kinetic limit on the Burrows and Kurkov combustor was limited to a very small region near the point of injection. This did not affect the downstream combustor region. The result is explained by the high temperature of the vitiated air stream. The kinetic limit resulted in suppressed combustion on the lower part of the DLR combustor which is not experimentally observed. In conclusion, the kinetic limit has not shown evident superiority on the standard EDM and its use was not further considered for primarily mixing-limited scramjets.

Simulating the experiment of Burrows and Kurkov with an estimate of the ignition delay did significantly improve the predictions in comparison with experimental data and is shown in Chapter 5. Prior to the estimated onset of ignition location, no combustion is allowed to occur. In the DLR and HyShot II combustor, different combustion zones were identified. A different value for A_{edm} could be applied in each zone and is considered as possible future work. This zonal use could as well be applied to the values of turbulence Prandtl and Schmidt numbers.

The EDM is applied to a scramjet configuration which is designed to be mainly kinetically limited, the scramjet of Lorrain in Chapter 5. The aim of this study is to assess if the EDM with kinetic limit is effective, and by doing so, extending the application of the approach considered in this work. The EDM is compared to the no-model approach with detailed reaction mechanism. The CFD study demonstrated the need for applying the kinetic limit in conjunction with the EDM in order to avoid an unstart behavior which is not experimentally observed. The motivation for this setting is explained by the near wall ignition of the flow coupled with a high specific dissipation rate predicted by the turbulence model. Similar values of thrust, with respect to the no-model approach, can be obtained by tuning the A_{edm} constant. The same observation is made for the wall pressure trace. A single setting of A_{edm} is unable to provide a good agreement with the different performance metrics (thrust and combustion efficiency).

The EDM was adopted in Chapter 6 for the study of the injection within the HyShot II combustor. For two different equivalence ratio's, locating the injector upstream the baseline location did significantly improve the combustion efficiency. The total pressure losses did as well increase but not as much as the latter parameter. A dual transverse (or cascade) injector topology was also compared to the baseline configuration at a single equivalence ratio. The gain in combustion efficiency of this passive approach was not much higher than the increased pressure losses. The thrust potential did not vary significantly between the different injection configurations indicating an overall poor performance of the current HyShot II combustor.

7.2 Future Research

During the realization of this work several research directions were identified which extended well beyond the scope of this work. These are now detailed:

Regarding the Eilmer flow solver

Simulations presented in this work have been obtained with the Eilmer3 flow solver which adopts explicit time stepping on structured grids. It has been mentioned that an updated flow solver, Eilmer4, is currently under development. This flow solver is unstructured and contains a steady-state solver based on a Newton-Krylov approach. The benefit in computational cost of the combustion model implemented in the solver can be increased by decreasing mesh size and performing steady-state simulations. Therefore, a first suggestion for future work would be to run some of the current scramjet combustors with the new tools available in Eilmer4.

Another working point could be the implementation of a variable turbulent Prandtl and Schmidt number approach. This would remove the necessity to specify a constant value for these number or the need to perform case dependent sensitivity studies. By adopting the EDM, the stiffness of the system of governing equations has been alleviated. A variable turbulent Prandtl and Schmidt number approach would result in the addition of two extra transport equations. The computational cost would increase but the benefit of the EDM will still remain.

Regarding the EDM for Scramjet Design

The EDM has a known limitation of overestimating the temperature and is unable to account for ignition and blow-out. The kinetic limit, which should improve these drawbacks, has proven to not be very effective in the scramjet conditions considered in this work. A review of the literature on the EDM discussed the attempt of tuning a-priori the model constants with the help of perfectly and partially stirred reactors. This methodology needs to be further explored and could potentially provide a simple way of dealing with current limitations of the model including blow-out.

Another possibility that could result in a decrease in the peak temperature predictions consists of considering the adiabatic flame temperature. This temperature is the maximum temperature which, given a certain composition, can physically be obtained. In other words, the new temperature obtained with the EDM should be compared to the adiabatic flame temperature and if exceeded, the reaction rate predicted by the EDM must be decreased. Ideally, this should be done in every cell of the computational domain but could become very costly and might require multiple iterations per cell. The idea of this approach could be exploited in order to formulate a more viable option.

Within this work, the possibility of applying the EDM in a zonal description has been identified. The approach should be tested and potential first test cases could be the DLR and HyShot II combustor. Note that this could only work if the flow field is steady state as the idea is to use geometric zones where the EDM constant(s) is varied based on the flame behavior, e.g. convection vs diffusion dominated. If proven beneficial, a more elaborate method could be considered for a spatio-temporally evolving flow field.

The EDM can be considered in the design process of the SPARTAN vehicle. More specifically, a propulsion database can be generated for the REST engine which can then be used in the trajectory optimization process. With this, the overall fidelity will be increased.

In this work only hydrogen-fueled scramjets have been considered. It has been pointed out that the benefits of the EDM in reducing the computational cost are larger when hydrocarbon fuels are considered. Therefore, scramjets with the latter fuel type should be explored next.

Bibliography

[1] S Bandyopadhyay, R Foust, GP Subramanian, S-J Chung, and FY Hadaegh. Review of formation flying and constellation missions using nanosatellites. *Journal of Spacecraft and Rockets*, (0):567–578, 2016.

[2] T Wekerle, JB Pessoa Filho, LEVL Costa, and LG Trabasso. Status and trends of smallsats and their launch vehicles—an up-to-date review. *Journal of Aerospace Technology and Management*, 9(3):269–286, 2017.

[3] K Maine, C Devieux, and P Swan. Overview of IRIDIUM satellite network. In *WESCON/'95. Conference record.'Microelectronics Communications Technology Producing Quality Products Mobile and Portable Power Emerging Technologies'*, page 483. IEEE, 1995.

[4] E Buchen. Small satellite market observations. In *29th Annusal AIAA/USU Conference on Small Satellites, SSC15-VII-7*, 2015.

[5] D Preller and MK Smart. Reusable launch of small satellites using scramjets. *Journal of Spacecraft and Rockets*, pages 1–13, 2017.

[6] C Niederstrasser and W Frick. Small launch vehicles–a 2015 state of the industry survey. In *29th Annusal AIAA/USU Conference on Small Satellites, SSC15-II-7*, 2015.

[7] T Jazra, D Preller, and MK Smart. Design of an airbreathing second stage for a rocket-scramjet-rocket launch vehicle. *Journal of Spacecraft and Rockets*, 50(2):411–422, 2013.

[8] MK Smart and MR Tetlow. Orbital delivery of small payloads using hypersonic airbreathing propulsion. *Journal of Spacecraft and Rockets*, 46(1):117–125, 2009.

[9] KW Flaherty, KM Andrews, and GW Liston. Operability benefits of airbreathing hypersonic propulsion for flexible access to space. *Journal of Spacecraft and Rockets*, 47(2):280–287, 2010.

[10] WO Landsberg. *Improving Performance of High Mach Number Scramjets: Fuelling Strategies and Combustor Design.* PhD thesis, University of Queensland, Australia, 2018.

[11] C Bruno and PA Czysz. *Future spacecraft propulsion systems: enabling technologies for space exploration.* Springer Science & Business Media, 2009.

[12] T Jazra and MK Smart. Design methodology for the airbreathing second stage of a rocket-scramjet-rocket launch vehicle. In *17th AIAA International Space Planes and Hypersonic Systems and Technologies Conference, San Francisco, California*, 2011.

[13] WJ Escher and BJ Flornes. A study of composite propulsion systems for advanced launch vehicle applications. Technical report, Vol 7, The Marquardt Corporation, Van Nuysm CA, 1966.

[14] JC Mankins. Highly reusable space transportation: Advanced concepts and the opening of the space frontier. *Acta Astronautica*, 51(10):727–742, 2002.

[15] L Bouheraoua. *Simulation aux grandes échelles et modélisation de la combustion supersonique*. PhD thesis, Rouen, INSA, 2014.

[16] LH Townend. Domain of the scramjet. *Journal of Propulsion and Power*, 17(6):1205–1213, 2001.

[17] S Resmi. Scramjet Engine: Why in News Headlines Now? https://www.clearias.com/scramjet-engine. Accessed: 2018-12-03.

[18] C Segal. *The scramjet engine: processes and characteristics*, volume 25. Cambridge University Press, 2009.

[19] MK Smart. Scramjet inlets. Technical report, University of Queensland, Center for Hypersonics, 2010.

[20] JP Drummond. Methods for prediction of high-speed reacting flows in aerospace propulsion. *AIAA journal*, 52(3):465–485, 2014.

[21] A Ferri. Possible directions of future research in air breathing engines. In *Proceedings of the Fourth AGARD Colloquium, Pergamon, New York*, 1961.

[22] S Defoort, M Ferrier, L Serre, J-L Pastre, C Paridaens, D Scherrer, A Ingenito, P Hendrick, and C Bruno. LAPCAT II: conceptual design of a Mach 8 TBCC civil aircraft, enforced by full Navier-Stokes 3D nose-to-tail computation. In *17th AIAA International Space Planes and Hypersonic Systems and Technologies Conference*, page 2317, 2011.

[23] T Langener, J Steelant, P Roncioni, P Natale, and M Marini. Preliminary performance analysis of the lapcat-mr2 by means of nose-to-tail computations. In *18th AIAA/3AF international space planes and hypersonic systems and technologies conference*, page 5872, 2012.

[24] TF O'Brien, RP Starkey, and MJ Lewis. Quasi-one-dimensional high-speed engine model with finite-rate chemistry. *Journal of propulsion and power*, 17(6):1366–1374, 2001.

[25] MK Smart, NE Hass, and A Paull. Flight data analysis of the hyshot 2 scramjet flight experiment. *AIAA journal*, 44(10):2366–2375, 2006.

[26] C McClinton. X-43-scramjet power breaks the hypersonic barrier: Dryden lectureship in research for 2006. In *44th AIAA aerospace sciences meeting and exhibit*, page 1, 2006.

[27] M Lewis. X-51 scrams into the future. *Aerospace America*, 48(9):27–31, 2010.

[28] J Hank, J Murphy, and R Mutzman. The x-51a scramjet engine flight demonstration program. In *15th AIAA International Space Planes and Hypersonic Systems and Technologies Conference*, page 2540, 2008.

[29] D Dolvin. Hypersonic international flight research and experimentation (hifire) fundamental science and technology development strategy. In *15th AIAA International Space Planes and Hypersonic Systems and Technologies Conference*, page 2581, 2008.

[30] MK Smart and MV Suraweera. HIFiRE 7-development of a 3-D scramjet for flight testing. *AIAA Paper*, 7259:2009, 2009.

[31] KG Bowcutt, A Paull, D Dolvin, and MK Smart. HIFiRE: An international collaboration to advance the science and technology of hypersonic flight. In *Proceedings of the 28th International Congress of the Aeronautical Sciences*, pages 2012–998. ICAS Secretariat RA Leiden, The Netherlands, 2012.

[32] AD Gardner, K Hannemann, A Paull, and J Steelant. Post flight analysis of the hyshot supersonic combustion flight experiment in heg. In *Fifth European Symposium on Aerothermodynamics for Space Vehicles*, volume 563, page 535, 2005.

[33] P Ferlemann. Hyper-x mach 10 scramjet preflight predictions and flight data. In *AIAA/CIRA 13th International Space Planes and Hypersonics Systems and Technologies Conference*, page 3352, 2005.

[34] T Mai. Technology Readiness Level. https://www.nasa.gov/directorates/heo/scan/engineering/technology/txt_accordion1.html. Accessed: 2018-04-16, Last Updated: 2012-08-07.

[35] KG Bowcutt and SJ Hatakeyama. Challenges, enabling technologies and technology maturity for responsive space. In *AIAA 2nd Responsive Space Conference. AIAA*, volume 6005, 2004.

[36] T Barber, B Maicke, and J Majdalani. Current state of high speed propulsion: Gaps, obstacles and technological challenges in hypersonic applications. In *45th AIAA/ASME/SAE/ASEE Joint Propulsion Conference & Exhibit*, page 5118, 2009.

[37] DJ Mee. Boundary-layer transition measurements in hypervelocity flows in a shock tunnel. *AIAA journal*, 40(8):1542–1548, 2002.

[38] T André, A Durant, and I Fedioun. Hypersonic boundary-layer transition tripped by wall injection: Global mode analysis. In *20th AIAA International Space Planes and Hypersonic Systems and Technologies Conference*, page 3525, 2015.

[39] MK Smart. How much compression should a scramjet inlet do? *AIAA journal*, 50(3):610–619, 2012.

[40] S Karl and J Steelant. Crossflow phenomena in streamline-traced hypersonic intakes. *Journal of Propulsion and Power*, pages 1–11, 2017.

[41] L Krishnan, ND Sandham, and J Steelant. Shock-wave/boundary-layer interactions in a model scramjet intake. *AIAA journal*, 47(7):1680–1691, 2009.

[42] ND Sandham, E Schülein, A Wagner, S Willems, and J Steelant. Transitional shock-wave/boundary-layer interactions in hypersonic flow. *Journal of Fluid Mechanics*, 752:349–382, 2014.

[43] J Larsson, S Laurence, I Bermejo-Moreno, J Bodart, S Karl, and R Vicquelin. Incipient thermal choking and stable shock-train formation in the heat-release region of a scramjet combustor. part ii: Large eddy simulations. *Combustion and Flame*, 162(4):907–920, 2015.

[44] NC Dröske. *Investigation of Thermal Loads onto a Cooled Strut Injector inside a Scramjet Combustion Chamber*. PhD thesis, University of Stuttgart, Germany, 2016.

[45] NC Dröske, FJ Förster, B Weigand, and J von Wolfersdorf. Thermal investigation of an internally cooled strut injector for scramjet application at moderate and hot gas conditions. *Acta Astronautica*, 132:177–191, 2017.

[46] J Lee, K-C Lin, and D Eklund. Challenges in fuel injection for high-speed propulsion systems. *AIAA Journal*, 53(6):1405–1423, 2015.

[47] S-H Lee. Characteristics of dual transverse injection in scramjet combustor, part 1: Mixing. *Journal of Propulsion and Power*, 22(5):1012–1019, 2006.

[48] S-H Lee. Characteristics of dual transverse injection in scramjet combustor, part 2: Combustion. *Journal of Propulsion and Power*, 22(5):1020–1026, 2006.

[49] WO Landsberg, V Wheatley, and A Veeraragavan. Characteristics of cascaded fuel injectors within an accelerating scramjet combustor. *AIAA Journal*, pages 3692–3700, 2016.

[50] TG Drozda and R Baurle. Cfd analysis of mixing characteristics of several fuel injectors at hypervelocity flow conditions. In *52nd AIAA/SAE/ASEE Joint Propulsion Conference*, page 4764, 2016.

[51] WO Landsberg, NN Gibbons, V Wheatley, MK Smart, and A Veeraragavan. Improving scramjet performance through flow field manipulation. *Journal of Propulsion and Power*, pages 1–13, 2017.

[52] JR Llobet Gomez. *Numerical and Experimental Investigation of Hypersonic Streamwise Vortices and their Effect on Mixing*. PhD thesis, University of Queensland, Australia, 2018.

[53] ZJ Denman, WYK Chan, S Brieschenk, A Veeraragavan, V Wheatley, and MK Smart. Ignition experiments of hydrocarbons in a mach 8 shape-transitioning scramjet engine. *Journal of Propulsion and Power*, 32(6):1462–1471, 2016.

[54] ZJ Denman. *Supersonic combustion of hydrocarbon fuels in a three-dimensional Mach 8 scramjet*. PhD thesis, University of Queensland, Australia, 2017.

[55] ED Gonzalez-Juez, AR Kerstein, R Ranjan, and S Menon. Advances and challenges in modeling high-speed turbulent combustion in propulsion systems. *Progress in Energy and Combustion Science*, 60:26–67, 2017.

[56] S Karl, S Laurence, JM Schramm, and K Hannemann. CFD Analysis of Unsteady Combustion Phenomena in the HyShot-II Scramjet Configuration. In *18th AIAA/3AF International Space Planes and Hypersonic Systems and Technologies Conference*, page 5912, 2012.

[57] J Steelant, M Dalenbring, M Kuhn, M Bouchez, and J von Wolfersdorf. Achievements obtained within ATLLAS-II on Aero-Thermal Loaded Material Investigations for High-Speed Vehicles. In *21st AIAA International Space Planes and Hypersonics Technologies Conference*, page 2393, 2017.

[58] U Mehta. Hydrogen for hypersonic civil transportation. Technical report, NASA Ames Research Center, 2017.

[59] SO Forbes-Spyratos, MP Kearney, MK Smart, and IH Jahn. Trajectory design of a rocket-scramjet-rocket multi-stage launch system. In *21st AIAA International Space Planes and Hypersonics Technologies Conference*, page 2107, 2017.

[60] P Toniato, D Gildfind, Andreas A, and RG Morgan. Full free-stream mach 12 scramjet testing in expansion tubes. In *AIAA Aviation and Aeronautics Forum and Exposition*, 2018.

[61] M Dharavath, P Manna, and D Chakraborty. Computational fluid dynamics simulation of tip-to-tail for hypersonic test vehicle. *Journal of Propulsion and Power*, 31(5):1370–1379, 2015.

[62] D Preller and MK Smart. Spartan: Scramjet powered accelerator for reusable technology advancement. In *Proceedings of the 12th Reinventing Space Conference*, pages 139–147. Springer, 2017.

[63] MK Smart. Scramjets. *The Aeronautical Journal*, 111(1124):605–619, 2007.

[64] MK Smart. Flow modeling of pseudoshocks in backpressured ducts. *AIAA Journal*, 53(12):3577–3588, 2015.

[65] EJ Nielsen and WL Kleb. Efficient construction of discrete adjoint operators on unstructured grids using complex variables. *AIAA journal*, 44(4):827–836, 2006.

[66] A Mogavero, IJ Taylor, and RE Brown. Hybrid propulsion parametric and modular model: a novel engine analysis tool conceived for design optimization. In *19th AIAA International Space Planes and Hypersonic Systems and Technologies Conference, Atlanta GA*, pages 16–20, 2014.

[67] A Mogavero. *Toward automated design of Combined Cycle Propulsion*. PhD thesis, 2016.

[68] A Mogavero and RE Brown. A modular fast model for the design and optimization of hypersonic vehicle propulsion systems. *Spacecraft and Rockets*, 2018. accepted for publication, 10.2514/1.A33676.

[69] R Wuilbercq, F Pescetelli, A Mogavero, E Minisci, and RE Brown. Robust multidisciplinary design and optimisation of a reusable launch vehicle. In *19th AIAA International Space Planes and Hypersonic Systems and Technologies Conference*, page 2363, 2014.

[70] MK Smart. Scramjet isolators. Technical report, University of Queensland, Center for Hypersonics, 2010.

[71] RJ Kee, FM Rupley, and JA Miller. Chemkin-ii: A fortran chemical kinetics package for the analysis of gas-phase chemical kinetics. Technical report, Sandia National Labs., Livermore, CA (USA), 1989.

[72] CH Birzer and CJ Doolan. Quasi-one-dimensional model of hydrogen-fueled scramjet combustors. *Journal of propulsion and power*, 25(6):1220–1225, 2009.

[73] S Torrez, J Driscoll, M Bolender, M Oppenheimer, and D Doman. Effects of improved propulsion modelling on the flight dynamics of hypersonic vehicles. In *AIAA Atmospheric Flight Mechanics Conference and Exhibit*, page 6386, 2008.

[74] SM Torrez, JF Driscoll, M Ihme, and ML Fotia. Reduced-order modeling of turbulent reacting flows with application to ramjets and scramjets. *Journal of propulsion and power*, 27(2):371–382, 2011.

[75] SM Torrez, DJ Dalle, and JF Driscoll. Design of dual-mode hypersonic vehicle flow paths using a reduced-order model. In *17th AIAA International Space Planes and Hypersonic Systems and Technologies Conference*, 2011.

[76] SM Torrez, DJ Dalle, and JF Driscoll. New method for computing performance of choked reacting flows and ram-to-scram transition. *Journal of Propulsion and Power*, 29(2):433–445, 2013.

[77] JT Walton. Srgull-an advanced engineering model for the prediction of airframe integrated scramjet cycle performance. 1994.

[78] SZ Pinckney, SM Ferlemann, G Mills, and N Takashima. Program manual for srgull, version 1.0: Second generation engineering model for the prediction of airframe-integrated subsonic/supersonic combustion ramjet cycle performance. *NASA Langley Research Center Report HX-829*, 2000.

[79] RA Baurle and RL Gaffney. Extraction of one-dimensional flow properties from multidimensional data sets. *Journal of Propulsion and Power*, 24(4):704–714, 2008.

[80] JR Edwards and JA Fulton. Development of a RANS and LES/RANS flow solver for high-speed engine flowpath simulations. In *20th AIAA International Space Planes and Hypersonic Systems and Technologies Conference*, page 3570, 2015.

[81] DG Goodwin, HK Moffat, and RL Speth. Cantera: An Object-oriented Software Toolkit for Chemical Kinetics, Thermodynamics, and Transport Processes. http://www.cantera.org, 2017. Version 2.3.0.

[82] Heliaq Advanced Engineering. SPARTAN Description. http://heliaq.com/project-information/spartan-description. Accessed: 2017-8-02.

[83] PD Vogel. Numerical simulation of a hypervelocity scramjet engine. Master's thesis, 2012.

[84] P Lorrain. *Flow structure/chemistry coupling in the ignition process in shock-induced-combustion scramjets*. PhD thesis, University of Queensland, Australia, 2014.

[85] RM Kirchhartz. *Upstream Wall Layer Effects on Drag Reduction with Boundary Layer Combustion*. PhD thesis, University of Queensland, Australia, 2009.

[86] S Karl. *Numerical investigation of a generic scramjet configuration*. PhD thesis, Saechsische Landesbibliothek-Staats-und Universitaetsbibliothek Dresden, 2011.

[87] ML Fotia. *Experimental study of shock-train/combustion coupling and flame dynamics in a heated supersonic flow*. PhD thesis, The University of Michigan, 2012.

[88] JE Barth. *Mixing and Combustion Enhancements in a Mach 12 Shape-Transitioning Scramjet Engine*. PhD thesis, University of Queensland, Australia, 2014.

[89] LJ Doherty. *An Experimental Investigation of an Airframe Integrated Three-Dimensional Scramjet Engine at a Mach 10 Flight Condition*. PhD thesis, University of Queensland, Australia, 2014.

[90] T Vanyai. *Experimental Investigation of a 3D Thermal Compression Scramjet Using Advanced Optical Techniques*. PhD thesis, University of Queensland, Australia, 2018.

[91] J Steelant, A Mack, K Hannemann, and AD Gardner. Comparison of supersonic combustion tests with shock tunnels, flight and CFD. In *42nd AIAA/ASME/SAE/ASEE Joint Propulsion Conference and Exhibit*, Sacramento, California, July 2006.

[92] AF Moura, V Wheatley, TJ McIntyre, and I Jahn. On the development of a mach 10 scramjet engine for investigation of supersonic combustion regimes. In *20th Australian Fluid Mechanics Conference, Perth, Australia*, 2016.

[93] RA Baurle. Modeling of high speed reacting flows: established practices and future challenges. *AIAA paper*, 267:2004, 2004.

[94] NJ Georgiadis, DA Yoder, MA Vyas, and WA Engblom. Status of turbulence modeling for hypersonic propulsion flowpaths. *Theoretical and Computational Fluid Dynamics*, 28(3):295–318, 2014.

[95] SK Lele and J Larsson. Shock-turbulence interaction: What we know and what we can learn from peta-scale simulations. In *Journal of Physics: Conference Series*, volume 180, page 012032. IOP Publishing, 2009.

[96] C Fureby, M Chapuis, E Fedina, and S Karl. Cfd analysis of the hyshot ii scramjet combustor. *Proceedings of the Combustion Institute*, 33(2):2399–2405, 2011.

[97] F Génin and S Menon. Simulation of turbulent mixing behind a strut injector in supersonic flow. *AIAA Journal*, 48(3):526, 2010.

[98] W Waidmann, F Alff, U Brummund, M Böhm, W Clauss, and M Oschwald. Experimental investigation of the combustion process in a supersonic combustion ramjet (scramjet). *DGLR Jahrbuch*, pages 629–638, 1994.

[99] AS Potturi and JR Edwards. Hybrid Large-Eddy/Reynolds-averaged Navier–Stokes simulations of flow through a model scramjet. *AIAA Journal*, 2014.

[100] MC Burrows and AP Kurkov. Analytical and experimental study of supersonic combustion of hydrogen in a vitiated airstream. Technical report, NASA Lewis Research Center, September 1973.

[101] JR Edwards, JA Boles, and RA Baurle. Large-eddy/Reynolds-averaged Navier–Stokes simulation of a supersonic reacting wall jet. *Combustion and Flame*, 159(3):1127–1138, 2012.

[102] S Karl, K Hannemann, A Mack, and J Steelant. CFD analysis of the HyShot II scramjet experiments in the HEG shock tunnel. In *15th AIAA International Space Planes and Hypersonic Systems and Technologies Conference*, page 2548, 2008.

[103] V Terrapon, F Ham, R Pecnik, and H Pitsch. A flamelet-based model for supersonic combustion. *Annual research briefs*, pages 47–58, 2009.

[104] W Huang, Z Wang, S Li, and W Liu. Influences of H2O mass fraction and chemical kinetics mechanism on the turbulent diffusion combustion of H2–O2 in supersonic flows. *Acta Astronautica*, 76:51–59, 2012.

[105] R Pecnik, VE Terrapon, F Ham, G Iaccarino, and H Pitsch. Reynolds-averaged navier-stokes simulations of the hyshot ii scramjet. *AIAA journal*, 50(8):1717–1732, 2012.

[106] JS Evans, CJ Schexnayder Jr, and HL Beach Jr. Application of a two-dimensional parabolic computer program to prediction of turbulent reacting flows. 1978.

[107] JS Evans and CJ Schexnayder. Influence of chemical kinetics and unmixedness on burning in supersonic hydrogen flames. *AIAA Journal*, 18(2):188–193, 1980.

[108] HB Ebrahimi. CFD validation for scramjet combustor and nozzle flows, part i. *AIAA Paper*, 1840:1993, 1993.

[109] Y d'Angelo. *Analyse et simulation numérique de phénomènes liés à la combustion supersonique*. PhD thesis, Ecole Nationale des Ponts et Chaussées, 1994.

[110] S Melen. *Modélisation et étude numérique de la combustion supersonique turbulente non-prémélangée, approche probabiliste*. PhD thesis, Université de Rouen, 1995.

[111] M Oevermann. Numerical investigation of turbulent hydrogen combustion in a scramjet using flamelet modeling. *Aerospace science and technology*, 4(7):463–480, 2000.

[112] WA Engblom, FC Frate, and Nelson CC. Progress in validation of Wind-US for ramjet/scramjet combustion. In *43rd AIAA Aerospace Sciences Meeting and Exhibit*, Reno, Nevada, January 2005.

[113] KW Brinckman, WH Calhoon, and SM Dash. Scalar fluctuation modeling for high-speed aeropropulsive flows. *AIAA Journal*, 45(5):1036–1046, 2007.

[114] J-F Izard, G Lehnasch, and A Mura. A lagrangian model of combustion in high-speed flows: Application to scramjet conditions. *Combustion Science and Technology*, 181(11):1372–1396, 2009.

[115] A Mura and JF Izard. Numerical simulation of supersonic nonpremixed turbulent combustion in a scramjet combustor model. *Journal of Propulsion and Power*, 26(4):858–868, 2010.

[116] L Gomet, V Robin, and A Mura. Influence of residence and scalar mixing time scales in non-premixed combustion in supersonic turbulent flows. *Combustion Science and Technology*, 184(10-11):1471–1501, 2012.

[117] M Dharavath, P Manna, and D Chakraborty. Thermochemical exploration of hydrogen combustion in generic scramjet combustor. *Aerospace Science and Technology*, 24(1):264–274, 2013.

[118] CG Rodriguez and AD Cutler. Numerical analysis of the scholar supersonic combustor. 2003.

[119] B Parent and JP Sislian. Validation of the wilcox k-omega model for flows characteristic to hypersonic airbreathing propulsion. *AIAA Journal*, 42(2):261–270, 2004.

[120] AD Cutler, GS Diskin, JP Drummond, and JA White. Supersonic coaxial jet experiment for computational fluid dynamics code validation. *AIAA journal*, 44(3):585–592, 2006.

[121] DC Alexander, JP Sislian, and B Parent. Hypervelocity fuel/air mixing in mixed-compression inlets of shcramjets. *AIAA journal*, 44(10):2145, 2006.

[122] DC Alexander and JP Sislian. Computational study of the propulsive characteristics of a shcramjet engine. *Journal of Propulsion and Power*, 24(1):34–44, 2008.

[123] WYK Chan, PA Jacobs, and DJ Mee. Suitability of the k–ω turbulence model for scramjet flowfield simulations. *International Journal for Numerical Methods in Fluids*, 70(4):493–514, 2012.

[124] RJ Yentsch, DV Gaitonde, and R Kimmel. Performance of turbulence modeling in simulation of the hifire-1 flight test. *Journal of Spacecraft and Rockets*, 51(1):117–127, 2013.

[125] Wilson YK Chan, David J Mee, Michael K Smart, and James C Turner. Drag reduction by boundary-layer combustion: Effects of flow disturbances from rectangular-to-elliptical-shape-transition inlets. *Journal of Propulsion and Power*, 31(5):1256–1267, 2015.

[126] J-Y Choi, F Ma, and V Yang. Combustion oscillations in a scramjet engine combustor with transverse fuel injection. *Proceedings of the Combustion Institute*, 30(2):2851–2858, 2005.

[127] V Bhagwandin, W Engblom, and N Georgiadis. Numerical simulation of a hydrogen-fueled dual-mode scramjet engine using Wind-US. In *45th AIAA/ASME/SAE/ASEE Joint Propulsion Conference & Exhibit*, page 5382, 2009.

[128] Y Moule. *Modélisation et Simulation de la Combustion dans les Ecoulements Rapides. Applications aux Superstatoréacteurs.* PhD thesis, Ecole Nationale Supérieure de Mécanique et d'Aérotechnique-Poitiers, 2013.

[129] Z Gao, C Jiang, S Pan, and CH Lee. Combustion heat-release effects on supersonic compressible turbulent boundary layers. *AIAA Journal*, 53(7):1949–1968, 2015.

[130] J Quinlan, JC McDaniel, TG Drozda, G Lacaze, and JC Oefelein. A priori analysis of flamelet-based modeling for a dual-mode scramjet combustor. In *50th AIAA/ASME/SAE/ASEE Joint Propulsion Conference*, page 3743, 2014.

[131] L Hou, D Niu, and Z Ren. Partially premixed flamelet modeling in a hydrogen-fueled supersonic combustor. *International Journal of Hydrogen Energy*, 39(17):9497–9504, 2014.

[132] N Droeske, P Nizenkov, JJ Vellaramkalayil, J von Wolfersdorf, K Makowka, and T Sattelmayer. Validation of a novel openfoam solver using a supersonic, non-reacting channel flow. In *19th AIAA International Space Planes and Hypersonic Systems and Technologies Conference*, page 3088, 2014.

[133] FR Menter. Two-equation eddy-viscosity turbulence models for engineering applications. *AIAA Journal*, 32(8):1598–1605, 1994.

[134] DC Wilcox. Formulation of the k-ω turbulence model revisited. *AIAA Journal*, 46(11):2823–2838, 2008.

[135] JJOE Hoste, V Casseau, M Fossati, IJ Taylor, and RJ Gollan. Numerical modeling and simulation of supersonic flows in propulsion systems by open-source solvers. In *21st AIAA International Space Planes and Hypersonics Technologies Conference*, page 2411, 2017.

[136] DC Wilcox et al. *Turbulence modeling for CFD, Third Edition*. DCW industries La Canada, CA, 2006.

[137] T Poinsot and D Veynante. *Theoretical and Numerical Combustion, third edition*. RT Edwards, Inc., 2012.

[138] JP Drummond, GS Diskin, and AD Cutler. Fuel-air mixing and combustion in scramjets. 2002.

[139] T Mitani and T Kouchi. Flame structures and combustion efficiency computed for a mach 6 scramjet engine. *Combustion and Flame*, 142(3):187–196, 2005.

[140] T Kouchi, G Masuya, T Mitani, and S Tomioka. Mechanism and control of combustion-mode transition in a scramjet engine. *Journal of Propulsion and Power*, 28(1):106–112, 2012.

[141] PG Keistler, RL Gaffney, X Xiao, and HA Hassan. Turbulence modeling for scramjet applications. *AIAA paper*, 5382:2005, 2005.

[142] MSR Chandra Murty, D Chakraborty, and RD Mishal. Numerical simulation of supersonic combustion with parallel injection of hydrogen fuel. *Defence Science Journal*, 60(5), 2010.

[143] MSR Chandra Murty and D Chakraborty. Numerical simulation of angular injection of hydrogen fuel in scramjet combustor. *Proceedings of the Institution of Mechanical Engineers, Part G: Journal of Aerospace Engineering*, 226(7):861–872, 2012.

[144] Z Gao, J Wang, C Jiang, and C Lee. Application and theoretical analysis of the flamelet model for supersonic turbulent combustion flows in the scramjet engine. *Combustion Theory and Modelling*, 18(6):652–691, 2014.

[145] OR Kummitha. Numerical analysis of hydrogen fuel scramjet combustor with turbulence development inserts and with different turbulence models. *International Journal of Hydrogen Energy*, 42(9):6360–6368, 2017.

[146] M Chapuis, E Fedina, Christer Fureby, Klaus Hannemann, Sebastian Karl, and J Martinez Schramm. A computational study of the HyShot II combustor performance. *Proceedings of the Combustion Institute*, 34(2):2101–2109, 2013.

[147] TS Cheng, JA Wehrmeyer, RW Pitz, O Jarrett Jr, and GB Northam. Raman measurement of mixing and finite-rate chemistry in a supersonic hydrogen-air diffusion flame. *Combustion and Flame*, 99(1):157–173, 1994.

[148] CT Johansen, CD McRae, PM Danehy, ECA Gallo, LML Cantu, G Magnotti, AD Cutler, RD Rockwell, CP Goyne, and JC McDaniel. Oh plif visualization of the uva supersonic combustion experiment: configuration a. *Journal of Visualization*, 17(2):131–141, 2014.

[149] CJ Jachimowski. An analysis of combustion studies in shock expansion tunnels and reflected shock tunnels. 1992.

[150] J Odam and A Paull. Radical farming in scramjets. In *New Results in Numerical and Experimental Fluid Mechanics VI*, pages 276–283. Springer, 2007.

[151] A Ingenito and C Bruno. Physics and regimes of supersonic combustion. *AIAA Journal*, 48(3):515, 2010.

[152] Antonio Ferri. Mixing-controlled supersonic combustion. *Annual Review of Fluid Mechanics*, 5(1):301–338, 1973.

[153] BF Magnussen and BH Hjertager. On mathematical modeling of turbulent combustion with special emphasis on soot formation and combustion. In *Symposium (international) on Combustion*, volume 16, pages 719–729. Elsevier, 1977.

[154] J Urzay. Supersonic combustion in air-breathing propulsion systems for hypersonic flight. *Annual Review of Fluid Mechanics*, 50:593–627, 2018.

[155] JCT Turner. *An Experimental Investigation of Inlet Fuel Injection in a Three-Dimensional Scramjet Engine*. PhD thesis, University of Queensland, Australia, 2010.

[156] T Mitani, N Chinzei, and T Kanda. Reaction and mixing-controlled combustion in scramjet engines. *Journal of Propulsion and Power*, 17(2):308–314, 2001.

[157] Michael Smayda, P Vogel, I Schultz, R Hanson, Robert Foelsche, Chingyi Tsai, Daniel Cresci, and Christopher Goyne. Hypervelocity testing of a dual-mode scramjet. In *50th AIAA Aerospace Sciences Meeting Including the New Horizons Forum and Aerospace Exposition*, page 481, 2012.

[158] A Storch, M Bynum, J Liu, and M Gruber. Combustor operability and performance verification for hifire flight 2. In *17th AIAA International Space Planes and Hypersonic Systems and Technologies Conference*, page 2249, 2011.

[159] T Abdel-Salam, S Tiwari, S Chaturvedi, and T Mohieldin. Mixing and combustion in scramjet combustor with raised and relieved ramp. In *36th AIAA/ASME/SAE/ASEE Joint Propulsion Conference and Exhibit*, page 3709, 2000.

[160] TO Mohieldin, SN Tiwari, and David E Reubush. Numerical investigation of dual-mode scramjet combustor with large upstream interaction. 2004.

[161] N Luetke, T Mohieldin, and S Tiwari. Unsteady numerical analysis of hydrogen combustion in a dual mode engine. In *43rd AIAA/ASME/SAE/ASEE Joint Propulsion Conference & Exhibit*, page 5425, 2007.

[162] ANSYS. 7.1.2 The Generalized Finite-Rate Formulation for Reaction Modeling. http://www.afs.enea.it/project/neptunius/docs/fluent/html/th/node129.htm. Accessed: 2018-03-03, Last Updated: 2009-23-01.

[163] T Belmrabet, M Talice, G Delussu, and S Hanchi. Simulation numérique de la combustion dans un scramjet avec injection transversale de carburant. *Revue des Energies Renouvelables CISM*, 2008.

[164] D Chakraborty. Numerical simulation of liquid fueled scramjet combustor flow fields. *International Journal of Hypersonics*, 1(1):13–29, 2010.

[165] MSR Chandra Murty and D Chakraborty. Effect of injection angle in mixing and combustion characteristics of scramjet combustor. *Int. J. Hypersonics*, 2(1-2):15–27, 2011.

[166] M Dharavath, P Manna, and D Chakraborty. Numerical simulation of hydrogen air supersonic coaxial jet. *Journal of The Institution of Engineers (India): Series C*, 98(5):575–585, 2017.

[167] OR Kummitha. Numerical analysis of hydrogen fuel scramjet combustor with turbulence development inserts and with different turbulence models. *International Journal of Hydrogen Energy*, 42(9):6360–6368, 2017.

[168] OR Kummitha, L Suneetha, and KM Pandey. Numerical analysis of scramjet combustor with innovative strut and fuel injection techniques. *International journal of hydrogen energy*, 42(15):10524–10535, 2017.

[169] OR Kummitha. Numerical analysis of passive techniques for optimizing the performance of scramjet combustor. *International journal of hydrogen energy*, 42(15):10455–10465, 2017.

[170] OR Kummitha, KM Pandey, and R Gupta. Cfd analysis of a scramjet combustor with cavity based flame holders. *Acta Astronautica*, 2018.

[171] S Jindala and S Kumarb. Cfd modelling of scramjet combustor. In *International Conference on Theoretical, Applied, Computational and Experimental Mechanics, Kharagpur, India*, 2017.

[172] TG Drozda, RA Baurle, and JP Drummond. Impact of flight enthalpy, fuel simulant, and chemical reactions on the mixing characteristics of several injectors at hypervelocity flow conditions. Technical report, NASA Langley Research Center, Hampton, VA, United States, 2016.

[173] Jian Li, Fuhua Ma, Vigor Yang, Kuo-Cheng Lin, and Thomas Jackson. A comprehensive study of ignition transient in an ethylene-fueled scramjet combustor. In *43rd AIAA/ASME/SAE/ASEE Joint Propulsion Conference & Exhibit*, page 5025, 2007.

[174] L Zhang, V Yang, and K-C Lin. Transient operation of an ethylene-fueled scramjet engine with fuel staging. In *51st AIAA Aerospace Sciences Meeting*, pages 07–10, 2013.

[175] P Manna, R Behera, and D Chakraborty. Liquid-fueled strut-based scramjet combustor design: a computational fluid dynamics approach. *Journal of Propulsion and Power*, 24(2):274–281, 2008.

[176] P Manna, M Dharavath, PK Sinha, and D Chakraborty. Optimization of a flight-worthy scramjet combustor through cfd. *Aerospace science and technology*, 27(1):138–146, 2013.

[177] M Bynum and R Baurle. A design of experiments study for the hifire flight 2 ground test computational fluid dynamics results. In *17th AIAA International Space Planes and Hypersonic Systems and Technologies Conference*, page 2203, 2011.

[178] MR Borghi, WA Engblom, and NJ Georgiadis. Evaluation of mixing-limited quasi-global wind-us model for hifire 2 flowpath. In *52nd Aerospace Sciences Meeting*, page 1160, 2014.

[179] MR Borghi. Evaluation of mixing-limited quasi-global wind-us model for hifire 2 flowpath. Master's thesis, 2014.

[180] M Dharavath, P Manna, and D Chakraborty. Numerical exploration of mixing and combustion in ethylene fueled scramjet combustor. *Acta Astronautica*, 117:305–318, 2015.

[181] AT Norris. A-priori tuning of modified magnussen combustion model. 2016.

[182] LF Richardson. *Weather prediction by numerical process, First Edition*. Cambridge University Press, 1922.

[183] SB Pope. *Turbulent flows*. IOP Publishing, 2001.

[184] AN Kolmogorov. The local structure of turbulence in incompressible viscous fluid for very large reynolds numbers. In *Dokl. Akad. Nauk SSSR*, volume 30, pages 299–303, 1941.

[185] D Jou. Intermittent turbulence: a short introduction. *Scientia Marina*, 61:57–62, 1997.

[186] EF Toro. *Riemann solvers and numerical methods for fluid dynamics: a practical introduction,Third Edition*. Springer-Verlag, 2009.

[187] C Rumsey. Implementing Turbulence Models into the Compressible RANS Equations. https://turbmodels.larc.nasa.gov/implementrans.html. Accessed: 2018-05-02, Last Updated: 2017-10-01.

[188] C Rumsey. The Spalart-Allmaras Turbulence Model. https://turbmodels.larc.nasa.gov/spalart.html. Accessed: 2018-05-02, Last Updated: 2017-10-30.

[189] C Rumsey. The wilcox k-omega turbulence model. https://turbmodels.larc.nasa.gov/wilcox.html. Accessed: 2018-02-13, Last Updated:2016-10-08.

[190] CL Rumsey. Compressibility Considerations for k-ω Turbulence Models in Hypersonic Boundary-Layer Applications. *Journal of Spacecraft and Rockets*, 47(1):11–20, 2010.

[191] X Xiao, HA Hassan, and RA Baurle. Modeling scramjet flows with variable turbulent Prandtl and Schmidt numbers. *AIAA journal*, 45(6):1415–1423, 2007.

[192] P Keistler. *A variable turbulent Prandtl and Schmidt number model study for scramjet applications*. PhD thesis, 2009.

[193] A Bakker. Modeling Chemical Reactions with CFD: Reacting Flows - Lecture 10. http://www.bakker.org/dartmouth06/engs199/, 2006. Accessed: 2018-05-02, Last Updated: 2008-02-08.

[194] AT Norris and A Hsu. Comparison of pdf and moment closure methods in the modeling of turbulent reacting flows. In *30th Joint Propulsion Conference and Exhibit*, page 3356, 1994.

[195] H Pitsch. Modeling Turbulent Combustion: CEFRC Combustion Summer School. https://cefrc.princeton.edu/combustion-summer-school/archived-programs/2014-session/lecture-notes, 2014. Accessed: 2018-06-02.

[196] RJ Gollan and PA Jacobs. About the formulation, verification and validation of the hypersonic flow solver Eilmer. *International Journal for Numerical Methods in Fluids*, 73(1):19–57, 2013.

[197] PA Jacobs, RJ Gollan, AJ Denman, BT O'Flaherty, DF Potter, PJ Petrie-Repar, and IA Johnston. Eilmer's theory book: basic models for gas dynamics and thermochemistry. Technical report, The University of Queensland, 2012.

[198] PA Jacobs and RJ Gollan. Implementation of a compressible-flow simulation code in the D programming language. In *Applied Mechanics and Materials*, volume 846, pages 54–60. Trans Tech Publ, 2016.

[199] JP Drummond. A two-dimensional numerical simulation of a supersonic, chemically reacting mixing layer. 1988.

[200] M Carpenter. Three-dimensional computations of cross-flow injection and combustion in a supersonic flow. In *20th Fluid Dynamics, Plasma Dynamics and Lasers Conference*, page 1870, 1989.

[201] P Jacobs, RJ Gollan, D Potter, and many others. Eilmer3. http://cfcfd.mechmining.uq.edu.au/eilmer3.html, 2012.

[202] V Sridhar, SL Gai, and H Kleine. A numerical investigation of supersonic cavity flow at mach 2. In *18th Australasian Fluid Mechanics Conference, Launceston, Australia*, 2012.

[203] V Sridhar, SL Gai, and H Kleine. Supersonic flow over a rectangular open cavity: effect of length-to-depth ratio. In *29th International Symposium on Shock Waves 1*, pages 429–434. Springer, 2015.

[204] NR Deepak, SL Gai, and AJ Neely. Aerothermodynamics of hypersonic shock wave boundary layer interactions. In *Proc. of 17th Australian Fluid Mechanics Conference*, 2010.

[205] X Kang, RJ Gollan, PA Jacobs, and A Veeraragavan. Numerical simulations of premixed combustion in narrow channels. In *19th Australasian Fluid Mechanics Conference*. RMIT University, 2014.

[206] KA Damm, RJ Gollan, and PA Jacobs. Verification of the least-squares procedure within an unstructured-grid flow solver. In *20th Australasian Fluid Mechanics Conference*, 2016.

[207] P Jacobs, RJ Gollan, , and many others. Eilmer4. http://cfcfd.mechmining.uq.edu.au/eilmer, 2015.

[208] DA Knoll and DE Keyes. Jacobian-free newton–krylov methods: a survey of approaches and applications. *Journal of Computational Physics*, 193(2):357–397, 2004.

[209] P Jacobs, RJ Gollan, , and many others. D language Gas Dynamic simulation tools for compressible flow. https://bitbucket.org/cfcfd/dgd/, 2015.

[210] ES Oran and JP Boris. *Numerical simulation of reactive flow*. Cambridge University Press, 2005.

[211] MN Macrossan. The equilibrium flux method for the calculation of flows with non-equilibrium chemical reactions. *Journal of Computational Physics*, 80(1):204–231, 1989.

[212] MS Liou. Ten years in the making - AUSM-family. *AIAA Paper*, pages 2001–2521, 2001.

[213] TJ Barth and H Deconinck. *High-order methods for computational physics*, volume 9. Springer Science & Business Media, 2013.

[214] DR Mott. *New Quasi-steady-state and Partial-equlibrium Methods for Integrating Chemically Reacting Systems*. PhD thesis, University of Michigan Ann Arbor, 1999.

[215] WYK Chan. *Effects of flow non-uniformities on the drag reduction by boundary layer combustion*. PhD thesis, University of Queensland, 2012.

[216] J Tu, G-H Yeoh, and C Liu. *Computational Fluid Dynamics: a practical approach, Third Edition*. Butterworth-Heinemann, 2018.

[217] MC Burrows and AP Kurkov. An analytical and experimental study of supersonic combustion of hydrogen in vitiated air stream. *AIAA Journal*, 11(9):1217–1218, 1973.

[218] J-H Kim, Y Yoon, I-S Jeung, H Huh, and J-Y Choi. Numerical study of mixing enhancement by shock waves in model scramiet engine. *AIAA Journal*, 41(6):1074–1080, 2003.

[219] D Papamoschou and A Roshko. The compressible turbulent shear layer: an experimental study. *Journal of fluid Mechanics*, 197:453–477, 1988.

[220] O Zeman. Dilatation dissipation: the concept and application in modeling compressible mixing layers. *Physics of Fluids A: Fluid Dynamics*, 2(2):178–188, 1990.

[221] A Potturi and JR Edwards. Les/rans simulation of a supersonic combustion experiment. *AIAA Paper*, 611:2012, 2012.

[222] M Berglund and C Fureby. Les of supersonic combustion in a scramjet engine model. *Proceedings of the Combustion Institute*, 31(2):2497–2504, 2007.

[223] V Terrapon, R Pecnik, F Ham, and H Pitsch. Full-system rans of the hyshot ii scramjet part 2: Reactive cases. *Annual Research Briefs*, pages 69–80, 2010.

[224] RH Nichols and CC Nelson. Wall function boundary conditions including heat transfer and compressibility. *AIAA journal*, 42(6):1107–1114, 2004.

[225] P Lorrain, B Capra, S Brieschecnk, and R Boyce. A detailed investigation of nominally 2-D radical farming scramjet combustion. In *18th AIAA/3AF International Space Planes and Hypersonic Systems and Technologies Conference*, page 5812, 2012.

[226] P Lorrain, S Brieschenk, and R Boyce. Experimental investigation of inlet-injection radical-farming scramjet combustion. In *XXI International Symposium on Air Breathing Engines (ISABE 2013)*, volume 1, pages 1–9. Curran Associates, 2013.

[227] S Tirtey, R Boyce, M Brown, B Capra, M Creagh, A Dedman, I Dimitrijevic, A Pudsey, B Sharp, P Van Standen, et al. Scramspace: Radical-farming scramjet for access to space. *STO-EN-AVT-234 Hypersonic Flight Testing*, 2014.

[228] U Goldberg, O Peroomian, S Chakravarthy, and B Sekar. Validation of CFD++ code capability for supersonic combustor flowfields. *AIAA paper*, 3271, 1997.

[229] JJOE Hoste, M Fossati, IJ Taylor, and RJ Gollan. Modeling scramjet supersonic combustion via eddy dissipation model. In *68th International Astronautical Congress (IAC), Adelaide*, 2017.

[230] JJOE Hoste, M Fossati, IJ Taylor, and RJ Gollan. Turbulence chemistry interaction via eddy dissipation model for scramjet analysis and design. In *7th European Conference on Computational Fluid Dynamics (ECFD), Glasgow*, 2018.

[231] M Mulas and M Talice. Fully compressible simulation of low-speed premixed reactive flows. In *33rd AIAA Fluid Dynamics Conference and Exhibit*, page 4253, 2003.

[232] B Sekar and HS Mukunda. A computational study of direct simulation of high speed mixing layers without and with chemical heat release. In *Symposium (International) on Combustion*, volume 23, pages 707–713. Elsevier, 1991.

[233] TR Young and JP Boris. A numerical technique for solving stiff ordinary differential equations associated with the chemical kinetics of reactive-flow problems. *The Journal of Physical Chemistry*, 81(25):2424–2427, 1977.

[234] DA Bittker and VJ Scullin. General chemical kinetics computer program for static and flow reactions, with application to combustion and shock-tube kinetics. 1972.

[235] H Pergament. A theoretical analysis of non-equilibrium hydrogen-air reactions in flow systems. In *Hypersonic Ramjet Conference*, page 113, 1963.

[236] RM Kirchhartz, DJ Mee, RJ Stalker, PA Jacobs, and MK Smart. Supersonic boundary-layer combustion: effects of upstream entropy and shear-layer thickness. *Journal of Propulsion and Power*, 26(1):57–66, 2010.

[237] C Fureby, E Fedina, and J Tegnér. A computational study of supersonic combustion behind a wedge-shaped flameholder. *Shock waves*, 24(1):41–50, 2014.

[238] AF Moura, V Wheatley, and I Jahn. Thermofluidic compression effects to achieve combustion in a low-compression scramjet engine. *Shock Waves*, pages 1–13, 2017.

[239] G Iaccarino, A Ooi, PA Durbin, and M Behnia. Reynolds averaged simulation of unsteady separated flow. *International Journal of Heat and Fluid Flow*, 24(2):147–156, 2003.

[240] A Sadiki, A Maltsev, B Wegner, F Flemming, A Kempf, and J Janicka. Unsteady methods (urans and les) for simulation of combustion systems. *International Journal of Thermal Sciences*, 45(8):760–773, 2006.

[241] WH Heiser and DT Pratt. *Hypersonic airbreathing propulsion*. AIAA Education Series, 1994.

[242] JA Schetz, L Maddalena, and SK Burger. Molecular weight and shock-wave effects on transverse injection in supersonic flow. *Journal of Propulsion and Power*, 26(5):1102–1113, 2010.

[243] A Ben-Yakar. *Experimental investigation of mixing and ignition of transverse jets in supersonic crossflows*. PhD thesis, Stanford University, 2000.

[244] Y You, H Lüdeke, and K Hannemann. On the flow physics of a low momentum flux ratio jet in a supersonic turbulent crossflow. *EPL (Europhysics Letters)*, 97(2):24001, 2012.

[245] DW Riggins, CR McClinton, and PH Vitt. Thrust losses in hypersonic engines part 1: methodology. *Journal of Propulsion and Power*, 13(2):281–287, 1997.

[246] JW Slater. Burrows and kurkov supersonic mixing/combustion. http://www.grc.nasa.gov/WWW/wind/valid/bk/bk.html. Last update: 2015-01-14.

[247] W Huang, Z Wang, S Luo, and J Liu. Parametric effects on the combustion flow field of a typical strut-based scramjet combustor. *Chinese Science Bulletin*, 56(35):3871–3877, 2011.

[248] Z-W Huang, G-Q He, F Qin, and X-Q Wei. Large eddy simulation of flame structure and combustion mode in a hydrogen fueled supersonic combustor. *international journal of hydrogen energy*, 40(31):9815–9824, 2015.

[249] J Wu, Z Wang, X Bai, M Sun, and H Wang. The hybrid rans/les of partially premixed supersonic combustion using g/z flamelet model. *Acta Astronautica*, 127:375–383, 2016.

[250] G Choubey, KM Pandey, A Maji, T Deshmukhya, and A Debbarma. Computational investigation of multi-strut injection of hydrogen in a scramjet combustor. *Materials Today: Proceedings*, 4(2):2608–2614, 2017.

[251] Z-W Huang, G-Q He, S Wang, F Qin, X-Q Wei, and L Shi. Simulations of combustion oscillation and flame dynamics in a strut-based supersonic combustor. *International Journal of Hydrogen Energy*, 42(12):8278–8287, 2017.

[252] ND Sandham. Effects of compressibility and shock-wave interactions on turbulent shear flows. *Flow, Turbulence and Combustion*, 97(1):1–25, 2016.

[253] S Sarkar, G Erlebacher, MY Hussaini, and HO Kreiss. The analysis and modelling of dilatational terms in compressible turbulence. *Journal of Fluid Mechanics*, 227:473–493, 1991.

Appendix A

Summary of Literature on Selected Combustors in this Thesis

This Appendix summarizes the numerical studies from the literature performed on the three scramjet configurations selected for investigation of the EDM in this work (Section 5.1). The information is presented in chronological order and information on the turbulence modeling approach, adopted TCI, reaction mechanism and setting for $\mathrm{Pr_t}$, $\mathrm{Sc_t}$ are given when available. The keyword "variable" for the latter parameters indicates a flow dependent setting which requires extra transport equations in order to be specified. Only the first author of the work is listed.

A.1 Burrow-Kurkov

Table A.1: Overview of papers studying Burrows-Kurkov experiment.

Authors	RANS/LES	Turb / Chem	reac mech	$\mathrm{Pr_t}$, $\mathrm{Sc_t}$
Evans [106] (1978)	k-ε	EBU	single-step reaction	$\mathrm{Pr_t} = \mathrm{Sc_t} = 0.7$
Evans [107] (1980)	k-ε	None	7 species, 8 reactions (Spiegler), 12 species, 25 reactions	$\mathrm{Pr_t} = \mathrm{Sc_t} = 0.7$
Ebrahimi [108] (1993)	k-ε	None	8 step reaction mechanism	not specified

Authors	RANS/LES	Turb / Chem	reac mech	Pr_t , Sc_t
D'Angelo [109] (1994, PhD)	k-ε	assumed (beta) PDF (on T, neglect concentration effects)	? 9 species, 22 reactions ?	$Pr_t = 0.9$, $Sc_t = ?$
Parent [119] (2004)	k-ω 1998	None	Jachimowski	$Pr_t = Sc_t = 0.5$
Keistler [141] (2005)	k-ζ, Menter SST	None, assumed PDF	7 species, 7 steps	$Pr_t = 0.5$, $Sc_t = 0.5$ or variable
Engblom [112]	k-ε and k-ω SST	None	Evans-Schexnayder + third body efficiencies of Jachimowski	$Sc_t = 0.9$, $Pr_t = 0.5$ or 0.9
Brinkcman [113] (2007)	k-ε	None	Jachimowski (without N2) = 9 species, 20 reactions	variable
Xiao[191] (2007)	k-ζ (variance of vorticity))	modeling of averages (no PDF)	7 species, 7 reactions (Jachimowski) AND 9 species 19 reactions (Connaire)	variable
Keistler [192] (2009)	k-ζ	modeling of averages (no PDF)	7 species, 7 reactions (Jachimowski) AND 9 species 19 reactions (Connaire)	variable
Bhagwandin [127] (2009)	k-ω SST	None	different including 1 step and Evans-Schexnayder	$Pr_t = Sc_t = 0.7$

Authors	RANS/LES	Turb / Chem	reac mech	Prt, Sct
Edwards [101] (2012)	hybrid RANS (k-ω SST)-LES (95 % LES)	None and Gaussian quadratue	7 species (Drummond, Eklund) and 9 species (Jachimowski)	$\mathrm{Pr_t}$ = 0.9, $\mathrm{Sc_t}$ = 0.5
Huang [104] (2012)	Spalart-Allmaras	None	2-step and 7-step	$\mathrm{Sc_t}$ = 0.7, $\mathrm{Pr_t}$ = 0.85
Gao [129] (2015)	k-ω SST	None	7 species, 8 reactions (Spiegler)	$\mathrm{Pr_t}$ = $\mathrm{Sc_t}$ = 0.9
NASA online [246] (? 2015)	k-ω SST	None	13 species, 27 reactions	$\mathrm{Pr_t}$ = $\mathrm{Sc_t}$ = 0.7

Table A.2: Supersonic inflow profile for second part of simulation (half channel, symmetry) : part 1.

y (cm)	**p (Pa)**	**T (K)**	**u (m/s)**	**v (m/s)**	**k (m^2/s^2)**	**ω (1/s)**
0.4763	97433	451	132	-0.608	101	367617700
0.4768	96971	644	332	-0.936	2170	106168200
0.4774	96433	745	456	-0.748	4980	55062730
0.4781	96057	805	540	-0.436	6856	34942210
0.4788	95836	847	603	-0.274	8135	24603460
0.4796	95694	878	653	-0.184	9061	18447870
0.4804	95597	903	695	-0.130	9766	14421930
0.4814	95527	924	732	-0.096	10325	11612120
0.4824	95475	942	765	-0.072	10782	9555960
0.4836	95435	958	795	-0.055	11165	7996324
0.4848	95403	973	823	-0.042	11492	6779713
0.4862	95377	985	849	-0.031	11776	5809227
0.4877	95357	997	874	-0.022	12026	5020869
0.4893	95340	1008	897	-0.015	12247	4370771
0.4911	95326	1018	919	-0.008	12444	3827911
0.4931	95315	1028	941	-0.002	12621	3369763
0.4953	95306	1037	962	0.004	12781	2979590
0.4977	95299	1046	982	0.010	12925	2644712
0.5003	95294	1054	1002	0.016	13055	2355349
0.5032	95291	1061	1021	0.022	13173	2103845
0.5063	95288	1069	1040	0.028	13278	1884125
0.5098	95287	1076	1058	0.035	13373	1691304
0.5136	95288	1083	1077	0.042	13456	1521417
0.5177	95290	1089	1095	0.050	13529	1371208
0.5222	95293	1096	1113	0.059	13591	1237985
0.5272	95297	1102	1130	0.069	13643	1119499
0.5327	95303	1108	1148	0.079	13684	1013858
0.5387	95310	1114	1165	0.091	13713	919464
0.5452	95319	1119	1183	0.104	13731	834952
0.5524	95330	1125	1200	0.119	13737	759156
0.5603	95342	1130	1217	0.135	13729	691070
0.5689	95356	1135	1235	0.154	13708	629810
0.5783	95373	1140	1252	0.174	13672	574610
0.5886	95392	1145	1269	0.197	13619	524802
0.5999	95413	1150	1286	0.223	13549	479803
0.6123	95437	1154	1304	0.252	13459	439100
0.6258	95465	1159	1321	0.284	13349	402243
0.6406	95495	1163	1338	0.321	13216	368832
0.6568	95530	1167	1356	0.361	13058	338516

Table A.3: Supersonic inflow profile for second part of simulation (half channel, symmetry): part 2.

y (cm)	**p (Pa)**	**T (K)**	**u (m/s)**	**v (m/s)**	**k** (m^2/s^2)	ω **(1/s)**
0.6744	95568	1171	1373	0.407	12873	310978
0.6937	95611	1175	1391	0.459	12659	285938
0.7148	95659	1179	1409	0.516	12411	263145
0.7378	95712	1183	1427	0.581	12128	242371
0.7629	95772	1187	1445	0.654	11807	223412
0.7903	95838	1191	1463	0.737	11444	206086
0.8201	95910	1195	1481	0.830	11038	190232
0.8526	95990	1199	1500	0.935	10585	175697
0.8880	96078	1203	1519	1.053	10079	162305
0.9265	96174	1207	1538	1.183	9516	149897
0.9683	96280	1211	1558	1.324	8887	138288
1.0137	96397	1214	1578	1.476	8188	127325
1.0630	96523	1218	1598	1.635	7420	116884
1.1164	96659	1222	1618	1.804	6589	106855
1.1742	96809	1225	1637	1.995	5691	97008
1.2366	96971	1229	1658	2.218	4713	86905
1.3041	97143	1232	1679	2.469	3652	76062
1.3768	97317	1236	1701	2.710	2537	64059
1.4551	97473	1241	1721	2.885	1473	51158
1.5393	97582	1245	1737	2.940	670	39426
1.6296	97630	1248	1745	2.911	330	33348
1.7264	97640	1249	1747	2.883	267	32082
1.8298	97636	1250	1748	2.866	260	31944
1.9400	97628	1250	1748	2.841	260	31931
2.0573	97615	1250	1748	2.798	260	31928
2.1819	97596	1250	1748	2.729	260	31926
2.3137	97572	1250	1748	2.629	260	31924
2.4529	97540	1250	1748	2.493	260	31921
2.5995	97501	1249	1748	2.318	260	31917
2.7533	97455	1249	1748	2.105	259	31912
2.9142	97403	1249	1748	1.859	259	31907
3.0820	97347	1249	1748	1.592	259	31902
3.2563	97290	1249	1749	1.316	259	31897
3.4368	97236	1249	1749	1.047	259	31892
3.6230	97186	1249	1749	0.800	259	31888
3.8143	97143	1248	1749	0.585	259	31884
4.0101	97108	1248	1749	0.408	259	31881
4.2096	97081	1248	1749	0.270	259	31878
4.4121	97062	1248	1749	0.166	259	31877
4.6168	97050	1248	1749	0.088	259	31876
4.8228	97044	1248	1749	0.028	259	31875

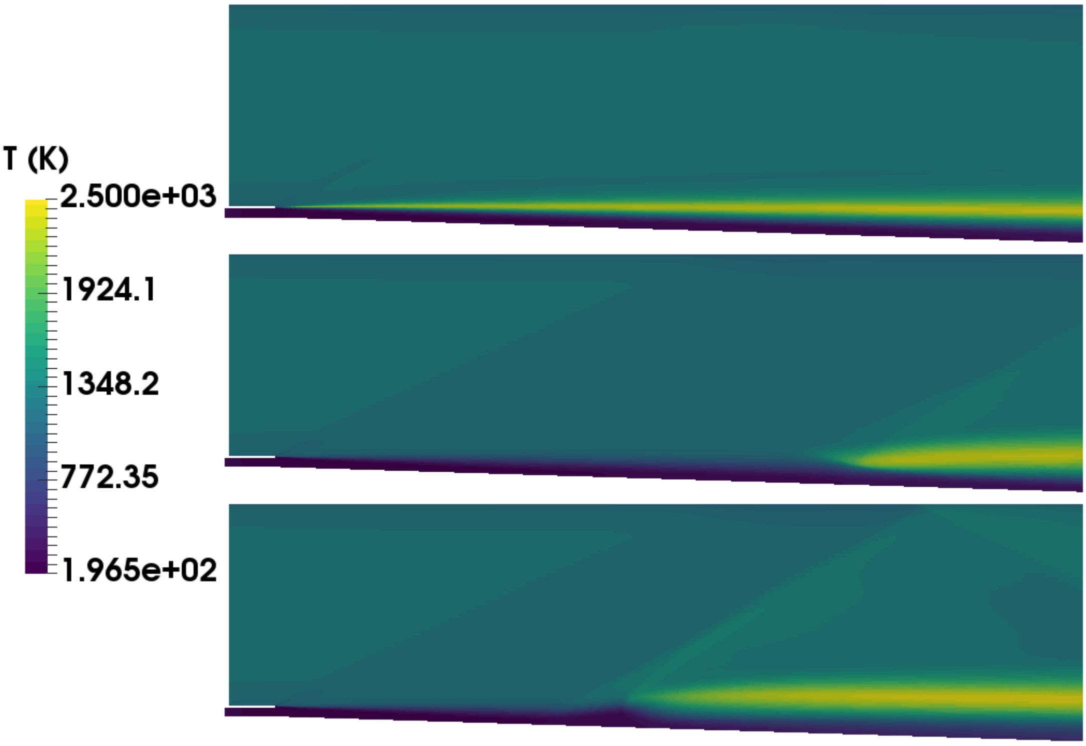

Figure A.1: Temperature contour with from top to bottom: EDM (A_{edm} = 6), E-S, EDM zone (A_{edm} = 4).

A.2 DLR

Table A.4: Overview of papers studying DLR experiment numerically.

Authors	Turb	Turb / Chem	reac mech	Prt, Sct	BC
Oevermann [111] (2000)	k-ε	flamelet	Maas and Warnatz, 9 species	Le=1, Pr_t = Sc_t = 0.7	inviscid slip walls
Berglund et al. [222] (2007)	LES	flamelet	two -step, Rogers and Clinitz	?	adiabatic no-slip walls
Genin et al. [97] (2010)	LES	none	7 reactions (Eklund / Baurle)	Pr_t = 0.4 - 0.9, Sc_t = 0.7	slip up/ low, adiabatic no-slip strut

Authors	Turb	Turb / Chem	reac mech	Prt, Sct	BC
Mura et al. [115] (2010)	k-ε	MIL	Jachimowski, 13 sp, 33 reac	Sc_t = 0.7 , Pr_t = ?	inviscid slip walls
Huang et al. [247] (2011)	k-ω SST	EDM	1,2step Rogers and Clinitz	?	no-slip (adiabatic?)
Potturi et al. [221] (2012)	RANS / LES, k-ω SST	none	9 sp, 18 reac (Jachimowski), 7 sp, 7 reac (Jachimowski)	Sc_t = Sc = 0.5, Pr_t = 0.9 , Pr = 0.72	no slip adiabatic everywhere
Dharavath et al. [117] (2013)	k-ε	EDM	1 step	Sc_t = 0.9, Pr_t = ?	no-slip adiabatic
Potturi et al. [99] (2014)	RANS / LES k-ω SST	none / PaSR	Connaire, Jachimowski	Sc_t = Sc = 0.5, Pr_t = 0.9 , Pr = 0.72	no slip adiabatic everywhere
Gao et al. [144] (2014)	k-ω SST	flamelet / none	7sp 8 reac, 9sp, 19 reac	Pr_t = Sc_t = 0.9 , Le=1	no-slip (adiabatic?)
Hou et al. [131] (2014)	k-ω SST	flamelet	9 sp, 19 reac of Maas and Warnatz	?	no-slip (adiabatic?)
Fureby et al. [237] (2014)	LES	PaSR / flamelet	2step Rogers and Clinitz, 7step Davidenko	Sc_s individual species , Sc_t =0.7, Pr_t = 0.9	no-slip adiabatic
Huang et al. [248] (2015)	LES	PaSR	9sp, 27reac	?	slip walls
Wu et al. [249] (2016)	RANS / LES, Menter BSL	no-model, flamelet	9sp, 19 reac	?	slip uper/lower, no slip adiabatic strut
Choubey et al. [250] (2017)	k-ω SST	EDM	1 step	?	slip?
Kummitha [145] (2017)	k-ε, k-ω SST, LES	none	1 step	?	no-slip, adiabatic?
Huang et al. [251] (2017)	LES	PaSR	9sp, 27 reac	?	slip walls

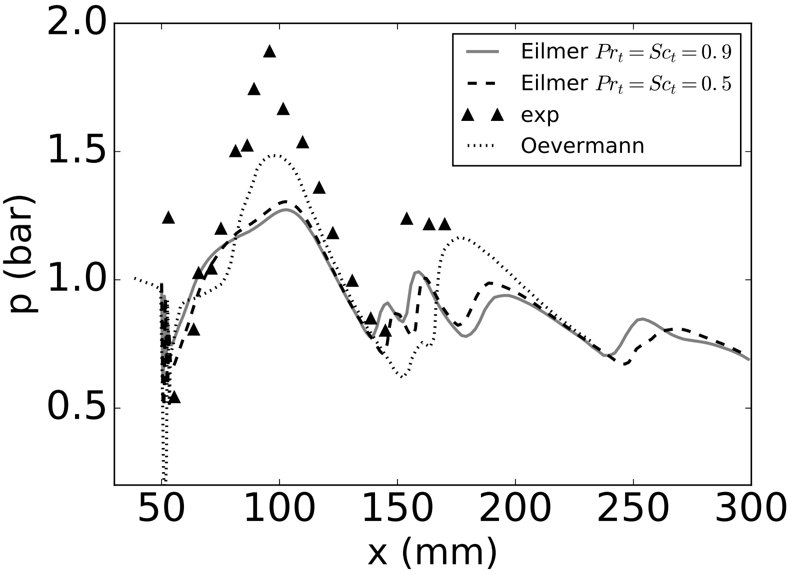

Figure A.2: Profile of pressure along the centerline in the non-reacting DLR configuration.

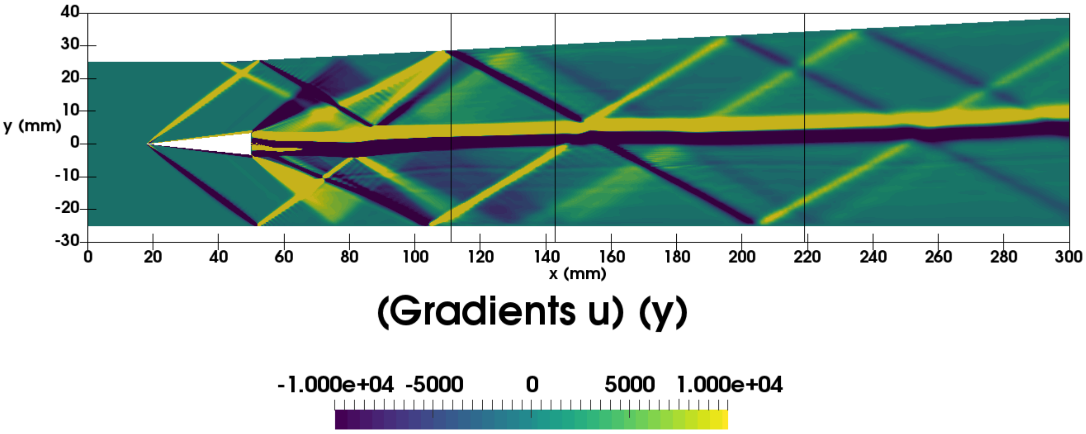

Figure A.3: Vertical component of the gradient of streamwise velocity in the non-reacting DLR configuration. $\mathrm{Pr_t} = \mathrm{Sc_t} = 0.5$

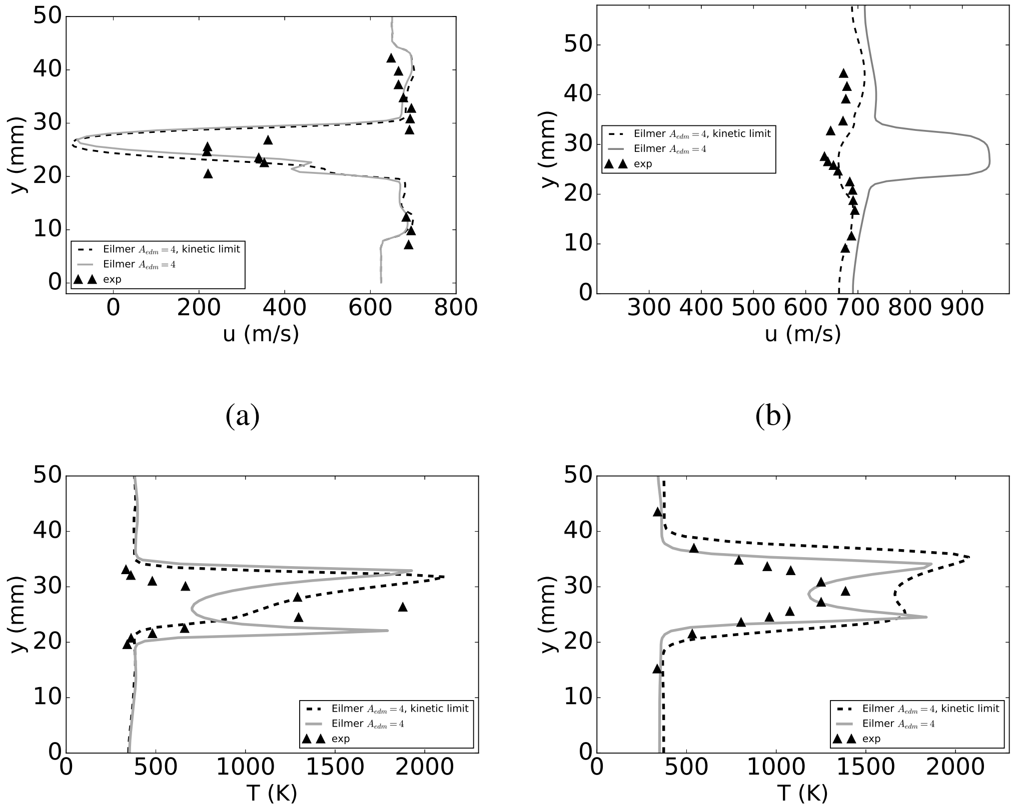

(a)

(b)

(c)

(d)

Figure A.4: Effect of kinetic limit (A_{edm} = 4) on the DLR combustor profiles of streamwise velocity at axial locations (a) x = 64 mm , (b) x = 193 mm and temperature at (c) x = 111 mm, (d) x = 219 mm. $Pr_t = Sc_t = 0.9$.

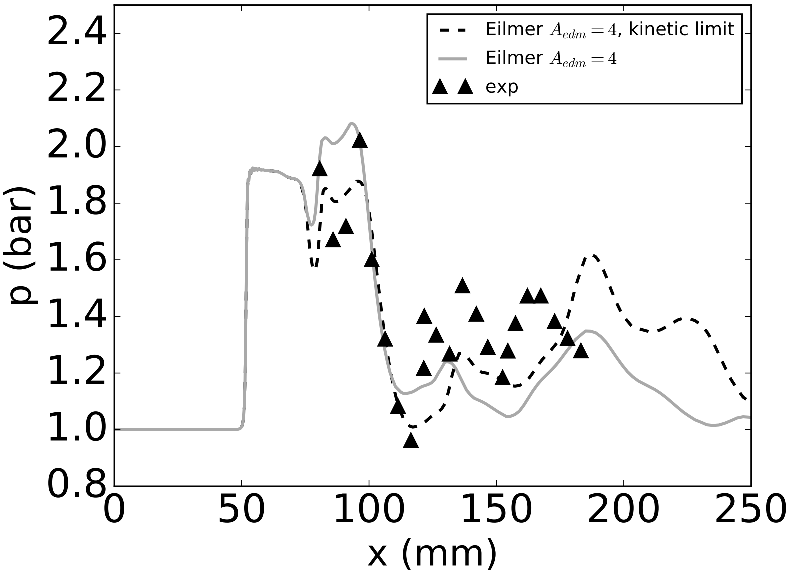

Figure A.5: Effect of kinetic limit (A_{edm} = 4) on the lower wall pressure for the DLR combustor with $Pr_t = Sc_t = 0.9$

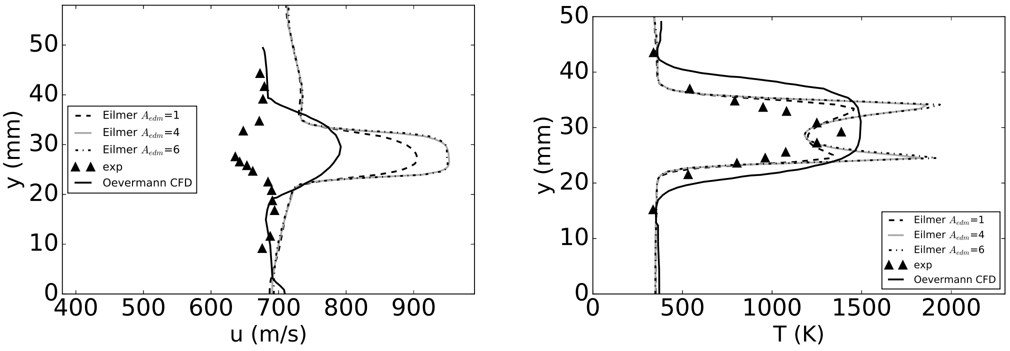

(a) (b)

Figure A.6: Effect of A_{edm} on the streamwise velocity and (b) temperature in the DLR combustor at axial locations (a) x = 193 mm, (b) x = 219 mm with $Pr_t = Sc_t = 0.9$.

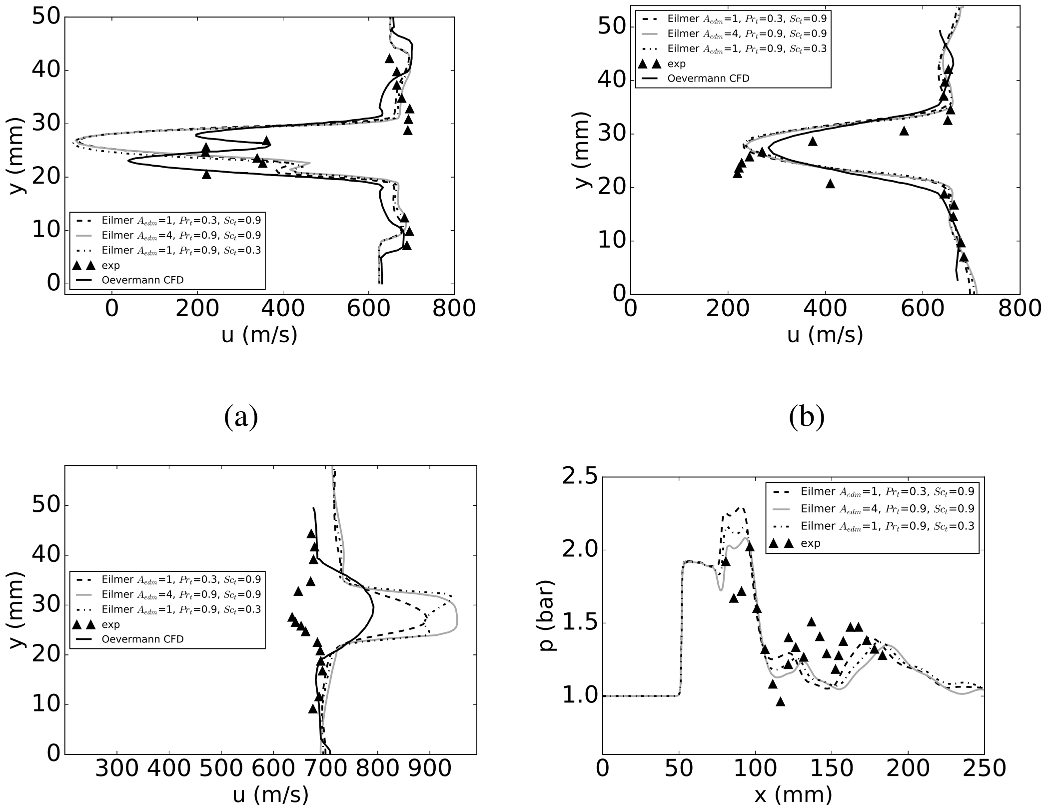

(a)

(b)

(c)

(d)

Figure A.7: Effect of A_{edm}, $Pr_t = Sc_t$ on the streamwise velocity in the DLR combustor at axial locations (a) x = 64 mm, (b) x = 111 mm, (c) x = 193 mm and (d) lower wall pressure.

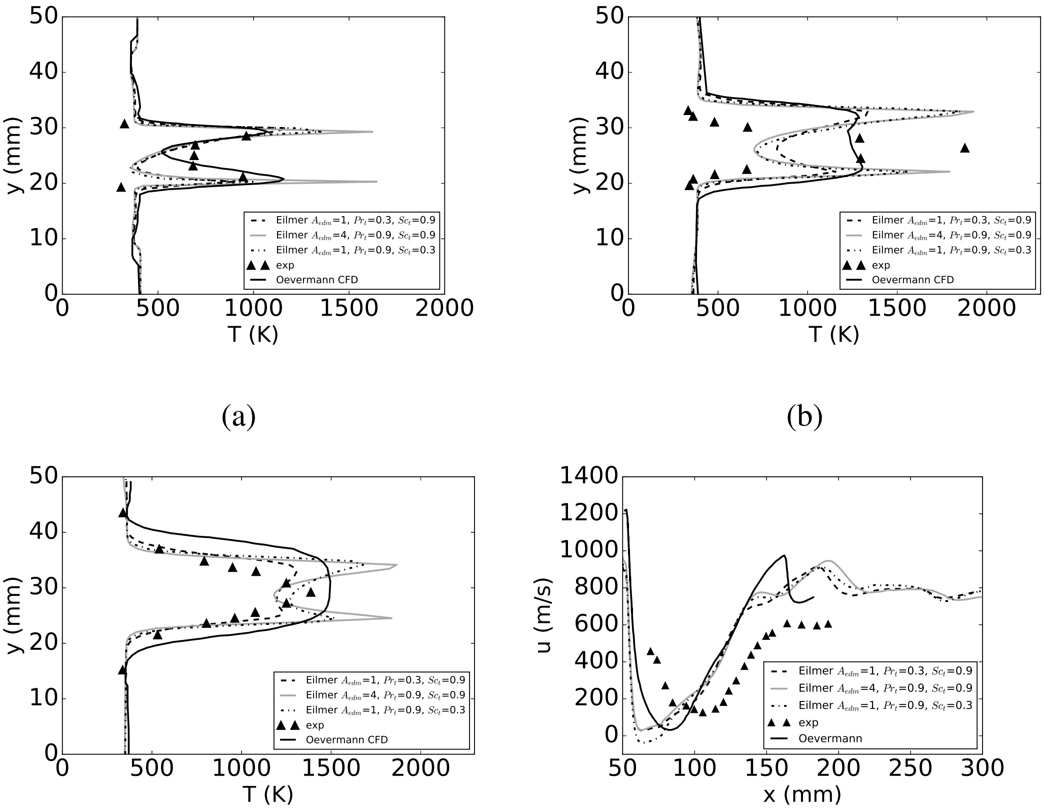

(a)

(b)

(c)

(d)

Figure A.8: Effect of A_{edm}, $Pr_t = Sc_t$ on the temperature in the DLR combustor at axial locations (a) x = 64 mm, (b) x = 111 mm, (c) x = 219 mm and (d) centerline velocity.

A.3 HyShot II

Table A.5: Overview of papers studying the HyShot II combustor numerically.

Authors	Turb	Turb / Chem	reac mech	Prt, Sct
Karl [102] (2008)	Spalart-Allmaras, k-ω	none, assumed PDF	modified Jachimowski	$\mathrm{Pr_t}$ = 0.9 ? and $\mathrm{Sc_t}$ = 0.35 ?
Terrapon [103] (2009)	Spalart-Allmaras	flamelet	9sp, 28 reac	$\mathrm{Pr_t}$ = 0.5 and $\mathrm{Sc_t}$ = 0.5
Terrapon [223] (2010)	k-ω SST	flamelet	9sp, 28 reac	$\mathrm{Pr_t}$ = 0.5 and $\mathrm{Sc_t}$ = 0.5
Karl [86] (2011)	Spalart-Allmaras, k-ω SST, k-ω	none, assumed PDF	modified Jachimowski	$\mathrm{Pr_t}$ = 0.9 and $\mathrm{Sc_t}$ = 0.35,0.7, 1.4
Fureby [96] (2011)	RANS (Spalart-Allmaras) / LES	presumed PDF for RANS, PaSR for LES	9 sp, 19 reac for RANS / 7 sp, 7 reac for LES	?
Pecnik [105] (2012)	Spalart-Allmaras, k-ω SST	flamelet	9sp, 28 reac	$\mathrm{Pr_t}$ = 0.5,0.9 and $\mathrm{Sc_t}$ = 0.35,0.5,0.9
Karl [56] (2012)	Spalart-Allmaras (URANS)	none	modified Jachimowski	$\mathrm{Pr_t}$ = 0.9 ? and $\mathrm{Sc_t}$ = 0.7
Chapuis [146] (2013)	RANS (k-ω) / LES	presumed PDF for RANS, PaSR for LES	9 sp, 19 reac for RANS / 7 sp, 7 reac for LES	?

Appendix B

Dilatation Dissipation Correction

The idea behind the introduction of a compressibility correction can be traced back to the early work of Papamoschou and Roshko [219] on compressible turbulent shear layers. The motivation of their experiment follows from a previous observation that a turbulent shear layer with one supersonic stream and one stream at rest (such as e.g. jet in stationary air) spreads more slowly, i.e. lower growth rate, than an incompressible shear layer. They wanted to find a way to describe the effect by introducing an adequate parameter which became known as the convective Mach number ($\mathrm{M_c}$). To do so, ten experimental settings at different Mach numbers and with different test gases were investigated [219]. $\mathrm{M_c}$ is defined as

$$M_c = \frac{U_1 - U_c}{a_1} = \frac{U_c - U_2}{a_2} \tag{B.1}$$

and can be interpreted as the free stream Mach number seen by a turbulent eddy convecting downstream at a velocity $\mathrm{U_c}$ [252]. The latter parameter represents the velocity of the dominant waves and structures and is defined as (for streams with equal ratio's of heat capacities)

$$U_c = \frac{(U_1\, a_2 + U_2\, a_1)}{a_1 + a_2} \tag{B.2}$$

with U_i and a_i the velocity and sonic speed. The subscript 1 refers to the faster of the two streams. From a convective Mach number of about 0.5 [86, 219, 220], the shear layer growth rate reduces significantly (≈ 1/5th of the incompressible growth rate) due to compressibility effects. A correction is consequently required to account for this effect. Without it, the eddy viscosity turbulence model will overpredict the spreading rate of a shear layer. In the search for a physical explanation of the growth rate dependence on $\mathrm{M_c}$, Zeman [220] introduced the concept of dilatation dissipation ε_d.

The author postulates the existence of so-called eddy shocklets which are responsible for ε_d. Moreover, the dilatation dissipation is found dependent on the rms or turbulent Mach number $\mathrm{M_t}$ (Equation 3.22) and is included in the proposed compressibility correction. The latter parameter is itself dependent on the convective Mach number and Zeman demonstrates that the proposed model follows experimental trends of mixing layer growth rates as a function of $\mathrm{M_c}$. Sarkar et al. [253] introduced a similar formulation with a monotone increase of the dilatation dissipation as a function of $\mathrm{M_t}$ based on fundamentally different assumptions. However, it has been shown in subsequent research that the effect of dilatation dissipation is extremely small in practical flows where the Reynolds number is high [136]. Nevertheless, the corrections of Sarkar and Zeman correlate well with the decrease in shear layer growth as a function of convective Mach number. This in turn explains the note in Section 3.2 stating that the corrections are useful, albeit for the wrong reasons. Both corrections are developed specifically for free shear flows and have an undesirable effect on boundary layers. Wilcox [136] introduced a compressibility correction, based on the Zeman / Sarkar formulations, which does minimize the undesired effects on boundary layers. It is therefore considered in the present work.